Assessment of therapy response and differentiation between tumor recurrence and therapy-related effects in high-grade glioma using PET and MRI

Julie Bolcaen

Thesis submitted to obtain the degree of Doctor in Medical Sciences

2017

Promotor: Prof. Dr. Ingeborg Goethals

Copromotor: Prof. Dr. Ing. Christian Vanhove & Prof. Dr. Karel Deblaere

About the cover: The cover is a selection of images acquired throughout my thesis.

Upper row:

^{18}F-FDG PET of F98 rat glioblastoma (Molecubes β-cube)

CE-T1 MRI of F98 rat glioblastoma (Pharmascan Bruker BioSpin)

Evans Blue leakage on frozen rat brain with a radiation necrosis lesion

Middle row:

γH2AX staining on a rat brain tissue section 1 h post-irradiation (3*3 mm beam)

^{18}F-FDG PET/CT of F98 rat glioblastoma (Molecubes X and β-cube)

HE staining of F98 rat glioblastoma

Bottom row:

Small animal radiation research platform (SARRP)

CE-T1 MRI of human glioblastoma (3T Siemens Trio Trim scanner)

^{18}F-FCho PET of human glioblastoma (PET Allegro Philips system)

Members of the Examination Committee

Prof. Dr. Ir. Carlos De Wagter
Department of Radiation Oncology, Ghent University Hospital, Belgium

Prof. Dr. Eric Achten
Department of Radiology, Ghent University Hospital, Belgium

Prof. Dr. Ir. Roel Vanholen
IBiTech-MEDISIP, Department of Electronics and Information Systems, Ghent University, Belgium

Prof. Dr. Rudi Dierckx
Department of Nuclear Medicine and Molecular Imaging, University Medical Center Groningen, The Netherlands

Prof. Dr. Steven De Vleeschouwer
Department of Neurosurgery, Leuven University Hospital, Belgium

Dr. Ir. André Dobbeleir
Department of Nuclear Medicine, Ghent University Hospital, Belgium

Dr. Ken Kersemans
Department of Nuclear Medicine, Ghent University Hospital, Belgium

Members of the Supervisory Committee

Prof. Dr. Filip De Vos
Department of Radiopharmacy, Ghent University, Belgium

Prof. Dr. Christophe Van De Wiele
Department of Nuclear Medicine, AZ Groeninge, Belgium

The author and promotors give the authorization to consult and to copy parts of this thesis for personal use only. Any other use is limited by the Laws of Copyright, especially concerning the obligation to refer to the source whenever results are cited from this thesis.

De auteur en promotoren geven de toestemming dit proefschrift voor raadpleging ter beschikking te stellen en delen ervan te kopiëren voor persoonlijk gebruik. Elk ander gebruik valt onder de beperking van het auteursrecht, in het bijzonder tot de verplichting de bron te vermelden bij het aanhalen van resultaten uit deze thesis.

Gent, March 2017,

Julie Bolcaen

Dankwoord

Eerst en vooral wil ik mijn promotor Prof. Ingeborg Goethals bedanken om me de kans te geven om te doctoreren op de dienst Nucleaire Geneeskunde en een boeiend onderwerp aan te reiken in het vakgebied van de neuro-oncologie. Bedankt om in me te geloven en me zelfstandig keuzes te laten maken. Bedankt voor de leuke samenwerking, voor uw ideeën en om mijn teksten na te lezen. Bedankt om me de kans te geven om mijn resultaten te presenteren op nationale en internationale congressen en opleidingen te volgen om me verder te verdiepen in mijn onderwerp. Door deze ervaringen ben ik echt gegroeid en hopelijk kunnen we onze passies voor onderzoek nog verder zetten.

Ik wil ook Prof. Christian Vanhove bedanken voor zijn onvoorwaardelijke steun en geloof. Chris, bedankt om er altijd te zijn als ik vragen had, bedankt voor de aangename samenwerkingen, discussies en uw wetenschappelijke input. Zonder u was mijn thesis nooit zo'n succes geworden. Het was altijd boeiend om uw inzichten en mening te horen over mijn zoveelste dilemma en dit werkte heel motiverend. Hopelijk kunnen we dit in de toekomst verder zetten.

Mijn tweede co-promotor Prof. Karel Deblaere wil ik ook graag bedanken voor uw hulp bij mijn praktische vragen en om me wegwijs te brengen in de complexe MRI wereld. De vele discussies over onverwachte MRI beelden van de proefdieren zal ik nooit vergeten en je kon me altijd raad geven bij het nemen van een beslissing en dit stelde me gerust.

Verder wil ik Prof. Filip De Vos bedanken voor zijn wetenschappelijke input, het beschikbaar stellen van het radiofarmacie labo indien ik dit nodig had en er altijd te zijn als ik vragen had. Zonder uw input was ik er zeker niet in geslaagd om kinetische modellering van PET tot een goed einde te brengen.

Mijn promotoren wil ik ook bedanken voor de oneindig leuke herinneringen in en naast het werkveld, tijdens de congressen en sociale events.

Verder wil ik al mijn collega's bedanken voor de motiverende gesprekken en de aangename werksfeer. Eerst wil ik Koen en Gilles bedanken om me te verwelkomen in de bureau als ik begon met mijn doctoraat. Ik voelde me meteen thuis. Bedankt Koen om me alles aan te leren en uw kennis door te geven om me klaar te stomen voor wat komen zou. Na een lange periode alleen in de bureau was ik blij toen Julie Schatteman me kwam vergezellen. We konden het meteen met elkaar vinden ☺. Bedankt voor de leuke gesprekken, voor de motiverende woorden en om samen te vloeken en te lachen. Ik wens je alle geluk toe met je wondertje en veel succes met je verder onderzoek en carrière.

Bedankt Scharon om me te introduceren in het proefdierwerk met alle ups en downs die er mee gepaard gingen. Bedankt voor alle hulp bij de experimenten en de leuke gesprekken tussen door (in het plat West-Vlaams dan nog ☺). De vele momenten samen in het lab brachten ons dichter bij elkaar. Ik ben blij dat we blijvend contact hebben en kijk altijd uit naar een nieuwe reuni met Sara.

Bedankt Bene voor de leuke tijd samen op Infinity. Uw MRI kennis was van goudwaarde maar naast uw wetenschappelijke input wou ik je bedanken voor de leuke samenwerking. Ik vergeet nooit het moment wanneer we tot 's avonds aan het vloeken waren op het plaatsen van intraveneuse lijntjes terwijl we de choline activiteit zagen wegtikken ☺, stressssss. Bedankt om er altijd te zijn als ik hulp nodig had tijdens de experimenten, om teksten na te lezen en voor je mening over alle wetenschappelijke dilemma's. Ik wens jou en Joris en kleine Benoit alle geluk toe!

Bedankt aan het secretariaat, Denise, Tina, Els, Nathalie en Eva om er te zijn als ik jullie nodig had, om de MOC blaadjes af te printen en de verfrissende gesprekken tussen door ☺. Denise, Isabel en Nathalie wil ik special bedanken voor de vele paperassen die gepaard gingen met de vele congressen. Els wil ik hard bedanken om alle documenten van de choline studie bij te houden en een duidelijk overzicht te maken. Dit heeft me veel werk gespaard!

Liefste Sara en Val, we zijn in de laatste jaren goeie vriendinnen geworden. Bedankt voor de aanmoedigende gesprekken op en naast het werk, de steun in goeie en moeilijkere periodes en het vertrouwen. Merci voor de ontelbare zalige momenten op congres, de middag lunchjes, het afzien tijdens de spinning met den Hugo, de 'girls-nights' na het werk zonder een seconde stilte, de gelnagels, de

slappe lach momenten (inclusief de high-tech WC in Seoul ☺),… En er zullen zeker nog ontelbare mooie momenten volgen, waaronder een must: Hawaii-reuni ☺ #BFFs.

Lieselotte wil ik bedanken om me te introduceren in de wereld van kinetische modellering. Zonder jou begreep ik het waarschijnlijk nog niet ☺. Naast je kennis wou ik je ook bedanken voor de vele gesprekken over het werk maar ook daar buiten. We houden contact en ik wens je heel veel liefde toe met je tweede spruit!

Alle artsen, verpleegkundigen en artsen in opleiding van de dienst wil ik graag bedanken voor de aangename werksfeer en middagpauzes. Bedankt om de patiënten in de choline studie met alle goede zorgen te scannen. Ik zal niet iedereen opsommen want ik vergeet sowieso iemand maar wou toch Peggy bedanken voor je aanstekelijke lach, Glenn en Theo voor jullie opgewektheid als we elkaar even kruisten en Stephanie voor je positieve vibes in de groep. Philippe zou ik ook graag bedanken om alles in goede banen te leiden. Ook bedankt aan Pieterjan, Kathia, Dieter, Amelientje, Bliede,… voor de motiverende gesprekken. De ingenieurs Yves, Johan en André wil ik eveneens bedanken voor hun hulp bij wat meer technische vragen en om me vooruit te helpen indien nodig!

Verder wil ik het cyclotron hard bedanken voor de vele producties in het kader van mijn onderzoek. Filip, Jan, Cedric, John, Lieselotte, Nick, Sam, Ken, Johan, Glenn,… bedankt om altijd klaar te staan en om me wat activiteit te laten stelen.

Bedankt ook aan alle collega's van het FFW! Bedankt Jeroen voor de leuke samenwerking in de laatste jaren en bedankt dat ik je mocht stalken de dagen voor mijn interne verediging ☺. Bedankt voor het nalezen van mijn thesis en voor je kritische vragen. Bedankt om te helpen bij experimenten, altijd klaar te staan en me te vergezellen naar de MOC en onze zalige momenten in Zürich (wanneer opnieuw Negroni-tijd☺?). Nick en Ken wil ik bedanken voor hun hulp doorheen mijn doctoraat en de onvergetelijke 100 uur trektocht door Zuid-Korea. Dit was echt onvergetelijk!!! Kim, Caroline, Stef, Glenn, Tristan, Valerie, Nico en Ghilaine wil ik bedanken voor de leuke momenten in het lab maar zeker naast het lab, tijdens lunchjes en de onvergetelijke sportdagen, etentjes en als er eens gevierd moest worden ☺.

Prof. Anne Vral en Leen Pieters zou ik graag bedanken voor de hulp bij de H&E en immuunkleuringen van de rattencoupes. Ook was de γH2AX bundelkleuring nooit gelukt zonder de hulp van Prof. Leybaert en Elke Decrock. Bedankt voor dit mooie resultaat! Dr. Caroline Van den Broecke zou ik ook graag bedanken voor het bekijken van alle gekleurde rattencoupes. Zonder uw input was het niet mogelijk geweest om bepaalde conclusies te trekken.

Ik wil ook graag de dienst neurochirurgie en de dienst radiotherapie van het UZGent bedanken, in het bijzonder Prof. Tom boterberg, voor zijn inzet in het includeren van patiënten in de choline studie. De inclusies verliepen niet van een leien dakje maar toch bleef u gemotiveerd om de studie voor te stellen aan de glioma patiënten. Ook wil ik u bedanken voor uw wetenschappelijke input en hopelijk kan het onderzoek verder gezet worden met de nieuwe DPBN studie in glioma.

Prof. Jean-Pierre Kalala en Dr. Giorgio Hallaert zou ik graag bedanken voor hun hulp bij de talrijke inoculaties van de ratten. Zonder jullie hulp ging dit zeker niet zo vlot gaan en het was altijd een aangename samenwerking. Ook bedankt voor jullie inspanningen bij inclusies van patiënten in de choline studie.

Dr. Marjan Acou zou ik ook graag bedanken voor de samenwerking in de voorbije jaren. We hadden samen heel veel ideeën en konden er blijven over discussiëren. Bedankt voor je input en je motivatie. Ik wens je veel succes met je verder onderzoek!

Ook bedankt aan de collega's van MEDISIP voor de hulp bij meer technische vraagstukken. Bedankt Prof. Roel Vanholen, Stijn, Carmen en Karen om te geloven in het project in verband met de textuuranalyse en me te helpen bij het maken van de software en interpretatie van de resultaten. Ik geloof sterk in het slagen van het radiomics project in de toekomst.

Mijn thesisstudenten Kelly en Josephine zou ik ook graag bedanken voor hun hulp bij de experimenten. Ik heb geluk gehad met gedreven studenten zoals jullie.

Graag zou ik ook alle leden van het BMIC organiserend comité bedanken. In het bijzonder de jarenlange samenwerking met Elisabeth, Sam, Sara, Rafael en Carlien! Het organiseren van jaarlijkse symposia en sociale events was heel leerrijk en veel fun!!

Last but not least wil ik mijn familie en vrienden bedanken. Ma, pa, Céline, Jérôme, Alain, Tatie, bedankt om er altijd te zijn en om in me te geloven! Mijn ouders wil ik speciaal bedanken voor de kansen die ze me gegeven hebben en de vrijheid om mijn doelen te bereiken op en naast het werk. Bedankt om in me te geloven en altijd klaar te staan.

Mijn motivatie had ik ook nooit kunnen aanhouden zonder mijn schat aan vrienden. Bedankt zeugen 🐷 om er altijd te zijn ☺!!! Bedankt voor de vele ontspanningen, oneindige tettermomenten en lieve woorden als ik het nodig had. Ik ben echt een bofkont met jullie (Petra, Jessie, Lien, Drieke, Marlies, Jasmijn, Marieke, Lies, Caro, Anne-Sophie, Emma, Silke, Marie,…). De mannelijke aanhangsels, aka de beren, wil ik ook bedanken voor de leuke momenten in mijn vrije tijd. In het bijzonder de 3 broers, met alle ups and downs in de voorbije jaren en de familie Essel voor alle steun en om in me te geloven. Drieke wil ik speciaal bedanken voor de steun in moeilijke momenten. Mijn doctoraat halen was ook nooit gelukt zonder Liezie; na het college, studies en samen doctoreren kennen we elkaar door en door en begrijpen we elkaar zo goed. Bedankt voor alles poedie en zoveel liefde voor je twee (drie) ventjes. Verder wil ik ook de andere sexy meiskes bedanken voor alle leuke tussendoortjes ;) : Abbie, Lisa, Jolle, Hanny en Els. Natuurlijk kan ik de BMW-chicks niet vergeten: Sofie, Lieselotte, Liezie en Florence, merci voor de steun en de vele topmomenten, onze band is voor levenslang! Bedankt ook Petra en Caro voor de vele avonturen in het buitenland, om mijn gedachten even volledig te verzetten en te laten in zien hoe mooi de wereld is, met alle wanderlust tot gevolg. Ik kijk zo uit naar onze zotte avonturen over de hele wereld Peetje 🌍!!

Finaal ne dikke merci aan iedereen die ik vergeten ben ☺

Julie

Table of contents

Chapter 1. General Introduction

Chapter 2: Biological imaging in neuro-oncology

DSC-MRI
MR-spectroscopy

PART II: PET IN NEURO-ONCOLOGY

    A. PET
    B. Image-degrading effect in PET
    C. PET tracers in neuro-oncology
             ^{18}F-Fluorodeoxyglucose [^{18}F-FDG]
             ^{18}F-Fluoroethyltyrosine [^{18}F-FET]
             ^{18}F-Fluoromethylcholine [^{18}F-FCho]
             Hypoxia-PET
             ^{18}F-fluorothymidine [^{18}F-FLT]

PART III: IMAGE ANALYSIS OF PET AND MRI

    A. Semi-quantitative image analysis
            PET
            DCE-MRI
    B. Quantitative image analysis
            Kinetic modeling in PET
            Graphical analysis in PET
                     Patlak plot or Patlak/Gjedde plot
                     Logan plot
            Kinetic modeling in DCE-MRI
            Model selection criteria

PART IV: SPECIFICS OF SMALL ANIMAL PET AND MRI

    A. Small animal PET
    B. Small animal MRI
    C. Data analysis in small animal imaging

REFERENCES

Chapter 3. Scope and aims

    A. Therapy response assessment in GB as early as possible using PET and MRI

        Question 1   Are we able to assess therapy response in glioblastoma patients post-treatment using ^{18}F-FCho PET and MRI according to the RANO criteria?

        Question 2   Are we able to assess the effect of therapy in a rat model of GB using PET and MRI?

    B. Differentiation between radiation necrosis and tumor recurrence using PET and MRI

        Question 3   Are ^{18}F-FCho, ^{18}F-FET and ^{18}F-FDG PET able to discriminate between recurrent glioblastoma and radiation necrosis in rats?

        Question 4   Is *in-vivo* DCE-MRI able to discriminate between glioblastoma and radiation necrosis in rats?

Chapter 4. Therapy response assessment in GB patients using ^{18}F-FCho PET and MRI according to the RANO criteria.

INTRODUCTION

MATERIALS AND METHODS
        Patients and treatments
        Response assessment
        PET imaging with ^{18}F-FCho
        Semi-quantitative PET analysis
        Magnetic resonance imaging
        Statistical analysis

RESULTS
        Response evaluation
        Semi-quantitative PET analysis

DISCUSSION

REFERENCES

Chapter 5. Assessment of the effect of therapy in a rat model of GB using PET and MRI

INTRODUCTION

MATERIALS AND METHODS
        F98 GB rat model
        MR imaging to localize the tumor
        MRI-guided 3D conformal arc micro-irradiation
        Beam targeting validation using γH2AX immunohistochemistry
        Assessment of the effect of image-guided irradiation using MRI
        Assessment of biological response of the tumor using ^{18}F-FDG and ^{18}F-FCho PET
        Statistical analysis

RESULTS
        F98 GB rat model
        Dose distributions and dose volume histograms
        Beam targeting validation using γH2AX immunohistochemistry
        Assessment of the effect of image-guided irradiation using MRI
        Assessment of biological response of the tumor using ^{18}F-FDG and ^{18}F-FCho PET

DISCUSSION

REFERENCES

Chapter 6. ^{18}F-FCho, ^{18}F-FET and ^{18}F-FDG PET for the discrimination between glioblastoma and radiation necrosis in rats.

INTRODUCTION

MATERIALS AND METHODS

> F98 GB rat model
> Induction of RN
> MRI
> ^{18}F-FDG, ^{18}F-FET and ^{18}F-FCho PET
> > *Semi-quantitative PET*
> > *Quantitative PET*
> Semi-quantitative PET analysis
> Quantitative PET analysis
> > *Whole blood AIF corrections*
> > *Kinetic modeling*
> > *Graphical analysis*
> Evans Blue staining
> Statistical analysis

RESULTS

> RN rat model
> Visual PET analysis
> Semi-quantitative PET analysis
> Quantitative PET analysis
> > *Whole blood AIF corrections*
> > *Kinetic modeling*
> > *Graphical analysis*
> Correlation between semi-quantitative and quantitative analysis
> Evans Blue staining

DISCUSSION

REFERENCES

Chapter 7. *In vivo* DCE-MRI for the discrimination between glioblastoma and radiation necrosis in rats.

INTRODUCTION

MATERIALS AND METHODS

> DCE-MRI
> Semi-quantitative DCE-MRI analysis
> Quantitative DCE-MRI analysis

RESULTS

> F98 GB and RN rat model
> Semi-quantitative DCE-MRI analysis
> Quantitative DCE-MRI analysis
> ROC analysis

DISCUSSION

REFERENCES

Chapter 8. General discussion

Chapter 9. Broader international context, relevance, and future perspectives.

PART I: BROADER INTERNATIONAL CONTEXT AND RELEVANCE

PART II: FUTURE PERSPECTIVES

      A. Standardization and validation of imaging biomarkers

      B. Radiomics
            Personalized medicine
            Dose painting by numbers

REFERENCES

Chapter 10. Summary – Samenvatting – Curriculum Vitae

SUMMARY

SAMENVATTING

CURRICULUM VITAE

List of abbreviations

1C1i	One Compartment and One input function
2C1i	Two Compartment and One input function
3C2i	Three Compartments and Two input functions
2D	Two-Dimensional
3D	Three-Dimensional
AA	Anaplastic Astrocytoma
ADC	Apparent Diffusion Coefficient
AIC	Akaike Information Criterion
AIF	Arterial Input Function
AUC	Area Under the Curve
BBB	Blood Brain Barrier
BIC	Bayesian Information Criterion
BLI	Bioluminescence Imaging
BTV	Biological Tumor Volume
GB	Glioblastoma
^{11}C	Carbon-11
^{11}C-MET	^{11}C-Methionine
CBV	Cerebral Blood Volume
Cho	Choline
CK	Choline Kinase
CNS	Central Nervous System
Cp	Tracer Concentration in Arterial Blood Plasma
CR	Complete Response
Cr	Creatine
CT	Computed Tomography
DAB	Diaminobenzidine
DCE-MRI	Dynamic Contrast-Enhanced Magnetic Resonance Imaging
DMSO	Dimethylsulfoxide
DNA	Deoxyribonucleic Acid
DPBN	Dose Painting By Numbers
DSC-MRI	Dynamic Susceptibility weighted Contrast enhanced perfusion MRI
DVH	Dose Volume Histograms
DWI	Diffusion-Weighted MRI
EB	Evans Blue
EES	Extravascular Extracellular Space
EORTC	European Organization for Research and Treatment of Cancer
^{18}F	Fluorine-18
FBP	Filtered Backprojection
^{18}F-FAZA	^{18}F-fluoroazomycin arabinoside
^{18}F-FBet	^{18}F-Fluorobetaine
^{18}F-FDG	^{18}F-Fluorodeoxyglucose
^{18}F-FDOPA	3,4-dihydroxy-6-^{18}F-fluoro-l-phenylalanine
^{18}F-FET	^{18}F-Fluoroethyltyrosine
^{18}F-FCho	^{18}F-Fluoromethylcholine
FITC	Fluorescein Isothiocyanate Fluorochrome
FLASH	Fast Low Angle Shot sequence
^{18}F-FLT	^{18}F-fluorothymidine
^{18}F-FMISO	^{18}F-fluoromisonidazole
^{18}F-ML-10	^{18}F-2-(5-fluoro-pentyl)-2-methyl-malonic acid
^{18}F-RGD	integrin α(v)β3-targeting ^{18}F-AlF-NOTA-PRGD2

FLAIR	Fluid Attenuated Inversion Recovery
FOV	Field of View
Gd	Gadolinium
GdTV	Contrast enhancing Tumor Volume
Gl	Glutamate
GEM	Genetically Engineered Mice
GLUT	Glucose Transporters
GSO	Bismuth Germinate
GTV	Gross Target Volume
H&E	Hematoxylin and Eosin
HGG	High-Grade Glioma
HPLC	High-Pressure Liquid Chromatography
IDH	Isocitrate Dehydrogenase
IMRT	Intensity Modulated Radiation Therapy
IV	Intravenous
k	Kinetic rate constant
keV	kilo electronVolt
KM	Kinetic Modeling
K_{trans}	Rate constant for transfer of contrast agent from plasma to extravascular, extracellular space
K_{ep}	Rate constant for transfer of contrast agent from EES to plasma
LAT	Large Amino-acid Transporters
LGG	Low-Grade Glioma
LNR	Lesion to Normal (brain) Ratio
LOR	Line of Response
LSO	Lutetium Orthosilicate
LYSO	Lutetium-yttrium Orthosilicate
MGMT	Methyl Guanine Methyl Transferase
MI	Molecular Imaging
mI	Myo-Inositol
MLEM	Maximum Likelihood Expectation Maximization algorithm
MRI	Magnetic Resonance Imaging
MRS	Magnetic Resonance Spectroscopy
MSC	Model Selection Criterion
MTV	Metabolic Tumor Volume
MV	Megavoltage
MVD	Microvessel Density
NAA	N-acetylaspartate
NR	Non-responders
^{15}O	Oxygen-15
PBS	Phosphate Buffered Saline
PCV	Procarbazine, CCNU (lomustine) and Vincristine
PD	Progressive Disease
PET	Positron Emission Tomography
PMT	Photomultiplier Tube
PR	Partial Response
PVE	Partial Volume Effect
PWI	Perfusion-Weighted MRI
R	Responders
RANO	Response Assessment in Neuro-Oncology
RF	Radiofrequency
RN	Radiation Necrosis

ROC	Receiver Operating Characteristic
ROI	Region Of Interest
RT	Radiation Therapy
SARRP	Small Animal Radiation Research Platform
SC	Schwartz Criterion
SD	Stable Disease
SE	Standard Error
SiPM	Silicon Photomultipliers
SNR	Signal to Noise Ratio
SUV	Standard Uptake Value
TAC	Time Activity Curve
TNR	Tumor to Normal tissue Ratio
TBR	Tumor to Normal Brain tissue Ratio
TE	Echo Time
TMZ	Temozolomide
TR	Repetition Time
TRITC	Tertramethylrhodamine Isothiocyanate
TSPO	Translocator Protein
TTP	Time To Peak
VEGF	Vascular Endothelial Growth Factor
VOI	Volume Of Interest
V_d	Distribution Volume of the tracer
V_e	Volume of the Extravascular Extracellular Space
V_p	Plasma Volume
V_T	Total distribution Volume of the tracer
WBRT	Whole Brain Radiation Therapy
WHO	World Health Organization

Chapter 1.

General Introduction

"Neurons are the brain's rock stars. But without glial cells – astrocytes, microglia and oligodendrocytes – there would be no show at all" [Goldman B].

PART I: GLIOMAS

A. Central nervous system

The human central nervous system (CNS) consists of the brain and the spinal cord. The brain is encased by the skull and the spinal cord lies within the spinal canal. Globally, the brain can be subdivided into the cerebrum, the cerebellum and the brain stem (Figure 1.1). The cerebral hemispheres are subdivided into five main parts or lobes: lobus frontalis, lobus parietalis, lobus temporalis, lobus occipitalis and lobus limbicus. Most of the boundaries between the lobes coincide with sulci or fissures [1].
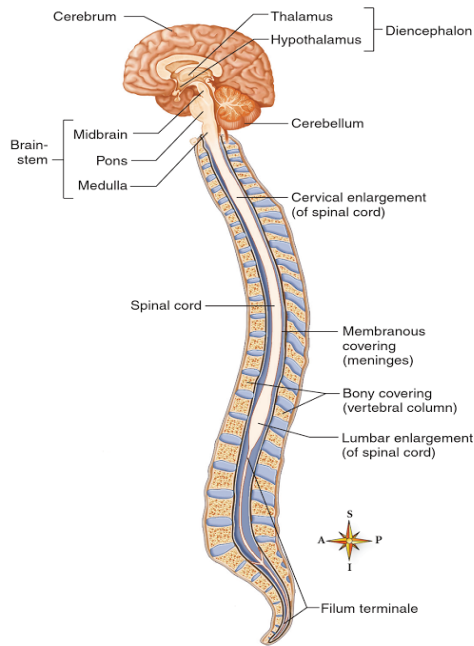
Figure 1.1. The central nervous system [2].

On average the human brain has a network of 86 billion neurons [3]. The defining characteristic of a neuron is its ability to transmit rapid electrical signals in the form of action potentials [4]. Glial cells are less numerous in the brain than neurons [3]. Glia were originally believed to be passive cells, only physically supporting neurons, hence the name glia meaning 'glue'. Glial cells' importance has been reconsidered because of the evidence on their involvement in defining CNS architecture, brain metabolism, the survival of neurons, development and modulation of synaptic transmission, propagation of nerve impulses, and many other physiological functions. Furthermore, increasing evidence shows that glia are involved in the mechanisms of a broad spectrum of pathologies of the CNS [5]. Glial cells include **oligodendrocytes**, **astrocytes**, and **microglia** that interact with neurons and the surrounding blood vessels, see Figure 1.2. Astrocytes provide a link between the vasculature and neurons. Oligodendrocytes wrap myelin around axons to speed up neuronal transmission. Microglia keep the brain under surveillance for damage or infection [4].
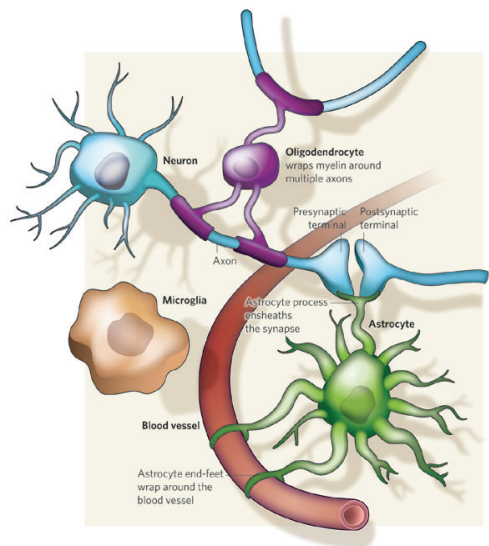
Figure 1.2. Interactions between glial cells and neurons [4].

B. **Blood brain barrier**

The blood brain barrier or BBB is a physio-anatomic interface that protects the neural tissue from variations in blood composition and toxins. The BBB is formed primarily by specialized tight junctions that join cerebral endothelial cells, a thick basement membrane and astrocytic end-processes (Figure 1.3). These components form a neurovascular unit of which the integrity is tightly regulated by interactions with adjacent pericytes. The BBB controls the trafficking of most molecules, including therapeutic agents, to and from the brain. With the exception of small (< 400 Da) and relatively lipophilic molecules, the BBB limits entry to ~98 % of all drugs. Therefore, systemically administered chemotherapies, for example, reach the brain in low concentrations [6].
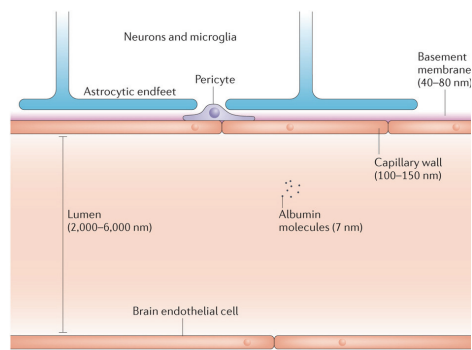

Figure 1.3. Schematic with dimensions of the vascular blood brain barrier (BBB), including the capillary lumen and walls, and the basement membrane, relatively scaled [7].

C. Brain tumors

Brain tumors are relatively rare when compared with breast, lung, prostate and colorectal cancer but cause considerable suffering and have a high case fatality ratio [8]. The most common brain tumors are metastases, meningeal tumors, and tumors developing from glial cells, the so-called gliomas. Gliomas are the most common primary brain tumors with a peak incidence in the fifth and sixth decade of life [9,10]. Gliomas can affect any part of the central nervous system, but they usually occur more supratentorially in adults and infratentorially in children [10]. The ability of glioma cells to migrate is an important factor rendering glial tumors aggressive [11]. More than half of all glial tumors are astrocytic tumors [10]. Other types of brain tumors are ependymal tumors, choroid plexus tumors, neuronal and mixed neuronal-glial tumors, embryonal tumors, tumors of the pineal region and tumors of the cranial and paraspinal nerves [12]. The diagnosis might be suspected by clinical history, but proper neuroimaging is required and before any treatment is started histological confirmation is mandatory [11].

D. Epidemiology of brain tumors

Gliomas represent 80 % of all primary brain tumors [13]. Gliomas are slightly more common in men than women (1.5:1 ratio) and significantly more common in white than black people [10]. From 45 years of age and older, meningioma is the most frequent and glioblastoma (GB) the second most frequent primary brain tumor. In children and adolescents, pilocytic astrocytoma and embryonal tumors are more relevant [13]. More than 250 000 new cases of primary malignant brain tumors are diagnosed annually worldwide, 77 % of which are gliomas [12].

E. Molecular classification of brain tumors

Gliomas form a heterogeneous group of tumors of the CNS and are traditionally classified based on histologic type and malignancy grade. Pathologic diagnosis of malignant gliomas depends in large part upon the degree of nuclear atypia, mitosis, microvascular proliferation and necrosis [14]. Analysis of the most malignant region of the tumors establishes grading: low-grade, or World Health Organization (WHO) grades **I** (pilocytic astrocytoma) and **II** (astrocytoma/oligodendroglioma), and high-grade, or WHO grades **III** (anaplastic astrocytoma/oligodendroglioma) and **IV** (GB). The course of progression of low-grade glioma (LGG) to anaplastic astrocytoma (AA) varies considerably with time intervals ranging from less than one year to more than 10 years [10]. Compared to grade II astrocytoma, AA has increased cellularity, more nuclear pleomorphism and atypia, increased proliferation and presence of > 1 mitotic figures [15]. Almost all AA originate as a benign tumor and have a tendency for malignant progression to high-grade glioma (HGG), such as GB [10]. GB is the highest grade of infiltrating astrocytoma. In addition to the histopathologic findings of AA, either microvascular hyperplasia or necrosis, often with pseudopalisading, are required for the diagnosis of GB (Figure 1.4) [12,15].
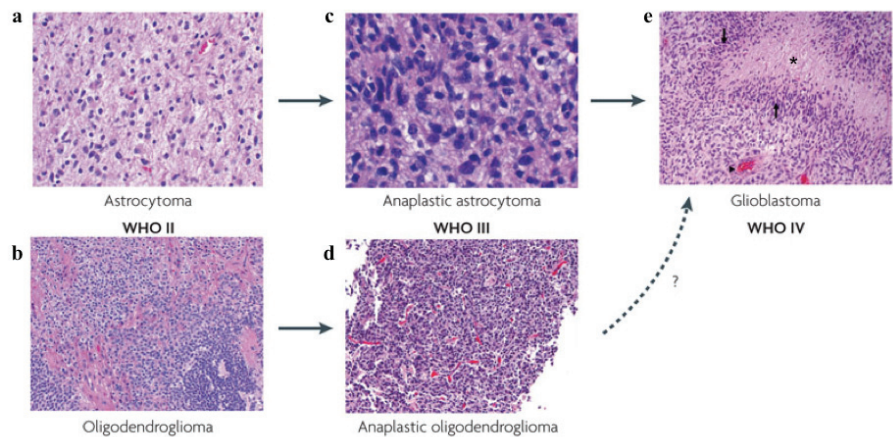
Figure 1.4. Schematic showing the classification of diffuse gliomas of astrocytic (a,c,e) and oligodendroglial (b,d) lineages. The hallmark histological features of glioblastoma including microvascular proliferation (black arrowhead), pseudopalisading (black arrows) and necrosis (asterisk) are indicated (e). Adapted from [16].

However, it is now established that information on the molecular status often allow for a more robust classification of glial neoplasms [17,18]. Therefore, the **new 2016 WHO classification** no longer relies solely on histological criteria but additionally employs molecular biomarkers (see Figure 1.5) [18]. This new integrated diagnosis is redrawing the pedigree chart of brain tumors with rearrangement of tumor groups based on geno-phenotypical behaviors into clinically meaningful groups [19]. The molecular profiling of gliomas is currently based mainly on four markers: (1) mutation of the isocitrate dehydrogenase genes 1 or 2 (IDH mutation), (2) whole-arm codeletion of the chromosomal arms 1p and 19q (1p/19q codeletion), (3) mutations in codon 27 of the histone 3 family genes H3F3A or (4) HIST1H3B/C leading to substitution of the amino acid lysine to methionine (H3-K27M mutation) and the formation of RELA fusion genes. In rare cases, where molecular testing is not possible or remains inconclusive, the term 'NOS' (not otherwise specified) has been introduced to indicate that the diagnosis is based on histology only [18]. As such, the new WHO classification groups all diffusely infiltrating gliomas into seven main entities (Table 1.1 and Figure 1.5).

Table 1.1. New 2016 WHO classification

IDH-mutant astrocytic gliomas
      1. diffuse astrocytoma-IDH mutant
      2. anaplastic astrocytoma-IDH mutant
      3. glioblastoma-IDH mutant
IDH-mutant and 1p19q-codeleted oligodendroglial gliomas
      4. ODG-IDH mutant and 1p/19q codeleted
      5. anaplastic ODG-IDH mutant and 1p/19q codeleted
6. IDH-wildtype glioblastomas
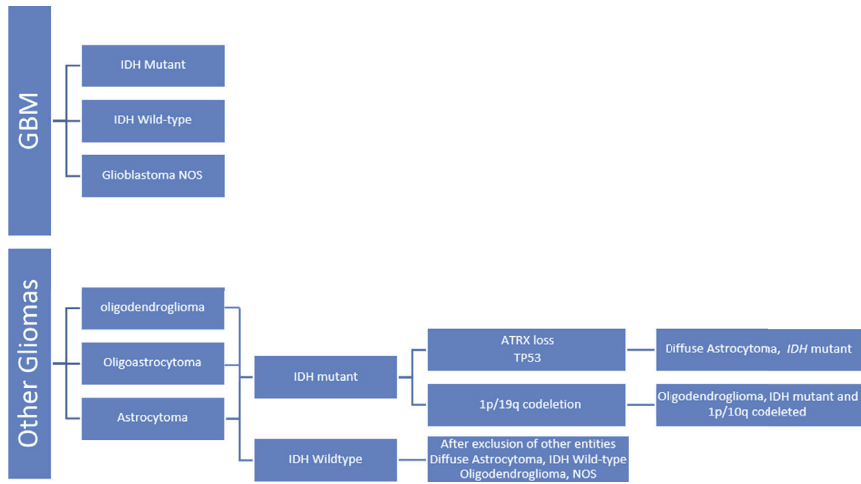**7. Diffuse midline gliomas, H3-K27M-mutant (grade IV)**

Figure 1.5. The classification of diffuse gliomas based on histological and genetic features according to the new WHO classification [19].

F. Glioblastoma

In this work we will focus on GBs that represent the highest grade of gliomas (WHO grade IV), accounting for more than half of all glial tumors and is a highly invasive solid tumor type [6,10]. GBs are most often found in cerebral hemispheres, particularly in frontal, parietal, and temporal lobes, although they can be situated in any lobe. They can arise "*de novo*" (primary GB), or after progression of an AA (secondary GB) [10,16]. Usually, GBs are poorly delineated, heterogeneous tumors with necrosis, hemorrhage, and increased vascularity. Central necrosis (Figure 1.4.e) is the hallmark of GBs and may occupy as much as 80 % of total tumor mass [10]. GB cell infiltration into the surrounding brain parenchyma renders a complete surgical resection mostly difficult without producing significant neurological injury. Residual glioma cells at the tumor margins frequently lead to tumor recurrence [6]. Another major characteristic of HGG is a disruption of the BBB.

G. Clinical course of brain tumors

Focal symptoms and signs occurring during brain tumor clinical presentation are dependent on a number of factors. Location and rate of growth are the most critical, followed by overall lesion size and cerebrospinal fluid obstruction. Additional factors include extent of infiltration, displacement of neural structures and the presence or extent of associated pathology, including edema, hemorrhage, vascular compromise, and cerebrospinal fluid obstruction [20]. Frequent symptoms of HGG are headache, seizures, personality changes and focal neurologic deficits [9,10]. The most important prognostic factors in the survival of patients with gliomas are the patient age at diagnosis, functional status and histological grade [8]. AA have a poor prognosis with an average of 2-year survival rate. The clinical course of aggressive GB tumors is usually rapid, with a mean survival time between 6 and 12 months [10].

H. Treatment of brain tumors

Surgical resection remains one of the most effective treatments for intra-axial gliomas [8,20]. It has been shown that patients who had a gross total resection also have a better response to subsequent adjuvant treatments than those who had only a partial resection or biopsy [8]. However, in about half of the patients, (total) resection is not possible [21]. The current standard of care for patients with GB has slowly evolved over the course of several decades. In the early 1960s, systemic corticosteroids were shown to have a dramatic impact on patients' quality of life by reducing peritumoral edema. Shortly thereafter, whole brain radiation therapy (WBRT) became recognized as an effective adjuvant therapy. However, the dose was limited by potential toxicity to the surrounding normal brain [6]. New developments in radiation therapy (RT) enabled to shape the radiation dose conform the tumor target, limiting the dose to normal tissues or so-called conformal RT. Intensity Modulated Radiation Therapy (IMRT) allows even greater control over the shape of the dose distribution using variable intensities of the radiation beam, see Figure 1.6 [22,23].
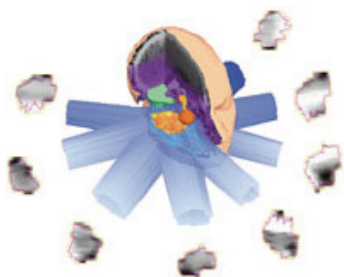

Figure 1.6. Intensity modulated radiation therapy (IMRT) delivers radiation beams in multiple arcs, similar to 3D conformal RT. It uses sophisticated inverse planning software and multileaf collimators to both shape the radiation beam and change the intensity within each beam to deliver the optimum dose. Modified from [24].

In an effort to complement the beneficial effects of corticosteroids and RT, systemic chemotherapeutic agents were also studied in the 1990s. DNA alkylating agents, in particular carmustine, improved median survival by ± 2 months and became widely utilized despite significant systemic side effects. In the 2000s, focus shifted to temozolomide (TMZ) [6]. In 2005, Stupp et al. established the superiority of surgery and combined chemoradiation therapy with TMZ over surgery and RT alone. As a result, for newly GB diagnosed patients with a good performance status, the standard of care now includes maximal surgical resection followed by combined external beam RT (60 Gy in 30 fractions) and TMZ (75 mg/m^2 daily for 6 weeks concomitant with RT), followed by maintenance TMZ (150–200 mg/m^2/d x 5 days, every 28 days for six cycles) [25-27]. TMZ is an oral DNA alkylating agent with good BBB penetration. It is usually well tolerated with thrombocytopenia as its main and dose-limiting toxicity. In contrast to TMZ, nitrosoureas such as lomustine (CCNU), carmustine (BCNU), nimustine (ACNU) or fotemustine can induce prolonged leukopenia and thrombocytopenia, requiring dose reductions for the subsequent cycles, or a change of regimen. Nitrosoureas are now agents as second choice relative to TMZ for glioma treatment. In low-grade gliomas, RT followed by procarbazine, CCNU and vincristine (PCV) constitutes as a new standard of care due to a prolonged survival reported in the RTOG 9802 trial [28].

Chapter 1. General Introduction

The most recent development with respect to novel therapies for GBM involves the use of angiogenesis inhibitors, such as avastin, which improve the quality of life of patients due to their capacity to reduce vessel leakiness, resulting in diminished intracranial edema. However, the latter may enhance the invasive character of these already very invasive tumors and may even further impede the delivery and efficacy of concomitantly administered agents [29].

I. Small animal models of brain tumors

Preclinical glioma small animal models are needed to improve treatment response in gliomas by refining traditional therapeutic delivery schedules, combining new agents and investigating various modes of delivery and concentrations of agents [30]. Rodent models of gliomas can also be employed to elucidate genes involved in tumor initiation versus tumor progression, evaluating recurrence of the tumor and the overall response to treatment [31]. There is a general consensus that valid brain tumor models should fulfill the following criteria [32]:

(1) they should be derived from glial cells;

(2) it should be possible to grow and clone them *in vitro* as continuous cell lines and propagate them *in vivo* by serial transplantation;

(3) tumor growth rates should be predictable and reproducible;

(4) the tumors should have glioma-like growth characteristics within the brain including neovascularization, alteration of the BBB, an invasive pattern of growth, and lack of encapsulation;

(5) host survival time following intra-cerebral tumor implantation should be of sufficient duration to permit therapy and determination of efficacy;

(6) for therapy studies, the tumors should be either non or weakly immunogenic in syngeneic hosts;

(7) they should not grow into the epidural space or extend beyond the brain, and finally

(8) their response, or lack of response, to conventional treatment should be predictive of the response in human brain tumors.

Rat models have remained the mainstay of neuro-oncology research for over 30 years. Mouse, cat and dog models have been utilized previously, but the size limitations of the former and the increased costs for the latter two have limited the widespread utility of these models [33]. Traditional ectopic (subcutaneous) rodent models are widely used to study the *in vivo* efficacy of therapeutics, mainly because of their simplicity. However, there is a growing awareness that these tumors bare little relevance with respect to human [29]. Flank injection is safe and technically simple but results in the formation of encapsulated, non-invasive tumors, while orthotopic tumors are widely infiltrative [31]. As a consequence, orthotopic xenograft and allograft mouse or rat models generated by intra-cerebral injection of human or rodent glioma derived cell lines or solid explant are more appropriate [29].

Figure 1.7. F98 GB rat model (3D volumes from Somersault®).

Currently, several rat brain tumor models are in use. The C6 and 9L gliomas were induced by repeated injections of methylnitrosourea to adult rats. The C6 glioma has been used extensively for a variety of studies, however, it is not syngeneic to any inbred strain, and its potential to evoke an alloimmune response is a serious limitation [32,33-35]. The 9L gliosarcoma has been widely used but can be immunogenic in syngeneic hosts.

The U251 xenograft model shows histological characteristics of human GB, displays similarities at the genetic level of human GB but is criticized for not reproducing the tumor-host immune response [36].

The U87 GB model displays key dissimilarities to the U251 model and human GB at the histopathological level. Unlike GB, U87 tumors show a non-diffusely infiltrative growth pattern, with more homogeneous and leaky vessels [29,36,37].

The RG2 and F98 gliomas were both chemically induced by administering ethylnitrosourea to pregnant rats, the progeny of which developed brain tumors that subsequently were propagated *in vitro* and cloned [32,33,38]. The F98 GB model exhibits features of the human GB in its aggressiveness, histological appearance and lack of immunogenicity [33]. As such, this rodent F98 GB model was selected for the preclinical studies in this dissertation, see Figure 1.7.

To reduce *in vitro* selection pressure by cell culturing, tumor pieces from glioma patients were directly transplanted and expanded in the flanks of mice before being heterotransplanted into the brain and resembled the human disease more closely than traditional cell lines [29]. In more recent years, genetically engineered mouse (GEM) models of gliomas have been created inducing ''gain of function'' (oncogene) or ''loss-of-function'' (tumor suppressor) modifications in mice [29,31]. Transgenic mouse lines are commonly derived by direct pronuclear microinjection of transgenes into fertilized oocytes, followed by implantation into pseudo-pregnant females. The resulting germline mutations are maintained through breeding. Gene targeting of embryonic stem cells by electroporation has also been used [31]. A few examples are transgenic mice with EGFR amplification/Ras activation as a model for classical GB, NF1 loss as a model for mesenchymal GB and PDGF amplification as a model for proneural GB. New

techniques, such as viral-mediated methods and Cre recombinase transgenics, have been developed that allow control of gene expression in a particular organ, cell-type or stage of development, or so-called somatic GEM models [29,31,39]. These tumors arise in the normal host microenvironment and share many (genetical and patho-histological) similarities with human gliomas. Unfortunately, GEM models or ''patient-like'' models have not yet been widely implemented for preclinical testing of novel therapeutics [29]. An overview of all HGG mouse models that have been established thus far is presented in [29,31].

PART II: THERAPY-RESPONSE ASSESSMENT OF HIGH-GRADE GLIOMA

A. From MacDonald Criteria to RANO criteria

Until 2010, mainly MacDonald Criteria were used for assessing response to therapy in HGG. Although the MacDonald Criteria were developed primarily for computed tomography (CT) scans, they have been extrapolated to magnetic resonance imaging (MRI). The criteria are based on two-dimensional (2D) tumor measurements on CT or MRI, in addition to a clinical assessment and corticosteroid use and dose [40]. In the MacDonald Criteria, a significant increase (≥ 25 %) in the contrast-enhancing lesion is used as a reliable marker for tumor progression. However, contrast enhancement after the administration of gadolinium is nonspecific and primarily reflects the passage of contrast material across a disrupted BBB. Furthermore, in 20-30 % of patients, pathological contrast enhancement on MRI subsiding without any change in therapy is shown on the first post-irradiation MRI. This phenomenon, known as "*pseudoprogression*", likely results from a combination of transiently increased permeability of the tumor vasculature from irradiation, treatment-induced necrosis and post-operative infarcts and should always be considered in the first 3 months after concurrent chemoradiation for gliomas [40-42]. In addition, it is worth mentioning that pseudoprogression may be reinforced by chemotherapy with TMZ [21,40,43]. This treatment related effect complicates the determination of tumor progression immediately after the completion of RT and may result in premature discontinuation of effective adjuvant therapy [40,43]. Furthermore, since the introduction of antiangiogenic agents the phenomenon "*pseudoresponse*" needs to be taken into account. These agents can produce a marked decrease in contrast enhancement as early as 1 to 2 days after initiation of therapy, which may be partly a result of normalization of abnormally permeable tumor vessels and not a true antiglioma effect as non-enhancing tumors may continue to grow [40,41]. This normalization of BBB disruption is often combined with a regression of perifocal edema followed by an improvement of neurological symptoms and consequently a reduction of corticosteroid use [43].

In an attempt to more accurately assess treatment response, new response criteria for Response Assessment in Neuro-Oncology (RANO) were introduced in 2010, including the tumor size (in 2D) as measured on T2- and Fluid Attenuated Inversion Recovery (FLAIR)-weighted images, in addition to the contrast-enhancing tumor part. A summary of the proposed RANO response criteria is given in Table 1.2 [40].

Table 1.2. Summary of the proposed RANO response criteria

Criterion	CR	PR	SD	PD
T1 gadolinium enhancing disease	None	≥ 50% ↓	< 50% ↓ but < 25% ↑	≥ 25% ↑*
T2/FLAIR	Stable or ↓	Stable or ↓	Stable or ↓	↑*
New lesion	None	None	None	Present*
Corticosteroids	None	Stable or ↓	Stable or ↓	NA#
Clinical status	Stable or ↑	Stable or ↑	Stable or ↑	↓*
Requirement for response	All	All	All	Any*

RANO, Response Assessment in Neuro-Oncology
CR, complete response; PR, partial response; SD, stable disease; PD, progressive disease
FLAIR, fluid-attenuated inversion recovery
NA, not applicable
* Progression occurs when this criterion is present.
# Increase in corticosteroids alone will not be taken into account in determining progression in the absence of persistent clinical deterioration.

Complete response (CR) requires all of the following: complete disappearance of all contrast-enhancing, measurable and nonmeasurable lesions sustained for at least 4 weeks; no new lesions; stable or improved nonenhancing (T2/FLAIR) lesions; and patient must be off corticosteroids or on physiologic replacement doses only, and stable or improved clinically.

Partial response (PR) requires all of the following: ≥ 50 % decrease, compared with baseline, in the sum of products of perpendicular diameters of all measurable contrast enhancing lesions sustained for at least 4 weeks; no progression of nonmeasurable disease; no new lesions; stable or improved nonenhancing (T2/FLAIR) lesions on same or lower dose of corticosteroids compared with baseline scan and patient must be on a corticosteroid dose not greater than the dose at time of baseline scan and is stable or improved clinically.

Stable disease (SD) occurs if the patient does not qualify for complete response, partial response, or progression (see next section) and requires the following: stable nonenhancing (T2/FLAIR) lesions on same or lower dose of corticosteroids compared with baseline scan and clinically stable status.

Progression (PD) is defined by any of the following: ≥ 25 % increase in sum of the products of perpendicular diameters of contrast enhancing lesions (compared with baseline if no decrease) on stable or increasing doses of corticosteroids; a significant increase in T2/FLAIR nonenhancing lesions on stable or increasing doses of corticosteroids compared with baseline scan or best response after initiation of therapy, not due to comorbid events; the appearance of any new lesions; clear progression of nonmeasurable lesions; or definite clinical deterioration not attributable to other causes apart from the tumor, or to decrease in corticosteroid dose. Failure to return for evaluation as a result of death or deteriorating condition should also be considered as progression [40].

B. Therapy related side effects

Early and late therapy related effects on brain tissue are an unwanted but unavoidable consequence after RT. Examples of early RT induced toxicity include worsening cerebral edema and focal deficit. Late delayed toxicity includes leucoencephalopathy and cognitive decline, parkinsonism and radiation necrosis (RN) [8]. Although few therapy related effects have been reported thus far, the incidence is increasing with greater utilization of stereotatic radiosurgery and combined modality therapy for brain tumors [41,42]. These therapy related effects on the brain, such as radiation injury, add to the complexity of imaging response and recurrence patterns, which is particularly important in patients with HGG in which recurrence is commonly seen [41,42].

Radiation necrosis

Radiation injury is known to potentially target glial cells and vascular endothelial cells and has been divided into acute, early-delayed, and late-delayed reactions [41, 44]. Acute RN (during RT to 3 months after completion of RT) is a consequence of injury to the vasculature, more specifically radiation-induced endothelial cell apoptosis, leading to capillary leakiness and edema. Up to 12 weeks following RT, early-delayed injury can occur due to a delay in myelin synthesis (injury to oligodendrocytes). However, pseudoprogression must be considered. Late vascular changes include vessel wall thickening with resulting occlusive vasculopathy and perivascular parenchymal coagulative necrosis. In addition, inflammation plays a role in the development of late RN. Late-delayed reactions are reported to occur in 3-24 % of patients from 3 months to 13 years after the completion of RT [44-47]. The risk increases with increasing radiation dose, fraction size, irradiated volume and the (concomittant) administration of chemotherapy [45]. The pattern of radiation injury may vary from diffuse periventricular white matter lesions to focal or multifocal lesions and may occur even distant from the original treatment [48].

Radiation necrosis vs tumor recurrence

Differentiation between RN and recurrent brain tumor presents a diagnostic dilemma as both entities frequently develop at the resection site and often have a similar appearance on conventional MRI [41,42]. Both types of lesions can have similar clinical presentations, such as seizures, focal neurologic deficits, and increased intracranial pressure [46]. Obviously, a correct diagnosis is important for further patient management. RN may require the administration of steroids whereas tumor recurrence necessitates second line treatment [41,49]. However, a definite diagnosis requires a biopsy. Unfortunately, a biopsy is subject to sampling error, is invasive and can lead to potential complications such as brain hemorrhage [42].

C. Limitations of the RANO criteria

Although the RANO criteria addressed some of the limitations of the MacDonald criteria for evaluation of therapy in HGG, the above-mentioned treatment related side effects hamper correct response assessment. To address the issue of pseudoprogression, the proposed new response criteria suggest that within the first 3 months after completion of RT, progression can only be determined if the majority of the new enhancement is outside of the radiation field or if there is pathologic confirmation of progressive disease. This means that response assessment shortly after the end of RT is not accepted [43]. Furthermore, increased enhancement and FLAIR/T2 hyperintense signal abnormalities can also occur due to treatment-related inflammation, postsurgical changes, subacute irradiation effects and RN [40]. As such, determination of recurrence versus treatment effects on CT or conventional MRI cannot be accurately evaluated [21].

To address this problem, incorporating changes in tumor biology measured by advanced MRI and positron emission tomography (PET) imaging, which may precede anatomical changes of the tumor volume, are promising [21,50,51]. Currently, MRI techniques that interrogate the vascular density and permeability of tumor vasculature, such as dynamic contrast enhanced MRI (DCE-MRI), diffusion-weighted MRI (DWI-MRI) and perfusion-weighted MRI (PWI-MRI), metabolite concentrations using MR spectroscopy (MRS), as well as multiple PET tracers are being evaluated as imaging biomarkers of tumor response in treatment trials [21]. In the future, incorporation of these advanced imaging techniques into the RANO criteria is necessary but needs standardization and requires rigorous clinical validation studies before they can be incorporated into response criteria used in clinical trials in HGG [40]. Currently, the decision tree given in Figure 1.8 can be proposed for the follow-up of HGG [52]. The next chapter will give an overview on conventional and more advanced imaging modalities in neuro-oncology.
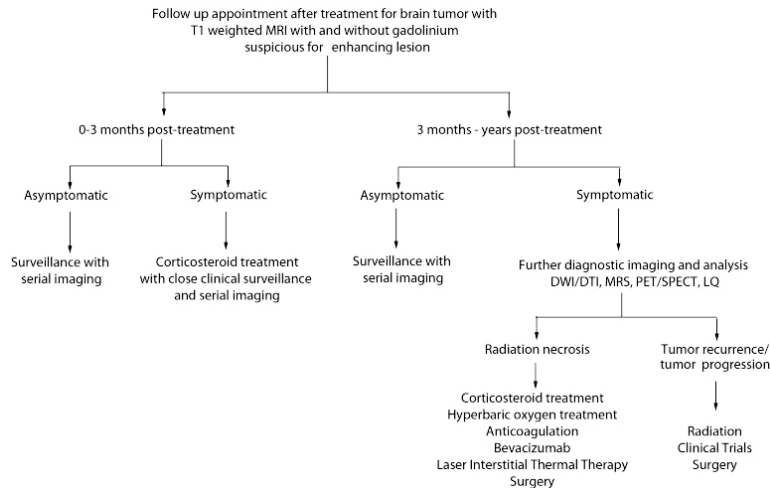

Figure 1.8. Decision tree for post-treatment follow-up in high-grade gliomas [52].

REFERENCES

[1] Nieuwenhuys R, Voogd J, van Huijzen C. The human central nervous system. Section 1: Orientation, development, gross anatomy, blood supply and meninges. Chapter: orientation. Berlin, Heidelberg: Springer 2008;3.

[2] Patton KT, Thibodeau GA. Anatomy & Physiology, ninth edition. St Louis, Missouri: Elsevier 2015;Figure 20-1.

[3] von Bartheld CS, Bahney J, Herculano-Houzel S. The search for true numbers of neurons and glial cells in the human brain: A review of 150 years of cell counting. Journal of Comparative Neurology 2016;524(18):3865-3895.

[4] Allen NJ, Barres BA. Neuroscience: Glia - more than just brain glue. Nature 2009;5;457(7230):675-677.

[5] von Bernhardi R, von Bernhardi JE, Flores B, et al. Glial Cells and Integrity of the Nervous System. Chapter 1: Glial Cells in Health and Disease of the CNS. Advances in Experimental Medicine and Biology. Switzerland: Springer 2016;949:1-24.

[6] Wadajkar AS, Dancy JG, Hersh DS, et al. Tumor-targeted nanotherapeutics: overcoming treatment barriers for glioblastoma. Wiley Interdisciplinary Reviews Nanomedicine and Nanobiotechnology 2016;1-17.

[7] Banks WA. From blood–brain barrier to blood-brain interface: new opportunities for CNS drug delivery. Nature Reviews Drug Discovery 2016;15:275-292.

[8] Rees JH. Diagnosis and treatment in neuro-oncology: an oncological perspective. The British Journal of Radiology 2011;84:S82-S89.

[9] Omuro A, DeAngelis LM. Glioblastoma and other malignant gliomas. A clinical review. JAMA 2013;310(17):1842-1850.

[10] Drevelegas A, Karkavelas G. Imaging of brain tumors with histological correlations. Chapter 6: High-grade gliomas. Berlin, Heidelberg: Springer 2011:157.

[11] Lopci E, Franzese C, Grimaldi M, et al. Imaging biomarkers in primary brain tumours. European Journal of Nuclear Medicine and Molecular Imaging 2015;42(4):597-612.

[12] Louis DN, Ohgaki H, Wiestler OD, et al. The 2007 WHO classification of tumours of the central nervous system. Acta Neuropathologica 2007;114(2):97-109.

[13] Ostrom QT, Bauchet L, Davis FG, The epidemiology of glioma in adults: a "state of the science" review. Neuro Oncology 2014;16(7):896-913.

[14] Chen W. Clinical applications of PET in brain tumors. Journal of Nuclear Medicine 2007;48(9):1468-1481.

[15] Brat DJ, Prayson RA, Ryken TC, et al. Diagnosis of malignant glioma: role of neuropathology. Journal of Neurooncology 2008;89(3):287-311.

[16] Huse JT, Holland EC. Targeting brain cancer: advances in the molecular pathology of malignant glioma and medulloblastoma. Nature Reviews Cancer 2010;10(5):319-331.

[17] Weller M, Weber RG, Willscher E, et al. Molecular classification of diffuse cerebral WHO grade II/III gliomas using genome- and transcriptome-wide profiling improves stratification of prognostically distinct patient groups. Acta Neuropathologica 2015;129(5):679-693.

[18] Louis DN, Perry A, Reifenberger G, et al. The 2016 World Health Organization Classification of Tumors of the Central Nervous System: a summary. Acta Neuropathologica 2016;131(6):803-820.

Chapter 1. General Introduction

[19] Colen RR, Hassan I, Elshafeey N, et al. Shedding Light on the 2016 World Health Organization Classification of Tumors of the Central Nervous System in the Era of Radiomics and Radiogenomics. Magnetic Resonance Imaging Clinics of North America 2016;24(4):741-749.

[20] Watts C, Sanai N. Surgical approaches for the gliomas. Handbook of Clinical Neurology 2016;134:51-69.

[21] Ahmed R, Oborski MJ, Hwang M, et al. Malignant gliomas: current perspectives in diagnosis, treatment, and early response assessment using advanced quantitative imaging methods. Cancer Management and Research 2014;6:149-170.

[22] Khan FM. The physics of radiation therapy, Fifth Edition. Chapter 20: Intensity-modulated radiation therapy. Baltimore: Wolters Kluwer Health - Lippincott Williams & Wilkins 2010;430.

[23] Kirsch DG, Tarbell NJ. Conformal radiation therapy for childhood CNS tumors. Oncologist. 2004;9(4):442-450.

[24] http://precisionradiotherapy.com/RadiationTherapy.html

[25] Stupp R, Dietrich PY, Ostermann Kraljevic S, et al. Promising survival for patients with newly diagnosed glioblastoma multiforme treated with concomitant radiation plus temozolomide followed by adjuvant temozolomide. Journal of Clinical Oncology 2002;20:1375-1382.

[26] Anton K, Baehring JM, Mayer T. Glioblastoma multiforme: overview of current treatment and future perspectives. Hematology Oncology Clinics of North America 2012;26(4):825-853.

[27] Siu A, Wind JJ, Iorgulescu JB, et al. Radiation necrosis following treatment of high grade glioma-a review of the literature and current understanding. Acta Neurochirurgica 2012;154(2):191-201.

[28] van den Bent MJ. Practice changing mature results of RTOG study 9802: another positive PCV trial makes adjuvant chemotherapy part of standard of care in low-grade glioma. Neuro Oncology 2014;16(12):1570-1574.

[29] de Vries NA, Beijnen JH, van Tellingen O. High-grade glioma mouse models and their applicability for preclinical testing. Cancer Treatment Reviews 2009;35:714-723.

[30] Barnett HG. High-grade gliomas. Diagnosis and treatment. Totowa, New Jersey: Humana Press Inc 2007:Preface.

[31] Janbazian L, Karamchandani J, Das S. Mouse models of glioblastoma: lessons learned and questions to be answered. Journal of Neurooncology 2014;118(1):1-8.

[32] Barth RF, Kaur B. Rat brain tumor models in experimental neuro-oncology: the C6, 9L, T9, RG2, F98, BT4C, RT-2 and CNS-1 gliomas. Journal of Neurooncology 2009;94:299-312.

[33] Bryant MJ, Chuah TL, Luff J, et al. A novel rat model for glioblastoma multiforme using a bioluminescent F98 cell line. Journal of Clinical Neuroscience 2008;15:545-551.

[34] Benda P, Someda K, Messer J, et al. Morphological and immunochemical studies of rat glial tumors and clonal strains propagated in culture. Journal of Neurosurgery 1971;34:310-323.

[35] Schmidek HH, Nielsen SL, Schiller AL, et al. Morphological studies of rat brain tumours induced by N-nitrosomethylurea. Journal of Neurosurgery 1971;34:335-340.

[36] Jacobs VL, Valdes PA, Hickey WF, et al. Current review of in vivo GBM rodent models: emphasis on the CNS-1 tumour model. Amercian Society for Neurochemistry 2011;3(3):e00063.

[37] Ponten J. Neoplastic human glia cells in culture. Fogh J. In Human Tumor Cells in Vitro. New York: Plenum Press 1975;175-185.

[38] Ko L, Koestner A, Wechsler W. Morphological characterization of nitrosourea-induced glioma cell lines and clones. Acta Neuropathologica 1980;51:23-31.

[39] Lim SK, Llaguno SR, McKay RM, et al. Glioblastoma multiforme: a perspective on recent findings in human cancer and mouse models. BMB reports 2011;44(3):158-164.

[40] Wen PY, Macdonald DR, Reardon DA, et al. Updated response assessment criteria for high-grade gliomas: response assessment in neuro-oncology working group. Journal of Clinical Oncology 2010;28:1963-1972.

[41] Jain R, Narang J, Sundgren PM, et al. Treatment induced necrosis versus recurrent/progressing brain tumor: going beyond the boundaries of conventional morphologic imaging. Journal of Neurooncology 2010;100(1):17-29.

[42] Chao ST, Suh JH, Raja S, et al. The sensitivity and specificity of FDG PET in distinguishing recurrent brain tumor from radionecrosis in patients treated with stereotactic radiosurgery. International Journal of Cancer 2001;96:191-197.

[43] Lutz K, Radbruch A, Wiestler B, et al. Neuroradiological Response Criteria for High-grade Gliomas. Clinical Neuroradioliogy 2011;21:199-205.

[44] Langleben DD, Segall GM. PET in differentiation of recurrent brain tumor from radiation injury. Journal of Nuclear Medicine 2000;41:1861-1867.

[45] Ruben JD, Dally M, Bailey M, et al. Cerebral radiation necrosis: incidence, outcomes, and risk factors with emphasis on radiation parameters and chemotherapy. International Journal of Radiation Oncology Biology Physics 2006;65(2):499-508.

[46] Lizarraga KJ, Allen-Auerbach M, Czernin J, et al. 18F-FDOPA PET for Differentiating Recurrent or Progressive Brain Metastatic Tumors from Late or Delayed Radiation Injury After Radiation Treatment. Journal of Nuclear Medicine 2014;55(1):30-36.

[47] Rahmathulla G1, Marko NF, Weil RJ. Cerebral radiation necrosis: a review of the pathobiology, diagnosis and management considerations. Journal of Clinical Neuroscience 2013;20(4):485-502.

[48] Giglio P, Gilbert HR. Cerebral radiation necrosis. Neurologist 2003;9:180-188.

[49] Van Laere K, Ceyssens S, Van Calenbergh F, et al. Direct comparison of 18F-FDG and 11C-methionine PET in suspected recurrence of glioma: sensitivity, inter-observer variability and prognostic value. European Journal of Nuclear Medicine Molecular Imaging 2005;32:39-51.

[50] Hoekstra CJ, Paglianiti I, Hoekstra OS, et al. Monitoring response to therapy in cancer using [18F]-2-fluoro-2-deoxy-D-glucose and positron emission tomography- an overview of different analytical methods. European Journal of Nuclear Medicine 2000;27:731-743.

[51] Dhermain FG, Hau P, Lanfermann H, et al. Advanced MRI and PET imaging for assessment of treatment response in patients with gliomas. Lancet Neurol 2010;9:906-920.

[52] Parvez K, Parvez A, Zadeh G. The diagnosis and treatment of pseudoprogression, radiation necrosis and brain tumor recurrence. International Journal of Molecular Sciences 2014;15(7):11832-11846.

Chapter 2. Biological imaging in neuro-oncology

Chapter 2.

Biological imaging in neuro-oncology

"Visual interpretation gives you an impression, standardized and validated quantification brings you knowledge" [R. Boellaard].

INTRODUCTION

Molecular imaging (MI) is revolutionizing the way we study the inner workings of the human body, diagnose diseases, approach drug design, and assess therapies. One may define MI as the noninvasive, real time visualization of biochemical events at the cellular and molecular level within living cells, tissues, and/or intact subjects. Generally speaking, MI involves specialized instrumentation, used alone or in combination with targeted imaging agents, to visualize tissue characteristics and/or biochemical markers [1]. In most strategies, a MI probe must first be introduced into the living subject, e.g. by injection into the blood stream. A MI probe is usually composed of a chemically specific compound that interacts with the intended molecular target (e.g. a protein), a signaling component that produces a signal that can hopefully be detected, and a possible linker between the two components [2]. An overview of the key MI modalities is given in Figure 2.1.
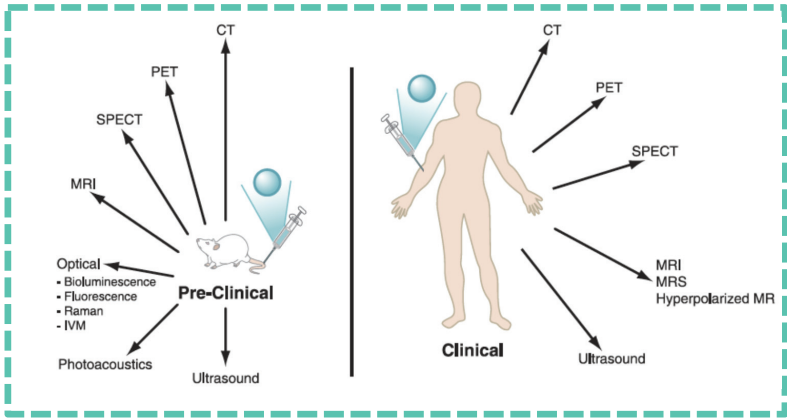

Figure 2.1. Key molecular imaging modalities for preclinical and/or clinical applications. CT, computed tomography; PET, positron emission tomography; SPECT, single photon emission computed tomography, MRI, magnetic resonance imaging; MRS, magnetic resonance spectroscopy; IVM, intravital microscopy. The blue circle is an appropriate contrast agent or molecular imaging agent [1].

In patients with suspected brain tumor, after medical history taking and clinical examination, the most important diagnostic procedure is magnetic resonance imaging (MRI) of the brain with contrast-enhancing agent. However, the diagnosis should be confirmed via a stereotactic biopsy or, when appropriate, via resection. Innovative imaging has gained a lot of attention in the last decade. Before confirmation of the diagnosis via tissue analysis, MR spectroscopy (MRS), perfusion weighted MRI (PWI), and positron emission tomography (PET) imaging can be helpful. After the diagnosis has been confirmed pathologically, these innovative imaging modalities can be even more valuable. In particular, they may be useful for planning of radiation therapy (RT) and for the monitoring during therapy and follow-up [3]. In this chapter the most important imaging modalities in neuro-oncology will be covered.

PART 1: MRI IN NEURO-ONCOLOGY

A. Developing an MRI signal

From quantum physics to classical mechanics due to the amount of protons in a voxel

MR physics can essentially be understood using principles of classical physics, however, for a more comprehensive understanding the reader is directed to an excellent review by Plewes et al. [4]. MR takes advantage of the behavior of a system of protons in the presence of a magnetic field and how this behavior changes based on the micro- and macroscopic environment. Living tissue can be considered to consist of 60 - 80 % water. Both water and macromolecules have protons. MRI is based on the disturbance of the spin of these protons by radiofrequent waves and subsequent analysis of emitted signals after relaxation of the system. In the nucleus, each neutron and proton spins on its axis, yielding a magnetic moment that causes the particle to behave like a small magnet. In most nuclei, the neutrons and protons align so that their spins and magnetizations cancel. As such, atoms only have a nuclear spin when the nucleus contains an odd number of protons or neutrons. Examples of such atoms are ^1H, ^{13}C, ^{19}F and ^{31}P. Among these, Hydrogen, with a single proton in its nucleus, is the most commonly used element because it is the most abundant atom in the body. This proton generates a small magnetic field, represented by a vector along the axis of spin. In a substance with a lot of Hydrogen atoms and in the absence of an external magnetic field, these protons are randomly oriented, so that the substance possesses no net magnetization [4,5].

Magnetization of tissues by B0

When a magnetic field is applied to the substance, the dipoles become aligned with respect to the magnetic field in a predictable and finite number of orientations. For Hydrogen two orientations are possible. In one orientation the protons are aligned parallel with the magnetic external field and in other anti-parallel to the external magnetic field. Since the parallel orientation is preferred, this results in a net magnetization vector M_0, aligned with the external magnetic field B_0 and the longitudinal axis of our body (z-axis), see Figure 2.2.a and 2.2.b. The spinning protons also precess (rotational movement of the axis of a spinning body) around the applied magnetic field (B_0), with a frequency given by the Larmor relationship ($\omega_0 = \Upsilon B_0$). The gyromagnetic ratio, Υ, is characteristic for the nucleus considered [5].

Magnetic resonance

In MRI our objective is to disturb the alignment of the protons with a radio frequency (RF) pulse with a frequence that equals the Larmor frequency. The protons absorb the energy, called resonance, and their dipoles reach a new steady state by tilting the magnetic moment out of alignment with the field. As such, the precessing spins (M_0) can be pushed from the longitudinal axis (Z-axis) to transverse plane (XY-plane, M_{XY}), see Figure 2.2. Different tilt angles or flip angles (for example 90° or 180°) can be created by simply adjusting the duration and strength of the RF pulse [5-7]..

B. Relaxation phenomena

When the magnetic moment of a sample is pulsed out of alignment with the applied field (B_0), and as the pulse ends, they 'relax' back to their undistorted 'equilibrium' position, called 'relaxation', causing emission of an RF signal (the Echo) that can be picked up by the receiver coil. This signal decreases by a sinusoidal pattern, called the free induction decay (FID). This relaxation is a time-dependent process and is characterized by a rate constant known as the relaxation time. Two relaxation times can be measured, the longitudinal relaxation time (T1) and transverse relaxation time (T2). T1 is the time required for the excited nuclei to re-align for 63 % back to their original position as they were before the RF pulse. This process is called spin-lattice relaxation and occurs by emitting energy. T2 refers to the loss of phase coherence of spins because protons dissipate their energies to the surrounding nuclei at their level and is called spin-spin relaxation. This means that the spins are not in phase anymore but orient again randomly. T2 refers to the time in which only 37 % of the transversal magnetization is left after a 90° pulse [5-7].

The contrast between different tissues in MRI is generated due to the different T1 and T2 relaxation times of each tissue. For instance, proton nuclei in solid substances, rigidly held in place, have relatively long T1 relaxation times. Most biologic tissues are more liquid-like, which accelerates the spin-lattice relaxation and have therefore lower T1 values.
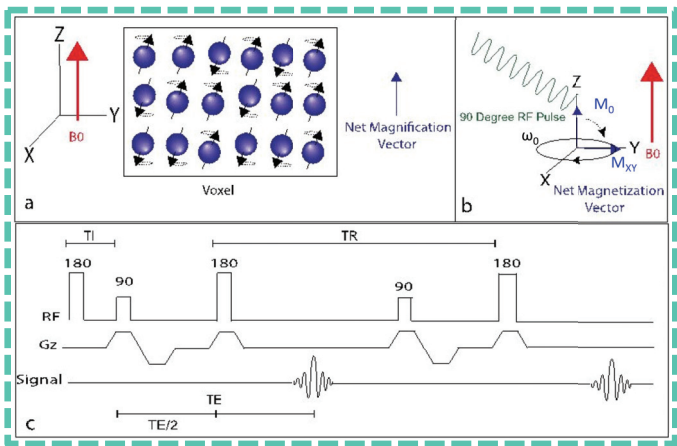

Figure 2.2. **Physics underlying MRI.** Hydrogen atoms align parallel and antiparallel to a strong magnetic field, producing a net magnification vector (a). When a radio frequency pulse is applied at the Larmor frequency, the net magnetization vector is tipped away from the main magnetic field (b). Example of a simple pulse sequence showing timing parameters of the application of radio frequency pulse (RF), the onset of gradients in the Z direction (Gz), and the timing of signal acquisition (Signal) (c). Adapted from [5].

C. The basics of MR imaging

Gradients

Spatial localization can be provided by applying gradients in the three directions X (left-right), Y (anterior-posterior) and Z (head-feet). Gradients are spatially changing magnetic fields, typically within 1-3 % of the main static field. Using these gradients, the precession of protons in a slice with higher field strength will accelerate more, leading to a phase difference when the gradient stops. The gradient G_z is used for slice selection. Within this slice, spatial localization is possible applying 2 orthogonal gradients: a frequency-encoding gradient G_x, which creates a gradient of frequencies along the left-right axis and a phase-encoding gradient G_y, which manipulates the phase of the spins along this axis. These gradients are applied to be able to divide a slice within the tissue into different voxels to locate the signal depending on the change in phase and change in frequency induced by these gradients [4-7].

Fourier and K-space

The signals measured by the receiver coil(s) are characterized by their phase, frequency and amplitude. They are amplified and digitized and these raw data are stored in a 2D or 3D matrix, called K-space. The information stored in the K-space is reconstructed by a mathematical procedure, an inverse Fourier transformation, to obtain an image. Different strategies exist to optimize the process of K-space sampling [4-7].

D. MRI sequences and contrasts

Building a sequence

Depending on the image that needs to be obtained, different methods exist in MRI. Different schemes can be applied exciting the tissue and reading the emitted signal in a specific manner. All pulse-imaging methods begin with the magnetization vector aligned with the magnetic field along the z-axis. Then an RF-pulse is applied to orient the vector away from the z-axis. At a slightly later time, the first RF pulse is followed by one or more additional pulses applied before relaxation is complete. Each imaging method uses a different combination of the first and succeeding pulses and the time interval between them. This process is described by a pulse sequence. A simple pulse sequence indicating RF and gradient timing is illustrated in Figure 2.2.c [5].

Pulse sequences can differ in the nature of the pulse but also in the timing between the pulses. Using certain pulse sequences in which the timing parameters of a set of RF pulses are modified, differences in relaxation times can be exploited thereby preferentially sensitizing image contrast to differences in either T1 or T2. The most fundamental timing parameters of relevance are the repetition time (TR) and the echo time (TE). TR is the time between 2 excitation pulses and by decreasing TR, T1-contrast can be increased (see Figure 2.3). For example, when an image is T1 weighted, a subacute hemorrhage will appear brighter than normal brain tissue, since hemorrhage has a shorter T1 than brain tissue [1]. As such, for T1-weighted images, short TRs will be chosen, mostly < 500 ms. TE is the time from the onset of the excitation pulse until the emitted signal is received by refocusing. With an equal TE, tissues with a shorter T2 will generate less signal than tissues with a high T2 due to a faster dephasing. As such, a long

TE can exploit the differences in dephasing and can lead to an increase in T2 contrast, see Figure 2.3, which is applied in T2-weighted MRI [8].

An imaging method called saturation recovery consists of a series of equally spaced 90° pulses. Spin echo imaging uses a 90° pulse followed by a 180° pulse given on TE/2, causing a rephasing and a second signal, called 'the echo' before the first signal has stopped. Importantly, simply by manipulating the TE and TR a range of MR contrasts can be obtained with varying sensitivity to different tissue types [2,7,9].
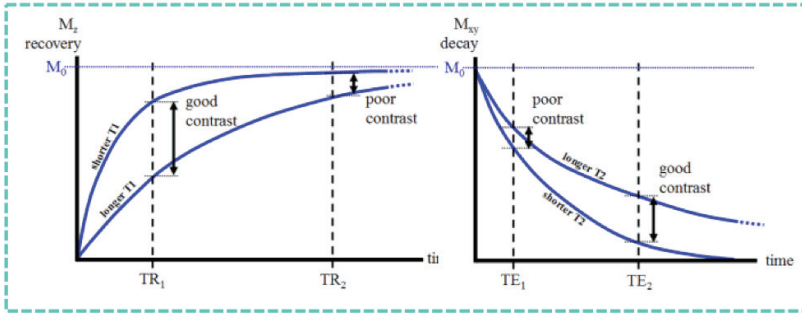

Figure 2.3. Importance of TR and TE [8].

Brain tumor MRI

MRI is the method of choice for imaging CNS diseases, as it is superior to CT in several ways:

- Does not involve x-rays
- MRI resolution, sensitivity and tissue contrast are higher
- There is less chance of artifact in the posterior fossa or pituitary fossa
- MRI provides a more accurate 3D reconstruction of the tumor, which can better guide surgical resection or biopsy
- By varying the parameters of the pulse sequence, different contrasts may be generated between tissues and advanced techniques such as diffusion, spectroscopy and perfusion allow for precise tissue characterisation

CT is an alternative in case of emergency or MRI contra-indications and remains superior for demonstrating acute hemorrhage [6,10]. Currently, there are no standardized MR imaging protocols for brain tumors but an optimal MRI protocol should contain T2 and fluid-attenuated inversion recovery (FLAIR) or proton density sequences. They should be combined with T1-weighted sequences before and after intravenous administration of a contrast agent, as sequences with identical parameters. A proposed protocol is given in table 2.1 [6]. In the non-contrast Tl-weighted images, hyperintense structures are often seen in oligodendrogliomas and in malignant brain tumors. Hyperintense signal on contrast-enhanced T1-weighted MRI is a sign of contrast leakage due to blood brain barrier (BBB) breakdown. Contrast agents, such as gadolinium, produce their contrast by disturbing the local magnetic field in which they are placed. T2-weighted images reflect cell density of a tumor, because tumors with compact

small cell matrix are rather isointense to gray matter. In contrast, tumors with loose cell structures are hyperintense [6]. If there is a suspicion of prior hemorrhage, it is necessary to perform a T2*-weighted gradient echo acquisition with a relatively long echo time. Such sequences will accentuate foci of prior hemorrhage as irregular foci of hypointensity [11]. FLAIR images provide better definition between edema and tumor [12].

Table 2.1. Image protocol for brain tumors. Sequences used at Ghent University Hospital.
Adapted from [6].

	Slice thickness/gab	Weighting	Important features
Sag	3 mm/0–0.3 mm	T1-weighted imaging	Pre-contrast imaging for positioning
Axial	3 mm/0–0.3 mm	T2-weighted imaging	Cortical ribbon sign, infiltration of insula, basal ganglia
Axial	3 mm/0–0.3 mm	FLAIR	
Axial	3 mm/0–0.3 mm	Diffusion weighted imaging	Low ADC: postsurgical infarcts, cell density, abscess, antiangiogenic therapy
Axial	3 mm/0–0.3 mm	T1-weighted imaging before administration of contrast agent	
Injection of contrast agent			
Axial		T1-weighted imaging after administration of contrast agent	
		Perfusion weighted MRI (DSC-MRI)	Increased CBV is a sign of malignancy
Axial, Coronal and Sagittal	3 mm/0–0.3 mm	T1-weighted imaging after administration of contrast agent	

E. Glioblastoma MRI characteristics

The cerebral hemispheres are the most common location for GB with a tendency to cross the midline along the white matter tracts in the "butterfly" pattern. The majority of GB are solitary lesions; multifocal or multicentric GB occur in about 3 % of cases. In general terms, high-grade glial neoplasms are conventionally thought of as infiltrative parenchymal masses that are hyperintense on FLAIR and T2-weighted images, hypointense on unenhanced T1-weighted images, possibly extend into the corpus callosum, are surrounded by extensive vasogenic edema, and prominently enhance following gadolinium administration, see an example in Figure 2.5. This marked heterogeneity on MRI corresponds to the pathologic hallmark findings of necrosis and hemorrhage as well as marked cellular pleomorphism. Contrast enhancement in these masses is usually quite heterogeneous and generally more prominent peripherally as a thick, irregular rim surrounding a central area of necrosis that may occupy up to 80 % of the volume of the overall mass. Vasogenic edema is common and can extend along the white matter tracts, representing a combination of an infiltrating tumor and accompanying edema [11,13]. It must be

pointed out that this description is just a generalization as many high-grade neoplasms do not follow these "rules" and some of these characteristics may even be seen in low-grade neoplasms [11].
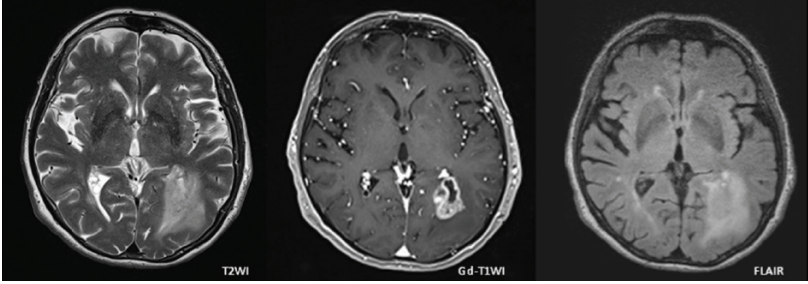

Figure 2.4. Comparison of conventional MRI sequences for imaging a left occipital GB. From left to right: T2-weighted MRI, gadolinium-enhanced T1-weighted MRI and fluid attenuated inversion-recovery (FLAIR) MRI. Adapted from [14].

F. Limitations of conventional MRI

One of the most critical elements involves the precise delineation of the neoplasm, with correct assessment of peripheral infiltration, since hyperintense signal displayed with T2/FLAIR sequences is not enough to distinguish between vasogenic edema and tumor spread [14]. Differentiation between treatment related effects, such as radiation necrosis (RN), and recurrent brain tumor presents also a diagnostic dilemma as both entities frequently develop at the resection site and often have a similar appearance on conventional MRI. Lesions are heterogenously hyperintense on T2-weighted images and contrast enhancing with surrounding edema on T1-weighted images [15,16]. An example is given in Figure 2.4. In recent years, however, a big effort has been made to incorporate new markers of functional, metabolic and molecular alterations into neuro-oncology imaging, described in the next part of this chapter.
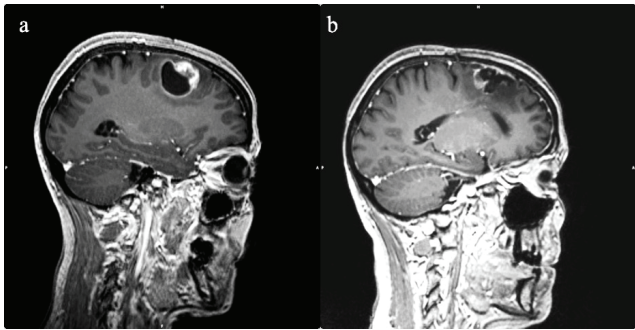

Figure 2.5. Differential diagnosis of tumor recurrence or radiation necrosis. Contrast-enhanced T1-weighted brain MRI pre-resection (a). A complete surgical resection was performed. Histological staining confirmed the diagnosis of GB. One year post-resection contrast-enhanced T1-weighted MRI (b) shows a new contrast-enhancement at the resection site with a differential diagnosis of tumor recurrence or treatment-related effects.

G. Advanced MRI in neuro-oncology

Apart from providing detailed anatomical information, MRI is capable of providing physiological information via various specialized MRI techniques. Most MRI techniques rely on different pulse sequences to generate different information about the tissues being interrogated [17]. A few examples of advanced MRI techniques include dynamic contrast-enhanced MRI (DCE-MRI), diffusion-weighted MRI (DWI), PWI and MRS. These techniques could help in discriminating therapy induced effects from recurrent tumor by assessing the physiological characteristics of the vasculature (DCE-MRI), the degree of tissue cellularity (DWI), tissue perfusion (PWI) and providing insights into changes in tumor environment related to metabolism (MRS) [17,18].

Diffusion-weighted MRI

DWI relies on the microscopic motion of water molecules (protons) within tissue [18]. Strong magnetic gradients are applied in each of three orthogonal directions and diffusing protons within these voxels cause a loss of phase coherence over time that accounts for signal loss within those voxels. The signal loss is proportional to the distance the diffusing protons moved over that time period. Protons whose diffusion is "restricted" by physical barriers or because they are bound to macromolecules will not change their net phases. Apparent diffusion coefficients (ADCs) can be calculated by ratios of intravoxel signal intensities taken from at least two sequences with differing gradient strengths [11].

ADC decreases with an increase in viscosity, cellular density, and reduction of extracellular space. Low values in ADC maps in solid gliomas are associated with higher-grade tumors [18]. The use of DWI in excluding RN is still unclear. Low ADC values have been suggested as characteristics of recurrence as a consequence of dense packing, while higher ADC values are more favorable for RN due to a higher interstitial water movement due to severe tissue damage. However the opposite has also been hypothesized [19]. An example of DWI of a GB is given in Figure 2.8a.

Perfusion-weighted MRI

DCE-MRI

DCE-MRI involves the dynamic acquisition of T1-weighted MR images before, during, and after the administration of an appropriate contrast agent. Low-molecular-weight paramagnetic gadolinium complexes are the most common contrast agents for DCE-MRI, which shorten the T1 relaxation times, leading to positive contrast [17]. DCE-MRI helps in obtaining a better estimation of vascular leakiness due to BBB disruption based on the extravasation of the contrast agent from arteries to the parenchyma [20]. Subsequently, the recorded signal intensity is analyzed through pharmacokinetic models for the estimation of DCE-MRI parameters for quantification of the vessel leakage on a specific lesion (i.e. solid tumor with abnormal vasculature). See part III of this chapter [21]. An example of DCE-MRI in a patient with glioma is given in Figure 2.6 [22].
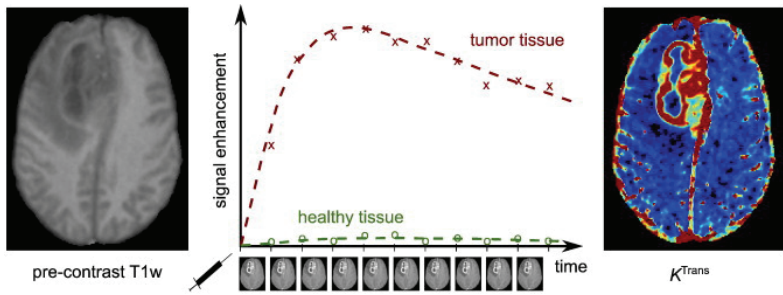
Figure 2.6. Illustration of DCE-MRI in a patient with a glioma. The repeated acquisition of T1-weighted images after contrast agent injection allows the calculation of signal enhancement as a function of time (middle) when compared to the pre-contrast signal intensity (left). These curves can be used to calculate maps of quantitative pharmacokinetic parameters (e.g. K^{Trans}, right) [22].

DSC-MRI

DSC-MRI involves the quantification of cerebral blood volume (CBV) after contrast administration with a dynamic MRI sequence sensitive to $T2^*$ effects. A graph of contrast enhancement is generated to calculate the area under the signal curve as an estimate of relative CBV (rCBV), see Figure 2.7. rCBV refers to the normalization of the values within tumour to an area of normal tissue, most commonly contralateral white matter. High-grade gliomas (HGG), in particular, are associated with disruption of the BBB, which causes more contrast extravasation and consequent adjustments to rCBV calculations with sophisticated mathematical models [18]. PWI could help in discriminating recurrence from RN. RN induces a decrease in CBV due to vessel injury, occlusive vasculopathy and ischemia while in tumor the CBV increases due to angiogenesis and a high density of tumor vessels, see Figure 2.8b. Sugahara et al. concluded that the rCBV ratio < 0.6 may suggest a non-neoplastic contrast enhancing lesion [23]. However, a hypoperfusion is also possible in tumor due to edema and fast tumor growth [24]. Within irradiated tissue, in addition to occlusive vasculopathy, aneurysmal formation, telangiectasia, vascular elongation and proliferation of endothelial cells in the capillary bed can lead to an increase in CBV and therefore induce some overlap of the perfusion parameters between tumor recurrence and RN [24].
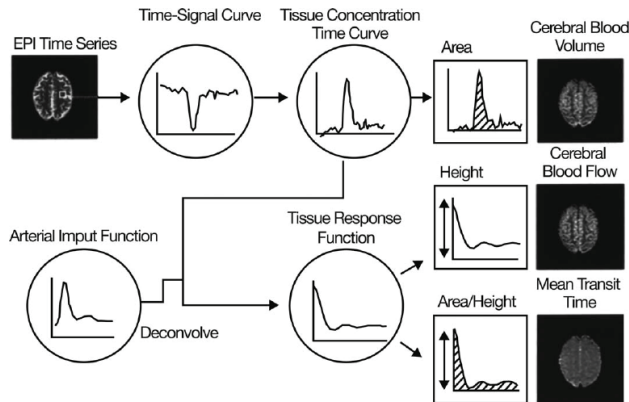

Figure 2.7. Diagram explaining calculation of relative cerebral blood volume (rCBV), cerebral blood flow (CBF), and mean transit time (MTT) using dynamic contrast-enhanced T2-weighted echo planar imaging (EPI) [25].

MR-spectroscopy

^{1}H-MRS is able to provide information on the metabolic composition of tissue. Data can be obtained using single-voxel or multi-voxel techniques with either 2D or 3D chemical shift imaging sequences [26]. The magnetic resonance spectrum from ^{1}H-MRS contains peaks representative of different (hydrogen-containing) metabolites. The relative concentration of each metabolite is derived from the area under the corresponding peak, see Figure 2.6 [18]. The metabolites analyzed include lipids (representing anaerobic glycolysis), NAA (neuronal marker), glutamine (neurotransmitter), creatine (energy metabolism), and choline (cell membrane marker) [26]. In the case of tumor monitoring, tumor metabolite data are compared to those of the contralateral healthy side, see figure 2.6.b [18]. Spectra from regions of interest (ROI) may be obtained as either a single spectrum from each region (i.e., single-voxel MRS) or as a multidimensional array of spectra which is also known as chemical shift imaging, providing significant increase in spatial resolution. MRS, is important for HGG as these tumors are histologically heterogeneous even within the regions appearing uniform on anatomical imaging, and, tumor cells are often present beyond the area depicted on MRI [27].

Spectral patterns with low levels of all metabolites are seen in RN except for a broad peak corresponding to cellular debris containing fatty acids, lipids due to necrosis, lactate due to anaerobe metabolism, and amino acids, while high choline and low NAA levels are found in recurrent tumor (see Figure 2.6.d). Rock et al. compared MRS measures directly with histopathology and concluded a sevenfold-increased likelihood of being pure tumor compared with pure necrosis with a Cho/Cr ratio of > 1.79 or lipid and lactate/Cho ratio of < 0.75 [28]. Limitations of this technique are a limited spatial resolution, the requirement of longer scan times to obtain reproducible data and lack of absolute quantification.
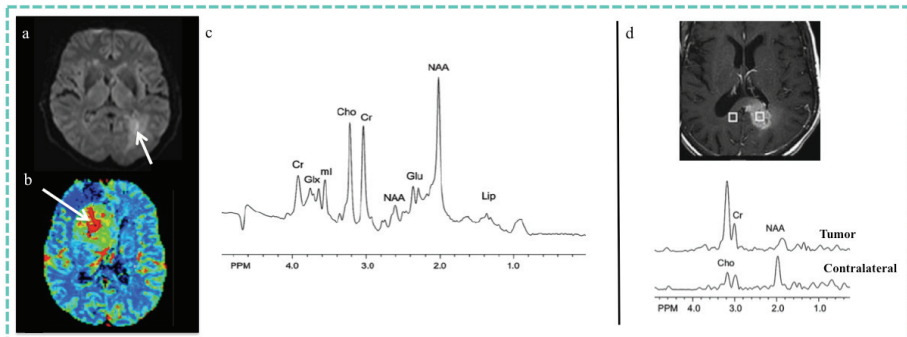

Figure 2.8. Diffusion weighted MRI (DWI), perfusion weighted MRI (PWI) and MR spectroscopy (MRS). (a) DWI in GB (arrow). (b) Calculation of the rCBV ratio using PWI. The figure shows the ROI location covering the maximal values of CBV in the parametric map (arrow). (c) Spectrum recorded from the anterior cingulate gyrus of a normal adult human brain. Peak assignments are: NAA (N-acetylaspartate), Cho (choline-containing compounds), Cr (creatine), mI (myo-inositol), Glu (glutamate), Glx (glutamate and glutamine), Lip (Lipid). (d) Representative brain tumor spectra from a GB involving the splenium of the corpus callosum, showing high Cho and low NAA compared to the contralateral hemisphere [adapted from 14,29 and 30].

PART II: PET IN NEURO-ONCOLOGY

D. PET

Positron emission tomography (PET) is a highly sensitive nuclear imaging technique that enables non-invasive *in vivo* monitoring of metabolic processes [31]. To image a certain molecular target using PET, one needs to first identify and synthesize a radioactive labeled imaging agent that is specific and selective for the target of interest. Following this, a nanomolar amount of the chosen radiolabeled agent is administered to the patient/subject, typically via an intravenous injection. The radioactivity is then traced through the body and its distribution determined from scans obtained with a PET camera [17].

The amount of radioactivity of a radionuclide decays over time. The time-dependence of the amount of radioactivity of a radionuclide is typically expressed as its half-life. The half-life is defined as the time during which the amount of radioactivity reduces to half of its initial value In general, for PET imaging short-lived radionuclides, such as carbon-11 [^{11}C], fluorine-18 [^{18}F] and oxygen-15 [^{15}O], are used [31]. These radionuclides are produced by a particle accelerator (a cyclotron). For example, to produce ^{18}F, a beam of accelerated protons hits a target containing enriched water ($H_2{}^{18}O$). From the interaction of a proton and the ^{18}O nucleus, a ^{18}F nucleus and neutron are emitted [32].

PET imaging is based on the principle of <u>coincidence detection</u> of two 511 keV photons arising from positron emitters, such as ^{11}C, ^{15}O and ^{18}F, see Figure 2.7. PET tracers are molecules of interest that are labeled with a positron emitting radionuclide, which decays by emission of a positron from its nucleus that almost immediately results in the simultaneous emission of two gamma photons in opposite direction after collision with an electron, also called an annihilation event [31,33].
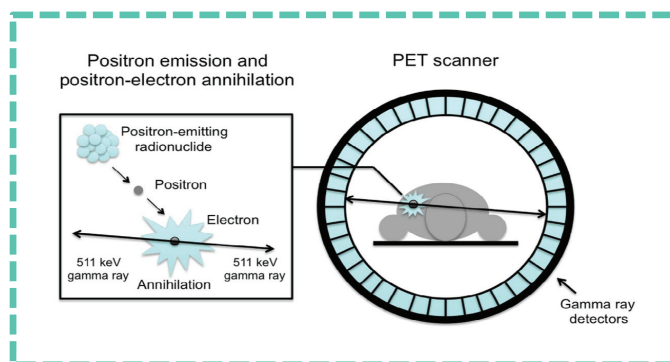

Figure 2.9. Schematic illustration of an annihilation reaction and the subsequent coincidence detection.
Positrons released from the nucleus of the radionuclide annihilate with electrons in tissue, releasing two coincidence photons of 511 keV (left), which are detected by scintillation crystals (blue rectangles). Coincidence detection of annihilated photons identifies a line-of-response (LOR) and makes it possible to localize the source of the annihilation (right) [31].

PET imaging devices take the form of a closed ring of PET detectors, surrounding the subject to be imaged, see Figure 2.7. The PET <u>detectors</u> consist of a scintillation crystal that converts energy from the 511 keV photon into low-energy light photons which are then converted into photoelectrons and

multiplied in the photomultiplier [32]. In current PET scanners, mostly block detectors are used, where one photomultiplier is coupled to multiple scintillation crystals. Common scintillation crystals used in PET are Bismuth Germinate (GSO), Lutetium Orthosilicate (LSO) and Lutetium-yttrium Orthosilicate (LYSO). The photomultipliers can be photomultiplier tubes (PMT) or silicon photomultipliers (SiPM). Generally, the block detectors are arranged into a polygonal configuration with multiple rings covering an axial extent in the range of 15 to 25 cm and having a bore diameter of 80 to 90 cm [33]. Since PET cameras are axially fixed, they are equipped with a <u>computer-controlled horizontal bed</u> for patients to lie on for scanning. The bed along with a patient can be moved to different axial positions in the bore for scanning an organ or a body segment of the patient. Whole body imaging is accomplished by moving the bed and collecting data at adjacent bed positions. The total scan time depends on the patient's body length and the axial field of view (FOV) of the PET scanner [33,34].

The closed ring configuration of PET scanners is able to detect annihilation events (two gamma photons in opposite direction), convert them to electrical signals and place the events into a sinogram that can be reconstructed into a tomographic image [17]. The detection of two photons within a predefined time window, typically in the order of 5 to 20 ns, is called a coincidence event and is an indication that there was an annihilation somewhere along the line connecting the associated detectors. This line is called a line of response (LOR). The number of coincidence events detected on a particular LOR indicates the amount of radioactivity present along that line during the scan [32].

Data can be acquired in either frame mode or list mode. In <u>frame mode</u>, coincidence events are stored into a sinogram during a specified time or total number of events. In <u>list mode</u>, coincidence events are coded with "time marks" as they are received in sequence and stored as individual events as they occur. In frame mode, data can be acquired as static or dynamic images. Whereas static images provide an estimate of gross tracer uptake, dynamic imaging provides the kinetics of tracer uptake in an organ [34]. In static imaging, a single-frame image is acquired by collecting data over a specific period of time, while in dynamic imaging data are collected in multiple frames, each of a predetermined period of duration. List-mode data have the advantage that they can be reconstructed into either static or dynamic images, where frame durations can be determined after finishing the acquisition.

As already mentioned, the coincidence events in PET are stored in the form of a sinogram, in contrast to conventional planar imaging where individual events are stored into an two-dimensional (2D) matrix. The sinogram is basically a 2D histogram of the LORs in distance-angle coordinates in a given plane [34]. These sinograms can be reconstructed into cross-sectional images (transverse, coronal and sagittal) that represent the tracer distribution into a subject. For PET there are two categories of <u>reconstruction algorithms</u>, namely filtered backprojection (FBP) and iterative methods [32,35]. Although, FBP is computationally very efficient, mostly iterative reconstruction techniques are being used in PET. One of the reasons for this is that PET is considered as a quantitative imaging modality. However, to obtain quantitative image information the acquired data should be corrected for image degrading effect during the reconstruction process.

E. Image-degrading effects in PET

PET imaging is affected by a number of image degrading effects. These effects can be related to the physics of positron emission, to the PET detector and to the subject being imaged.

Positron emitters have physics that intrinsically limit the spatial resolution of the PET imaging system. Photon non-collinearity is caused by the fact that the net momentum for an emitted positron, and the electron with which it annihilates, can be non-zero, this results in deviations from 180° between the trajectories of the two emitted photons as shown in Figure 2.8 [36]. The spatial resolution in PET is also impaired due to the positron range. Emitted positrons travel a certain distance in the surrounding medium before they can reach thermal energies in order to be annihilated. This distance is referred to as the positron range, see Figure 2.8. Positron range (and photon non-collinearity) are conventionally not discussed as physical phenomenon that can be corrected for; rather, they are often seen as limitations of PET imaging. However, with the arrival of iterative reconstruction algorithms, even though it is not possible to determine these effects for each particular detected event, it is possible to calculate and incorporate their probability distributions into the reconstruction algorithm [36].

Detector-related image degrading effects in PET are caused by the physical size of the detector crystals, parallax error, dead-time effects and variations in detector efficiencies between detector pairs. The physical size of the detector scintillation crystals plays an important role on the spatial resolution of the PET system, because the exact position where a photon hits a specific detector element is not known. Parallax error is another resolution limiting effect that occurs when photons enter a scintillation crystal at oblique angles. Crystal size can be reduced and depth of interactions of the 511 keV photons have to be determined in order to reduce these detector related effects. Another problem is the loss of signal due to the dead time of the detector. This is the time needed from the absorption of the photon in the crystal and the detection of a coincidence event. During this time the detection system is unable to process a second event, which will be lost. This loss can be reduced by using detectors with shorter scintillation decay time and faster electronics. Variations in detector efficiencies reduces the quantitative accuracy in PET and should be corrected. The process of correcting for this effects is referred to as normalization, accomplished by exposing uniformly all detector pairs to a 511 keV photon source (e.g., ^{68}Ge source), without a subject in the FOV [34].
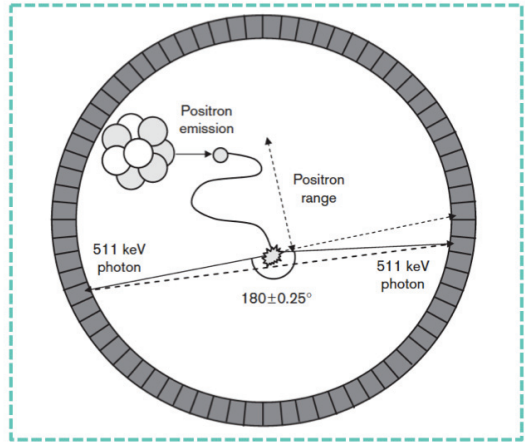
Figure 2.10. Positron range and positron non-collinearity [36].

Subject related image-degrading effects can be classified as scattered coincidences, random coincidences and photon attenuation. In the case of scatter coincidence, one photon from annihilation travels without interaction, and other annihilation photon is deflected because of Compton scattering in the patient, see Figure 2.9.b. Random coincidences are events where two annihilation photons from two separate annihilation events are detected by a detector pair within the same time window, see Figure 2.9.c. These events raise the background in the image causing loss of image contrast [34,36,37]. Corrections for random and scattered coincidences are covered in [31] and are required for quantitative PET. Photon attenuation refers to the property of emitted radiation to interact with tissue and other materials as it passes through the body. As a result one (or both) annihilation photons are possibly not detected, see Figure 2.9.d [32,34,37]. Attenuation correction can be performed by the incorporation of the attenuation factors for each LOR determined by dividing the counts obtained during a transmission scan by the counts obtained during a blank scan, which is a transmission scan performed with an empty gantry. Another possibility is the use of x-ray CT as the transmission data [32,34,36]. For this reason, PET is often combined with CT and both are co-registered to be able to perform attenuation correction, but also to provide some anatomical reference to the PET data.
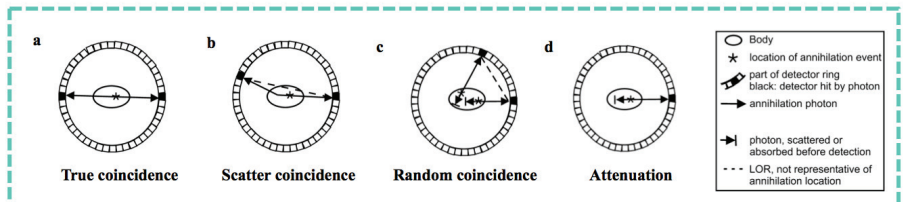

Figure 2.11. (a) True coincidence (b) Scatter coincidence (c) Random coincidence (d) Attenuation. In scatter and random coincidences, the line of response (LOR) drawn between 2 detectors is not representative of annihilation location. Three or more photons (multiples) detected in coincidence are rejected by PET coincidence electronics [adapted from 37].

Finally, another factor that needs to be kept in mind when tracer uptake in small tumors is measured in PET imaging is the partial volume effect (PVE) [38]. PVE refers to two distinct phenomena that make intensity values in images differ from what they ideally should be. The first effect is image blurring introduced by the finite spatial resolution of the imaging system. Because of the limit of the spatial resolution of current PET scanners, "hot" spots that are smaller than twice the spatial resolution of the PET scanner show partial loss of intensity, and the activity around the structure appears to be smeared over a larger area than it occupies in the reconstructed image. While the total counts are preserved the object appears to be larger and have a lower activity concentration than it actually has. This has been shown to result in large biases in the estimates of regional radioactivity concentrations [35,36]. The second phenomenon causing PVE is image sampling. In PET, the radiotracer distribution is sampled on a voxel grid. Obviously, the contours of the voxels do not match the actual contours of the tracer distribution. Most voxels therefore include different types of tissues, see Figure 2.10.b. Motion, especially respiratory motion, also introduces a blurring effect that results in additional PVE. Smaller pixel sizes in the reconstructed images may prevent some structures from being affected by PVE and will reduce the biases introduced by PVE in others. Pixel size should also be kept small to reduce the tissue fraction effect [38].
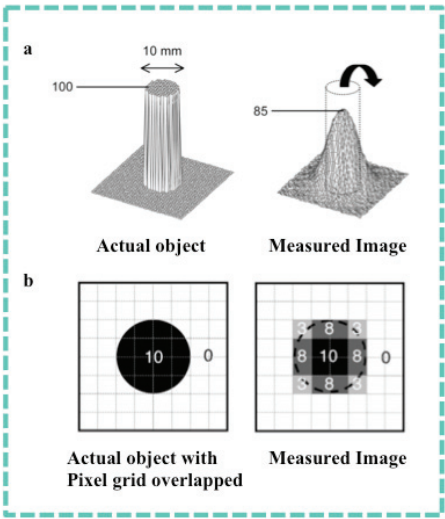
Figure 2.12. Two phenomena playing a role in the partial volume effect (PVE) in PET. Circular source (diameter of 10 mm) of uniform activity (100 arbitrary units) in nonradioactive background yields measured image in which part of signal emanating from source is seen outside actual source. Maximum activity in measured image is reduced to 85 (a). Pixels on edges of sources include both source and background tissues. Signal intensity in these pixels is mean of signal intensities of underlying tissues (b) [adapted from 38].

F. PET tracers in neuro-oncology

The capacity of conventional MRI to differentiate tumor tissue from nonspecific tissue changes may be limited especially after therapeutic interventions such as neurosurgical resection, radiotherapy, and chemotherapy. Molecular imaging using PET may provide relevant additional information on tumor metabolism, which allows for more accurate diagnostics especially in clinically equivocal situations. In the last decades, a variety of molecular targets have been addressed by specific PET tracers in neuro-oncology, see Figure 2.11 [14,39-41]. The most frequently used tracers and their PET applications in the study of HGG will be discussed :

^{18}F-Fluorodeoxyglucose [^{18}F-FDG]

^{18}F-Fluoroethyltyrosine [^{18}F-FET]

^{18}F-Fluoromethylcholine [^{18}F-FCho]

Hypoxia-PET

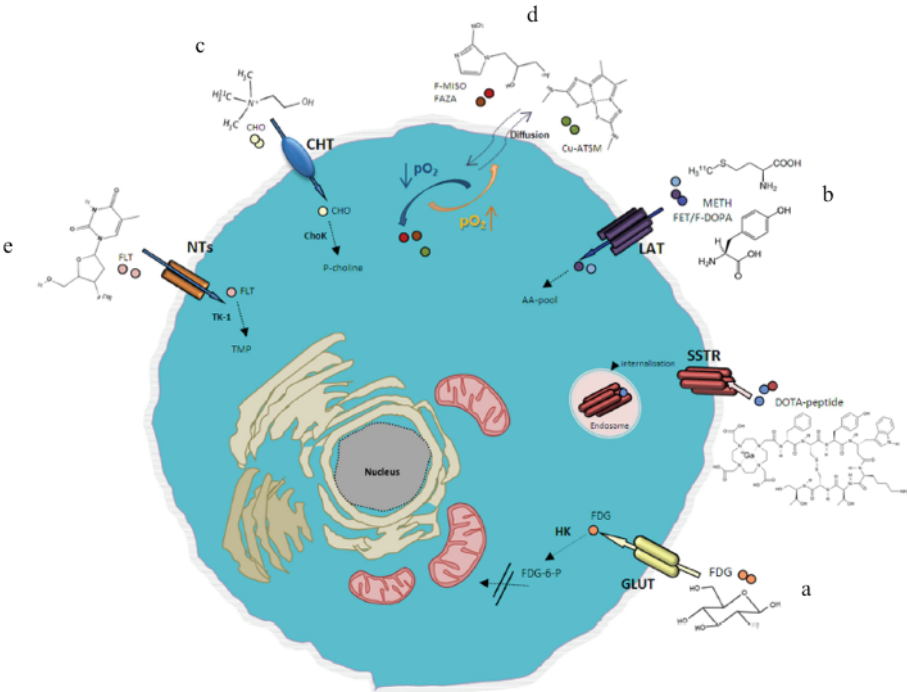^{18}F-fluorothymidine [^{18}F-FLT]

Figure 2.13. Broad range of radiopharmaceuticals in neuro-oncology [14].
^{18}F-FDG (a), amino-acid PET (b), ^{18}F-FCho (c), hypoxia-PET (d), ^{18}F-FLT (e) and less common somatostatin receptoranalogues (DOTA peptides), which have potential for theranostic use.

^{18}F-Fluorodeoxyglucose [^{18}F-FDG]

^{18}F-FDG is the most common clinically utilized PET tracer due to its high potential to detect tumors in the body based on increased energy demand of malignant tumors. ^{18}F-FDG PET measures cellular glucose metabolism as a function of the enzyme hexokinase, see Figure 2.12 [17,39,40]. ^{18}F-FDG-6-PO$_4$ accumulates in cells over time, leading to signal amplification and making this imaging agent a suitable indicator of hexokinase II activity as well as a cell's need for glucose [17]. In the brain, ^{18}F-FDG exhibits high uptake in normal gray matter, reflecting the metabolic demands of neurons and glia. This high uptake in normal brain parenchyma often makes the delineation and the localization of brain tumors difficult and only co-registration of ^{18}F-FDG PET with MRI allows the rating of glucose metabolism in specific areas of a tumor [39,40].
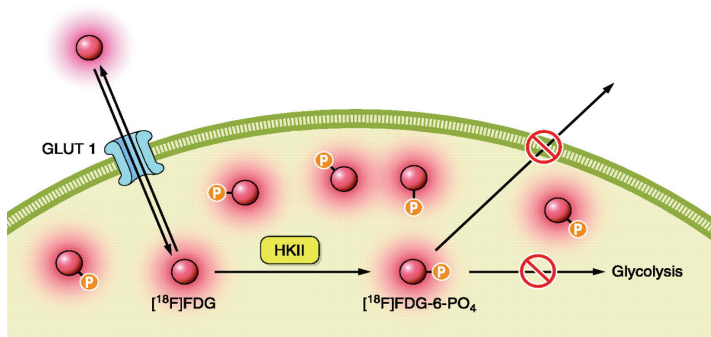

Figure 2.14. Mechanism of ^{18}F-FDG signal amplification. ^{18}F-FDG is an analog of glucose, whereby the 2-carbon hydroxyl group of glucose is substituted with a fluorine atom. Like glucose, ^{18}F-FDG is taken up by cells via the glucose transporter (GLUT1) and phosphorylated by hexokinase II (HKII) to form ^{18}F-FDG-6-PO$_4$; however, (unlike glucose), further metabolism is prevented due to the absence of the required 2-carbon hydroxyl, and hence ^{18}F-FDG remains trapped within the cell [17].

Multiple studies investigating the potential of ^{18}F-FDG in discriminating tumor recurrence and RN have been performed. However, these published equivocal results with sensitivities and specificities ranging from 40 to 100% [42,43-47]. Besides the high and variable uptake by the normal cortex, radiation injury can activate repair mechanisms or lead to inflammation, which can lead to false positive results [24]. It is hypothesized that delineation of gliomas from gray matter could be improved by extending the interval between the administration of ^{18}F-FDG and PET data acquisition, called "dual phase imaging", but the sensitivity to detect the extent of low-grade gliomas remains poor [48-51].

^{18}F-Fluoroethyltyrosine [^{18}F-FET]

Besides ^{18}F-FDG, radiolabeled amino acids are the most commonly used PET tracers for brain tumors. An advantage over ^{18}F-FDG is the relatively low uptake of amino acids by normal brain tissue. Therefore, cerebral gliomas can be distinguished from the surrounding normal tissue with higher contrast [39,40]. Labeled amino acid tracers developed so far for PET imaging are divided in 2 categories: tracers actively incorporated into the proteins, such as ^{11}C-Methionine (^{11}C-MET), potentially allowing studies of protein synthesis and tracers not integrated into proteins, such as ^{18}F-fluoroethyltyrosine (^{18}F-FET), which are valuable tools to evaluate amino-acid transport [52]. Most PET studies of cerebral gliomas have been performed with ^{11}C-MET, although the short half-life of ^{11}C (20 min) limits the use of this tracer to the few centers that are equipped with an on-site cyclotron facility. Results with ^{18}F-FET PET are similar to those with ^{11}C-MET [53], and due to its longer half-life (109 min) and no/minimal uptake in macrophages and inflammatory cells, ^{18}F-FET PET is preferred for clinical use [52,54-59]. The diagnostic potential of ^{18}F-FET PET in brain tumors is well documented, for example, a superior delineation of human gliomas by ^{18}F-FET PET compared with MRI, a high specificity for the detection of gliomas and biopsy site planning, and a promising role for the distinction between tumor recurrence and benign post-therapeutic changes [55,60,61]. Several studies have also indicated that time-activity curves of FET uptake contain biological information beyond that of static images, and this data may be helpful for glioma grading [61].
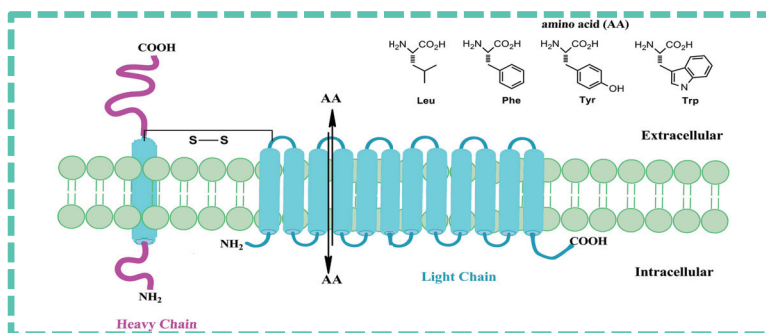
Figure 2.15. An illustration of the transmembrane L-type amino acid transporter-1 (LAT1). LAT1 is responsible for the transport of amino acids with large neutral side chains through an exchange mechanism [62].

The molecular mechanisms of amino acid uptake in gliomas are not yet fully explained [63]. The increased uptake of ^{18}F-FET by cerebral glioma tissue appears to be caused mainly by increased transport via sodium-independent amino acid transport system L for large neutral amino acids (LAT), see figure 2.11 and 2.13, and Na$^+$-dependent general amino acid transporters B$^{0,+}$ and B^0 [24,54]. The selectivity for radiolabeled amino acids targeting LAT1 over other system L transporters (LAT2, LAT3 and LAT4) is not demonstrated. This lack of selectivity is important because other system L transporters do not appear to be overexpressed to the same degree as LAT1 in human cancers [62]. Finally, it is important to note that since large neutral amino acids also enter normal brain tissue, a disruption of the BBB is not a prerequisite for intratumoral accumulation of these amino acids [63].

[18]F-Fluoromethylcholine [^{18}F-FCho]

Positron-labeled choline analogues appear to be successful as oncological PET probes because a major hallmark of cancer cells is increased lipogenesis [64,65]. Choline metabolism is presented in Figure 2.14. Phosphorylation by choline kinase (CK) constitutes an important step in the incorporation of choline into phospholipids, which is an essential component of all cell membranes. In cancer, there is often an increase in the cellular transport and phosphorylation of choline, as well as an increase in the expression of CK, increasing the uptake of radiolabeled choline [66-68]. Choline can be labeled with either ^{11}C or [18]F. As a tracer, ^{11}C-Cho is biochemically indistinguishable from natural choline, however, the short half-life of ^{11}C has led to the development of ^{18}F labeled derivatives, such as ^{18}F-Fluoromethylcholine [^{18}F-FCho] [69,70]. Previous *in vitro* studies have clearly documented that these fluorinated choline analogues are suitable substrates for the enzyme CK [69,71], although the rate of their incorporation in phospholipids may be slower than that of endogenous choline [72]. ^{18}F-labeled choline analogues have been investigated as oncological PET probes for the detection of (recurrent) local prostate cancer, but seems to have limited value for T (tumor) and N (nodal) staging. In the brain, excellent discrimination between tumor and normal tissue can be achieved due to low physiological uptake of ^{18}F-FCho. As such, ^{18}F-FCho has been shown to be highly sensitive in detecting tumor recurrence in post-treatment patients even in comparison with MRI and ^{18}F-FCho could play a role in differentiating between brain tumor recurrence and RN [64]. In addition, HGG, metastases, and benign lesions can be distinguished based on ^{18}F-FCho uptake [64]. However, several disadvantages need to be kept in mind, such as a rapidly oxidation to radiolabeled derivatives of betaine (Figure 2.14) and the fact that the uptake of ^{18}F-FCho is influenced by BBB damage and inflammation [40,64,67,70,73,74]. As such, correlative imaging with MRI is of utmost importance [64].
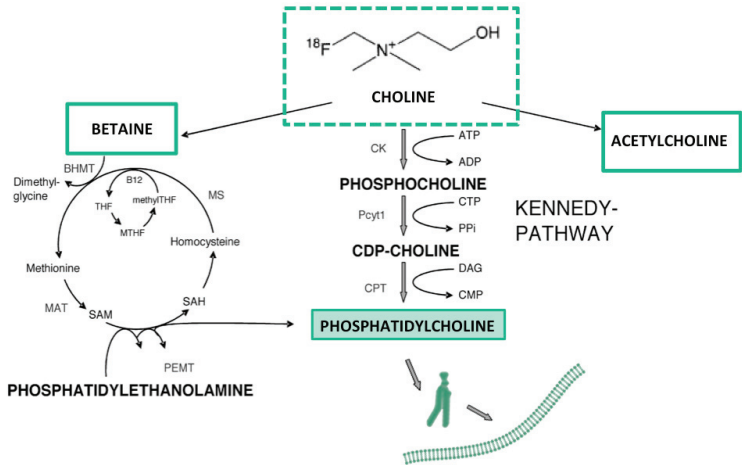

Figure 2.16. Choline metabolism. Choline is phosphorylated, acetylated, and oxidized. Phosphocholine is further converted to phosphatidylcholine, which is then incorporated into membrane synthesis [adapted from 74, 3D volumes from Somersault [®]].

Hypoxia-PET

Hypoxia is a pathological condition arising in living tissues when oxygen supply does not adequately cover the cellular metabolic demand. Detection of this phenomenon in tumors is of the utmost clinical relevance because tumor aggressiveness, metastatic spread, failure to achieve local tumor control, and increased rate of recurrence, and ultimate poor outcome are all associated with hypoxia [14,75,76]. A number of hypoxia tracers are available for PET. The uptake and retention mechanism of the first introduced hypoxia tracer, called ^{18}F-fluoromisonidazole (^{18}F-FMISO), is given in Figure 2.15 [14,17,39,40,67]. The slow uptake of ^{18}F-FMISO in target tissue and slow clearance of unbound ^{18}F-FMISO from non-hypoxic areas stimulated the development of ^{18}F-fluoroazomycin arabinoside (^{18}F-FAZA) with improved pharmacokinetics [14]. A highly increased uptake of ^{18}F-FAZA was observed in all glioma types, with a tumor to normal brain tissue ratio (TBR) ranging between 2 and 16 due to low uptake in normal brain tissue [77]. For a comprehensive review on hypoxia PET, see [14].
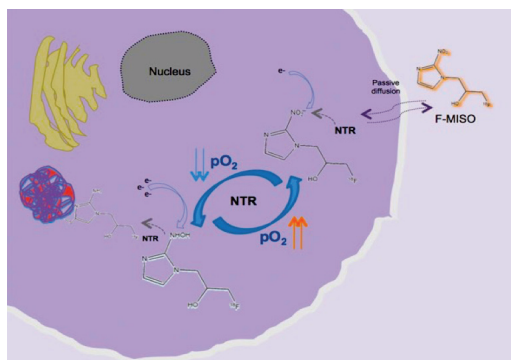

Figure 2.17. Uptake and retention mechanism of ^{18}F-FMISO. After passive diffusion through the membrane and in the presence of reduced pO_2, ^{18}F-FMISO undergoes progressive reduction by the nitroreductase enzyme (NTR). This process is reversible in the presence of sufficient O_2. Conversely, in hypoxic conditions the reduced ^{18}F-FMISO is covalently bound to the intracellular proteins resulting in tracer accumulation within the hypoxic cell [14].

[18]F-fluorothymidine [^{18}F-FLT]

Deoxyribonucleic acid (DNA) synthesis is required for cell growth and proliferation. Nucleotides of the four bases (cytosine, guanine, adenine and thymidine) are required for DNA synthesis. Of these four nucleosides, thymidine is the only one incorporated exclusively into DNA, and not ribonucleic acid (RNA), and provides a measure of DNA synthesis [78]. ^{18}F-fluorothymidine [^{18}F-FLT] has been proposed to directly assess DNA synthesis to estimate tumor cell proliferation and has been proposed for therapy monitoring, based on the concept that change in DNA synthesis should be the most direct index of therapeutic effects on tumor proliferation [52]. ^{18}F-FLT as an imaging biomarker seems to be predictive of overall survival in bevacizumab and irinotecan treated recurrent glioma patients and would allow differentiation between recurrent glioma and RN [79,80]. However, the sensitivity for the detection of anaplastic gliomas might be lower than required for clinical application, and dependence of ^{18}F-FLT uptake on BBB disruption raises the question of its specificity [52].

PART III: IMAGE ANALYSIS OF PET AND MRI

A. Semi-quantitative image analysis

PET

In clinical practice, visual inspection of PET or PET/CT images, based on differences in contrast, is the main tool for image interpretation, and for initial diagnosis, staging or restaging, this method is usually adequate [81-83]. However, evaluation of the response of solid tumors to therapy is more challenging and requires some form of quantification [80]. The standard uptake value (SUV) is the most widely used parameter for analysis of most tracers in oncology. The SUV represents the uptake of the radiotracer in a certain region of interest (ROI) measured over a certain interval after tracer administration normalized to the injected activity and to a factor (such as body weight) that takes into account the distribution throughout the body [80,82]. The SUV normalized to body weight is given by the following equation:

$$SUV = \frac{Radiotracer\ concentration\ \left(\frac{kBq}{ml}\right)}{\frac{Injected\ activity (Bq)}{Body\ weight\ (kg)}} \qquad (1)$$

A major advantage of using semi-quantitative SUV values is the simplicity of the experimental procedure, only requiring a static scan without input function [83,84]. However, many factors affect the outcome of the SUV. These factors can be either physiological, such as the uptake period, or technical, such as the scan acquisition parameters. An overview of these influencing factors is given in [81]. Despite its limits, the SUV, when computed in the same center with the same settings, has been shown effective in assessing the response to therapy by comparing its value in a given tumor before and after treatment, especially with ^{18}F-FDG [82]. Other frequently used semi-quantitative measures for PET are the tumor to normal tissue ratio (TNR) or the tumor to normal brain tissue ratio (TBR).

DCE-MRI

Diagnostic criteria in DCE-MRI include the evaluation of dynamic time-series of the signal intensity, extracted using manually selected ROIs within the lesion area. The analysis of dynamic time-series can be performed qualitatively (i.e. visual inspection of the curve shape), semi-quantitatively (non-model based) or quantitatively through pharmacokinetic modeling techniques [85]. Semi-quantitative analysis of the DCE-MRI data can provide parameters, such as:

- the *area under the curve (AUC)*
- *the time to maximum enhancement*
- *maximal enhancement*
- *wash-in or wash-out rate determined by the slope of the curve*

These measures have been successfully used in the past for evaluation of prostate, breast, cervical, and pancreatic cancers [86,87]. This approach has several advantages, such as being straightforward to implement and no advanced image processing is required. However, distinguishing between intra- and

extravascular contrast is not possible and semi-quantitative parameters can be influenced by the acquisition parameters and other variables. Quantitative analysis on the other hand aims to provide a link between the tissue signal enhancement and physiologically relevant parameters, see part III.B [87].

B. Quantitative image analysis

Ultimately, PET was developed as a quantitative tool, and its quantitative characteristics are increasingly being recognized as providing an objective, more accurate, and less observer-dependent measure for prognosis and response monitoring purposes than visual inspection alone. Furthermore, it allows an easier comparison between centers and in order to properly analyze data coming from a variety of tracers having different kinetic properties, visual inspection and SUV are not sufficient [81,82]. The most accurate method to analyze PET and DCE-MRI data is compartmental modeling or kinetic modeling (KM). A general overview of the mathematics underlying KM can be found in [88,89].

Kinetic modeling in PET

In KM, the PET radiotracer is assumed to be exchanged between compartments, each compartment representing a homogeneous physiological or biochemical entity, and the rates at which the tracer is transferred between compartments are described by first-order differential equations, see Figure 2.19 [81]. KM requires a more complex and time-consuming study procedure, i.e. dynamic scanning to measure the time course of tracer concentration in the tumor (time activity curve, TAC) and arterial blood sampling to measure the time course of tracer concentration in plasma (arterial input function, AIF) [82,84].
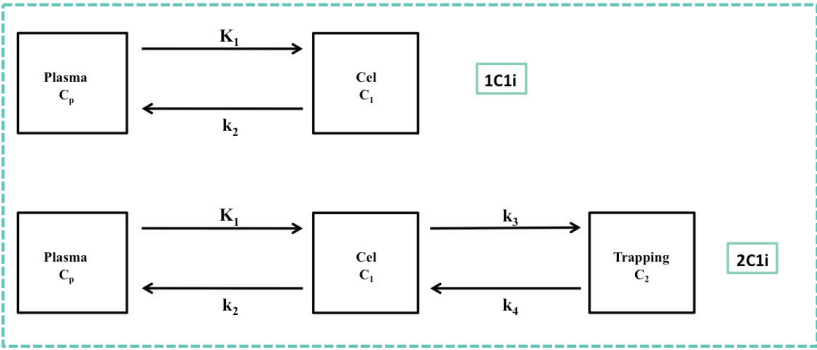
Figure 2.18. Most important compartmental models used in dynamic PET. Scheme of a one-tissue compartmental model (1 compartment 1 input function (1C1i)) and a two-tissue compartmental model (2 compartments and 1 input function (2C1i)). C_p denotes the tracer concentration in arterial blood plasma, C_1 and C_2 the total concentration in tissue 1 and 2, respectively. K_1 (ml/ccm/min) indicates the rate of the tracer delivery into tissue, k_2 (1/min) the rate of efflux of tissue, k_3 (1/min) the specific binding of tracer to a receptor, transporter or enzyme, and k4 (1/min) the dissociation from that specific binding [82,90].

For example, in case of ^{18}F-FDG, a 2-compartmental model is proposed in which the radiotracer passes from the arterial blood (C_p) into the brain (first compartment, C_1) and it subsequently trapped inside the cell after phosphorylation by hexokinase (second compartment, C_2). Note that C_p is the time course of the tracer in arterial plasma or the AIF. When first order kinetics are applied to this 2-compartmental model,

the concentration of the tracer in compartments C_1 and C_2 in function of time can be described by two differential equations:

$$\frac{dC1(t)}{dt} = k1Cp(t) - (k2 + k3)C1(t) + k4C2(t) \qquad (2)$$

$$\frac{dC2(t)}{dt} = k3C1(t) - k4C2(t) \qquad (3)$$

Furthermore, the total concentration of the activity in the tissue of interest (tumor) is: $C_i(t) = C_1(t) + C_2(t)$. When the TACs in the tissue and the AIF are given, the rate constants (k_1 - k_4) can be calculated through a numerical procedure known as the non-linear least squares (NLLS) [82,84,88].

Another issue that needs to be taken into account is that the measurement of the AIF includes all radiolabeled molecules and therefore not only intact tracer but also the radiolabeled metabolites present in the circulation. To obtain the correct AIF, the measured input function needs to be corrected by a function describing the fraction of intact tracer over time. The latter is obtained by taking blood samples at different time points and by analyzing them with High Pressure Liquid Chromatography (HPLC) [91,92]. Furthermore, the obtained blood curve needs to be corrected for decay, propagation delay and dispersion. Finally a conversion of the blood curve into a plasma curve is necessary by calculating the blood/plasma ratio [93-95].

Graphical analysis in PET

Graphical methods refer to the transformation of measurements of time-series of plasma and tissue uptake data into a linear plot, the slope of which is related to the number of available tracer binding sites [90]. There are two types of graphical methods: the Patlak plot and the Logan plot, which can be applied to irreversible and reversible tracers, respectively [82]. An example is given in figure 2.20.

Patlak plot or Patlak/Gjedde plot

It can be shown that after a certain time t*, which depends on the tracer, subject and ROI, the relationship between the ratio of the tissue TAC $C_T(t)$ and plasma TAC $C_P(t)$, and between the integral and the instantaneous value of $C_P(t)$, becomes linear as expressed by:

$$\frac{C_T(t)}{C_P(t)} = K_i \frac{\int_0^t C_P(\tau)d\tau}{C_P(t)} + const \qquad t > t* \qquad (4)$$

K_i denotes the so-called irreversible uptake rate constant, the parameter of interest, which quantifies the rate at which the tracer is irreversibly trapped [82,96].

Logan plot

The Logan plot is the counterpart of the Patlak plot for reversible radiotracers. It can be shown that after a certain time t* the ratio between the integral of $C_P(t)$ and the instantaneous value of $C_T(t)$, and between the integral and the instantaneous value of $C_T(t)$, become linearly related according to:

$$\frac{\int_0^t C_T(\tau)d\tau}{C_T(t)} = V_T \frac{\int_0^t C_P(\tau)d\tau}{C_T(t)} + const \qquad t > t* \qquad (5)$$

where V_T (ml/cm^{-3}) denotes the distribution volume of the tracer, or the ratio at equilibrium between the tracer concentration in the ROI and the plasma, which is a measure of the overall uptake of the tracer relative to the plasma compartment [82,90].

Both graphical methods require arterial blood sampling and dynamic scanning, but fast frames over the initial phase are not required. A disadvantage of the Patlak and Logan plot compared to KM is its inability to estimate kinetic parameters separately, however, calculations are faster and they are less sensitive to noise [82,84].
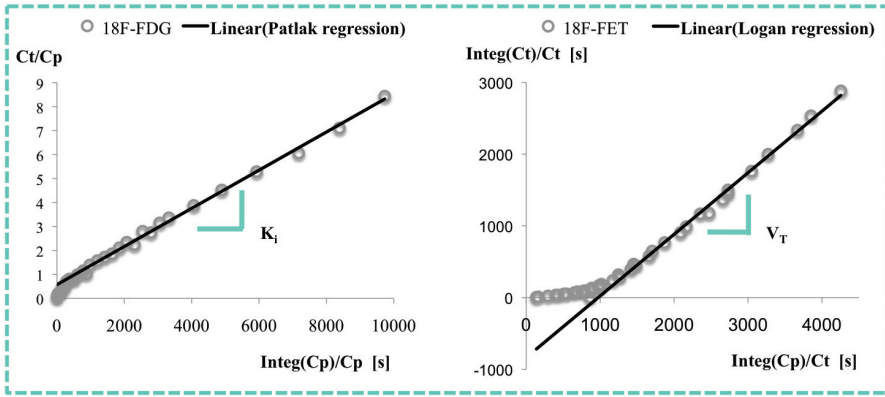
Figure 2.19. Example of a Patlak plot (^{18}F-FDG) and a Logan plot (^{18}F-FET).

Kinetic modeling in DCE-MRI

Applying KM analysis to DCE-MRI data allows the quantification of vessel leakage of a specific lesion. Detailed reviews of tracer KM approaches in DCE-MRI have been published by Sourbron and Buckley [97,98]. The most commonly used model in literature is the 1-compartmental Tofts model. Tofts et al. assumed that following intravenous bolus administration, MR contrast agents are distributed rapidly without any protein binding and will pass the disrupted blood vessel endothelium and move to the extravascular extracellular space (EES). Using this model, transfer constant rates of capillary permeability from the vessel to the EES (k_{trans}) and backwards (k_{ep}), together with the volume of the EES (V_e) and blood plasma volume (V_p) are estimated. These quantitative parameters can be used for diagnosis of the lesion as well as for response in treatment. Tofts et al. extended the original model to a 2-compartmental model by introducing the vascular term as an external compartment and considering bidirectional transport between the blood plasma and the EES, see Figure 2.21. The result was to separate the enhancement caused by contrast leakage from that caused by intravascular contrast. The extended Tofts model is described by the following equation [20,21,87]:

$$C_t(t) = K_{trans} \, e^{-k_{ep} t} * C_P(t) + V_P C_P(t) \qquad (6)$$

$C_t(t)$ and $C_p(t)$ represent the time-series in the tissue of interest and the plasma, respectively. The '*' indicates the convolution operation and V_p is the volume fraction of the plasma compartment. KM for DCE-MRI data also require the accurate estimation of an AIF of the contrast agent. Usually, AIF determination is done by direct measurement of a near-by vessel, such as an artery on the lesion's site, or by applying population average measured AIF profiles [21].
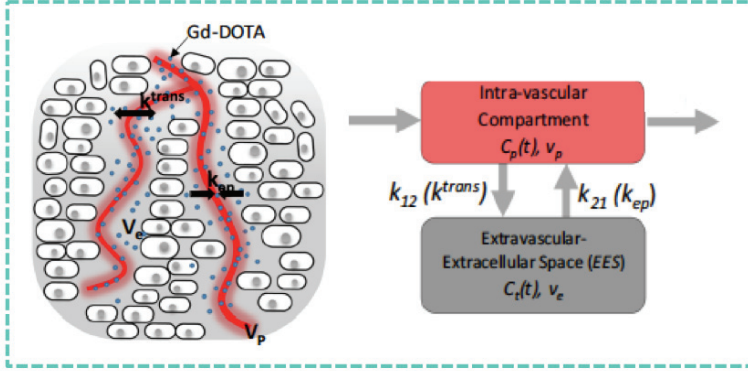
Figure 2.20. KM analysis of DCE-MRI. Tissue distribution of the tracer (dots) in a lesion site and DCE-MRI parameters (k_{trans}, k_{ep}, V_e, V_p) (left) and the 2-compartment model that is implemented in the extended Toft's model (right) [adapted from 21].

Model selection criteria

When applying KM, model fitting is mostly performed using MATLAB (Mathworks, Natick, MA, USA) or PMOD (PMOD technologies®, Zürich, Switserland) [86]. Model fitting can be optimized by [98,99]:

- visual inspection
- evaluation of standard errors (SE)
- goodness-of-fit displayed by the Akaike information criterion (AIC), Schwartz criterion (SC) and model selection criterion (MSC)
- chi-square value

The AIC criterion estimates an information-theoretic measure, the Kullback-Leibler distance, which quantifies the information lost, if a model is used which only approximates the true model [100]. The Schwartz criterion (SC), also called Bayesian Information Criterion (BIC), attempts to identify *a posteriori* what the most probable model is for a particular data set. The SC is similar to the AIC but includes an additional penalty for the number of data points and therefore favors simpler models. Another criterion used is the Model Selection Criterion (MSC), which is a reciprocal modification of AIC [99]. The preferred model is the one with the lowest chi square, lowest AIC value, the lowest SC value and the highest MSC value. More complex models should only be accepted when they produce a significant improvement in fit quality [97,99].

PART IV: SPECIFICS OF SMALL ANIMAL PET AND MRI

D. Small animal PET

In addition to its clinical utility, μPET has a wide range of applications in the basic research and preclinical arenas. For example, μPET can be used to investigate basic physiological and molecular mechanisms of human disease through the use of appropriate radiolabeled imaging agents and rodent models. Furthermore, μPET can be used to evaluate novel radiolabeled PET imaging agents, effectiveness of new therapies, and biodistribution of novel pharmaceuticals [17]. However, small animal imaging must have sufficiently high spatial resolution to allow anatomic localization as well as sufficient specificity and sensitivity to provide an accurate description of the molecular distribution and concentration [101]. Therefore, a dedicated small animal PET scanner is required, see Figure 2.16. Small-animal PET systems are often modified versions of their clinical equivalent, where rats and mice form the majority of the experimental animal population, mostly immobilized during the scan using volatile anaesthetics. μPET systems also use a cylindrical geometry with a typical diameter of ± 15 cm as compared to ± 80 cm for clinical PET systems. The axial field-of-view of preclinical PET systems is typically ± 8 cm, which is more or less equal to the length of a mouse, allowing to measure the whole-body dynamic biodistribution of a labeled compound in a single scan [102]. The superior resolution of μPET is achieved by the application of smaller detector elements. This also reduces the effect of photon non-collinearity [36]. Sensitivity can be improved by using smaller detector ring diameter, by increasing the length of the detector ring, by using novel detector geometries that improve the photon absorption efficiency and by using detectors with better timing resolution and faster decay [101,102]. To our knowledge, the best spatial resolution reported for state-of-the-art μPET systems has been about 0.7 mm full-width-at-half-maximum and the maximum sensitivity is ± 9-10 % for scans of the whole body of animals [103-105].
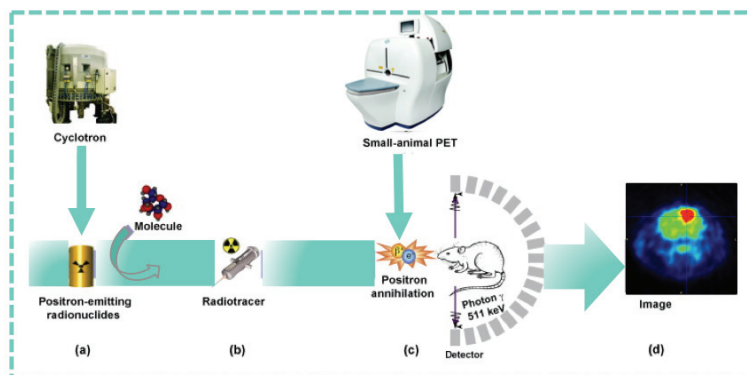
Figure 2.21. Schematic representation of the principle underpinning μPET. The cyclotron creates the positron-emitting radionuclides (a). These radionuclides are incorporated into molecules during the radiosynthesis (b). μPET scans are acquired following intravenous injection of the radiotracer. The radiotracer accumulates in the tissue to be studied, and annihilations are detected by the PET camera and simultaneously localized within a fixed period of time by a series of opposing detectors (c). By collecting a statistically significant number of radioactive events, mathematical algorithms reconstruct a three-dimensional image that shows the distribution of the positron-emitting molecules in the brain. (e.g. ^{18}F-FDG uptake in F98 GB in rat brain) (d) [adapted from 105].

E. Small animal MRI

Specialized MRI hardware for mouse imaging includes high field small bore magnets, gradient systems with rapid rise times and high amplitudes, and small radiofrequency (RF) coils, see Figure 2.17 [101]. Most preclinical studies have been performed at field strengths from 4.7-11.7 Tesla. The main advantage of increasing field strength is a higher signal-to-noise ratio (SNR), which can then be traded for improved spatial resolution or shorter scan times. Also, RF coils of the appropriate size are typically used to further improve SNR. During MR, mice are commonly lightly anesthetized using isoflurane or other anesthetics, and core temperature is typically maintained near 36-37° using circulating heated water or warm air [17,101].
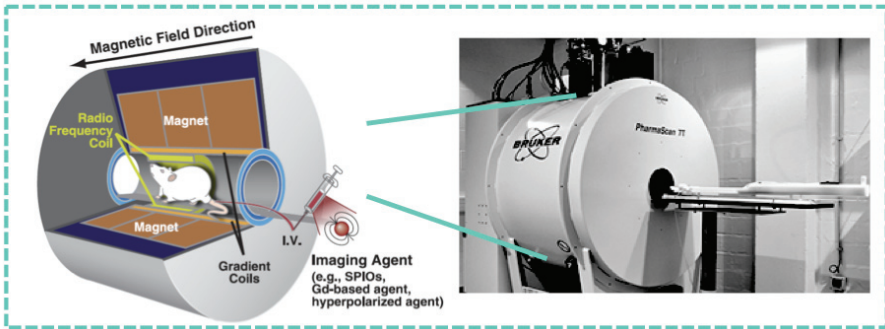
Figure 2.22. Small animal MRI. In general, a μMRI scanner is comprized of a set of embedded coils: one coil that generates the main relatively homogenous magnetic field, "gradient coils" that produce variations in the magnetic field in the X, Y, and Z directions that are used to localize the source of the MR signal, and finally "RF coils" that generate an RF pulse responsible for altering the alignment of the magnetic dipoles [adapted from 17].

F. Data analysis in small animal imaging

In many cases the same or similar methods and models as for human imaging can be used for small animal KM, although results obtained in humans cannot be extrapolated directly to animals. KM in small animal imaging with PET presents several issues, reviewed in [91]. A major issue is blood sampling because only a small fraction of total blood can be sampled to avoid side effects. However, recent developments in automated blood-sampling allow to take very small blood samples or measuring blood activity without any blood loss at all. The Twilite system (Swisstrace GmbH, Switserland) is such a sampling device that enables the measurement of the radioactivity continuously during the total PET acquisition without any blood loss. This system enables a continuous blood flow using a shunt, connecting the arteria femoralis and vena femoralis, and a pump system. An alternative to blood sampling is to derive the AIF directly from the dynamic images by deriving TAC from a blood pool VOI. However, given the size of the heart in small animals and the limited FOV, the definition of the VOI is not always trivial [91,94,106].

REFERENCES

[1] James ML, Gambhir SS. A molecular imaging primer: modalities, imaging agents, and applications. Physiology Reviews 2012;92(2):897-965.

[2] Weissleder R, Ross BDR, Rehemtulla A, et al. Molecular imaging: principles and practice. Part I: Molecular Imaging Technologies. Chapter 1: General Principles of Molecular Imaging. People's medical publishing house-USA 2010;1-9.

[3] Hattingen E, Pilatus U. Brain tumor Imaging. Bahr O, Steinbach JP, Weller M. Chapter: Brain Tumor Imaging. Medical Radiology and Radiation Oncology. Berlin, Heidelberg: Springer 2016; 1-11.

[4] Plewes DB, Kucharczyk W. Physics of MRI: a primer. Journal of Magnetic Resonance Imaging 2012;35(5):1038-1054.

[5] Zerr I. Understanding Alzheimer's disease. Mason EJ, Donahue MJ, Ally BA. Chapter 10: Using magnetic resonance imaging in the early detection of Alzheimer's disease. InTech 2013;225-247.

[6] Hattingen E, Pilatus U. Brain tumor imaging. Hattingen E, Warmuth-Metz M. Chapter: MR imaging of brain tumors. Berlin, Heidelberg: Springer 2016;11-55.

[7] Hendee WR, Morgan CJ. Magnetic resonance imaging. Part I-physical principles. The Western Journal of Medicine 1984;141(4):491-500.

[8] http://www.revisemri.com/images/t1differences.gif
    http://www.revisemri.com/images/t2differences.gif

[9] Vlaardingerbroek MT, Boer JA. Magnetic resonance imaging: theory and practice. Chapter 2: MRI and its hardware. Berlin, Heidelberg: Springer 2003:9-54.

[10] Barnett HG. High-grade gliomas. Diagnosis and treatment. Totowa, New Jersey: Humana Press Inc 2007;65.

[11] Barnett HG. High-grade gliomas. Diagnosis and treatment. Totowa, New Jersey: Humana Press Inc 2007;109.

[12] Drevelegas A, Papanikolaou N. Imaging of brain tumors with histological correlations. Chapter 2: Imaging modalities in brain tumors. Berlin, Heidelberg: Springer 2011;13-33.

[13] Barnett HG. High-grade gliomas. Diagnosis and treatment. Totowa, New Jersey: Humana Press Inc 2007:92-93.

[14] Lopci E, Grassi I, Chiti A, et al. PET radiopharmaceuticals for imaging of tumor hypoxia: a review of the evidence. American Journal of Nuclear Medicine and Molecular Imaging 2014;4(4):365-384.

[15] Bobek-Billewicz B, Stasik-Pres G, Majchrzak H, et al. Differentiation between brain tumor recurrence and radiation injury using perfusion, diffusion-weighted imaging and MR spectroscopy. Folia Neuropathologica 2010; 48(2):81-92.

[16] Alexiou GA, Tsiouris S, Kyritsis AP, et al. Glioma recurrence versus radiation necrosis: accuracy of current imaging modalities. Journal of Neurooncology 2009;95:1-11.

[17] James ML, Gambhir SS. A molecular imaging primer: modalities, imaging agents, and applications. Physiology Reviews 2012;92(2):897-965.

[18] Ahmed R, Oborski MJ, Hwang M, et al. Malignant gliomas: current perspectives in diagnosis, treatment, and early response assessment using advanced quantitative imaging methods. Cancer Management and Research 2014;6:149-170.

[19] Sundgren PC. MR spectroscopy in radiation injury. American Journal of Neuroradiology 2009;30:1469-1476.

[20] Kontopodis E, Kanli G, Manikis GC, et al. Assessing Treatment Response Through Generalized Pharmacokinetic Modeling of DCE-MRI Data. Cancer Informatics 2015;14:41-51.

[21] Spanakis M, Kontopodis E, Van Cauter S, et al. Assessment of DCE-MRI parameters for brain tumors through implementation of physiologically-based pharmacokinetic model approaches for Gd-DOTA. Journal of Pharmacokinetics and Pharmacodynamics 2016;43(5):529-547.

[22] Heye AK, Culling RD, Valdés Hernández MDC, et al. Assessment of blood–brain barrier disruption using dynamic contrast-enhanced MRI. A systematic review. NeuroImage: Clinical 2014;6:262-274.

[23] Sugahara T, Korogi Y, Shigematsu Y, et al. Value of dynamic susceptibility contrast magnetic resonance imaging in the evaluation of intracranial tumors. Topics in Magnetic Resonance Imaging 1999;10(2):114-124.

[24] Jain R, Narang J, Sundgren PM, et al. Treatment induced necrosis versus recurrent/progressing brain tumor: going beyond the boundaries of conventional morphologic imaging. Journal of Neurooncology 2010;100(1):17-29.

[25] Shiroishi MS, Castellazzi G, Boxerman JL, et al. Principles of T2*-Weighted Dynamic Susceptibility Contrast MRI Technique in Brain Tumor Imaging. Journal of Magnetic Resonance Imaging 2015;41(2):296-313.

[26] Chao ST, Suh JH, Raja S, et al. The sensitivity and specificity of FDG PET in distinguishing recurrent brain tumor from radionecrosis in patients treated with stereotactic radiosurgery. International Journal of Cancer 2001;96:191-197.

[27] Barnett HG. High-grade gliomas. Diagnosis and treatment. Totowa, New Jersey: Humana Press Inc 2007:133.

[28] Rock JP, Scarpace L, Hearshen D, et al. Associations among magnetic resonance spectroscopy, apparent diffusion coefficients, and image-guided histopathology with special attention to radiation necrosis. Neurosurgery 2004;54:1111-1117.

[29] Pillai JJ. Functional brain tumor imaging. Barker PB. Chapter: Diagnosis and Characterization of Brain Tumors: MR Spectroscopic Imaging. New York: Springer science & business media 2014;40.

[30] Guzmán-De-Villoria JA, Mateos-Pérez JM, Fernández-García P, et al. Added value of advanced over conventional magnetic resonance imaging in grading gliomas and other primary brain tumors. Cancer Imaging 2014;14:35.

[31] van der Veldt AA, Smit EF, Lammertsma AA. Positron Emission Tomography as a Method for Measuring Drug Delivery to Tumors in vivo: The Example of [(11)C]docetaxel. Frontiers in Oncology 2013;13(3):208:1-7.

[32] Shreve P, Townsend DW. Clinical PET-CT in Radiology: Integrated Imaging in Oncology. Turkington TG. Chapter 2: PET imaging basics. New York: Springer Science and Business Media 2011;21-28.

[33] Saha GB. Basics of PET imaging: Physics, chemistry and regulations. Chapter 2: PET scanning systems. Switzerland: Springer international publishing 3rd edition 2015.

[34] Saha GB. Basics of PET imaging: Physics, chemistry and regulations. Chapter 3: Data acquisition and correction. Switzerland: Springer international publishing 3rd edition 2015.

[35] Saha GB. Basics of PET imaging: Physics, chemistry and regulations. Chapter 4: Image reconstruction. Switzerland: Springer international publishing 3rd edition 2015.

[36] Rahmim A, Zaidi H. PET versus SPECT: strengths, limitations and challenges. Nuclear Medicine Communications 2008;29:193-207.

[37] Verel I, Visser GWM, van Dongen GA. The promise of immune-PET in radioimmunotherapy. Journal of Nuclear Medicine 2005;46:164S-171S.

[38] Soret M, Bacharach SL, Buvat I. Partial-Volume effect in PET tumor imaging. Journal of Nuclear Medicine 2007;48:932-945.

[39] Demetriades AK1, Almeida AC, Bhangoo RS, et al. Applications of positron emission tomography in neuro-oncology: a clinical approach. Surgeon 2014;12(3):148-157.

[40] Hattingen E, Pilatus U. Brain tumor imaging. Langen KJ, Galldiks N. Chapter: PET imaging of brain tumors. Berlin, Heidelberg: Springer 2016;121-135.

[41] Frosina G. Positron emission tomography of high-grade gliomas. Journal of Neurooncology 2016;127:415-425.

[42] Van Laere K, Ceyssens S, Van Calenbergh F, et al. Direct comparison of 18F-FDG and 11C-methionine PET in suspected recurrence of glioma: sensitivity, inter-observer variability and prognostic value. European Journal of Nuclear Medicine and Molecular Imaging 2005;32:39-51.

[43] Chao ST, Suh JH, Raja S, et al. The sensitivity and specificity of FDG PET in distinguishing recurrent brain tumor from radionecrosis in patients treated with stereotactic radiosurgery. International Journal of Cancer 2001;96:191-197.

[44] Doyle WK, Budinger TF, Valk PE, et al. Differentiation of cerebral radiation necrosis from tumor recurrence by [18F]FDG and 82Rb positron emission tomography. Journal of Computer Assisted Tomography 1987;11(4):563-570.

[45] Kahn D, Follett KA, Bushnell DL, et al. Diagnosis of recurrent brain tumor: value of 201T1 SPECT vs 18F-fluorodeoxyglucose PET. American Journal of Roentgenology 1994;163:1459-1465.

[46] Ricci PE, Karis JP, Heiserman JE, et al. Differentiating recurrent tumor from radiation necrosis: time for re-evaluation of positron emission tomography? American Journal of Neuroradiology 1998;19:407-413.

[47] Kim YH, Oh SW, Lim YJ, et al. Differentiating radiation necrosis from tumor recurrence in high-grade gliomas: assessing the efficacy of 18F-FDG PET, 11C-methionine PET and perfusion MRI. Clinical Neurology and Neurosurgery 2010;112(9):758-765.

[48] Mertens K, Acou M, Van Hauwe J, et al. Validation of 18F-FDG PET at conventional and delayed intervals for the discrimination of high-grade from low-grade gliomas: a stereotactic PET and MRI study. Clinical Nuclear Medicine 2013;38(7):495-500.

[49] Spence AM, Muzi M, Mankoff DA, et al. 18F-FDG PET of gliomas at delayed intervals: improved distinction between tumor and normal gray matter. Journal of Nuclear Medicine 2004;45(10):1653-1659.

[50] Prieto E, Martí-Climent JM, Domínguez-Prado I, et al. Voxel-based analysis of dual-time-point 18F-FDG PET images for brain tumor identification and delineation. Journal of Nuclear Medicine 2011;52(6):865-872.

[51] Horky LL1, Hsiao EM, Weiss SE, et al. Dual phase FDG-PET imaging of brain metastases provides superior assessment of recurrence versus post-treatment necrosis. Journal of Neurooncology 2011;103(1):137-146.

[52] Juweid ME, Hoekstra OS. Positron emission tomography. Goldman S, Pirotte BJM. Chapter 16: Brain tumors. Methods in molecular biology, Humana Press 2011;727:291-315.

[53] Grosu AL, Astner ST, Riedel E, et al. An interindividual comparison of O-(2-[18F]fluoroethyl)-L-tyrosine (FET)- and L-[methyl-11C]methionine (MET)-PET in patients with brain gliomas and metastases. International Journal of Radiation Oncology Biology Physics 2011;81(4):1049-1058.

[54] Becherer A, Karanikas G, Szabó M, et al. Brain tumour imaging with PET: a comparison between [18F]fluorodopa and [11C]methionine. European Journal of Nuclear Medicine and Molecular Imaging 2003;30(11):1561-1567.

[55] Langen KJ, Hamacher K, Weckesser M, et al. O-(2-[18F]fluoroethyl)-L-tyrosine: uptake mechanisms and clinical applications. Nuclear Medicine and Biology 2006;33(3):287-294.

[56] Langen KJ, Tatsch K, Grosu AL, et al. Diagnostics of cerebral gliomas with radiolabeled amino acids. Deutsches Ärzteblatt International 2008;105(4):55-61.

[57] Chen W. Clinical applications of PET in brain tumors. Journal of Nuclear Medicine 2007;48(9):1468-1481.

[58] Herholz K, Langen KJ, Schiepers C, et al. Brain tumors. Seminars in Nuclear Medicine 2012;42:356-370.

[59] Walter F, Cloughesy T, Walter MA, et al. Impact of 3,4-dihydroxy-6-18F-fluoro-L-phenylalanine PET/CT on managing patients with brain tumors: the referring physician's perspective. Journal of Nuclear Medicine 2012;53(3):393-398.

[60] Floeth FW, Sabel M, Stoffels G, et al. Prognostic Value of 18F-Fluoroethyl-L-Tyrosine PET and MRI in Small Nonspecific Incidental Brain Lesions. Journal of Nuclear Medicine 2008;49:730-737.

[61] Galldiks N, Law I, Pope WB, et al. The use of amino acid PET and conventional MRI for monitoring of brain tumor therapy. Neuroimage Clinical 2016;13:386-394.

[62] Ikotun OF, Marquez BV, Huang C, et al. Imaging the L-type amino acid transporter-1 (LAT1) with Zr-89 immunoPET. PLoS One 2013;15;8(10):e77476.

[63] Piroth MD, Pinkawa M, Holy R, et al. Prognostic value of early [18F]fluoroethyltyrosine positron emission tomography after radiochemotherapy in glioblastoma multiforme. International Journal of Radiation Oncology Biology Physics 2011;80(1):176-184.

[64] Calabria FF, Barbarisi M, Gangemi V, et al. Molecular imaging of brain tumors with radiolabeled choline PET. Neurosurgery Reviews 2016;1-10.

[65] Mertens K, Slaets D, Lambert B, et al. PET with (18)F-labelled choline-based tracers for tumour imaging: a review of the literature. European Journal of Nuclear Medicine and Molecular Imaging 2010;37(11):2188-2193.

[66] Kwee SA, Ko JP, Jiang CS, et al. Solitary brain lesions enhancing at MR imaging: evaluation with fluorine 18 fluorocholine PET. Radiology. 2007;244(2):557-565.

[67] Vallabhajosula S. ^{18}F-labelled Positron Emission Tomographic Radiopharmaceuticals in Oncology: An Overview of Radiochemistry and Mechanisms of Tumor Localization. Seminars in Nuclear Medicine 2007;37:400-419.

[68] Nakagami K, Uchida T, Ohwada S, et al. Increased choline kinase activity and elevated phosphocholine levels in human colon cancer. Japanese Journal of Cancer Research 1999;90(4):419-424.

[69] DeGrado TR, Coleman RE, Wang S, et al. Synthesis and evaluation of 18F-labeled choline as an oncologic tracer for positron emission tomography: initial findings in prostate cancer. Cancer Research 2001;61:110-117.

[70] Treglia G1, Giovannini E, Di Franco D, et al. The role of positron emission tomography using carbon-11 and fluorine-18 choline in tumors other than prostate cancer: a systematic review. Annals of Nuclear Medicine 2012;26(6):451-461.

[71] Hara T, Kosaka N, Kishi H. Development of (18)F-fluoroethylcholine for cancer imaging with PET: synthesis, biochemistry, and prostate cancer imaging. Journal of Nuclear Medicine 2002;43:187-199.

[72] Bansal A, Shuyan W, Hara T, et al. Biodisposition and metabolism of [(18)F]fluorocholine in 9L glioma cells and 9L glioma-bearing fisher rats. European Journal of Nuclear Medicine and Molecular Imaging 2008;35:1192-1203.

[73] Roelcke U, Bruehlmeier M, Hefti M, et al. F-18 choline PET does not detect increased metabolism in F-18 fluoroethyltyrosine-negative low-grade gliomas. Clinical Nuclear Medicine 2012;37(1):e1-3.

[74] Roivainen A, Forsback S, Gronroos T, et al. Blood metabolism of [methyl-11C]choline; implications for in vivo imaging with positron emission tomography. European Journal of Nuclear Medicine 2000;27:25-32.

[75] Nordsmark M, Overgaard J. Tumor hypoxia is independent of hemoglobin and prognostic for loco-regional tumor control after primary radiotherapy in advanced head and neck cancer. Acta Oncologica 2004;43(4):396-403.

[76] Rajendran JG, Krohn KA. F-18 fluoromisonidazole for imaging tumor hypoxia: imaging the microenvironment for personalized cancer therapy. Seminars in Nuclear Medicine 2015;45(2):151-162.

[77] Postema EJ, McEwan AJ, Riauka TA, et al. Initial results of hypoxia imaging using 1-alpha-D:-(5-deoxy-5-[18F]-fluoroarabinofuranosyl)-2-nitroimidazole (18F-FAZA). European Journal of Nuclear Medicine and Molecular Imaging 2009;36(10):1565-1573.

[78] Mankoff DA, Shields AF, Krohn KA. PET imaging of cellular proliferation. Radiology Clinics of North America 2005;43:153-167.

[79] Chen W, Delaloye S, Silverman DH, et al. Predicting treatment response of malignant gliomas to bevacizumab and irinotecan by imaging proliferation with [18F] fluorothymidine positron emission tomography: a pilot study. Journal of Clinical Oncology 2007;20;25(30):4714-4721.

[80] Enslow MS, Zollinger LV, Morton KA, et al. Comparison of 18F-fluorodeoxyglucose and 18F-fluorothymidine PET in differentiating radiation necrosis from recurrent glioma. Clinical Nuclear Medicine 2012;37(9):854-861.

[81] Boellaard R. Standards for PET Image Acquisition and Quantitative Data Analysis. Journal of Nuclear Medicine 2009;50:11S-20S.

[82] Tomasi G1, Turkheimer F, Aboagye E. Importance of quantification for the analysis of PET data in oncology: review of current methods and trends for the future. Molecular Imaging and Biology 2012;14(2):131-146.

[83] Hoekstra CJ, Paglianiti I, Hoekstra OS, et al. Monitoring response to therapy in cancer using [18F]-2-fluoro-2-deoxy-D-glucose and positron emission tomography: an overview of different analytical methods. European Journal of Nuclear Medicine 2000;27(6):731-743.

[84] Lammertsma AA, Hoekstra CJ, Giaccone G, et al. How should we analyse FDG PET studies for monitoring tumour response? European Journal of Nuclear Medicine and Molecular Imaging 2006;33(S1):16-21.

[85] Karahaliou A, Vassiou K, Arikidis NS, et al. Assessing heterogeneity of lesion enhancement kinetics in dynamic contrast-enhanced MRI for breast cancer diagnosis. British Journal of Radiology 2010;83(988):296-309.

[86] Narang J, Jain R, Arbab AS, et al. Differentiating treatment-induced necrosis from recurrent/progressive brain tumor using nonmodel-based semiquantitative indices derived from dynamic contrast-enhanced T1-weighted MR perfusion. Neuro-Oncology 2011;13(9):1037-1046.

[87] Heye AK, Thrippleton MJ, Armitage PA, et al. Tracer kinetic modelling for DCE-MRI quantification of subtle blood-brain barrier permeability. Neuroimage 2016;125:446-455.

[88] Watabe H, Ikoma Y, Kimura Y, et al. PET kinetic analysis-compartmental model. Annals in Nuclear Medicine 2006;20(9):583-588.

[89] Gunn RN, Gunn SR, Cunningham VJ. Positron emission tomography compartmental models. Journal of Cerebral Blood Flow & Metabolism 2001;21(6):635-652.

[90] Logan J. Graphical analysis of PET data applied to reversible and irreversible tracers. Nuclear Medicine and Biology 2000;27(7):661-670.

[91] Dupont P, Warwick J. Kinetic modelling in small animal imaging with PET. Methods 2009;48(2):98-103.

[92] Bansal A1, Shuyan W, Hara T, et al. Biodisposition and metabolism of [(18)F]fluorocholine in 9L glioma cells and 9L glioma-bearing fisher rats. European Journal of Nuclear Medicine and Molecular Imaging 2008;35(6):1192-1203.

[93] Slaets D, De Vos F. Comparison between kinetic modelling and graphical analysis for the quantification of 18F-fluoromethylcholine uptake in mice. European Journal of Nuclear Medicine and Molecular Imaging 2013;3:66.

[94] Convert L, Morin-Brassard G, Cadorette J, et al. A new tool for molecular imaging: the microvolumetric β blood counter. Journal of Nuclear Medicine 2007;48:1197-1206.

[95] Moerman L, De Naeyer D, Boon P, et al. P-glycoprotein at the blood-brain barrier: kinetic modeling of 11C-desmethylloperamide in mice using a 18F-FDG PET scan to determine the input function. European Journal of Nuclear Medicine and Molecular Imaging 2011;1(1):12.

[96] Patlak CS, Blasberg RG, Fenstermacher JD. Graphical evaluation of blood-to-brain transfer constants from multiple-time uptake data. Journal of Cerebral Blood Flow and Metabolism 1983;3(1):1–7.

[97] Sourbron SP, Buckley DL. Tracer kinetic modelling in MRI: estimating perfusion and capillary permeability. Physics in Medicine and Biology 2012;57:R1-33.

[98] Sourbron, SP, Buckley DL. Classic models for dynamic contrast-enhanced MRI. Nuclear magnetic resonance in Biomedicine 2013;26:1004-1027.

[99] PMOD technologies. User's Guide PMOD Kinetic Modeling (PKIN). 2012;3.4:55-56.

[100] Glatting G, Kletting P, Reske SN, et al. Choosing the optimal fit function: comparison of the Akaike information criterion and the F-test. Medical Physics 2007;34:4285-4292.

[101] de Kemp RA, Epstein FH, Catana C, et al. Symposium on multimodality cardiovascular molecular imaging technology – part 2. Journal of Nuclear Medicine 2010;51:18S-32S.

[102] Vanhove C, Bankstahl JP, Krämer SD, et al. Accurate molecular imaging of small animals taking into account animal models, handling, anaesthesia, quality control and imaging system performance. European Journal of Nuclear Medicine and Molecular Imaging Physics 2015;2(1):31.

[103] España S, Marcinkowski R, Keereman V, et al. DigiPET: sub-millimeter spatial resolution small-animal PET imaging using thin monolithic scintillators. Physics in Medicine and Biology 2014;59(13):3405-3420.

[104] Marcinkowski R, Mollet P, Van Holen R, et al. Sub-millimetre DOI detector based on monolithic LYSO and digital SiPM for a dedicated small-animal PET system. Physics in Medicine and Biology 2016;61(5):2196-2212.

[105] Lancelot S, Zimmer L. Small-animal positron emission tomography as a tool for Neuropharmacology. Trends in Pharmacological Sciences 2010;31(9):411-417.

[106] Weber B, Burger C, Biro P, et al. A femoral arteriovenous shunt facilitates arterial whole blood sampling in animals. European Journal of Nuclear Medicine 2002;29(3):319-323.

Chapter 3. Scope and aims

Chapter 3.

Scope and aims

"There are no secrets to success. It is the result of preparation, hard work, and learning from failure" [Colin Powell].

A. Early therapy response assessment in GB using PET and MRI

Although the Response Assessment in Neuro-Oncology (RANO) criteria address some of the limitations of the previous MacDonald criteria for the evaluation of therapy in high-grade gliomas, they do not take into account changes in tumor biology, which may precede anatomical changes of the tumor volume. To address this problem, incorporating biological changes measured by advanced magnetic resonance imaging (MRI) and positron emission tomography (PET) are promising. Due to diagnostic limitations of ^{18}F-fluorodeoxyglucose (^{18}F-FDG) PET, that is the high uptake in normal brain tissue and nonspecific uptake in e.g. inflammation, our goal was to investigate the potential of ^{18}F-fluoromethylcholine (^{18}F-FCho) PET for response prediction in glioblastoma (GB) patients treated with the Stupp regimen. Hence our first question is as follows:

Question 1: Are we able to assess therapy response in GB patients post-treatment using ^{18}F-FCho PET and MRI according to the RANO criteria?

In chapter 4, our study in which we performed PET and MRI scans prior to the start of treatment (pre-RT), during RT (2, 4 and 6 weeks) and 1 month after the completion of RT (post-RT) in a homogeneous group of 11 GB patients was described. Our first aim was to investigate whether therapy response could be predicted by ^{18}F-FCho PET and MRI. Secondly, the imaging modality which allows prediction of therapy response first was investigated.

From the experience gained in this field, it became apparent that in order to study new techniques allowing an accurate assessment of the effect of RT, a preclinical model that mimics human GB treatment is mandatory. This brings us to the next question:

Question 2: Are we able to assess the effect of therapy in a rat model of GB using PET and MRI?

In chapter 5, an orthothopic allograft F98 GB rat model was described. Subsequently, using this GB rat model, MRI-guided 3D conformal arc RT using a Small Animal Radiation Research Platform (SARRP), which mimics the isocentric external-beam treatment device that is used to deliver image-guided RT in humans was described and validated. Furthermore, the effect of treatment was validated using follow-up MRI and PET using two different tracers, ^{18}F-FDG and ^{18}F-FCho, to investigated which modality was most suited for the early detection of treatment response in this optimized rat model of GB.

B. Differentiation between radiation necrosis and tumor recurrence using PET and MRI

Early and late therapy-related effects on brain tissue are an unwanted but unavoidable consequence after RT. This often results in a major problem in the clinic to differentiate recurrent brain tumor from radiation necrosis (RN) as both entities frequently develop at the resection site and often have a similar appearance on conventional MRI. Obviously, a correct diagnosis is important for further patient management and a definite diagnosis can currently only be achieved by brain biopsy. Hence, our goal was to investigate whether PET was able to differentiate GB from RN. Because pathological confirmation of RN in the clinic is mostly lacking, we performed *in vivo* experiments using our F98 GB rat model to be able to answer the following questions:

Question 3: Are ^{18}F-FCho, ^{18}F-FET and ^{18}F-FDG PET able to discriminate between recurrent GB and RN in rats?

A first step to answer this question was the development of a RN rat model that is described in Chapter 6. Subsequently, the uptake of 3 PET tracers, ^{18}F-FDG, ^{18}F-fluoroethyltyrosine (^{18}F-FET) and ^{18}F-FCho, in both the GB and RN rat model was compared. First, a semi-quantitative analysis using standard uptake values (SUV) and lesion to normal brain ratios (LNRs) was performed. Furthermore, the uptake mechanism of ^{18}F-FDG, ^{18}F-FET and ^{18}F-FCho in GB and RN was clarified by applying kinetic modeling (KM). A higher k_3 was hypothesized in GB compared to RN when applying a two-tissue compartmental model for ^{18}F-FDG PET. Secondly, assuming a higher amount of amino acid transport mechanisms in tumor, K_1 of ^{18}F-FET was hypothesized to be higher in GB than in RN applying a one-tissue compartment model analysis. Finally, the kinetic model for quantifying ^{18}F-FCho uptake by applying a one-compartment model, a two-compartment model and a model using three compartments, containing two input functions (^{18}F-FCho and ^{18}F-Fluorobetaine) was optimized. Also graphical analysis was performed.

Advanced MRI techniques also yielded promising results to discriminate GB from RN. Dynamic contrast-enhanced MRI (DCE-MRI) allows the straightforward characterization of the vascular microenvironment of a post-treatment brain tumor and because vascular properties, such as vascular density, permeability, blood flow and the composition of the extravascular space are probably different between GB and RN. Hence, our next question was the following:

Question 4: Is *in-vivo* DCE-MRI able to discriminate between GB and RN in rats?

In chapter 7, changes in signal intensities in contrast-enhanced MRI using pharmacokinetic modeling based on quantitative parameters with semi-quantitative parameters extracted from dynamic time series were compared in a histologically confirmed GB and RN rat model.

Chapter 4.

Therapy response assessment in GB patients using ^{18}F-FCho PET and MRI according to the RANO criteria

This chapter includes data from:

Julie Bolcaen M.Sc.[1], Marjan Acou M.D.[2], Tom Boterberg M.D. Ph.D.[3], Christian Vanhove Ph.D.[4], Filip De Vos Pharm. Ph.D.[5], Caroline Van den Broecke M.D.[6], Roel Van Holen Ph.D.[4], Karel Deblaere M.D. Ph.D.[2], Ingeborg Goethals M.D. Ph.D.[1]

[1]Department of Nuclear Medicine, Ghent University Hospital
[2]Department of Radiology, Ghent University Hospital
[3]Department of Radiation Oncology, Ghent University Hospital
[4]IBiTech - MEDISIP - Department of Electronics and Information Systems, Ghent University
[5]Department of Radiopharmacy, Ghent University
[6]Department of Pathology, Ghent University Hospital

De Pintelaan 185, 9000 Gent, Belgium

Chapter 4. Therapy response assessment in GB patients using ^{18}F-FCho PET and MRI according to the RANO criteria

INTRODUCTION

Glioblastoma (GB) is the most malignant and most common glioma type in adults, accounting for 60 to 70 % of all malignant gliomas and has a high morbidity and mortality rate [1]. For newly diagnosed patients with a good performance status, the standard of care includes maximal surgical resection followed by combined external beam radiation therapy (RT), temozolomide (TMZ) and maintenance TMZ, see Chapter 1 [2,3,4]. Even with optimal treatment, median survival is only 12-14 months [1]. Several prognostic factors have been identified in patients with GB, such as age, Karnofsky performance status, neurological status, World Health Organization (WHO) tumor grade, tumor location, extent of surgery, genetic and molecular biomarker status, and concomitant TMZ [5,6].

The evolution of therapy response assessment in glioma is described in Chapter 1. Until 2010, mainly MacDonald criteria were used for assessing response to therapy in high-grade glioma (HGG) [7]. In an attempt to more accurately assess treatment response, new response criteria for Response Assessment in Neuro-Oncology (RANO) were introduced in 2010, including the tumor size (in 2D) as measured on T2- and Fluid Attenuated Inversion Recovery (FLAIR)-weighted magnetic resonance imaging (MRI) in addition to the contrast enhancing tumor part [7]. However, increased enhancement after the administration of gadolinium and FLAIR/T2 hyperintense signal abnormalities can also occur due to treatment-related inflammation, postsurgical changes, subacute irradiation effects and radiation necrosis (RN) [7,8]. As is the case for the MacDonald criteria, also the RANO criteria do not take into account changes in tumor biology, which may precede anatomical changes of the tumor volume [1,9]. To visualize changes in tumor biology, functional imaging techniques assessing for example proliferative activity or hypoxia are needed [10]. ^{18}F-fluorodeoxyglucose (^{18}F-FDG) PET, estimating glucose metabolism of (tumor) cells (see chapter 2), allows monitoring therapeutic response in brain tumors with a greater specificity than computed tomography (CT) or MRI [1]. However, a major disadvantage of ^{18}F-FDG is its high uptake in normal brain tissue, decreasing the sensitivity of ^{18}F-FDG PET for detecting recurrent or residual glioma [1]. Delayed ^{18}F-FDG PET imaging may however overcome this problem [1,11]. Our group showed that ^{18}F-FDG PET imaging at a delayed interval (300 min p.i.) better distinguishes tumor from normal gray matter than imaging at conventional intervals (60 min post-injection (p.i.)). Spence et al. performed kinetic modeling and found that this was due to a faster tracer clearance from normal brain tissue than from tumor [1,11,12]. ^{18}F-fluoroethyltyrosine (^{18}F-FET) PET, described in chapter 2, is also a promising tool for treatment monitoring of brain tumors [13-15], with ^{18}F-FET being able to detect tumor progression earlier than MRI [8]. Also another amino-acid PET tracer called 3,4-dihydroxy-6-^{18}F-fluoro-L-phenylalanine (^{18}F-FDOPA) identified treatment responders to antiangiogenic therapy as early as two weeks after treatment initiation [16].

In the present study, we investigated ^{18}F-fluorormehylcholine (^{18}F-FCho) PET (see Chapter 2) and MRI for response prediction in a homogeneous population of GB patients treated with the Stupp regimen [3]. In our study, we performed PET and MRI scans before the start of treatment (pre-RT), during RT (2, 4 and 6 weeks) and 1 month after the completion of RT (post-RT). Our first aim was to investigate whether therapy response can be predicted by ^{18}F-FCho PET and MRI. Secondly, we investigated which imaging modality allows prediction of therapy response first.

MATERIALS AND METHODS

Patients and treatments

A homogeneous population consisting of 11 GB patients were included in this study. There were 3 women and 8 men. Inclusion criteria were:

- histopathologically proven GB
- no surgery or debulking/submaximal resection only
- treatment with conformal external beam RT (60 Gy in 30 fractions) and TMZ (75 mg/m^2 for 6 weeks).

The study was approved by the local ethics committee and all patients gave written informed consent. Detailed patient characteristics are given in Table 4.1.

Response assessment

Taking into account a median survival of 12-15 months in GB patients receiving optimal treatment, RANO criteria were arbitrarily applied 6 months after the completion of RT to divide the patients into 2 categories: responders (R, including partial (PR) and complete (CR) responders) and non-responders (NR, including stable (SD) and progressive (PD) disease) (Table 4.1 and 4.2). A summary of the RANO response criteria and categories is given in Chapter 1 [7].

PET imaging with ^{18}F-FCho

^{18}F-FCho PET scans were acquired before the start of concomitant RT and TMZ treatment (pre-RT), during radiation therapy (at week 2, 4, 6) and 1 month post-RT. Missing data are shown in Table 4.1. The brain PET scans were acquired using a PET Allegro system (Philips Healthcare, Cleveland, OH) which consists of a gadolinium oxyorthosilicate full-ring PET scanner with a spatial resolution of 5.0 mm (full width at half-maximum). The system is able to acquire the whole brain using 1 bed position (field of view (FOV), Z-axis = 18 cm). PET images were acquired with a voxel size of 2 x 2 x 2 mm in a matrix of 128 x 128. The PET system also includes cesium sources for transmission scanning. The patients had fasted for at least 6 hours before ^{18}F-FCho was administered to avoid competition effects on ^{18}F-FCho transport across the cell membrane. A transmission scan of the head was performed first. Subsequently, the patients received an intravenous injection of 296-370 MBq (8-10 mCi) of ^{18}F-FCho that was synthesized using the method of Slaets et al. [17]. The PET images were reconstructed using a 3-dimensional (3D) RAMLA (row action maximum likelihood) algorithm provided by the manufacturer. Attenuation and scatter correction were applied. A 5-min image acquired 25-30 min post-injection was used for the analysis.

Table 4.1. Patient characteristics

Patient no.	Sex	Age (y)	Surgery	Tumor location	Multifocal disease	Concomittant radiation and chemotherapy	Pre-treatment MTV# (40% SUV$_{max}$) (ccm)	PET and MRI acquisition*					Response assessment 6 months post-RT°
								Pre-RT	w2	w4	w6	m1	
1	m	49	biopsy	Temporal lobe	-	60 Gy 145 mg/d	4.8	✓	✓	✓	✓	✓	PD
2	f	47	biopsy	Temporal lobe	-	60 Gy 150 mg/d	37.8	✓	✓	✓	✓	✓	PR
3	m	41	biopsy	Parietal lobe	+	60 Gy 150 mg/d	18.3	✓	✓	✓	✓	✓	PD
4	m	65	biopsy	Frontal lobe	+	60 Gy 135 mg/d	5.3	✓	✓	✓	✓	✓	PD
5	m	61	debulking only	Frontal and temporal lobe	-	60 Gy 150 mg/d	3.9	✓	✓	✓	✓	✓	PR
6	f	49	biopsy	Temporal lobe	-	60 Gy 125 mg/d	5.5	✓	✓	✓	✓	-	PD
7	m	64	debulking only	Temporal lobe	-	60 Gy 145 mg/d	2.0	✓	✓	✓	✓	✓	PR
8	m	71	biopsy	Parietal lobe	-	60 Gy 135 mg/d	26.8	✓	✓	✓	✓	✓	PD
9	m	71	biopsy	Frontal lobe	-	60 Gy 140 mg/d	47.6	-	✓	✓	✓	✓	SD
10	f	64	debulking only	Frontal lobe	-	60 Gy 140 mg/d	13.1	-	-	✓	✓	✓	PR
11	m	64	biopsy	Frontal and parietal lobe	-	60 Gy 75 mg/d	20.9	✓	-	✓	-	✓	PD

metabolic tumor volume (MTV), standard uptake values (SUV)

*w2, w4, w6 and m1: PET and MRI acquisitions during RT (week 2, week 4 and week 6) and 1 month after the completion of RT (m1)

° progressive disease (PD), partial responder (PR), stable disease (SD), with PD and SD classified as non-responders (NR) and PR as responder (R)

Table 4.2. Therapy response assessment using RANO criteria

Patient no.	T1 Gd	T2/FLAIR signal	New lesion	Corticosteroid dose	Clinical status during treatment	Response°
		RANO criteria°				
1	+ ≥25%	Increased	-	Increased	Decline	PD
2	- ≥50%	Decreased	-	Decreased	Improved	PR
3	n/a	n/a	+	Increased	Decline	PD
4	n/a	Increased	+	None	Decline	PD
5	- ≥50%	Stable	-	None	Stable	PR
6	+ ≥25%	Increased	-	Increased	Decline	PD
7	- ≥50%	Stable	-	None	Stable	PR
8	n/a	n/a	+	Stable	Stable	PD
9	- <50% but + <25%	Decreased	-	Stable	Improved	SD
10	- ≥50%	Stable	-	None	Stable	PR
11	+ ≥25%	Increased	-	Increased	Decline	PD

° Response Assessment in Neuro-Oncology (RANO) criteria were applied 6 months after the completion of RT to divide the patients into 2 categories: responders (R), including partial (PR) and complete (CR) responders and non-responders (NR), including stable (SD) and progressive (PD) disease. PD also occurs when a new lesion is present, making the measurement of the contrast-enhancing lesion expendable (n/a; not applicable).

Semi-quantitative PET analysis

The methodology for semi-quantitative PET analysis was described in Chapter 2. Standard uptake values (SUV) were calculated using PMOD software (version 3.405, PMOD technologies®, Zürich, Switzerland). In PMOD, the metabolic tumor volume (MTV) was defined using an automatic method applying a fixed threshold of 40 % of the maximum SUV value (SUV$_{max}$) [18]. The 40 % threshold was used because it corresponded best to the visually metabolically active tumor on the ^{18}F-FCho PET images. In addition, because it only makes sense to investigate treatment response (due to RT) within the tissue volume that received irradiation, the 40 % threshold was applied within the 95 % isodose of the RT plan (Figure 4.1). The 95 % isodose reflects the volume that received at least 95 % of the prescribed irradiation dose. It is worth mentioning that none of the patients showed increased ^{18}F-FCho uptake outside the 95 % isodose. Thus, first, ^{18}F-FCho PET and planning CT scans were imported into PMOD. PET-CT co-registration was done automatically using the rigid matching tool (mutual information algorithm). The 95 % isodose for every patient was extracted from the RT plan using the software system Eclipse (Varian®) and was transferred onto the PET-CT fusion. Within the 95 % isodose, a threshold of 40 % of SUV$_{max}$ was applied, defining MTV automatically (Figure 4.1). For tumors located adjacent to the lateral ventricle, physiological uptake of ^{18}F-FCho in the choroid plexus [19] was manually excluded from the MTV. The mean and maximum SUV within the MTV were calculated (SUV$_{mean}$ and SUV$_{max}$) in all repeat scans and the % change of these parameters between every time point was assessed.
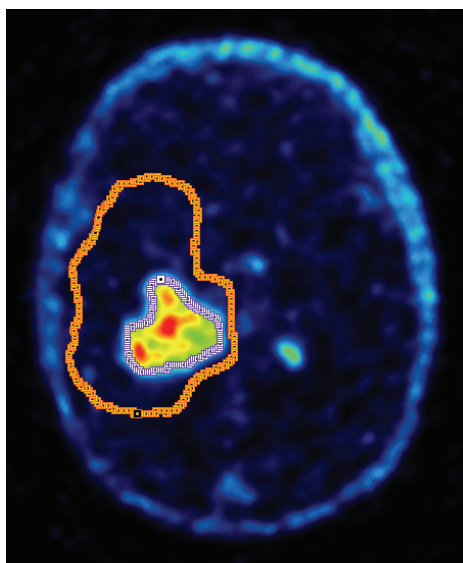

Figure 4.1. Automatic delineation of the metabolic tumor volume (MTV). The MTV was delineated on a 5-min PET image acquired 25-30 min post-injection applying a threshold of 40 % SUV$_{max}$ (purple) within the 95 % isodose (orange) (patient 4).

Magnetic resonance imaging

The MR examinations were performed on a 3-Tesla Siemens Trio Tim whole-body scanner (Erlangen, Germany), using a standard 12-channel phased array head coil. Structural images were acquired using a 3-dimensional T1-weighted gradient-echo sequence (MPRAGE) with isotropic voxels (176 sagittal slices, FOV read = 220 mm, voxel size 0.9 mm × 0.9 mm × 0.9 mm, TR = 1550 ms, TE = 2.39 ms, TI = 900 ms, matrix size = 256 × 256, GRAPPA factor 2) and a 3-dimensional T2-weighted inversion recovery sequence (FLAIR) with isotropic voxels (176 sagittal slices, FOV read = 250 mm, voxel size 1 mm × 1 mm × 1 mm, TR = 6000 ms, TE = 421 ms, TI = 2100 ms, matrix size = 256 × 238, GRAPPA factor 2). The MPRAGE sequence was repeated following administration of gadolinium contrast.

All 3D image volumes were reconstructed in 3 mm slices in 3 orthogonal planes (sagittal, axial, and coronal). MRI was performed on the same day as the PET scan, or if not possible, within the same week. The contrast-enhancing tumor volume (GdTV) was calculated by a senior neuroradiologist using the IMPAX software (Agfa healthcare®). The sum of products of the perpendicular diameters of each lesion was calculated. In one patient with multifocal disease, the 2 most voluminous lesions were measured (patient 3).

Statistical analysis

The Mann-Whitney U test was used to compare SUVs, MTVs and % change of all the variables between all time points in R and NR. For all tests, an alpha error up to 5 % ($p < 0.05$) was considered significant. Receiver operating curve (ROC) analyses were performed to determine the cut-off value with the highest sensitivity and specificity to discriminate R from NR. The statistical tests were performed using SPSS software (version 20).

RESULTS

Response evaluation

Applying the RANO criteria 6 months after the completion of RT, 4/11 patients (36 %) were classified as R (PR) and 7/11 patients (64 %) as NR (SD and PD) (see also Table 4.2). PD was present in 6/11 patients (55 %), showing a new lesion in 3/11 patients (27 %) and an increase of the tumor volume of $\geq$ 25 % on contrast-enhanced T1-weighted MR images in 3/11 patients (27 %). SD was present in 1/11 patients (see Figure 4.2 for examples of PR, SD and PD).
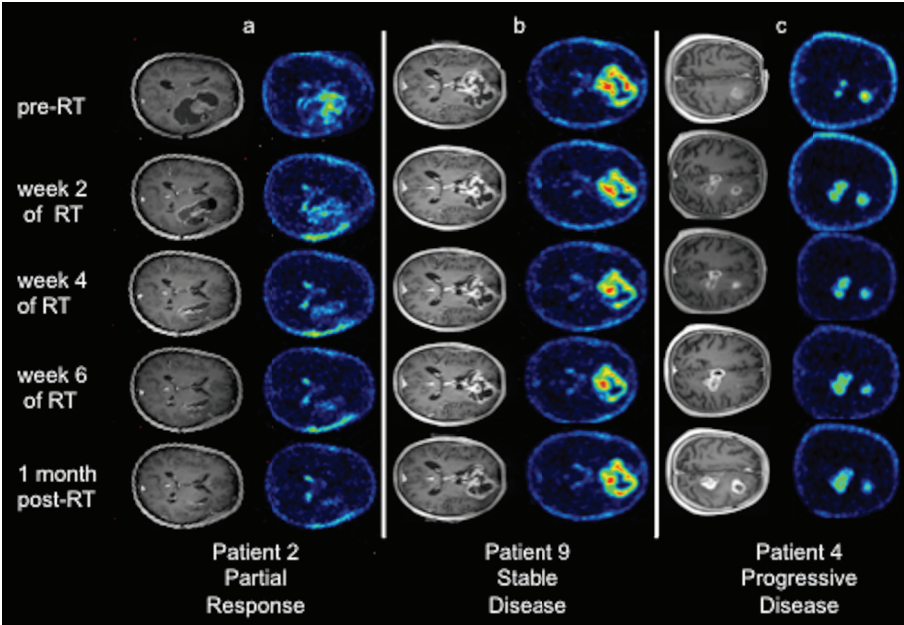
Figure 4.2. ^{18}F-Fluoromethylcholine (^{18}F-FCho) PET and contrast-enhanced T1-weighted MR images in patient 2 (a), patient 9 (b) and patient 4 (c). (a) A 47-year old female patient diagnosed with GB in the right frontal and temporal lobe. According to the RANO criteria the patient is categorized as a partial responder. A 60 % decrease in SUV$_{max}$ and SUV$_{mean}$ is observed from pre-RT to 1 month post-RT. (b) A 71-year old male patient diagnosed with a bifrontal GB. According to the RANO criteria, the patient was categorized as stable disease. From pre-RT to 1 month post-RT, SUV$_{max}$ decreased 17 % while SUV$_{mean}$ remained more or less stable. (c) A 66-year old male patient diagnosed with multifocal GB. A new lesion was visible on follow-up MRI, categorizing the patient as progressive disease. From pre-RT to 1 month post-RT SUV$_{max}$ and SUV$_{mean}$ decreased 52 % and 59 % respectively, while MTV increased with > 300 %.

Semi-quantitative PET analysis

Absolute SUV, MTV and GdTV values

Absolute SUV_{mean} and SUV_{max} values were not significantly different between R and NR at any time point (data not shown). An overview of all variables significantly different between R and NR ($p < 0.05$) is given in Table 4.3. Only parameters highly significantly different between R and NR ($p \leq 0.01$) are further discussed. Only MTV x SUV_{mean} 1 month post-RT was significantly higher in NR than in R ($p = 0.010$), see Figure 4.3.c. In addition, it is worth mentioning that in 3 NRs, SUV_{max} decreased over time, while MTV increased.

Change in SUV, MTV and GdTV values

Based on PET, only the change in SUV_{mean} between week 4 during RT and 1 month post-RT was significantly higher in R than in NR ($p = 0.010$). For MRI, GdTV changes between week 2 and 6 ($p = 0.010$), week 4 and 6 ($p = 0.006$) and week 2 and 1 month post-RT ($p = 0.010$) were significantly higher in R than in NR (Figure 4.3.a).

ROC analysis

A 100 % sensitivity and specificity to discriminate R from NR was achieved 1 month post-RT applying a cut-off value of 7.6 (cmm) for the PET derived parameter MTV x SUV_{mean}. Discrimination between R and NR was also achieved with 100 % sensitivity and specificity by applying a decrease of at least 9 % between week 4 during RT and 1 month post-RT for SUV_{mean}. For GdTV, response prediction is feasible with a 100 % sensitivity and specificity by applying a decrease of at least 53 % between week 2 during RT and 1 month post-RT, a decrease of at least 31 % between week 2 and 6 during RT and a decrease of at least 18 % between week 4 and 6 during RT. As such, the parameter that predicts response first is MR-derived, namely GdTV (Table 4.3).
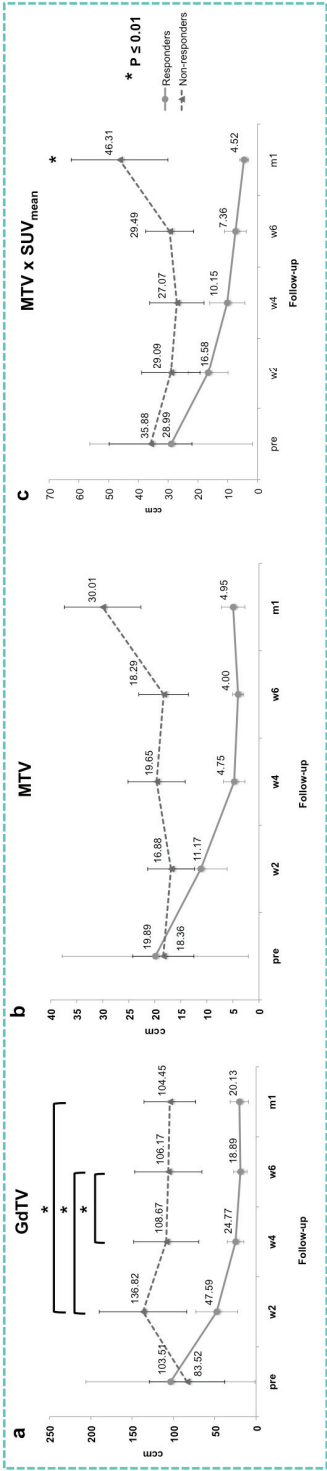
Figure 4.3. Evolution over time of the contrast-enhanced tumor volume (GdTV) (a), metabolic tumor volume (MTV) (b) and MTV x SUV$_{mean}$ (c) in responders (R) and non-responders (NR). Mean and standard error of the mean are given. Variables highly significantly different (p ≤ 0.01) between R and NR are marked with *.

Table 4.3. ROC analysis of variables significantly different between responders and non-responders

	Variable	Time point	n	Mann-Whitney U 1-tailed p-value	ROC Cut-off value	ROC Area under curve	Sensitivity (%)	Specificity (%)
Absolute values								
PET-based	MTV	w4	11	0.042	6.03	0.893	75	86
	MTV	w6	10	0.019	6.91	0.958	100	83
	MTV	m1	10	0.019	14.56	0.958	100	83
	MTVXSUV$_{mean}$	w6	10	0.019	17.66	0.958	100	83
	MTVXSUV$_{mean}$	**m1**	**10**	**0.010**	**7.55**	**1.000**	**100**	**100**
MR-based	GdTV	w4	11	0.042	50.22	0.893	86	100
	GdTV	w6	11	0.042	52.51	0.893	86	100
	GdTV	m1	11	0.024	30.88	0.929	100	75
% Change between 2 time points								
PET-based	MTV	pre-m1	8	0.071	-16.05 %	1.000	100	100
	MTV	w2-m1	9	0.032	0.01 %	0.950	100	80
	MTVXSUV$_{mean}$	pre-m1	8	0.071	-23.46 %	1.000	100	100
	MTVXSUV$_{mean}$	w2-m1	9	0.016	-33.25 %	1.000	100	100
	SUV$_{max}$	w4-w6	10	0.038	7.64 %	0.917	100	78
	SUV$_{mean}$	**w4-m1**	**10**	**0.010**	**-8.53 %**	**1.000**	**100**	**100**
MR-based	GdTV	pre-m1	9	0.056	-42.70 %	1.000	100	100
	GdTV	**w2-m1**	**10**	**0.010**	**-52.71 %**	**1.000**	**100**	**100**
	GdTV	pre-w6	9	0.056	-41.60 %	1.000	100	100
	GdTV	w2-w4	10	0.019	-13.99 %	0.958	83	100
	GdTV	*w2-w6*	*10*	*0.010*	*-31.04 %*	*1.000*	*100*	*100*
	GdTV	*w4-w6*	*11*	*0.006*	*-17.70 %*	*1.000*	*100*	*100*

Bold: parameters that are highly significantly different (p ≤ 0.01) between R and NR

Italic: parameters that predict response first.

Metabolic tumor volume (MTV), standard uptake value (SUV), gadolinium (Gd), pre-treatment (pre), week after initiation of treatment (w), month after the completion of radiation therapy (m).

DISCUSSION

In this study, we investigated ^{18}F-FCho PET and contrast-enhanced MRI for response assessment in 11 GB patients who were not good candidates for (maximal) surgery and received therapy according to the Stupp protocol [3]. ^{18}F-FCho PET was used because enhanced choline metabolism is a hallmark of malignancy and increased ^{18}F-FCho uptake is associated with oncogenesis and tumor progression [20-24]. ^{18}F-FCho PET has been shown to identify the boundaries of HGG because accumulation in surrounding normal brain tissue is low, making it a promising tool for diagnosis, image-guided biopsy and therapy response assessment in primary and recurrent HGG [19,23,25,26]. In a recent review, the authors stated that ^{18}F-FCho uptake by a brain tumor reflects tumor metabolism, but that there is no strong correlation between tumor grade and choline uptake [19,23,26].

For therapy response monitoring in glioma, promising results have been reported for ^{18}F-FET PET [8,13,14]. In a study by Piroth et al., the authors defined early treatment response in GB patients as a decrease of the maximal tumor-to-brain ratio (TBR$_{max}$) of at least 10 % between the start of RT and 7-10 days after the completion of RT [13]. The threshold also yielded a good discriminative power to separate prognostic groups in terms of progression free and overall survival [14]. Hutterer et al. reported a decrease of 45 % of MTV to define metabolic response in recurrent HGG patients treated with bevacizumab and irinotecan [27]. For ^{18}F-Fluorothymidine (^{18}F-FLT) PET, a > 25 % reduction in tumor SUV uptake was defined as a metabolic response in patients with recurrent malignant gliomas treated with bevacizumab and irinotecan [28]. Only a few papers investigated ^{18}F-FCho PET for therapy response assessment in malignancies. Parashar et al. suggested that there was a good correlation between a change in SUV$_{max}$ of the tumor during RT and response [29]. However, only 1 patient with a malignant glioma was included in this study. In another ^{11}C-Choline PET study, Li et al. reported that a TBR $\leq$ 1.4 might predict a longer overall survival in patients with suspected recurrent glioma after treatment [30]. It is however noteworthy that in the literature (early) PET response in malignant glioma is defined as decreased tracer uptake over time, but that proposed thresholds vary strongly between studies [13,14,27,28,29,30]. Importantly, different PET tracers visualize different biological processes, which probably (partly) explain the different threshold values. Also, therapy response is assessed at different time points in different studies, which may also (partly) explain the different threshold values. In addition, cut-off values are method specific because they are affected by acquisition parameters, the choice of reconstruction algorithm and ROI definition [18,31,32]. All these factors may explain the often large differences between thresholds and underline the importance of a validation of the proposed thresholds, ideally by histology. Despite the lack of a pathological proof in our study, we studied ^{18}F-FCho uptake before, during and after the completion of RT within the metabolically active tumor part that received at least 95 % of the prescribed irradiation dose (MTV). A 40 % threshold of SUV$_{max}$ was applied because it corresponded best with the visually enhanced tracer uptake in the tumor. Moreover, it is well known that an automatic threshold technique is the best guarantee that consistent VOIs are defined on repeat scans as are acquired in our study [31,33]. Other advantages of automatic thresholding are that the method is user-independent as well as independent of any changes in tumor geometry, which is of particular relevance in studies that assess therapy response because tumors may shrink as a result of effective treatments [34].

We found that **absolute SUV values pre-RT, during RT and 1 month post-RT did not predict response**. A decrease of at least 9 % of SUV_{mean} between week 4 during RT and 1 month post-RT discriminated R from NR with 100 % sensitivity and specificity. However, changes in tracer uptake of 10-20 % may be considered within the range of normal biological variability. More important and as mentioned above, we noted that in 3 NRs, absolute SUV values decreased during the course of the treatment while MTV increased. This means that **MTV must be taken into account**. Based on our results **GdTV at week 6 during RT** can be used for early response prediction in GB patients receiving combined RT and TMZ (Figure 4.3). However, this finding warrants caution due to the possibility of pseudoprogression occurring within 12 weeks after treatment in 20-30 % of GB patients [7]. Based on our results, an alternative is given by the ^{18}F-FCho PET-derived parameter, **MTV x SUV_{mean}, which allows prediction of therapy response as early as 1 month after the completion of RT**. In comparison with the results of other PET tracers in the literature and in particular ^{18}F-FET, our results indicate that ^{18}F-FCho PET is not superior to ^{18}F-FET PET, which enables prediction of response as early as 7-10 days after the completion of treatment [13,14,35]. Based on our and other results in the literature, inclusion of PET in the RANO criteria might be helpful for early therapy response prediction in high-grade glioma, more particularly in cases diagnosed with pseudoprogression on post-treatment MRI. However, this needs to be confirmed in larger studies. It will also be of interest to investigate the clinical role of advanced MRI techniques in combination with (^{18}F-FCho) PET for early therapy response assessment in GB patients.

Conclusion

Our data indicate that ^{18}F-FCho PET and contrast-enhanced T1-weighted MRI are able to predict response 1 month after the completion of RT and 6 weeks after treatment initiation, respectively. Further studies investigating the role of multimodality imaging for early therapy response assessment in GB thereby allowing patient-tailored therapy are however needed.

REFERENCES

[1] Ahmed R, Oborski MJ, Hwang M, et al. Malignant gliomas: current perspectives in diagnosis, treatment, and early response assessment using advanced quantitative imaging methods. Cancer Management Research 2014;6:149-170.

[2] Anton K, Baehring JM, Mayer T. Glioblastoma multiforme: overview of current treatment and future perspectives. Hematology Oncology Clinics of North America 2012;26:825-853.

[3] Stupp R, Dietrich PY, Kraljevic SO, et al. Promising Survival for Patients With Newly Diagnosed Glioblastoma Multiforme Treated With Concomitant Radiation Plus Temozolomide Followed by Adjuvant Temozolomide. Journal of Clinical Oncology 2002;20:1375-1382.

[4] Siu A, Wind JJ, Iorgulescu B, et al. Radiation necrosis following treatment of high grade glioma-a review of the literature and current understanding. Acta Neurochirurgica 2012;154:191-201.

[5] Gorlia T, van den Bent MJ, Hegi ME, et al. Nomograms for predicting survival of patients with newly diagnosed glioblastoma: prognostic factor analysis of EORTC and NCIC trial 26981-22981/CE.3. Lancet Oncology 2008;9:29-38.

[6] Ducray F, Idbaih A, Wang XW, et al. Predictive and prognostic factors for gliomas. Expert Review of Anticancer Therapy 2011;11:781-789.

[7] Wen PY, Macdonald DR, Reardon DA, et al. Updated response assessment criteria for high-grade gliomas: response assessment in neuro-oncology working group. Journal of Clinical Oncology 2010;28:1963-1972.

[8] Galldiks N, Rapp M, Stoffels G, et al. Response assessment of bevacizumab in patients with recurrent malignant glioma using [18F]Fluoroethyl-L-tyrosine PET in comparison to MRI. European Journal of Nuclear Medicine and Molecular Imaging 2013;40:22-33.

[9] Hoekstra CJ, Paglianiti I, Hoekstra OS, et al. Monitoring response to therapy in cancer using [18F]-2-fluoro-2-deoxy-D-glucose and positron emission tomography- an overview of different analytical methods. European Journal of Nuclear Medicine 2000;27:731-743.

[10] Dhermain FG, Hau P, Lanfermann H, et al. Advanced MRI and PET imaging for assessment of treatment response in patients with gliomas. Lancet Neurology 2010;9:906-920.

[11] Mertens K, Acou M, Van Hauwe J, et al. Validation of 18F-FDG PET at conventional and delayed intervals for the discrimination of high-grade from low-grade gliomas. Clinical Nuclear Medicine 2013;38:495-500.

[12] Spence AM, Muzi M, Mankoff DA, et al. 18F-FDG PET of gliomas at delayed intervals: improved distinction between tumor and normal gray matter. Journal of Nuclear Medicine 2004;45(10):1653-1659.

[13] Piroth MD, Pinkawa M, Holy R, et al. Prognostic value of early [18F]fluoroethyltyrosine positron emission tomography after radiochemotherapy in glioblastoma multiforme. International Journal of Radiation Oncology Biology Physics 2011;80:176-184.

[14] Galldiks N, Langen KJ, Holy R, et al. Assessment of treatment response in patients with glioblastoma using O-(2-18F-fluoroethyl)-L-tyrosine PET in comparison to MRI. Journal of Nuclear Medicine 2012;53:1048-1057.

[15] Wyss M, Hofer S, Bruehlmeier M, et al. Early metabolic responses in temozolomide treated low-grade glioma patients. Journal of Neurooncology 2009;95:87-93.

[16] Schwarzenberg J, Czernin J, Cloughesy TF, et al. Treatment response evaluation usinf 18F-FDOPA PET in patients with recurrent malignant glioma on bevacizumab therapy. Clinical Cancer Research 2014;20(13):3550-3559.

[17] Slaets D, De Bruyne S, Dumolyn C, et al. Reduced dimethylaminoethanol in [(18)F]fluoromethylcholine: an important step towards enhanced tumour visualization. European Journal of Nuclear Medicine and Molecular Imaging 2010;37:2136-2145.

[18] Cheebsumon P, Yaqub M, van Velden FHP, et al. Impact of [(18)F]FDG PET imaging parameters on automatic tumour delineation: need for improved tumour delineation methodology. European Journal of Nuclear Medicine and Molecular Imaging 2011;38:2136-2144.

[19] Mertens K, Ham H, Deblaere K, et al. Distribution Patterns of 18F-Labelled Fluoromethylcholine in Normal Structures and Tumors of the Head. A PET/MRI Evaluation. Clinical Nuclear Medicine 2012;37:e196-203.

[20] Kwee SA, Coel MN, Lim J, et al. Prostate cancer localization with 18fluorine fluorocholine positron emission tomography. Journal of Urology 2005;173:252-255.

[21] Kwee SA, Wei H, Sesterhenn I, et al. Localization of Primary Prostate Cancer with Dual-Phase 18F-Fluorocholine PET. Journal of Nuclear Medicine 2006;47:262-269.

[22] Husarik DB, Miralbell R, Dubs M, et al. Evaluation of [18F]-choline PET/CT for staging and restaging of prostate cancer. European Journal of Nuclear Medicine and Molecular Imaging 2008;35:253-263.

[23] Mertens K, Slaets D, Lambert B, et al. PET with (18)F-labelled choline-based tracers for tumour imaging: a review of the literature. European Journal of Nuclear Medicine and Molecular Imaging 2010;37:2188-2193.

[24] Talbot JN, Gutman F, Fartoux L, et al. PET/CT in patients with hepatocellular carcinoma using [18F] fluorocholine: preliminary comparison with [18F]FDG PET/CT. European Journal of Nuclear Medicine and Molecular Imaging 2006;33:1285-1289.

[25] Kwee SA, Ko JP, Jiang CS, et al. Solitary brain lesions enhancing at MR imaging: evaluation with fluorine 18-fluorocholine PET. Radiology 2007;244:557-565.

[26] Calabria FF, Barbarisi M, Gangemi V, et al. Molecular imaging of brain tumors with radiolabeled choline PET. Neurosurgery Reviews 2016;1-10.

[27] Hutterer M, Nowosielski M, Putzer D, et al. O-(2-18F-Fluoroethyl)-L-Tyrosine PET Predicts Failure of Antiangiogenic Treatment in Patients with Recurrent High-Grade Glioma. Journal of Nuclear Medicine 2011;52:856-864.

[28] Chen W, Delaloye S, Silvermann DHS, et al. Predicting treatment response of malignant gliomas to bevacizumab and irinotecan by imaging proliferation with (18F) Fluorothymidine positron emission tomography: A pilot study. Journal of Clinical Oncology 2007;25:4714-4721.

[29] Parashar B, Wernicke AG, Rice S, et al. Early assesment of radiation response using a novel functional imaging modality-[18F] Fluorocholine PET (FCH-PET): A pilot study. Discovery Medicine 2012;14:13-20.

[30] Li W, Ma L, Wang X, et al. 11C-choline PET/CT tumor recurrence detection and survival prediction in post-treatment patients with high-grade gliomas. Tumor Biology 2014;35:12353-12360.

[31] Lammerstma AA, Hoekstra CJ, Giaccone G, et al. How should we analyse FDG PET studies for monitoring tumour response? European Journal of Nuclear Medicine and Molecular Imaging 2006;33:S16-S21.

[32] Boellaard R. Standards for PET image acquisition and quantitative data analysis. Journal of Nuclear Medicine 2009;50:11S-20S.

[33] Jeraj R, Bradshaw T, Simoncic U. Molecular Imaging to Plan Radiotherapy and Evaluate Its Efficacy. Journal of Nuclear Medicine 2015;56:1752-1765.

[34] Krak NC, Boellaad R, Hoekstra OS, et al. Effects of ROI definition and reconstruction method on quantitative outcome and applicability in a response monitoring trial. European Journal of Nuclear Medicine and Molecular Imaging 2005;32:294-301.

[35] Roelcke U, Bruehlmeier M, Hefti M, et al. F-18 choline PET does not detect increased metabolism in F-18 fluoroethyltyrosine-negative low-grade gliomas. Clinical Nuclear Medicine 2012;37:e1-e3.

Chapter 5.

Assessment of the effect of therapy in a rat model of GB using PET and MRI

This chapter contains data from:

Julie Bolcaen M.Sc.[1], Benedicte Descamps M.Sc. Ph.D.[2], Karel Deblaere M.D. Ph.D.[3], Tom Boterberg M.D. Ph.D.[4], Giorgio Hallaert M.D.[5], Caroline Van den Broecke M.D.[6], Elke Decrock M.Sc. Ph.D.[7], Anne Vral M.D. Ph.D.[8], Luc Leybaert M.D. Ph.D.[7], Christian Vanhove M.Sc. Ph.D.[2], Ingeborg Goethals M.D. Ph.D.[1]

<u>AND</u>

Julie Bolcaen M.Sc.[1], Benedicte Descamps M.Sc. Ph.D.[2], Karel Deblaere M.D. Ph.D.[3], Filip De Vos Pharm. Ph.D.[9]., Tom Boterberg M.D. Ph.D.[4], Giorgio Hallaert M.D.[5], Caroline Van den Broecke M.D.[6], Christian Vanhove M.Sc. Ph.D.[2], Ingeborg Goethals M.D. Ph.D.[1]

[1] *Department of Nuclear Medicine, Ghent University Hospital*
[2] *IBiTech-MEDISIP, Department of Electronics and Information Systems, Ghent University*
[3] *Department of Radiology, Ghent University Hospital*
[4] *Department of Radiation Oncology, Ghent University Hospital*
[5] *Department of Neurosurgery, Ghent University Hospital*
[6] *Department of Pathology, Ghent University Hospital*
[7] *Department of Basic Medical Sciences-Physiology group, Ghent University*
[8] *Department of Basic Medical Sciences-Histology group, Ghent University*
[9]*Department of Radiopharmacy, Ghent University*

De Pintelaan 185, 9000 Gent, Belgium

INTRODUCTION

The clinical course of glioblastoma (GB) is usually rapid and current treatment strategies provide only moderate survival benefit with a median survival of approximately 1 year, see Chapter 1 [1]. Therefore, investigating new therapeutic approaches and methodologies to evaluate treatment response are crucial. However, to implement changes to the existing clinical standard of care, research must be conducted to develop alternative treatment strategies. This can be obtained with the introduction of small animal models. As such, our first goal was to develop a GB rat model that mimics human GB treatment to allow a translation between clinical and preclinical results.

A first step was to bridge the gap between clinical radiation technology and preclinical techniques. For many decades, small animal radiation research was mostly performed using fairly crude experimental setups. Delivery of radiation in small animals was achieved using fixed radiation sources [2,3,4] or linear accelerators producing megavoltage (MV) X-rays [5,6,7] and applying only a single radiation field [3,5,7,8]. These devices typically are only precise at the level of a few mm, while sub-millimeter precision is required for small animals [9]. A MV photon beam exhibits dose build-up at the air–tissue interface in the entrance region of the beam. The extent of this build-up region corresponds roughly to the order of the animal size itself. Furthermore, simple single-beam techniques were commonly used without the ability to target a specific tumor volume, hampering response assessment due to high doses delivered to healthy brain tissue [3,5,6,9,10]. The abovementioned technology significantly differs from the advanced three-dimensional (3D) image-guided radiotherapy (RT) techniques using conformal arcs in humans [11]. Hence, it is unclear to which extent current animal studies still are relevant for modern RT practice [9].

Conformal RT describes any technique in which radiation dose conforms to the tumor target, while dose is limited to normal tissues, decreasing long-term treatment-related side effects [12]. One type of conformal RT is called intensity modulated radiotherapy (IMRT). IMRT uses dynamic multi-leaf collimators to sculpt the radiation dose around particular structures in combination with variable intensities of the radiation beam to allow even greater control over the shape of the dose distribution [12,13]. To enable more accurate irradiation in small animal research, recently, precision image-guided small animal radiation research platforms were developed, such as the Small Animal Radiation Research Platform (SARRP, Xstrahl®, Surrey, UK), see Figure 5.1. The SARRP offers the possibility to deliver high resolution, sub-millimeter, optimally planned conformal radiation using kV photons and has on-board cone-beam CT guidance. The platform can perform high resolution imaging and accurate conformal beam therapy on standard animal models for human cancers [14]. The design specifications include a gantry with a maximal rotation of 120° and a robotic stage which support noncoplanar irradiation, an on-board CT which is achieved by rotating the horizontal animal between the stationary kV X-ray source and a flat panel detector, see Figure 5.1. The SARRP uses a dual-focal spot, constant voltage X-ray source with a source-to-isocenter distance of 35 cm. X-rays of 80-100 kVp from the smaller 0.4 mm focal spot are used for imaging. Both 0.4 mm and 3.0 mm focal spots operate at 225 kVp for irradiation [11]. Treatment planning on these SARRPs is based on computed tomography (CT), which is equivalent to human planning systems and currently the gold standard for radiation planning [15,16]. However, CT is often hampered by low soft-tissue contrast that makes it very challenging to

localize targets in soft tissue regions, such as brain tumors. As a result, CT on these radiation research platforms is more and more combined with other imaging modalities to improve target selection. These modalities include optical imaging, magnetic resonance imaging (MRI) and positron emission tomography (PET). To be able to apply MRI-guided RT, a combined CT and MRI dataset is necessary containing both the information required for targeting (MRI-based volumes) and for dose calculations (CT-based electron density). Obviously, correct registration between MRI and CT is necessary to obtain accurate treatment planning, which is facilitated by multi-modality markers or a multimodality bed, see Figure 5.1.
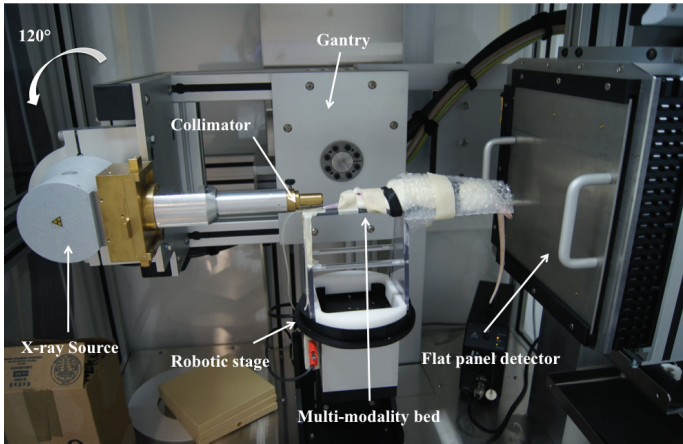

Fig 5.1. Small Animal Radiation Research Platform (SARRP) integrating a kV X-ray tube, a rotating gantry, a computer-controlled robotic stage, a collimating system to shape the beam and a flat-panel CT detector. The animal is placed on a multimodality bed to prevent movements between multiple imaging acquisitions, such as an MRI scan followed by a planning CT, which facilitates image fusion.

In this chapter we developed an orthothopic allograft F98 GB rat model. Subsequently, using this GB rat model, we described and validated a MRI guided 3D conformal arc RT with concomitant chemotherapy using the SARRP [11]. To clearly show the benefit of this 3D conformal multiple arc RT, we included a comparison with more commonly used small animal single beam or single arc irradiation methods. Cumulative dose volume histograms (DVHs) were defined within the tumor target volumes and surrounding normal brain tissue. DVHs are graphical representations providing information on the volume of a structure receiving a given dose over a range of doses within a 3D RT plan. Using one of the available collimators of the SARRP system, the radiation beam was shaped to a width of 3 x 3 mm. This beam targeting was validated using immunohistochemistry with a biomarker for DNA double strand brakes, called γH2AX. As such, we were able to confirm the shape of the beam.

Our second goal was to validate the effect of treatment using follow-up small animal MRI and PET, using two different tracers: ^{18}F-FDG and ^{18}F-FCho. PET enables visualization of biological changes preceding anatomical changes, which could be an important asset for treatment response assessment. Our final goal was to investigate which modality is best suitable for the early detection of treatment response in a rat model of GB. Currently we are also investigating the use of PET-guided irradiation in our F98 rat model, see future perspectives in Chapter 9.

MATERIALS AND METHODS

F98 GB rat model

F98 GB cells, obtained from ATCC, are cultured in monolayers using Dulbecco's modified Eagle Medium, 10 % calf serum, 1 % peni-strepto, 1 % L-glutamine and 0,1 % fungizone (Invitrogen®), and placed in a CO^2 incubator. Glioma cells are inoculated in the brain of female Fischer F344 rats (Charles River®) (body weight 173 ± 11 g, mean ± SD). The rats are anesthetized with ketamine/xylazine (4/3; 0,13 ml/100 g) and immobilized in a stereotactic device (David Kopf Model 902). After shaving, the skull is exposed through a scalp incision, and a 1 mm hole is made (diamond drill, Dremel®) 2 mm posterior and 2.5 mm lateral to the bregma in the right frontal hemisphere (Figure 5.2). A stereotactically guided insulin needle is inserted and 5 µl cell suspension (20 000 F98 GB cells) is injected 3 mm deep using an microsyringe pump controller (Micro 4TM, World Precision Instruments, Sarasota, USA). The syringe is slowly withdrawn, the incision is closed with bone wax (Aesculap AG®) and the skin is sutured. The study was approved by the ethics committee for animal experiments of our university (ECD 09/23).
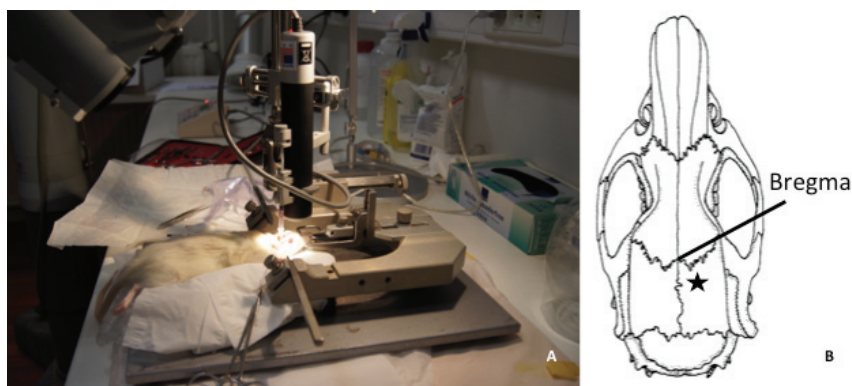
Figure 5.2. Inoculation of F98 glioblastoma cells (A) 2 mm posterior and 2.5 mm lateral to the bregma in the right frontal region (B).

MRI to localize the tumor

Nine days post-inoculation, MRI is performed using a 7-Tesla preclinical MRI system (PharmaScan 70/16, Bruker BioSpin, Ettlingen, Germany). First, a 30 Gauge needle connected to a 60 cm long tube is placed intravenously (IV). Rats are placed on an in-house made multimodality bed, making it easier to move the animal from the MRI scanner to the SARRP, while maintaining a fixed position. Three multimodality markers are fixed underneath, above and on the right side of the skull to simplify the co-registration process between MRI and treatment planning CT. The rats are anesthetized with 2 % isoflurane mixed with oxygen (0.3 L/min) and covered with a heated blanket. The bed is placed in a holder with fixed rat brain surface coil (Rapid Biomedical, Rimpar, Germany) that is positioned in a 72 mm rat whole body transmitter coil (Rapid Biomedical, Rimpar, Germany). A localizer scan is performed followed by a T2-weighted spin-echo scan (TR/TE 3661/37.1 ms, 109 µm isotropic in plane

resolution, 4 averages, TA 9'45") to assess tumor growth. Secondly, gadolinium-containing contrast (Dotarem, Guerbet, France; 0,4 ml/kg) is injected IV. Fifteen minutes later a contrast-enhanced T1-weighted spin echo sequence (TR/TE 1539/9.7 ms, 117 µm isotropic in plane resolution, 3 averages, TA 4'15") is performed. Typical contrast enhanced T1-weighted MR images are shown in Figure 5.3.B.

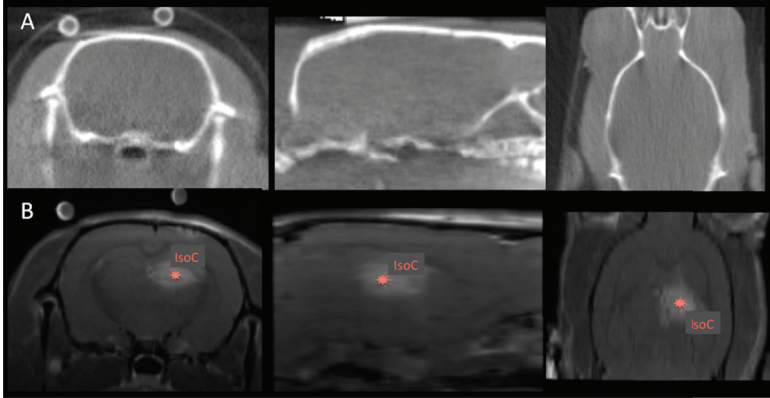**Figure 5.3. RT target selection.** CT scan of a rat with an F98 brain tumor. No tumor is visible, making it impossible to select the isocenter in the center of the tumor (A). Contrast-enhanced T1-weighted MRI visualizing clearly a rat F98 GB tumor. The center of the contrast-enhancement is selected as the isocenter for RT planning (B).

MRI-guided 3D conformal arc micro-irradiation

When a tumor was confirmed on MRI (Figure 5.3.B), the animal (fixed on the multimodality bed) is placed on a plastic holder secured the table of the SARRP. A high-resolution treatment planning CT scan is performed, using an aluminum filter of 1 mm and a 20 x 20 cm (1024 x 1024 pixel) amorphous Si flat panel detector. CT images are reconstructed with an isotropic voxel size of 0.2 mm (Figure 5.3.A). The tube voltage and tube current are fixed at 80 kV and 0.6 mA, respectively. A total of 720 projections are acquired over 360°.The CT and the T1-weighted contrast enhanced MRI scan are imported into 3D slicer v3.6.31 (www.slicer.org) and co-registered manually with rigid body transformations, using multimodality markers and the skull.

Four different dose plans are calculated to deliver 20 Gy to the target tumor volume: (A) using only the on-board CT and a single static beam, (B) using contrast-enhanced MRI and a single static beam, (C) using contrast-enhanced MRI and one single arc, and (D) using contrast-enhanced MRI and three non-coplanar arcs (D). In our F98 GB model, the tumor is located in the right frontal region that can be arbitrarily defined as the frontal half of the entire right hemisphere. Because the tumor is not visible on the CT images (Figure 5.3.A), a single antero-posterior beam with a width of 10 x 10 mm is selected to cover the whole right hemisphere and the isocenter is set in the middle right frontal region. MRI-guided treatment plans allow the use of 3 x 3 mm collimator because the isocenter can be precisely set in the center of a contrast-enhancing tumor with a maximal diameter of 3 mm at the time of treatment (Figure 5.3.B). In the MRI-guided treatment plan using one single arc, the arc covers an angle of 90°, while the couch angle is fixed to 0°. In the MRI-guided treatment plan using three non-coplanar arcs, the first arc

covers an angle of 90° with the couch positioned at 0° and the other 2 arc cover an angle of 60° with the couch positioned at 45° and 90°, respectively.

Mean/min/max cumulative DVHs of the tumor target volumes and normal brain tissue using the 4 dose plans are calculated by manually drawing a volume of interest (VOI) around the tumor and the normal brain on the T1-weighted contrast-enhanced MR images in five animals. The min DVH is the lowest DVH and the max DVH is the highest DVH within the animal group. As a surrogate for the maximal, mean and minimal dose to the tumor volume and the normal brain tissue volume, the D_2, D_{50} and D_{90} are calculated for the 4 dose plans, respectively (Table 5.1). D stands for the dose received by x % of the volume. Based on the similarity with current clinical practice and taking into account its optimal dose distribution, the dose plan using the three non-coplanar arcs was selected for the further irradiation of the rats. Therefore, the voltage of the X-ray source is fixed at 220 kV with a tube current of 13 mA and using a copper filter of 0.15 mm.

To further mimic the treatment of GB in patients, 5 rats that are treated with RT as described above also received concomittant chemotherapy. Intraperitoneal injections of 29 mg/kg temozolomide (TMZ, Sigma-Aldrich®) dissolved in saline with 25 % dimethylsulfoxide (DMSO, Sigma-Aldrich®) are performed for 5 days starting at the day of irradiation [17,18]. In a control group (n = 5), the animals only received intraperitoneal injections of an equal amount of DMSO and saline on 5 consecutive days, and no irradiations were performed.

Beam targeting validation using γH2AX immunohistochemistry

To confirm the exact delivery of the 3 mm beam, an immunohistochemical γH2AX staining is performed. Both diaminobenzidine (DAB) and fluorescein isothiocyanate (FITC) fluorochrome are used to highlight the γH2AX foci (Figure 5.8). The animal is irradiated at the right hemisphere with 20 Gy using 1 beam of 3 x 3 mm. The isocenter is selected on the CT scan, 6 mm posterior to the bone surrounding the olfactory bulb. One hour after irradiation the rat is euthanized using an IV injection of pentobarbital, the brain is isolated, immersed for 24 h in 4 % paraformaldehyde, embedded in paraffin and cut into 5 μm slices. The sections are pretreated for 10 min with 3 % H_2O_2 (DAB staining) and incubated for 30 min in blocking serum (1% bovine serum albumin, 5 % normal rabbit serum, 0.2 % tween 20). They are immunolabeled for 2 h with mouse anti-γH2AX antibody (1/500; Millipore 05-636), 30 min with biotin-conjugated rabbit anti-mouse (1/200; Dako E0464) and 30 min with horse radish peroxidase-conjugated (1/200 in PBS; Dako P0397) or FITC-conjugated streptavidin (1/200 in PBS; Dako F04222). The nuclei are counterstained with DAPI (1.5 μg/ml). Slices are mounted with vectashield (Vector laboratories H-1200). For the DAB staining, sections are immersed for 10 min in DAB (0.6 % DAB in Tris-HCl buffer; 0.03 % H_2O_2), followed by a 20 s counterstaining with haematoxylin and mounting (Richard-Allan scientific 4111). Fluorescently labeled sections are imaged with a BD pathway 435 automated imaging system (Becton Dickinson) equipped with an x 10 objective. A montage of 20 x 15 images provides a complete overview of the brain section. DAB-stained slices are photographed using a virtual microscope (Olympus BX51).

Assessment of the effect of image-guided irradiation using MRI

Follow-up MRI scans are performed 2, 5, 9 and 12 days after the start of treatment (day of RT and first TMZ injection or day of first control injection). Two animals in the treatment group had an additional scan on day 15 and 21. T2- and contrast enhanced T1-weighted spin echo sequences are performed. Using the PMOD software (version 3.31, PMOD technologies®, Zürich, Switzerland), the volume of the tumor is determined by manually drawing volumes of interest around the tumor on the contrast-enhanced T1-weighted MR images.

Assessment of biological response of the tumor using ^{18}F-FDG and ^{18}F-FCho PET

The assessment of the effect of treatment was also evaluated by small animal PET using ^{18}F-FDG and ^{18}F-FCho. Follow-up ^{18}F-FDG scans are performed 2, 5, 9 and 12 days after the start of treatment, while follow-up ^{18}F-FCho scans are performed 1, 6, 7 and 13 days after the start of treatment. An overview of the complete imaging scheme is shown in Figure 5.4.
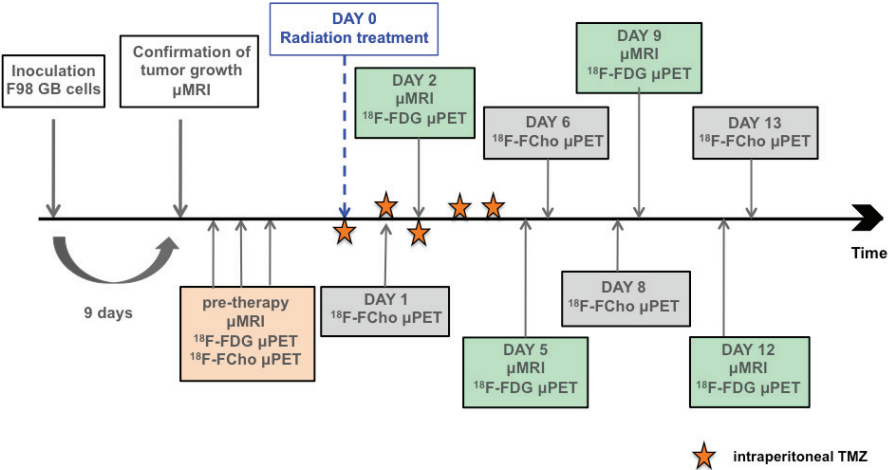
Figure 5.4. Study scheme for the assessment of the treatment effects using MRI, ^{18}F-FDG PET and ^{18}F-FCho PET.

Dynamic PET images are acquired in list mode using a dedicated small animal PET scanner (FLEX Triumph II, TriFoil Imaging®, Northridge CA). Animals are anesthetized with 2 % isoflurane mixed with oxygen (0.3 L/min). A 30-Gauge needle connected to a 10 cm long tube is inserted into the tail vein, enabling the injection of the radioactive tracer (37 MBq dissolved in 200 µL saline). The total acquisition time is 20 min for ^{18}F-FCho PET and 60 min for ^{18}F-FDG PET at conventional imaging time. In addition, a 30-min ^{18}F-FDG PET scan is acquired 240 min after ^{18}F-FDG administration (delayed imaging). All PET scans are reconstructed into a 200 × 200 × 64 matrix by a 2D Maximum Likelihood Expectation Maximization (MLEM) algorithm (LabPET Version 1.12.1, TriFoil Imaging®, Northridge CA) using 60 iterations and a voxel size of 0.5 × 0.5 × 1.157 mm. Default reconstruction parameters are applied, which

are identical for ^{18}F-FDG and ^{18}F-FCho PET. The dynamically acquired PET data are reconstructed into 6×20 s, 3×1 min, 3×5 min, 2×20 min for ^{18}F-FDG scans and 6×20 s, 3×1 min, 1×5 min, 1×10 min for ^{18}F-FCho scans.

The metabolic tumor volume (MTV) is calculated based on a semi-automatic thresholding method using the PMOD software (version 3.405, PMOD technologies®, Zürich, Switzerland). MTV is defined on the last time frame of the dynamic ^{18}F-FDG PET (40-60 min post-injection), the delayed ^{18}F-FDG PET (240 min post-injection) and on the last time frame of the dynamic ^{18}F-FCho scan (10-20 min post-injection). First, a circular VOI is manually placed over an increased tracer uptake excluding non-specific uptake, such as uptake in the scalp. Within this VOI, MTV is defined as all voxels with an uptake ≥ 60 % and ≥ 50 % of the maximum uptake for ^{18}F-FDG and ^{18}F-FCho, respectively. The selection of the thresholds is done arbitrarily and based on visual inspection of the ^{18}F-FDG PET scan 40-60 min post-injection, the delayed ^{18}F-FDG PET scan 240-270 min post-injection and the ^{18}F-FCho PET scan 10-20 min post-injection, see Figure 3. Average tracer uptake within the MTV is converted to a standard uptake value (SUV) according to the following formula:

$$ SUV = \left(\frac{Uptake\ in\ the\ MTV \left(\frac{Bq}{ml} \right)}{injected\ activity\ (Bq)} \right) x\ body\ weight\ (g) $$

Injected activity was corrected for decay and residual activity in the syringe. As in the clinical study in Chapter 4, MTV x SUV_{mean} was also calculated and included in the analysis.

^{18}F-FDG early   **[18]F-FDG late**   **[18]F-FCho**

40% - 50% - 60%   **40% - 50% - 60%**   **40% - 50% - 60% - 70%**
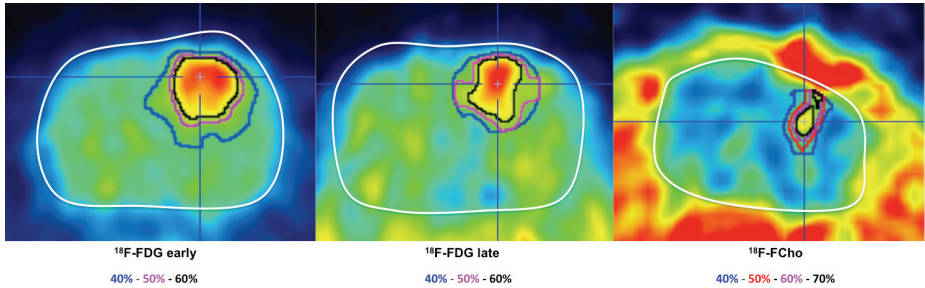
Figure 5.5. Selection of the threshold for defining of the metabolic tumor volume (MTV) on conventional ^{18}F-FDG PET (left), delayed ^{18}F-FDG PET (center) and ^{18}F-FCho PET (right). For clarity, the whole brain is contoured in white. For both ^{18}F-FDG PET (both 40-60 min post-injection and 240 min post-injection) a threshold contouring ≥ 60 % of the maximum uptake is selected (black VOI). For ^{18}F-FCho PET, a threshold contouring ≥ 50 % of the maximum uptake is selected (red VOI).

Statistical analysis

Statistical analysis of the MRI and PET-derived variables (MRGd tumor volumes, MTV and MTV x SUV_{mean}) between the control and treatment group are analyzed by the Mann-Whitney U non-parametric test. Statistical analysis of longitudinal differences within each group is performed using the Wilcoxon Signed Rank test and the Friedman test.

Statistical analysis of the D_2, D_{50} and D_{90} in the tumor volume and the normal brain tissue volume between the 4 dose plans is performed using the Kruskal-Wallis test. The Mann-Whitney U test is used to compare the D_2, D_{50} and D_{90} in both volumes between the CT-guided and the MRI-guided dose plans and between the single beam treatments versus the single or multiple arc treatments.

A probability value of $p < 0.05$ is considered statistically significant.

RESULTS

F98 GB rat model

To confirm the presence of GB, the brain of a rat with confirmed tumor on MRI was isolated. Several sections were stained with hematoxylin and eosin (HE), confirming the presence of a tumor with increased cellularity, nuclear atypia, high mitotic index and necrosis, as seen in human high grade gliomas (Figure 5.6) [19,20]. Without treatment, the tumors encompass almost the entire right cerebral hemisphere at 21 days post-inoculation, requiring euthanasia.
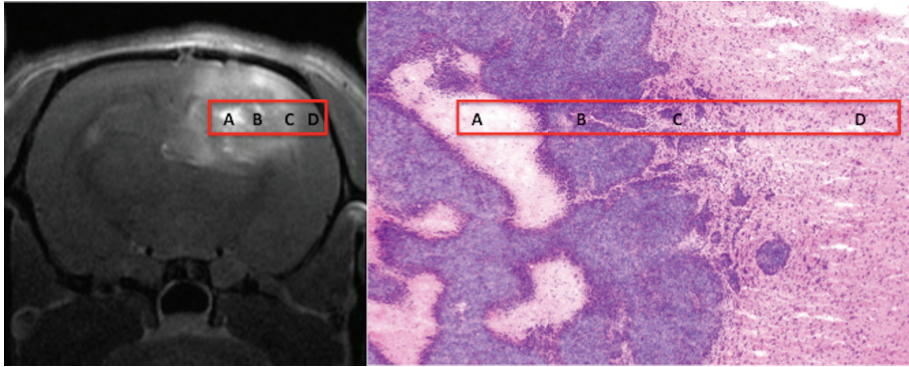
Figure 5.6. H&E staining of the tumor compared to contrast enhanced T1-weighted MR images: relatively low-enhancing viable glioblastoma tumor cells (B), infiltrating tumor cells and abundant blood vessels in the perinecrotic tumor rim with higher contrast leakage (C) and surrounding normal brain tissue (D). Contrast enhancement on T1 MR images in the center of the tumor corresponds to central tumor necrosis (A)

Dose distributions and dose volume histograms

The mean/min/max cumulative DVHs of the target volume and the normal brain tissue volume delineated on contrast enhanced T1-weighted MRI for five different animals are visualized in Figure 5.7. Values of D_2, D_{50} and D_{90} of the tumor volume and the normal brain tissue volume are given in Table 5.1. Using the on-board CT, it is clear that the dose distribution is more heterogeneous and that only 62 % of the tumor volume receives 20 Gy (Figure 5.7.A). Using MRI-guided delivery of a single beam (3 x 3 mm), the percentage of the target volume receiving 20 Gy is comparable (64 %, Figure 5.7.B). However, using a single arc or three non-coplanar arcs, the DVHs calculated within the tumor volume show a delivery of 20 Gy to 90 % of the target volume (Figure 5.7.C and 5.7.D). The homogeneity of the dose distribution increases respectively when using a CT-guided beam, an MRI-guided beam, an MRI-guided arc and MRI-guided multiple arcs (see DVHs Figure 5.7.). Also note that within the tumor volume, large dose variations are present between the animals using 1 CT-guided beam (see min/max DVH Figure 5.7.A).
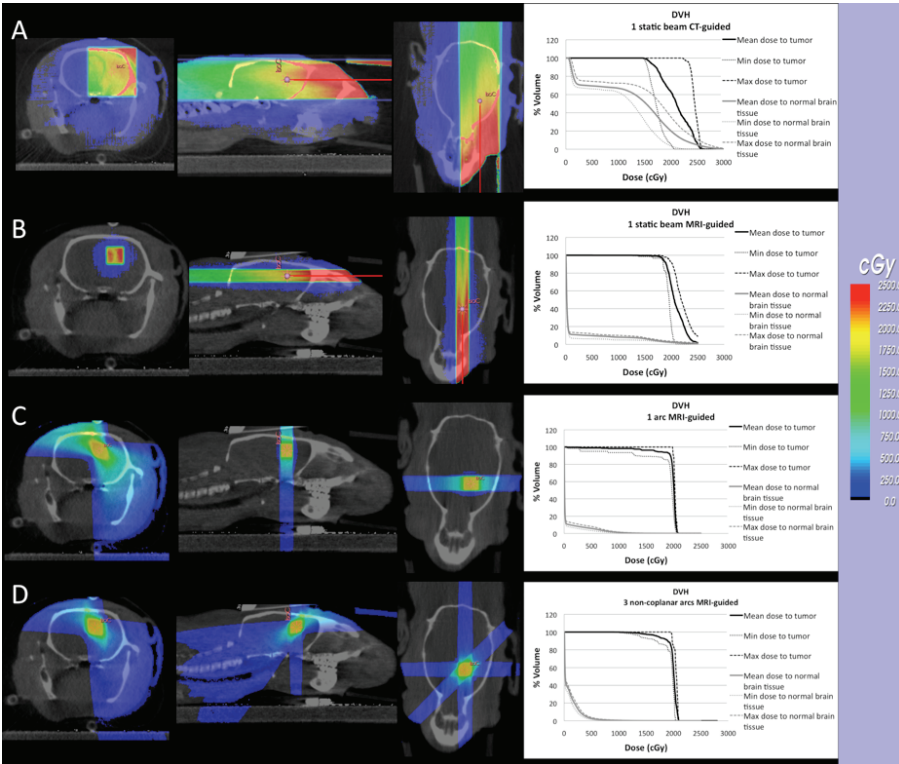
Figure 5.7. Four different dose plans to deliver 20 Gy to the target volume. Using only the on-board CT system, as single static beam in combination with the 10 x 10 mm collimator is selected (A). Dose plans using contrast-enhanced T1-weighted MR images and a single static beam (B), a single arc (C) and three non-coplanar arcs (D) in combination with the 3 x 3 mm collimator. On the right, cumulative Dose Volume Histograms (DVH) of the tumor volume and the normal brain tissue delineated on contrast-enhanced T1-weighted MRI are given. Mean, minimum and maximum DVH of five different animals are shown. Based on the similarity with current clinical practice and its optimal parameters, plan D was selected for irradiation.

The range in tumor D_2 is substantially higher using a single beam than using a single arc or multiple arcs. Mann-Whitney U test shows a significant higher D_2 within the tumor volume using a single beam compared to arc treatment (p = 0.009). However, the tumor coverage (D_{90}) is not significantly different between the 4 dose plans (p = 0.643).

The most important difference between using a single CT-guided beam (Figure 5.7.A), a single MRI-guided beam (Figure 5.7.B), a single MRI-guided arc (Figure 5.7.C) or three MRI-guided non-coplanar arcs (Figure 5.7.D) is the dose delivered to the normal brain tissue. The DVHs show, respectively, a delivery of 10 Gy to 67 %, 8 %, 1.6 % and 0.7 % of the normal brain tissue volume. D_2, D_{50} and D_{90} within the normal brain tissue volume are significantly higher using CT-guidance compared to MRI-guidance (p = 0.001, p < 0.001 and p < 0.001, respectively) and using a single beam compared to a single arc or multiple arcs (p < 0.001, p < 0.001 and p < 0.001).

Table 5.1. D_2, D_{50} and D_{90} of the tumor volume and the normal brain tissue volume using the 4 dose plans. Mean value is listed together with minimum and maximum values (between parentheses).

	One beam CT-guided Dose (Gy)[a]	One beam MRI-guided Dose (Gy)[a]	One arc MRI-guided Dose (Gy)[##]	Three non-coplanar arcs MRI-guided Dose (Gy)[a]	Kruskall-Wallis test (p value)	CT-MRI-guidance (p-value)	Beam-Arc (p-value)
						Mann-Whitney U test	
Tumor							
$D_{2\%}$	25.46	24.83	20.86	20.86	0.057	0.230	0.009
	(20.32 – 25.78)	(20.65 - 26.19)	(20.35 – 20.95)	(20.35 – 20.95)			
$D_{50\%}$	21.03	20.56	20.08	20.08	0.827	0.735	0.393
	(17.12 – 24.52)	(19.59 – 21.85)	(19.81 – 20.54)	(19.81 – 20.54)			
$D_{90\%}$	17.12	19.03	18.99	18.99	0.643	0.445	0.315
	(15.51 – 23.65)	(18.45 – 20.20)	(16.88 – 19.76)	(16.88 – 19.76)			
Normal brain tissue							
$D_{2\%}$	27.13	21.12	5.58	5.58	0.001	0.001	0.001
	(20.81 – 28.90)	(18.98 – 23.70)	(4.56 – 6.37)	(4.56 – 6.37)			
$D_{50\%}$	15.22	0.20	0.18	0.18	0.001	< 0.001	< 0.001
	(12.61 – 17.98)	(0.15 – 0.23)	(0.13 – 0.22)	(0.13 – 0.22)			
$D_{90\%}$	0.99	0.09	0.07	0.07	0.001	< 0.001	< 0.001
	(0.77 – 1.40)	(0.06 – 0.012)	(0.05 – 0.08)	(0.05 – 0.08)			

Beam targeting validation using γH2AX immunohistochemistry

After delivery of a single beam with a total dose of 20 Gy, γH2AX staining shows a well-demarcated region of positive foci within the 3 x 3 mm beam (Figure 5.8.B and 5.8.D). The beam edge is very sharp, as seen in Figure 5.8.C. The width of the beam on the DAB anti-γH2AX staining is 3 mm, suggesting that a tumor with a diameter of 2-2.5 mm is fully covered using three 3 x 3 mm beams.
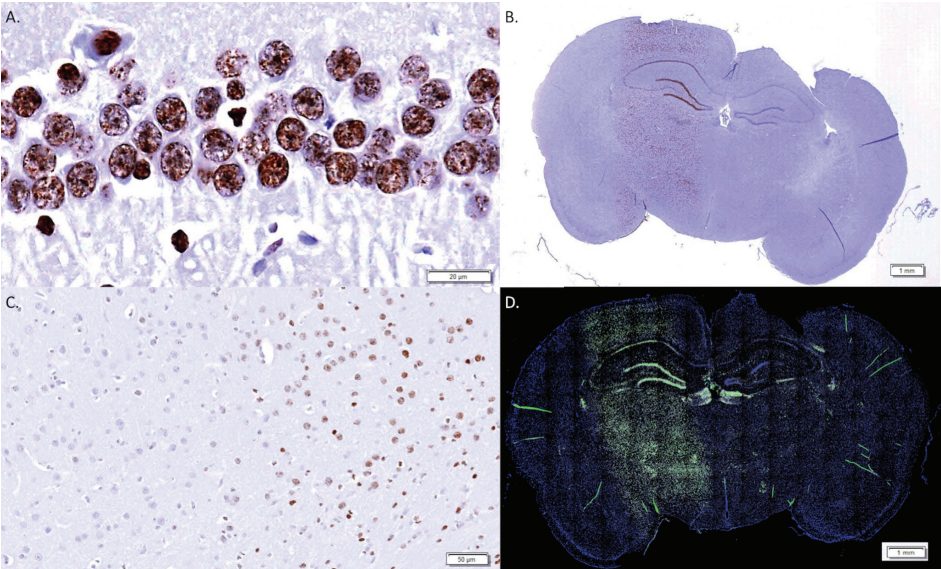
Figure 5.8. Immunohistochemical staining of γH2AX foci using two different staining methods. (A-C) 3,3'-Diaminobenzidine (DAB) staining (A) Accumulation of foci located in the nuclei of the hyppocampus (B-C) DAB staining visualizing the 3 x 3 mm beam and very sharp beam edges. (D) Merged image of sectioned rat brain stained with 46'-diamino-2-phenylindole-2 HCl for cell nuclei (blue color) and FITC labeled secondary antibody for correspondence with DNA ds breaks (green color).

Assessment of the effect of image-guided irradiation using MRI

To determine the exact tumor volume on MRI, HE staining was performed, correlating the imaging characteristics with pathology. In most cases, tumors on the contrast-enhanced T1-weighted MR images consisted of 2 or 3 differentially enhancing rims (Figure 5.6). The central area of the tumor showed intense contrast enhancement, surrounded by a rim of relative hypointense signal. The outer rim generally showed less intense contrast leakage. The central contrast enhancing area and the hypointense rim were identified as tumor necrosis and viable tumor cells, respectively. The surrounding infiltration of tumor cells with abundant proliferating blood vessels is responsible for the outer rim of contrast enhancement. As such, tumor volume is defined as the entire volume showing contrast-enhancement on the T1-weighted MR images.

Taking into account the abovementioned definition of tumor and to eliminate the influence of the starting tumor volume, data was normalized to the MRI tumor volume before starting therapy for each individual animal. The evolution of the normalized MRI tumor volumes is shown in Figure 5.9. A significant tumor growth was seen in both groups during the first 2 days after the start of treatment ($p = 0.031$). Afterwards, in the control group, a significant increase in tumor volume was observed from day 2 to day 5 ($p = 0.031$) and from day 5 to day 9 ($p = 0.031$). Later, from day 9 to day 12, the increase in tumor volume was not significant ($p = 0.063$). Tumor growth in the therapy group was different, with no significant increase in tumor volume from day 2 to day 5 ($p = 0.156$) and from day 5 to day 9 ($p = 0.313$). However, 9 days post treatment, tumor growth resumed with a significant tumor growth from day 9 to day 12 ($p = 0.031$). Two of the 5 animals with minor clinical symptoms at that time were further followed with MRI to further observe the evolution of the tumor growth (until day 21 after irradiation). On the MR images, tumor volume at day 21 was visually larger than on day 12, however not statistically significant due to small sample size. Friedman test showed a significant difference in tumor volume during follow-up (pre-therapy to day 12) in the control animals ($p = 0.003$), while no significant difference was found in the therapy group ($p = 0.054$). The Wilcoxon signed rank test is given in Table 5.2.

Table 5.2. Evaluation of tumor growth using MRI. Longitudinal differences within control and treated group. Result of Wilcoxon Signed Ranks test.

Volumes (ccm)	Ranks	Control group			Therapy group		
		n	Sum of ranks	Exact Sig. (one-tailed)	n	Sum of ranks	Exact Sig. (one-tailed)
D2 – PT	Negative	0	0	**0.031**	0	0	**0.031**
	Positive	5	15		5	15	
D5 – D2	Negative	0	0	**0.031**	3	12	0.156
	Positive	5	15		2	3	
D9 – D5	Negative	0	0	**0.031**	4	10	0.313
	Positive	5	15		1	5	
D12 – D9	Negative	0	0	0.063	0	0	**0.031**
	Positive	4	10		5	15	
D12 – D15	Negative	0	0	/	0	0	0.250
	Positive	1	1		2	3	
D15 – D21	Negative	0	0	/	0	0	0.250
	Positive	0	0		2	3	

ccm cubic millimeter

Chapter 5. Assessment of the effect of therapy in a rat model of GB using PET and MRI

The normalized MRI tumor volume was significantly different between control and treated group on day 5 (p = 0.008), day 9 (p = 0.016) and day 12 (p = 0.032) post-therapy (see asterisk in Figure 5.9. and Table 5.4.).

<div align="center">Assessment of biological response of the tumor using ¹⁸F-FDG and ¹⁸F-FCho PET</div>

Serial ^{18}F-FDG and ^{18}F-FCho PET scans are performed in 5 rats in the control group and 5 rats in the treatment group. Missing data are due to failed PET tracer synthesis, paravenous injection and hardware problems. A total of 128 PET scans is included in the analysis. An overview of the data is listed in Table 5.3.

To eliminate the influence of the starting tumor volume, for each individual animal, data was also normalized to the MTV pre-therapy. In Figure 5.10, tumor growth in a rat receiving control treatment is clearly visible on contrast-enhanced T1-weighted MRI, conventional ^{18}F-FDG, delayed ^{18}F-FDG and ^{18}F-FCho PET. Evolution of the normalized MTV and (SUV$_{mean}$ x normalized MTV) for ^{18}F-FDG (conventional and delayed) and ^{18}F-FCho PET are shown in Figure 5.9. Significant differences between control and therapy group are marked with an asterisk and listed in Table 5.4.

The MTV on conventional ^{18}F-FDG PET is significantly different between both groups on day 5 (p = 0.016). Using delayed ^{18}F-FDG PET imaging, significant differences in MTV were present between both groups on day 9 (p = 0.032) and 12 (p = 0.032). No significant differences were found at any time point for both the MTV of ^{18}F-FCho PET.

For ^{18}F-FDG PET at conventional time interval, (SUV$_{mean}$ x normalized MTV) is significantly different between the control and treated group on day 5 (p = 0.008) post-irradiation. On delayed ^{18}F-FDG PET a significant different (SUV$_{mean}$ x normalized MTV) is found on day 2 (p = 0.032), day 9 (p = 0.032) and day 12 (p = 0.016) post-irradiation. No significant differences were found at any time point for the (SUV$_{mean}$ x MTV) of ^{18}F-FCho PET.

Table 5.3. Overview of the imaging data in the longitudinal PET study.

Therapy	PRE-THERAPY			DAY 1	DAY 2		DAY 5		DAY 6	DAY 8	DAY 9		DAY 12		DAY 13
0 = Control 1 = RT+TMZ	^{18}F-FCho µPET	Early ^{18}F-FDG µPET	Late ^{18}F-FDG µPET	^{18}F-FCho µPET	Early ^{18}F-FDG µPET	Late ^{18}F-FDG µPET	Early ^{18}F-FDG µPET	Late ^{18}F-FDG µPET	^{18}F-FCho µPET	^{18}F-FCho µPET	Early ^{18}F-FDG µPET	Late ^{18}F-FDG µPET	Early ^{18}F-FDG µPET	Late ^{18}F-FDG µPET	^{18}F-FCho µPET
0	✓	✓	✓	✓	✓	✓	✓	✓	✓	✓	–	–	✓	✓	–
0	✓	✓	✓	✓	✓	✓	✓	✓	✓	✓	–	–	✓	✓	–
0	✓	✓	✓	✓	✓	✓	✓	–	–	–	–	–	✓	✓	✓
0	✓	✓	✓	✓	✓	✓	✓	✓	✓	–	✓	✓	–	–	–
0	✓	✓	–	✓	✓	✓	✓	–	✓	✓	✓	✓	✓	✓	✓
1	✓	✓	✓	✓	✓	✓	✓	✓	✓	✓	✓	✓	✓	✓	–
1	✓	✓	✓	✓	✓	✓	✓	✓	✓	✓	✓	✓	✓	✓	✓
1	✓	✓	✓	✓	✓	✓	✓	✓	✓	–	✓	✓	✓	✓	✓
1	✓	✓	✓	–	✓	✓	✓	✓	✓	✓	✓	✓	✓	✓	✓
1	✓	✓	✓	✓	✓	✓	✓	–	✓	✓	✓	✓	✓	✓	✓

105

Table 5.4. Assessment of the effect of therapy using MRI and PET. Differences between treatment and control groups at different time points during longitudinal follow-up using the Mann–Whitney U test.

Normalized variable		Time point	Mann-Whitney U exact Sig. (one-tailed)
MRI (Gd tumor volume)			
		Day 2	0.056
		Day 5	0.008*
		Day 9	0.016*
		Day 12	0.032*
PET (MTV)			
	Conventional ^{18}F-FDG μPET	Day 2	0.151
		Day 5	0.016*
		Day 9	0.063
		Day 12	0.190
	Delayed ^{18}F-FDG μPET	Day 2	0.151
		Day 5	0.114
		Day 9	0.032*
		Day 12	0.032*
	^{18}F-FCho μPET	Day 1	0.063
		Day 6	0.111
		Day 8	0.057
		Day 13	0.700
PET (SUV$_{mean}$ x MTV)			
	Conventional ^{18}F-FDG μPET	Day 2	0.056
		Day 5	0.008*
		Day 9	0.063
		Day 12	0.111
	Delayed ^{18}F-FDG μPET	Day 2	0.032*
		Day 5	0.057
		Day 9	0.032*
		Day 12	0.016*
	^{18}F-FCho μPET	Day 1	0.556
		Day 6	0.413
		Day 8	0.200
		Day 13	0.200

* = p ≤ 0.05
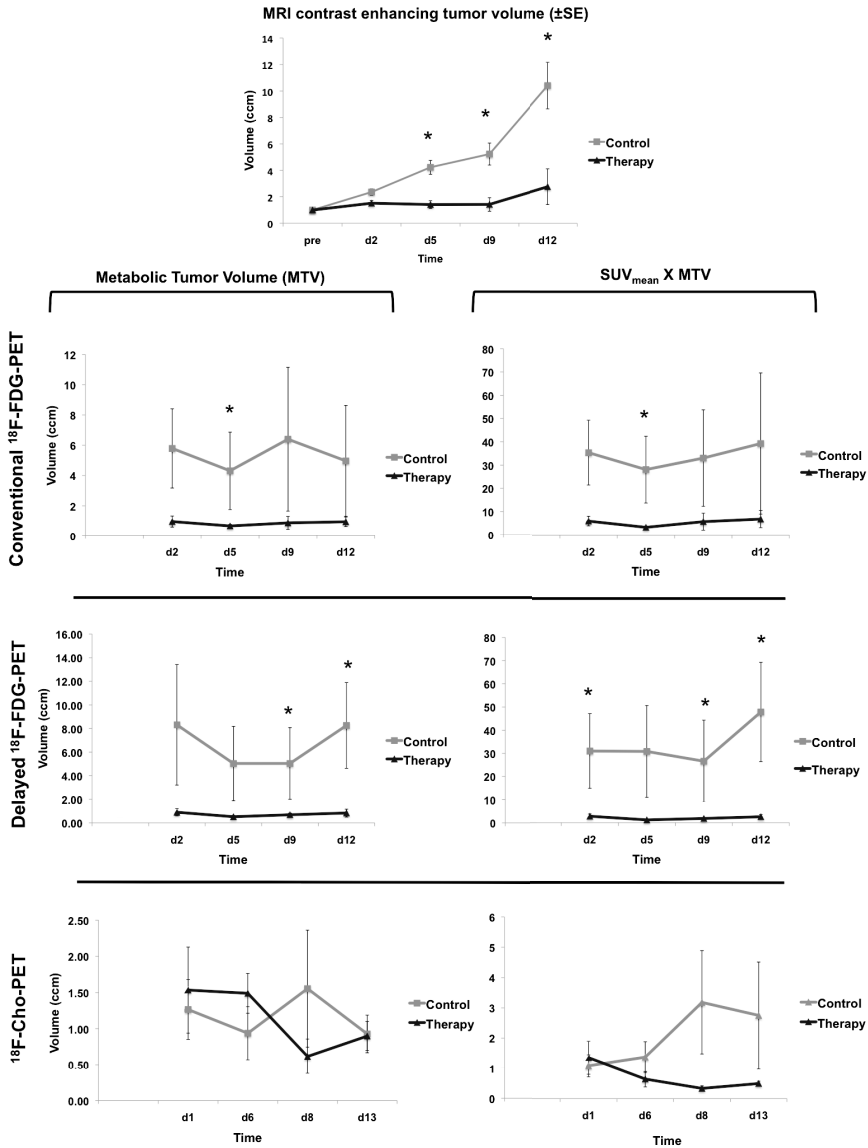
Figure 5.9. Evolution of tumor growth based on MRI and PET. Evolution of the mean tumor volumes (±SE) on T1-weighted contrast enhanced MR images in both treatment groups. Evolution of the metabolic tumor volume (MTV) and (SUV$_{mean}$ x MTV) of conventional and delayed ^{18}F-FDG and ^{18}F-FCho μ PET in the control and treatment group (±SE) are given. Significant differences between the control and treatment groups (p ≤ 0.05) are marked with an asterisk (*).

Figure 5.10. Tumor growth on contrast-enhanced T1-weighted MRI (top row), early ^{18}F-FDG PET (second row), delayed ^{18}F-FDG PET (third row) and ^{18}F-FCho PET images (bottom row) of a F98 GB rat brain (control group). For clarity, the brain is contoured in white. Data from the delayed ^{18}F-FDG PET scan on day 5 is missing.
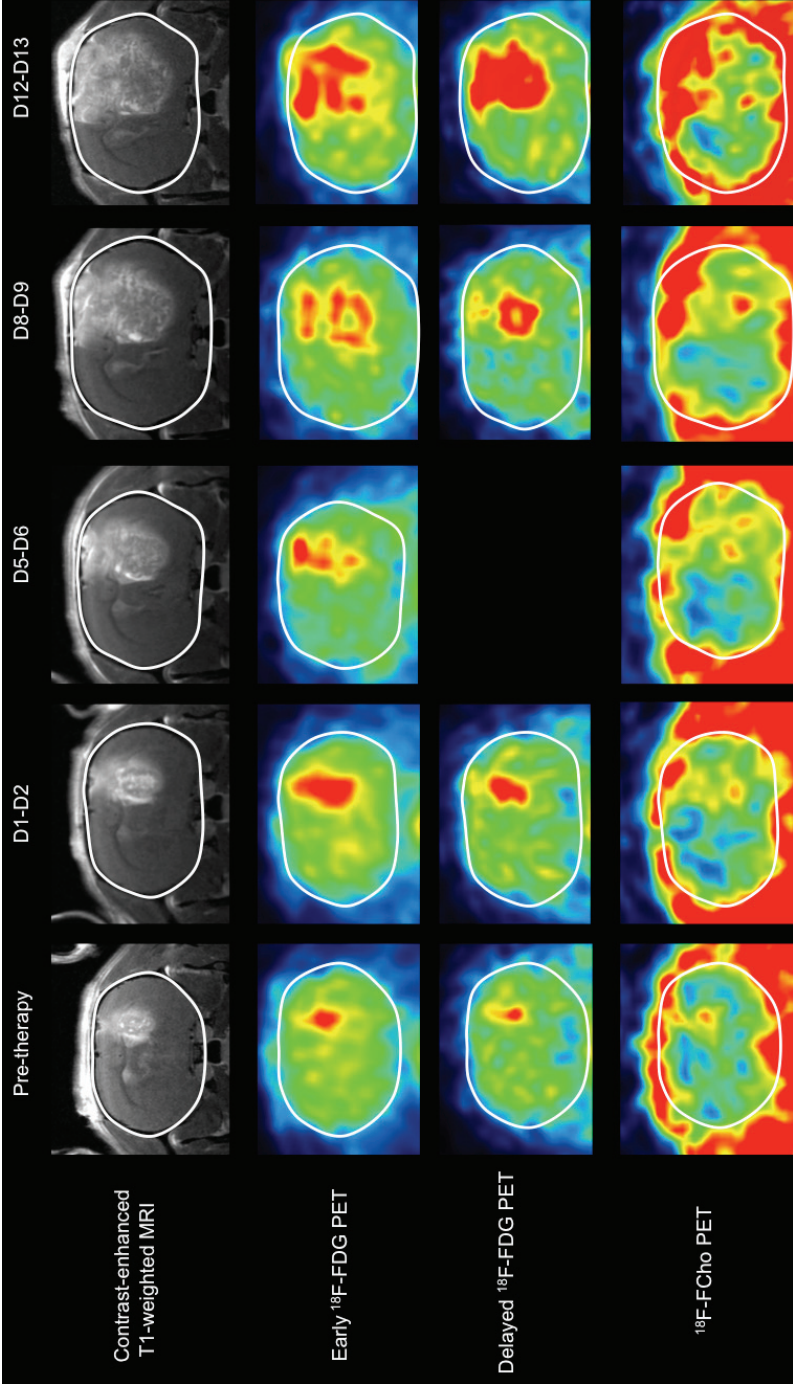
DISCUSSION

In this study, we present an experimental rat model for GB treatment. The advantage of our MRI-guided conformal multiple arc treatment compared to previous cranial RT models is the close resemblance to the clinical image-guided conformal RT with regard to beam usage. Delivery of radiation in small animals has been achieved using fixed radiation sources applying a single radiation field [3,4,7] and treatment planning is mostly not image-guided or not present at all. Collimators centered over the tumor implantation site [3], lead blocking to shield the surrounding normal tissue and whole brain irradiations [5,6,10,21] were often applied. Vinchon-Petit et al. proposed a whole brain irradiation protocol for a glioma rat model using a linear accelerator, delivering three fractions of 6 Gy with a unidirectional beam [5]. Kumar et al. developed an orthotopic model of radiation necrosis including a tumor by irradiating one portion of the tumor receiving 60 Gy dose in a single fraction [22]. However, in both abovementioned studies, MV X-rays were used. Exposing small animals to such beams causes dose build-up/build-down gradients of the order of the animal size itself. Furthermore, the lateral beam penumbra for MV beams is wide. Both make it challenging to deliver a uniform dose to the tumor, which lead to unacceptable dose distributions in rats [9]. Recent developments of small animal micro-irradiators, such as the SARRP, enable delivery of high resolution and optimally planned conformal RT using kV photons. As such, translation from *in vivo* studies to the clinic could be improved.

Baumann et al. established a bio-imageable mouse model for GB and an image-guided radiation delivery method. However, the authors only used MRI to determine the collimator size and isocenter depth. Tumor position was determined using a bioluminescent signal, indicated on the scalp with a marker and a unidirectional beam was delivered [8]. However, it has been reported that off-line bioluminescence imaging (BLI), including BLI-CBCT co-registration, requires the use of an undesirable large beam aperture. On-board BLI is necessary to improve accuracy [23]. To more closely mimic the clinical situation, we developed a F98 GB rat model. In clinical RT, target volume delineation is mostly based on MRI sequences, sometimes with complementary PET images. Several beams from different directions, often non-coplanar, are used to cover the target as accurate as possible, taking care to equally spare the organs at risk. To achieve both goals, IMRT techniques are frequently used. The F98 GB rat model was preferred because tumor growth and invasive characteristics are quite similar to those of human GB [19]. However, F98 tumors show more significant perivascular tumor cell growth, probably accounting for the rapid clinical decline. To achieve accurate irradiation of the tumor target, the SARRP's onboard CT guidance was not sufficient. Brain tumors are hardly visible due to inappropriate soft tissue contrast (Figure 5.3.A) and the DVHs obtained show a very heterogeneous target coverage (Figure 5.7.A). **Using MRI guidance, dose delivery to the target volume is more homogeneous and steadily increases using a single beam, a single arc and three non-coplanar arcs, respectively** (Figure 5.7.). Most importantly, our results confirm that MRI-guided non-coplanar arcs are preferred to minimize the dose delivered to the normal brain tissue (Figure 5.7.D and Table 5.1.).

As in the clinic, the aim was to incorporate MRI-based RT planning and the use of multiple non-coplanar arc beams. Using the 3D Slicer software and the SARRP interface **we were able to irradiate the tumor with three conformal non-coplanar arc beams using a 3 x 3 mm collimator** (Figure 5.7.D). **The**

Chapter 5. Assessment of the effect of therapy in a rat model of GB using PET and MRI

γH2AX staining of irradiated rat brain tissue confirmed a 3 x 3 mm beam with sharp beam edges (Figure 5.8.). The latter is a result of the small focal spot and relatively low-energy X rays [24,25]. To our knowledge, this is the first time multiple arcs for cranial irradiation are used in small animals. The advantage of arc treatment is that the target ultimately receives the prescribed dose, while the normal tissues only receive a fraction of it. A single dose of 20 Gy was chosen, because its biological effect roughly equals that of 30 fractions of 2 Gy used in the clinic. However, we cannot rule out differences in biological effect of the high dose used and the low dose used in humans.

Using the approach with the SARRP and concomitant TMZ, tumor growth observed on follow-up MRI was stable until 9 days post-irradiation, while continuous tumor growth was observed in the controls. From pre-treatment to day 12 post-irradiation, in the control group, the contrast enhancing tumor volume increased 10-fold, whereas in the therapy group, the contrast enhancing tumor volume increased only 3-fold. The increase in tumor volume from day 9-12 is not statistically significant (p = 0.063) in the sham group. However, this is likely due to the smaller sample size (1 animal was euthanized before day 12 due to clinical decline). The overall results confirm the effectiveness of the treatment and the mean cumulative DVH confirms delivery of 20 Gy to 90 % of the tumor target volume (Figure 5.7.D).

Our next goal was to investigate if PET was also able to observe the treatment effect as indicated by MRI. Two tracers were used, namely ^{18}F-FDG and ^{18}F-FCho. First, an automatic threshold technique was chosen because it is known to be the best guarantee that consistent VOIs are defined on repeat scans [26]. Hence, for ^{18}F-FDG and ^{18}F-FCho PET, a threshold of ≥ 60 % and ≥ 50 % of the maximum uptake, respectively, was selected based on visual inspection (Figure 5.5). ^{18}F-FDG PET was performed because ^{18}F-FDG is commonly used in (neuro-)oncology and because of its higher specificity to monitor therapeutic response in brain tumors than CT and MRI [27]. Based on our results, we found that the variable **(SUV_{mean} x MTV) is superior to MTV only in detecting the effect of therapy, both for ^{18}F-FDG at conventional and delayed time intervals** (Table 5.4). This is in agreement with our previous study in GB patients in which both MTV and the mean tracer uptake needed to be taken into account to be able to capture therapy effects (Chapter 4) [28]. Using (SUV_{mean} x MTV), conventional ^{18}F-FDG PET detects treatment effect starting as soon as day 5 post-therapy, comparable to contrast-enhanced MRI. Importantly, **delayed ^{18}F-FDG PET was able to detect the treatment effect earlier,** starting at day 2 post-irradiation (Table 5.4). Amino-acid PET tracers, such as ^{11}C-Methionine (^{11}C-MET) and ^{18}F-FET PET have been suggested to be better suited than ^{18}F-FDG for monitoring therapy response in brain tumor patients due to a higher tumor-to-normal-tissue contrast [27]. Available data in the literature suggests that a reduction of amino acid uptake by glioma is a sign of a favorable response and a decrease of tracer uptake as early as 7-10 days after the completion of treatment has been documented [29-32]. ^{18}F-FCho PET, first introduced for PET imaging of brain tumors by Delgrado et al., was selected because of its high contrast in uptake between high-grade brain tumors and adjacent normal brain tissue [33-35]. ^{18}F-FCho PET has previously been investigated for therapy response assessment in glioma, but only a few studies are available [36,37]. Li et al. reported that, for ^{11}C-Choline PET, a tumor to normal brain

ratio (TBR) $\leq$ 1.4 might predict a longer overall survival in patients with suspected recurrent glioma after treatment [36]. Parashar et al. suggested that there was a good correlation between a change in SUV_{max} of the tumor volume during RT and response [37]. However, in the latter study, only one patient with a high-grade glioma was included. In chapter 4, we investigated the potential of ^{18}F-FCho PET compared to state-of-the art conventional MRI using RANO criteria for early therapy response assessment in GB patients. MTV x SUV_{mean} allowed prediction of therapy response as early as 1 month after the completion of RT. Interestingly, the tumor volume derived from contrast-enhanced MRI was able to predict response earlier, already at week 6 during RT. However, due to the possibility of pseudoprogression and pseudoresponse on post-treatment MRI, we suggested inclusion of PET for early therapy response prediction in high-grade glioma [28]. In this preclinical study, ^{18}F-FCho PET was not able to detect the effects of radiochemotherapy early post-treatment. Importantly, visual comparison between clinical ^{18}F-FCho PET images and preclinical images revealed that the uptake in the small animal GB tumors was less well circumscribed compared to human GB. Several factors may contribute to this finding, such as differences in metabolism of ^{18}F-FCho between rats and humans. This means that most likely, full kinetic modeling is needed to provide a full explanation for our different results in small animals and human [38-41].

Conclusion

Based on our results, we confirm the applicability of this model for combined radiation and chemotherapy of GB in rats and for future research on new therapeutics for GB. As such, this approach is a major step forward in bridging the gap between preclinical and clinical RT technology. Furthermore, both MRI and (delayed) ^{18}F-FDG PET seem to be able to detect the effects of therapy early in GB rats. ^{18}F-FCho PET was not able to detect early treatment response in GB rats.

REFERENCES

[1] Anton K, Baehring JM, Mayer T. Glioblastoma multiforme: overview of current treatment and future perspectives. Hematology Oncology Clinics North America 2012;26(4):825-853.

[2] Kinsella TJ, Vielhuber KA, Kunugi KA, et al. Preclinical Toxicity and Efficacy Study of a 14-day Schedule of Oral 5-Iodo-2-pyrimidinone-2'-deoxyribose as a Prodrug for 5-Iodo-2'- deoxyuridine Radiosensitization in U251 Human Glioblastoma Xenografts. Clinical Cancer Research 2000;6:1468-1475.

[3] Vellimana AK, Recinos VR, Hwang L, et al. Combination of paclitaxel thermal gel depot with temozolomide and radiotherapy significantly prolongs survival in an experimental rodent glioma model. Journal of Neurooncology 2012;11(3):229-236.

[4] Kioi M, Vogel H, Schultz G, et al. Inhibition of vasculogenesis, but not angiogenesis, prevents the recurrence of glioblastoma after irradiation in mice. Journal of Clinical Investigation 2010;120(3):694-705.

[5] Vinchon-Petit S, Jarnet D, Jadaud E, et al. External irradiation models for intracranial 9L glioma studies. Journal of Experimental Clinical Cancer Research 2010;29:142.

[6] Yang W, Huo T, Barth RF, et al. Convection enhanced delivery of carboplatin in combination with radiotherapy for treatment of brain tumors. Journal of Neurooncology 2011;101:379-390.

[7] Rousseau J, Barth RF, Fernandez M, et al. Efficacy of intracerebral delivery of cisplatin in combination with photon irradiation for treatment of brain tumors. Journal of Neurooncology 2010;98:287-295.

[8] Baumann BC, Benci JL, Santoiemma PP, et al. An Integrated Method for Reproducible and Accurate Image-Guided Stereotactic Cranial Irradiation of Brain Tumors Using the Small Animal Radiation Research Platform. Translational Oncology 2012;5(4):230-237.

[9] Verhaegen F, Granton P, Tryggestad E. Small animal radiotherapy research platforms. Physics in Medicine and Biology 2011;56:R55-R83.

[10] Lee DY, Chunta JL, Park SS, et al. Pulsed versus conventional radiation therapy in combination with temozolomide in a murine orthotopic model of glioblastoma multiforme. International Journal of Radiation Oncology Biology Physics 2013;86(5):978-985.

[11] Wong J, Armour E, Kazanzides P, et al. High-resolution, small animal radiation research platform with X-ray tomographic guidance capabilities. International Journal of Radiation Oncology Biology Physics 2008;71(5):1591-1599.

[12] Kirsch DG1, Tarbell NJ. Conformal radiation therapy for childhood CNS tumors. Oncologist 2004;9(4):442-450.

[13] Khan FM. The physics of radiation therapy. PART III: modern radiation therapy. Chapter 20: Intensity modulated radiation therapy. Baltimore, Philadelphia: Wolter Kluwer-Lippincott Williams & Wilkins 2010 4rd edition;430-489.

[14] Matinfar M, Iordachita L, Ford E, et al. Precision radiotherapy for small animal research. Medical Image Computing Assisted Intervention 2008;11:619-626.

[15] Aird EGA, Conway J. CT simulation for radiotherapy treatment planning. British Journal of Radiology 2002;937-49.

[16] Baker GR. Localization: Conventional and CT simulation. British Journal of Radiology 2006;79.

[17] Banissi C, Ghiringhelli F, Chen L, et al. Treg depletion with a low-dose metronomic temozolomide regimen in a rat glioma model. Cancer Immunology Immunotherapy 2009;58:1627-1634.

[18] Robinson CG, Palomo JM, Rahmathulla G, et al. Effect of alternative temozolomide schedules on glioblastoma O6-methylguanine-DNA methyltransferase activity and survival. British Journal of Cancer 2010;103:498-504.

[19] Barth RF, Kaur B. Rat brain tumor models in experimental neuro-oncology: the C6, 9L, T9, RG2, F98, BT4C, RT-2 and CNS-1 gliomas. Journal of Neurooncology 2009;94:299-312.

[20] Brat DJ, Prayson RA, Rycken TC, et al. Diagnosis of malignant glioma: role of neuropathology. Journal of Neurooncology 2008;89:287-311.

[21] Lee DY, Chunta JL, Park SS, et al. Pulsed versus conventional radiation therapy in combination with temozolomide in a murine orthotopic model of glioblastoma multiforme. International Journal of Radiation Oncology Biology Physics 2013;86(5):978-985.

[22] Kumar S, Arbab AS, Jain R, et al. Development of a novel animal model to differentiate radiation necrosis from tumor recurrence. Journal of Neurooncology 2012;108(3):411-420.

[23] Tuli R, Armour M, Surmak A, et al. Accuracy of off-line bioluminescence imaging to localize targets in preclinical radiation research. Radiation Research 2013;179:416-421.

[24] Ford EC, Achanta P, Purger D, et al. Localized CT-guided irradiation inhibits neurogenesis in specific regions of the adult mouse brain. Radiation Research 2011;175:774-783.

[25] Tryggestad E, Armour M, Iordachita I, et al. A comprehensive system for dosimetric commissioning and Monte Carlo validation for the small animal radiation research platform. Physics in Medicine and Biology 2009;54:5341-5357.

[26] Lammertsma AA, Hoekstra CJ, Giaccone G, et al. How should we analyse FDG PET studies for monitoring tumour response? European Journal of Nuclear Medicine and Molecular Imaging 2006;33(S1):16-21.

[27] Ahmed R, Oborski MJ, Hwang M, et al. Malignant gliomas: current perspectives in diagnosis, treatment, and early response assessment using advanced quantitative imaging methods. Cancer Management and Research 2014;6:149-170.

[28] Bolcaen J, Acou M, Boterberg T, et al. ^{18}F-fluoromethylcholine (^{18}F-FCho) PET and MRI for the prediction of response in glioblastoma patients according to the RANO criteria. Journal of Nuclear Medicine Communications 2016; 2017;38(3):242-249.

[29] Galldiks N, Rapp M, Stoffels G, et al. Response assessment of bevacizumab in patients with recurrent malignant glioma using [18F]Fluoroethyl-L-tyrosine PET in comparison to MRI. European Journal of Nuclear Medicine and Molecular Imaging 2013;40:22-33.

[30] Piroth MD, Pinkawa M, Holy R, et al. Prognostic value of early [18F]fluoroethyltyrosine positron emission tomography after radiochemotherapy in glioblastoma multiforme. International Journal of Radiation Oncology Biology Physics 2011;80:176-184.

[31] Galldiks N, Langen KJ, Holy R, et al. Assessment of treatment response in patients with glioblastoma using O-(2-18F-fluoroethyl)-L-tyrosine PET in comparison to MRI. Journal of Nuclear Medicine 2012;53:1048-1057.

[32] Wyss M, Hofer S, Bruehlmeier M, et al. Early metabolic responses in temozolomide treated low-grade glioma patients. Journal of Neurooncology 2009;95:87-93.

[33] DeGrado TR, Coleman RE, Wang S, et al. Synthesis and evaluation of 18F-labeled choline as an oncologic tracer for positron emission tomography: initial findings in prostate cancer. Cancer Research 2001;61(1):110-117.

[34] Treglia G, Giovannini E, Di Franco D, et al. The role of positron emission tomography using carbon-11 and fluorine-18 choline in tumors other than prostate cancer: a systematic review. Annals of Nuclear Medicine 2012;26(6):451-461.

[35] Kwee SA, Ko JP, Jiang CS, et al. Solitary brain lesions enhancing at MR imaging: evaluation with fluorine 18-fluorocholine PET. Radiology 2007;244:557-565.

[36] Li W, Ma L, Wang X, et al. 11C-choline PET/CT tumor recurrence detection and survival prediction in post-treatment patients with high-grade gliomas. Tumor Biology 2014;35:12353-12360.

[37] Parashar B, Wernicke AG, Rice S, et al. Early assesment of radiation response using a novel functional imaging modality-[18F] Fluorocholine PET (FCH-PET): A pilot study. Discovery Medicine 2012;14:13-20.

[38] Verwer EE, Oprea-Lager DE, van den Eertwegh AJM, et al. Quantification of 18F-fluorocholine kinetics in patients with prostate cancer. Journal of Nuclear Medicine 2015;56:365-371.

[39] Weber B, Burger C, Biro P, et al. A femoral arteriovenous shunt facilitates arterial whole blood sampling in animals. European Journal of Nuclear Medicine 2002; 29(3):319-323.

[40] Roivainen A, Forsback S, Grönroos T, et al. Blood metabolism of [methyl-11C].choline; implications for in vivo imaging with positron emission tomography. European Journal of Nuclear Medicine 2000; 27(1):25-32.

[41] Tan H, Chen L, Guan Y, et al. Comparison of MRI, F-18 FDG, and 11C-choline PET/CT for their potentials in differentiating brain tumor recurrence from brain tumor necrosis following radiotherapy. Clinical Nuclear Medicine 2011; 36(11):978-981.

Chapter 6.

^{18}F-FCho, ^{18}F-FET and ^{18}F-FDG PET for the discrimination between glioblastoma and radiation necrosis in rats.

This chapter contains data from:

Julie Bolcaen M.Sc.[1], Benedicte Descamps M.Sc Ph.D.[2], Karel Deblaere M.D. Ph.D.[3], Tom Boterberg M.D. Ph.D.[4], Filip De Vos Dr. Apr.[5], Jean-Pierre Kalala M.D.[6], Caroline Van den Broecke M.D.[7], Christian Vanhove Eng. Ph.D.[2], Ingeborg Goethals M.D. Ph.D.[1]

AND

Julie Bolcaen M.Sc.[1], Kelly Lybaert M.Sc.[1], Lieselotte Moerman Pharm. Ph.D.[1], Benedicte Descamps M.Sc. Ph.D.[2], Karel Deblaere M.D. Ph.D.[3], Tom Boterberg M.D. Ph.D.[4], Jean-Pierre Kalala M.D.[6], Caroline Van den Broecke M.D.[7], Filip De Vos Pharm. Ph.D.[5], Christian Vanhove Eng. Ph.D.[2], Ingeborg Goethals M.D. Ph.D.[1]

[1]Department of Nuclear Medicine, Ghent University Hospital
[2]IBiTech - MEDISIP - Department of Electronics and Information Systems, Ghent University
[3]Department of Radiology, Ghent University Hospital
[4]Department of Radiation Oncology, Ghent University Hospital
[5]Department of Radiopharmacy, Ghent University
[6]Department of Neurosurgery, Ghent University Hospital
[7]Department of Pathology, Ghent University Hospital

De Pintelaan 185, 9000 Gent, Belgium

Chapter 6. ^{18}F-FCho, ^{18}F-FET and ^{18}F-FDG PET for the discrimination between glioblastoma and radiation necrosis in rats.

INTRODUCTION

Differentiating tumor recurrence form radiation necrosis (RN) during post-treatment follow-up of glioblastoma (GB) patients remains challenging. The incidence of RN in GB patients was reported to be 30 % and correct diagnosis has a large impact on further treatment and prognosis [1]. The primary mechanisms of RN are vascular endothelial injury or damage to oligodendroglia, see Chapter 1 [2]. Because of the disruption of the blood brain barrier (BBB) in both GB and RN, contrast enhancement is usually present on both magnetic resonance imaging (MRI) and computed tomography (CT). Therefore, these entities cannot be distinguished based on conventional CT or MRI only. In GB, increased membrane turnover, vascularity and cellularity found by MR spectroscopy (MRS), perfusion, and diffusion should lead to suspicion of a tumor [1]. However, in most institutions these techniques are not used routinely. Positron emission tomography (PET) is also promising, possibly able to visualize differences in metabolic activity between GB and RN. Multiple studies investigated the potential of ^{18}F-fluorodeoxyglucose (^{18}F-FDG) in discriminating RN from tumor, however, ambiguous results have been published [3-6]. A major advantage of ^{18}F-fluoroethyltyrosine (^{18}F-FET) is the lack of uptake in inflammatory tissue [7] and Pöpperl et al. confirmed that recurrence had focal ^{18}F-FET uptake with significantly higher uptake compared to non-recurrence [8]. Furthermore, ^{18}F-fluoromethylcholine (^{18}F-FCho) was suggested to be promising in separating RN from tumor recurrence [9-11]. Degrado et al. introduced ^{18}F-FCho for brain tumor imaging [12]. Unlike ^{18}F-FDG, ^{18}F-FET and ^{18}F-FCho show low uptake in normal brain tissue, resulting in higher tumor-to-normal tissue contrast [13]. However, it is worth noting that the latter tracers have mostly been evaluated in clinical studies that lack pathological confirmation of either tumor recurrence or RN. Therefore, using an *in vivo* rat GB and RN model, we investigated the potential value of ^{18}F-FDG, ^{18}F-FCho, and ^{18}F-FET PET in discriminating GB from RN.

As explained in Chapter 2, SUV is the most widely used parameter for PET analysis. As such, the first goal of this study was to compare SUV uptake values between GB and RN in rats. However, semi-quantitative analysis based on SUV does not take into account possible influences on quantification by blood volume and metabolite formation [14,15]. Therefore, our second goal was to characterize and further clarify the mechanism of uptake of ^{18}F-FDG, ^{18}F-FCho, and ^{18}F-FET PET in GB and RN using a quantitative approach based on kinetic modeling (KM), introduced in Chapter 2 [9]. For ^{18}F-FDG, a two tissue compartmental model with one input function (2C1i) was proposed [16,17] and suggested to be useful for differentiating high-grade glioma from brain lymphoma [18]. Our hypothesis suggests a higher k3 in GB compared to RN. Also Patlak graphical analysis (GA) has been proposed for analyzing ^{18}F-FDG PET [15,19,20]. For ^{18}F-FET PET in which uptake is mediated by large amino acid transporters (LAT), B^{0+} and B^0 transport mechanisms, Logan GA as well as one tissue compartment model analysis (1C1i) is feasible [7,21]. The only assumptions in applying Logan analysis were reversible binding of the tracer and linearity of the given expressions, which are met for ^{18}F-FET [15,19,21]. Assuming a higher amount of amino acid transport mechanisms in tumor, K_1 is hypothesized to be higher in GB than in RN. The kinetic model for ^{18}F-FCho is not very clear because of its oxidative metabolism to ^{18}F-Fluorobetaine (^{18}F-FBet) [14,21,22,23]. Therefore, in this study, three compartmental models were

evaluated, including 1C1i, 2C1i and a model using three compartments containing two input functions (^{18}F-FCho and ^{18}F-FBet) (3C2i).

Furthermore, non-specific leakage of the radiolabeled PET tracers, due to blood-brain barrier (BBB) breakdown, is present both in GB and RN. As such, it was our interest to assess the BBB integrity in the GB and RN rat model. In a preclinical setting several low and high molecular weight vascular permeability markers are available. Both radiolabeled markers including alpha-aminoisobutyric acid, sucrose and inulin and non-radioactive low molecular weight markers such as sodium fluorescein were developed for *ex vivo* assessment of the BBB integrity. Furthermore, high molecular weight markers were developed including horseradish peroxidase, dextran and Evans blue (EB). The non-toxic EB binds to albumin directly after intravenous injection and is therefore contained to the blood stream. When sites of BBB disruption are present, EB crosses the BBB, thus resulting in site-specific accumulation [29]. In this study we assessed BBB breakdown in GB and RN using EB.

MATERIALS AND METHODS

F98 GB rat model

Optimization of the F98 GB rat model was introduced previously in chapter 5 (Figure 6.1.A-D) [9]. In summary, F98 GB cells, obtained from ATCC® (CRL-2397), were inoculated in the right frontal hemisphere (Figure 6.1.A) of 39 female Fischer F344 rats (Charles River®) (body weight 177 ± 8 g). The rats were anesthetized with ketamine/xylazine (4/3; 0.13 ml/100 g). Post-surgery, a close follow-up of the animals was performed (body temperature, wound healing and behavior).

Induction of RN

Induction of RN in normal brain tissue in a second group of 34 female Fischer F344 rats (Charles River®) was achieved using the small animal radiation research platform (SARRP, Xstrahl®, Surrey, UK). To induce RN, non-coplanar multiple-arc micro-irradiation was performed. The isocenter for RT planning was positioned in the right frontal region on coronal, axial, and sagittal CT slices. Three arcs were used, one covering an angle of 90° (couch angle 0°) and two covering angles of 60° (couch angles 45° and 90°). For all three arcs, a 3 × 3 mm collimator was used for the delivery of 60 Gy in a single dose (Figure 6.1.E). For irradiation, the voltage of the SARRP's X-ray source was set to 220 kV with a tube current of 13 mA. A copper filter of 0.15 mm thickness was used.
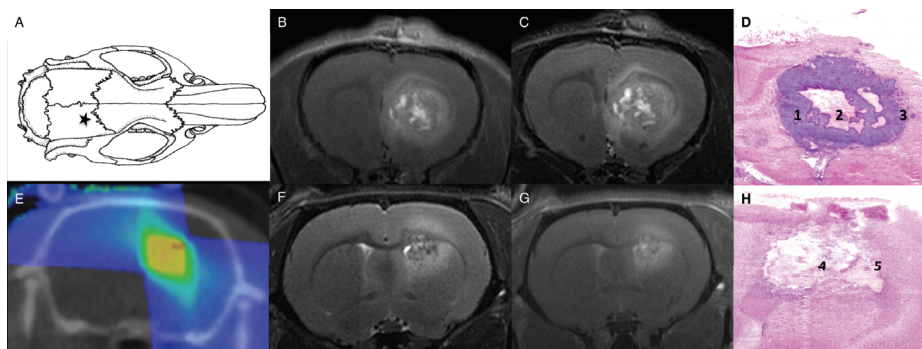
Figure 6.1. GB and RN model. Location for inoculation of F98 glioblastoma cells (★A), glioblastoma T2-weighted (B) and T1-weighted contrast-enhanced (C) MRI, hematoxylin and eosin staining (D) confirms the presence of glioblastoma tumor cells (1), central tumor necrosis (2) and abundant blood vessels in the perinecrotic tumor rim (3), dose plan for radiation therapy inducing RN (E), radiation necrosis T2-weighted (F) and T1-weighted contrast-enhanced (G) MRI and hematoxylin and eosin staining (H) confirming a large necrotic area with profound vascular changes (4), surrounded by a rim of macrophages (5).

All animals were kept under environmentally controlled conditions (12 h normal light/dark cycles, 20-24 °C, and 40-70 % relative humidity) with food and water ad libitum. The method of euthanasia was a lethal dose of pentobarbital sodium (160 mg/kg). Euthanasia was performed prior to the experimental endpoint if a decline of 20 % body weight was observed or when the normal behavior severely deteriorated (e.g. lack of grooming). The study was approved by the Ghent University Ethical Committee on animal experiments (ECD12/28-A2).

Chapter 6. <u>^{18}F-FCho, ^{18}F-FET and ^{18}F-FDG PET for the discrimination between glioblastoma and radiation necrosis in rats.</u>

MRI

Eight days post-inoculation MRI was performed using a 7 tesla dedicated small animal MR system (PharmaScan 70/16, Bruker BioSpin, Ettlingen, Germany) to confirm tumor growth in the GB group. Follow-up of tumor growth was done twice a week after inoculation using MRI. Serial MRI to detect radiation-induced brain tissue damage was done twice weekly from 3 months post-irradiation using the same small animal MRI scanner. The rats were anesthetized with 2 % isoflurane mixed with oxygen administered at a flow rate of 0.3 L/min through a nose cone fixed onto the animal holder. A heated blanket was placed on each animal. After fixation of the animal, a rat brain surface coil (Rapid Biomedical, Rimpar, Germany) was placed around the head of the animal. The holder was positioned in a 72 mm rat whole body transmitter coil (Rapid Biomedical, Rimpar, Germany). A localizer scan was performed followed by a T2-weighted spin-echo scan (TR/TE 3661/37.1 ms, 109 μm isotropic in plane resolution, 4 averages, TA 9'45") to localize the tumor or the RN lesion. If a tumor or RN was visible on T2-weighted images, a gadolinium-containing contrast agent (Dotarem, Guerbet, France; 0.4 mL/kg) was injected intravenously. For this purpose, a 30-Gauge needle connected to a 60 cm long tube was inserted intravenously into the tail vein. Fifteen minutes later a contrast-enhanced T1-weighted spin-echo sequence (TR/TE 1539/9.7 ms, 117 μm isotropic in plane resolution, 3 averages, TA 4'15") was performed. Additionally, T2*-weighted images were acquired in animals with RN lesions (3D FLASH sequence, TR/TE 30/10 ms, 120 μm in plane resolution, 2 averages, TA 10'1"). Typical T2- and contrast-enhanced T1-weighted MR images of GB and RN are shown in Figure 6.1.

In the GB group, in case of confirmed tumor growth eight days post-inoculation, PET scans were acquired on day 14-16 post-inoculation. In the RN group, in case of a confirmed contrast-enhancing RN lesion on MRI, PET was acquired within the week.

^{18}F-FDG, ^{18}F-FET and ^{18}F-FCho PET

Semi-quantitative PET

PET images were acquired in list mode by a micro-PET scanner (FLEX Triumph II, TriFoil Imaging®, Northridge CA) using ^{18}F-FDG, ^{18}F-FCho, and ^{18}F-FET as PET tracers. Animals were anesthetized with 2 % isoflurane mixed with oxygen administered at a flow rate of 0.3 L/min. A 30-Gauge needle connected to a 10 cm long tube was inserted intravenously into the tail vein, and the rats were positioned on the animal bed of the micro-PET scanner, receiving further anesthesia through a nose cone. Directly after intravenous injection of the radioactive tracer (37 MBq dissolved in 200 μL saline) a list-mode PET scan was acquired with a total acquisition time of 20 minutes for ^{18}F-FCho PET, 55 minutes for ^{18}F-FET PET, and 60 minutes for ^{18}F-FDG PET. In addition, a 30-minutes ^{18}F-FDG PET scan was acquired 240 minutes after ^{18}F-FDG administration.

All PET scans were reconstructed into a 200 × 200 × 64 matrix by a 2D Maximum Likelihood Expectation Maximization (MLEM) algorithm (LabPET Version 1.12.1, TriFoil Imaging®, Northridge CA) using 60 iterations and a voxel size of 0.5 × 0.5 × 1.157 mm. No corrections for attenuation, scatter and partial volume effects were performed. The same reconstruction parameters were applied for ^{18}F-FDG, ^{18}F-FCho, and ^{18}F-FET PET. From the list-mode data a static 20-minutes PET scans was reconstructed 40 minutes after tracer injection for ^{18}F-FDG, a static 20-minutes PET scans was

reconstructed 35 minutes after tracer injection for ^{18}F-FET, and a static 10-minutes PET scans was reconstructed 10 minutes after tracer injection for ^{18}F-FCho.

In the GB group, a total of 35 rats were included, where in total 8 dynamic ^{18}F-FCho PET scans, 7 dynamic ^{18}F-FET PET scans and 10 ^{18}F-FDG PET scans were performed. In the RN group, a total of 8 dynamic PET scans were included for each tracer.

Quantitative PET

To allow quantitative PET, arterial blood sampling (ABS) was applied by placing a catheter in the arteria femoralis and vena femoralis allowing the measure the arterial input function (AIF). Therefore, rats were anesthetized with 2 % isoflurane mixed with oxygen (0.3 L/min). Femoral vein, artery and nerve were separated (microscope, Optika®). The distal end of the vena/arteria was bound and blood flow was blocked. Using a 25G (BD®) needle an orifice was made to insert a 40 cm PE50 tubing filled with heparine solution (50 U/ml). At a distance of 10 cm the arterial catheter was fixed and inserted in the detector of the Twilite system (Swisstrace GmbH, Switserland). Using an arteria-vein shunt and a pump system a continuous blood flow was enabled (200 µl/min) allowing to perform ABS without blood loss (Figure 6.2).

During continuous ABS, dynamic list-mode PET acquisitions of 20 min for ^{18}F-FCho, 55 min for ^{18}F-FET and 60 min for ^{18}F-FDG PET were acquired immediately after tracer injection (37 MBq). In addition, a 30-min late ^{18}F-FDG PET static scan was acquired 240 min after tracer injection.

The reconstruction parameters were identical as abovementioned, however, from the list-mode data dynamic PET images were reconstructed. Time frames for ^{18}F-FDG scans were 12x10s/6x20s/6x1min/10x2min/6x5min, for ^{18}F-FCho 12x10s/6x20s/6x1min/2x5min and for ^{18}F-FET 12x10s/6x20s/6x1min/10x2min/5x5min.

In the GB group, a total of 16 rats were included, where 5 animals were used for dynamic ^{18}F-FCho PET, 5 for dynamic ^{18}F-FET and 6 for dynamic ^{18}F-FDG PET. In the RN group, a total of 15 animals were included, using 5 animals for each tracer.

Semi-quantitative PET analysis

PET and contrast-enhanced T1-weighted MRI images were imported into PMOD. PET-MRI co-registration was done automatically using the rigid matching tool in PMOD (mutual information algorithm). If unsuccessful, manual co-registration was performed by matching the isocontour of the PET image to the MRI contour. After co-registration, volumes of interest (VOIs) were manually drawn so that the contrast enhancement observed on the contrast-enhanced T1-weighted MRI was included in the VOI. Cubic VOIs of $3 \times 3 \times 3$ mm located in the contralateral occipital region were used as a reference. Tracer uptake in the VOI, expressed in Bq/ml, was converted to a standard uptake value (SUV). Injected activity was corrected for decay and residual activity in the syringe. SUV values were used to calculate lesion-to-normal tissue ratios (LNRs). The LNR_{mean} was defined as the ratio of the SUV_{mean} in the tumor or RN VOI to the SUV_{mean} in the reference VOI. The LNR_{max} was defined as the ratio of the SUV_{max} in the tumor or RN VOI to the SUV_{mean} in the reference VOI.
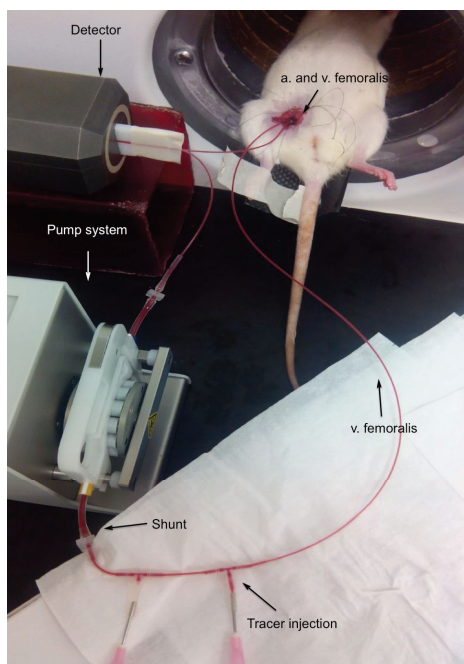
Figure 6.2. Arterial blood sampling set-up. The micro-PET system (FLEX Triumph II, TriFoil Imaging®, Northridge CA) was used. At a distance of 10 cm the arterial catheter was fixed and inserted in the detector of the Twilite system (Swisstrace GmbH, Switserland). Using a shunt and a pump system a continuous blood flow was enabled (200 µl/min). Data acquisition was performed with PMOD (3.405, PMOD technologies®, Zürich, Switserland). The system was calibrated weekly.

Quantitative PET analysis

Whole blood AIF corrections.

Calibration factor, dispersion, decay, and delay correction. The Twilite system is calibrated weekly. For calibrating the system a syringe with an activity of 5 MBq in 10 ml saline is used. 30 cm PE50 tubing is filled with the radioactive saline and the syringe is placed in the field of view of the PET scanner. The tubing is placed in the detector when the 10 min PET acquisition starts. The calibration factor is then calculated using the calibration TAC and PET acquisition in PMOD. The AIF was corrected for dispersion based on catheter internal diameter, withdrawal speed and distance between animal and detector using the formula of Convert et al. [24,25], see also Chapter 2. Decay correction was performed after defining the start time of the acquisition. A delay of 10 s was included.

Plasma-blood ratio. ^{18}F-FDG, plasma-blood ratios were described by Weber et al. [26]. ^{18}F-FET plasma-blood ratios were obtained by collecting blood 1, 30 and 55 min (n = 2), and 5, 15 and 40 min (n = 2) after tracer injection. ^{18}F-FCho plasma-blood ratios were determined 1, 5 and 15 min after tracer injection (n = 3).

Metabolite correction. Metabolite correction was required for ^{18}F-FCho due to its fast oxidation in the liver and kidneys, see Figure 6.3. Metabolites in plasma were determined using the method of Bansal et

al. [27]. Aqueous and organic fractions were separated and counted. The aqueous layer (100 µl) was injected to a HPLC column (Alltech®, Grace). The HPLC consisted of a Waters 1525 binary pump (Waters, Milford, MA, USA), a Waters Breeze data acquisition, and an Alltima silica NP column (5 µm, 10 x 250 mm). The eluent was collected in 30-sec fractions and measured using a γ counter (Cobra®, Packard Canberra).

Kinetic modeling.

KM was performed using PMOD selecting 2C1i for ^{18}F-FDG, 2C1i or 1C1i for ^{18}F-FET and 2C1i, 1C1i or 3C2i for ^{18}F-FCho. For FDG a lumped constant (LC) of 0.89 was selected [28] and the plasma glucose level was determined in a rat with 6 h food deprivation. The models were described by micro-parameters: K_1, k_2, k_3 and k_4 [16]. The influx (K_i) was calculated as $K_1*k_3/(k_2+k_3)$ and the phosphorylation rate (K_p) as $k_3/(k_2+k_3)$. The distribution volume V_d (K_1/k_2) was quantified when applying 1C1i. Tracer plasma curves were fitted using a three-exponential decay function. Model fitting was optimized by (1) visual inspection, (2) evaluation of standard errors (SE), and (3) goodness-of-fit displayed by the Akaike information criterion (AIC), Schwartz criterion (SC) and model selection criterion (MSC). The preferred model is the one with the lowest AIC value, the lowest SC value and the highest MSC value. For more details see Chapter 2. No threshold was applied.

Graphical analysis.

Patlak regression was applied characterizing ^{18}F-FDG, ^{18}F-FET and ^{18}F-FCho uptake. If the data were consistent with this model, the curve became linear with a slope K_i ($=K_1*k_3/k_2+k_3$) and an intercept V_t (distribution volume). Logan GA was applied to the ^{18}F-FET and ^{18}F-FCho data. The slope K_i represented K_1/k_2 for 1C1i and $K_1/(k_2(1+k_3/k_4))$ for 2C1i [15,19]. Parametric images of K_i and V_t were calculated and a Gaussian smoothing filter (FWHM 1*1*1 mm) was applied, see Figure 6.10.
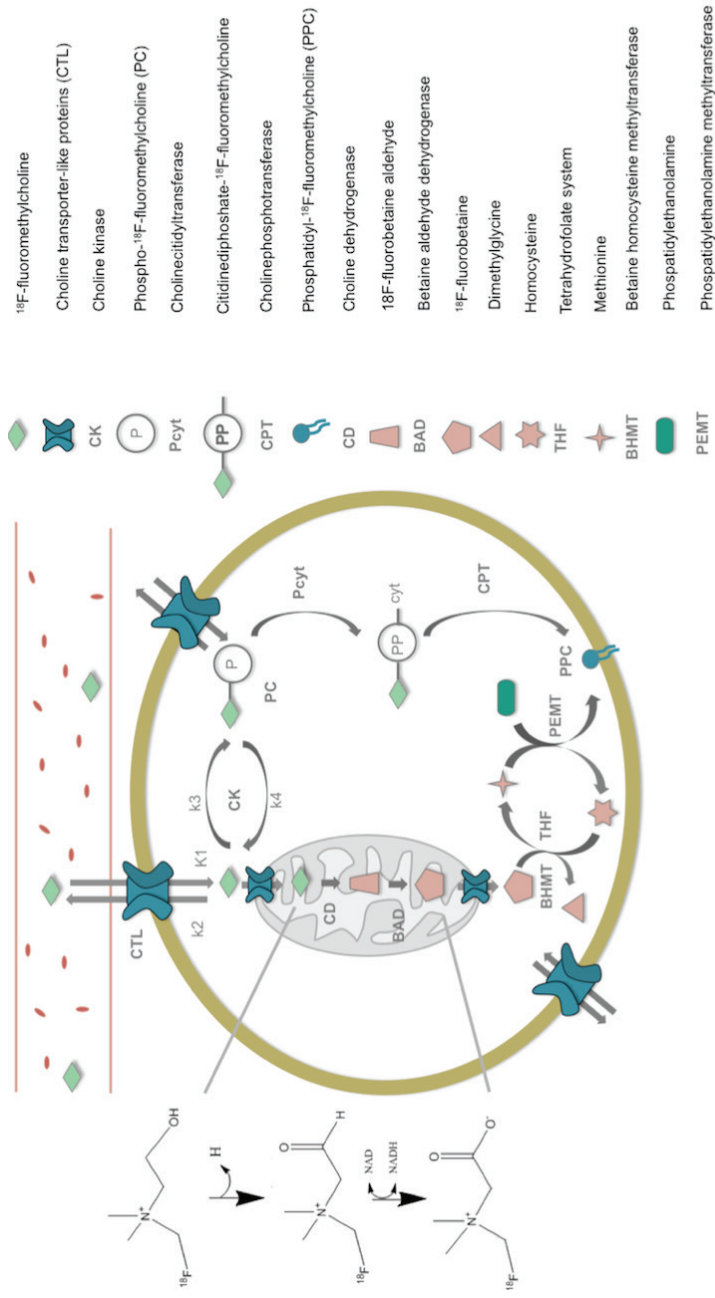
Figure 6.3. Metabolization pattern of ^{18}F-FCho. ^{18}F-FCho enters the cell by choline transporter-like (CTL) proteins, is mainly phosphorylated by choline kinase (CK) forming Phospho-^{18}F-fluoromethylcholine (PC) which, in turn, will be converted to Phosphatidyl-^{18}F-fluoromethylcholine (PPC) by Cholinecitidyltransferase (Pcyt) and Cholinephosphotransferase (CPT). PPC is a major constituent of the cellular membrane. In mitochondria of the liver and kidneys, choline is oxidized to betaine by Choline Dehydrogenase (CD) and Betaine Aldehyde Dehydrogenase (BAD), which enters the one-carbon cycle and serves as a methyl donor in the remethylation of homocysteine to methionine.

Chapter 6. ¹⁸F-FCho, ¹⁸F-FET and ¹⁸F-FDG PET for the discrimination between glioblastoma and radiation necrosis in rats.

Evans Blue staining

To compare BBB breakdown between GB and RN, we analyzed EB extravasation in GB on day 16 after inoculation and in RN after MRI confirmation. First, 4 % EB (Sigma-Aldrich®) dissolved in saline at a concentration of 4 mL per kg of body weight was injected intravenously. One hour later, rats were euthanized, and dissected rat brains were instantly frozen in isopentane (VWR®) cooled by liquid nitrogen for 2 min followed by 30 min incubation at -20 °C. The brains were then cut into 20 μm serial sections using a cryostat (Leica®, CM30505), with alternating slides for fluorescent staining and hematoxylin and eosin (H&E) stain. A picture was taken of the frozen brain tissue (Sony®), and TRITC (tetramethylrhodamine isothiocyanate) fluorescently labeled sections were imaged with a BD pathway 435 automated imaging system (Becton Dickinson) equipped with a 10× objective. A montage of 20×15 images provided a complete overview of the brain section, see Figure 6.12.B and D. Uptake of EB was quantified by manually drawing a VOI around the TRITC signal in ImageJ (National Institutes of Health) [30].

Statistical analysis

Statistical analysis of the SUV, LNRs, KM, GA and TRITC derived variables between GB and RN was performed using the Mann-Whitney U non-parametric test. Spearman correlations (R_s) between SUV variables and kinetic/graphical measures were calculated. A probability value $p < 0.05$ is considered statistically significant.

RESULTS

RN rat model

The time from irradiation to the development of RN was initially unknown and had to be determined using follow-up MRI. Radiation injury showed contrast enhancement on gadolinium-enhanced T1-weighted MRI, were characterized by a heterogeneously hyperintense signal in the center of the lesion on T2-weighted MRI, an isointense signal on T1-weighted MRI, and hypointense foci on T2*-weighted MRI, confirming the presence of blood degradation products (see Figure 6.4). H&E staining (see Figure 6.1.H) showed large necrotic areas with profound vascular changes including fibrinoid necrosis and occlusion of lumina and perivascular necrosis. In the area surrounding the RN lesions, reactive changes in brain parenchyma were noted with an abundance of macrophages. RN was visible on MRI 31 ± 6 weeks post-irradiation. On the day of PET imaging, the mean contrast enhancing volume of the RN lesions on T1-weighted MRI was 36 ± 20 mm^3.
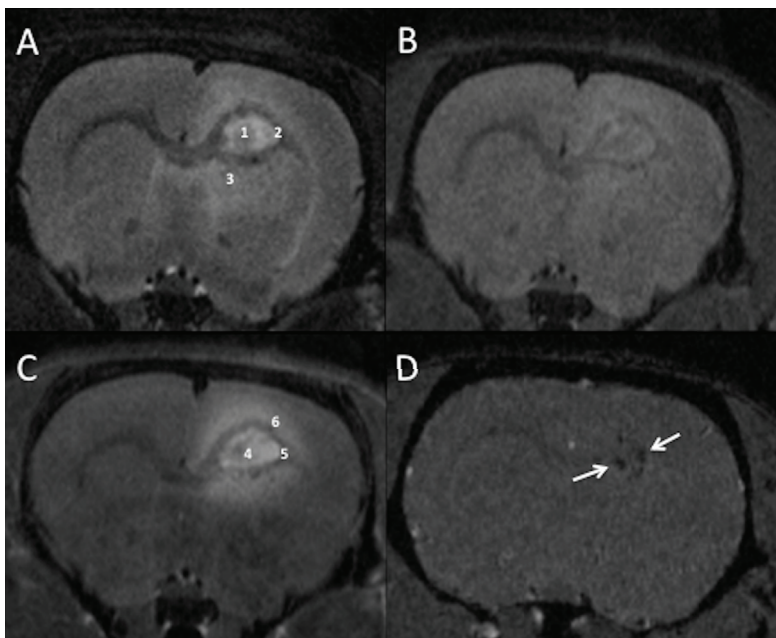
Figure 6.4. Typical MRI features of radiation necrosis (RN) in a rat 6 months postirradiation: a heterogeneous hyperintense signal in the center (1) surrounded by a thin hypointense rim (2) on the T2-weighted image (A). The lesion is circumscribed by a T2 hyperintense patchy zone representing edema (3). The entire RN lesion is isointense on the T1-weighted image (B). The contrast-enhanced T1-weighted image shows a relatively homogeneous enhancement in the center of the lesion (4), surrounded by a thin rim of hypointense signal (5) representing infiltrating inflammatory cells. The surrounding contrast blush (6) signifies blood brain barrier leakage (C). T2* images show hypointense signals (see arrows) confirming the presence of blood degradation products (hemosiderin)(D).

Chapter 6. ^{18}F-FCho, ^{18}F-FET and ^{18}F-FDG PET for the discrimination between glioblastoma and radiation necrosis in rats.

Visual PET analysis

^{18}F-FDG. Uptake in GB was high on early ^{18}F-FDG PET images (40 minutes post-injection) as well as on late ^{18}F-FDG PET images (240 minutes post-injection), which means that the uptake is higher than that in the cortex (Figure 6.5.A and 6.5.D). No increased ^{18}F-FDG uptake was visible in RN (Figure 6.5.B and 6.5.E). Interestingly, the difference in uptake between GB and RN was higher on late ^{18}F-FDG PET images (Figure 6.5.D versus 6.5.E) than on the early ^{18}F-FDG PET images (Figure 6.5.A versus 6.5.B).

^{18}F-FCho. To visually analyze the ^{18}F-FCho PET images, we used the criteria published in our previous work [31]; the scalp was used as a reference, and a four-point grading system was applied, as follows: grade 0 indicated faint uptake, that is, defined as equal to or higher than the uptake in the normal brain parenchyma but lower than in the scalp; grade 1 indicated moderate uptake, defined as comparable to that in the scalp; grade 2 indicated moderately intense uptake, defined as greater than in the scalp; and grade 3 indicated intense uptake. Uptake of ^{18}F-FCho, both in GB and RN, was heterogeneous and ranged from moderate (grade 1) to intense (grade 3). In addition, faint uptake of ^{18}F-FCho was noted in normal brain parenchyma (Figure 6.5.J and 6.5.K).

^{18}F-FET. To visually analyze the ^{18}F-FET PET images, the same criteria were used as for ^{18}F-FCho PET. As such, ^{18}F-FET uptake in GB was heterogeneous and moderately intense (grade 2). A more homogeneous and moderate uptake was visible in RN (grade 1) than in GB (Figure 6.5.G and 6.5.H).
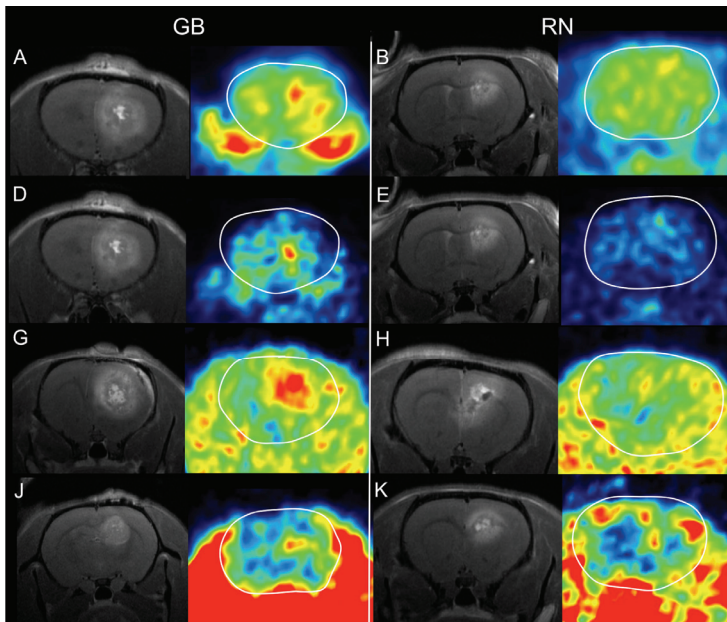

Figure 6.5. Contrast-enhanced MRI and PET of GB and RN. For clarity, the brain is contoured in white. ^{18}F-FDG PET 40 min post-injection (A-B) and 240 min post-injection (D-E). ^{18}F-FET PET 35 min post-injection (G-H) and ^{18}F-FCho PET 10 min post-injection (J-K).

Semi-quantitative PET analysis

Results are summarized in Figure 6.6 and Table 6.1.

^{18}F-FDG. On the early ^{18}F-FDG scans, SUV_{max} (8.91 ± 2.27 for GB and 4.35 ± 1.21 for RN), SUV_{mean} (5.07 ± 1.15 for GB and 3.39 ± 1.16 for RN), LNR_{mean} (1.44 ± 0.17 for GB and 1.00 ± 0.08 for RN) and LNR_{max} (2.53 ± 0.37 for GB and 1.31 ± 0.14 for RN) were significantly lower in RN compared to GB (p < 0.001, p = 0.009, p < 0.001 and p < 0.001, respectively).

Also in the late ^{18}F-FDG scans, SUV_{max} (6.87 ± 1.47 for GB and 3.10 ± 0.79 for RN), SUV_{mean} (3.41 ± 0.78 for GB and 2.09 ± 0.67 for RN), LNR_{mean} (2.01 ± 0.71 for GB vs. 1.22 ± 0.13 for RN) and LNR_{max} (3.97 ± 0.78 for GB vs. 1.85 ± 0.26 for RN) were significantly lower in RN compared to GB.

The difference in LNR_{mean} and LNR_{max} was clearly higher on the late ^{18}F-FDG PET images than on the early ^{18}F-FDG PET images.

^{18}F-FET. The SUV_{max} (4.03 ± 0.66 for GB and 2.14 ± 0.58 for RN), SUV_{mean} (2.31 ± 0.42 for GB and 1.42 ± 0.41), LNR_{mean} (2.17 ± 0.13 for GB and 1.65 ± 0.22 for RN) and LNR_{max} (3.79 ± 0.22 for GB and 2.55 ± 0.65 for RN) were statistically significantly different between GB and RN (p = 0.001, p = 0.002, p < 0.001 and p = 0.004, respectively).

18F-FCho. SUV_{max} (0.93 ± 0.34 for GB and 0.97 ± 0.21 for RN) and SUV_{mean} (0.38 ± 0.12 for GB and 0.44 ± 0.05 for RN) were not significantly different between GB and and RN (p = 0.645 and p = 0.279, respectively). Also the LNR_{mean} and the LNR_{max} were not significantly different between GB and RN (p = 0.328 and p = 1.000, respectively), with slightly lower values for GB (1.89 ± 0.60 and 4.84 ± 2.49, respectively) compared to RN (2.07 ± 0.40 and 4.76 ± 1.68, respectively).
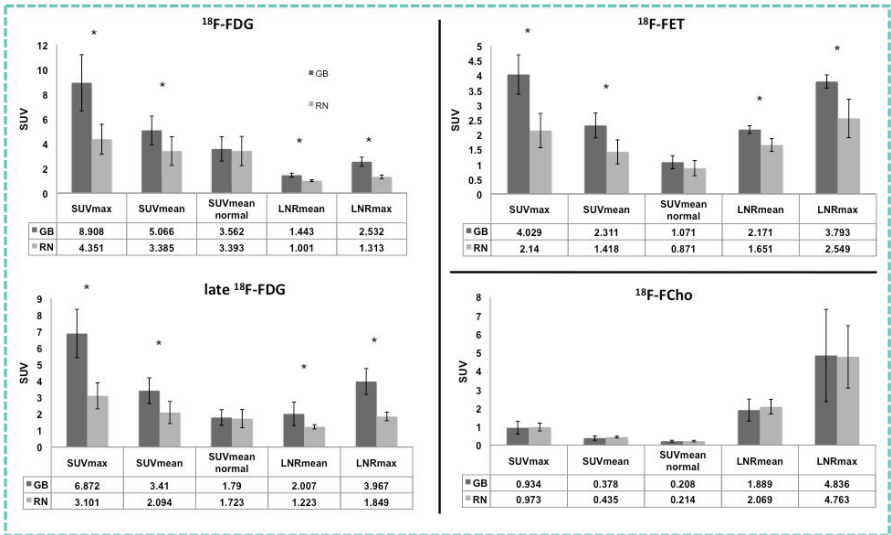
Figure 6.6. Results of the semi-quantitative PET analysis.

Table 6.1. Results of the semi-quantitative PET analysis

		GB		RN		P value (1-tailed)
		mean	SD	mean	SD	
^{18}F-FDG	SUV$_{max}$	8.908	2.268	4.351	1.209	**<0.001**
	SUV$_{mean}$	5.066	1.154	3.385	1.157	**0.009**
	SUV$_{mean}$ normal	3.562	0.980	3.393	1.182	0.539
	LNR$_{mean}$	1.443	0.165	1.001	0.075	**<0.001**
	LNR$_{max}$	2.532	0.367	1.313	0.142	**<0.001**
late ^{18}F-FDG	SUV$_{max}$	6.872	1.465	3.101	0.788	**<0.001**
	SUV$_{mean}$	3.41	0.78	2.094	0.67	**0.002**
	SUV$_{mean}$ normal	1.79	0.474	1.723	0.548	1
	LNR$_{mean}$	2.007	0.709	1.223	0.131	**<0.001**
	LNR$_{max}$	3.967	0.785	1.849	0.257	**<0.001**
^{18}F-FET	SUV$_{max}$	4.029	0.663	2.14	0.579	**0.001**
	SUV$_{mean}$	2.311	0.418	1.418	0.406	**0.002**
	SUV$_{mean}$ normal	1.071	0.22	0.871	0.255	0.121
	LNR$_{mean}$	2.171	0.131	1.651	0.218	**<0.001**
	LNR$_{max}$	3.793	0.222	2.549	0.649	**0.004**
^{18}F-FCho	SUV$_{max}$	0.934	0.341	0.973	0.211	0.645
	SUV$_{mean}$	0.378	0.115	0.435	0.049	0.279
	SUV$_{mean}$ normal	0.208	0.051	0.214	0.043	0.959
	LNR$_{mean}$	1.889	0.595	2.069	0.396	0.328
	LNR$_{max}$	4.836	2.492	4.763	1.684	1

Quantitative PET analysis

Whole blood AIF corrections

Dispersion. Based on the catheter internal diameter (span$_v$ = 43.5), withdrawal speed (v = 200 µl/min) and distance between animal and detector (d = 10 cm), τ_{disp} was 4.63 s [24]. The original blood curves and their dispersion-corrected blood curves are displayed in Figure 6.7.A.
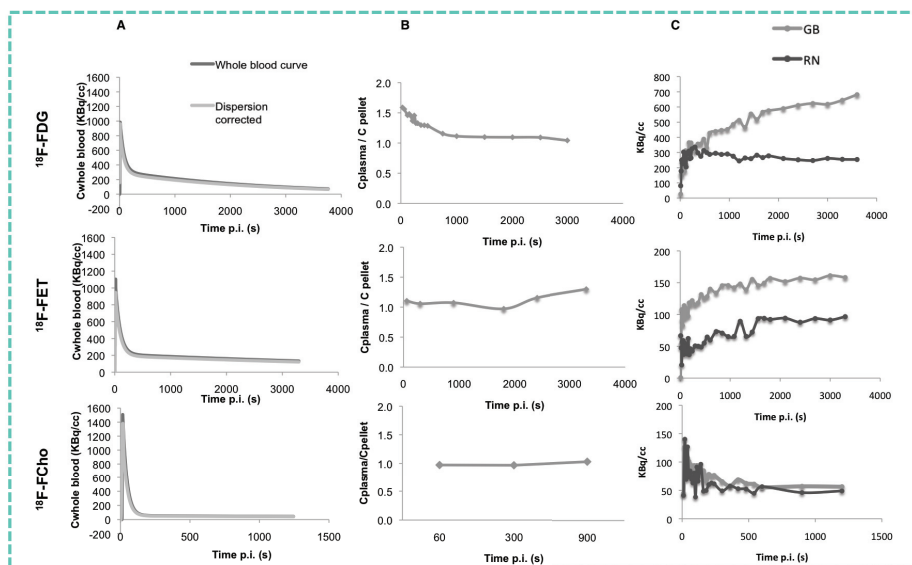
Figure 6.7. Whole blood and dispersion corrected blood curve (A), plasma-blood ratios (B) and time activity curves (TACs) (C) of ¹⁸F-FDG, ¹⁸F-FET and ¹⁸F-FCho in GB and RN.

Plasma-blood ratio. The plasma-to-blood ratios, given in Figure 6.7.B were included in the kinetic analysis. The plasma-to-blood ratio for ¹⁸F-FDG decreased from 1.59 to 1.04 [26]. For ¹⁸F-FET, the ratio slightly increased from 1.10 to 1.30. The ¹⁸F-FCho ratio was stable over time (0.97 to 1.03).

Metabolites of ¹⁸F-FCho. The fraction of lipophilic compounds in plasma was lower than 15 % for all time points, see Table 6.2 and Figure 6.8 More than 85 % of the radioactivity was found in the hydrophilic fraction, which was injected onto the HPLC. One hydrophilic metabolite, assumed to be ¹⁸F-FBet, appeared in plasma and amounts to 29.3 % 15 min after tracer injection. The fraction of plasma radioactivity contributing to ¹⁸F-FCho decreased to 17.2 %. Phospho-¹⁸F-FCho was detected at low plasma concentrations (2.8 % 15 min after tracer injection). Metabolite correction was applied in the analysis described by a 3-exponential function, including a parent fraction curve. The ¹⁸F-FBet fraction curve was included applying 3C2i.

Table 6.2. Percentage of ^{18}F-FCho metabolites present in arterial plasma.

Time post-injection (min)	Hydrophilic metabolites (%)	Lipophilic metabolites (%)	^{18}F-FCho (%)	^{18}F-FBet (%)	Phospho-^{18}F-FCho (%)	Other metabolites (%)
0	0	0	**100**	**0**	**0**	0
1	86.7 ± 0.5	13.3 ± 0.5	**81.1**	**3.4**	**0.4**	15.2
5	93.4 ± 1.9	6.6 ± 1.9	**62.4**	**2.7**	**2.6**	32.3
15	93.4 ± 0.5	6.7 ± 0.5	**17.2**	**29.3**	**2.8**	21.4
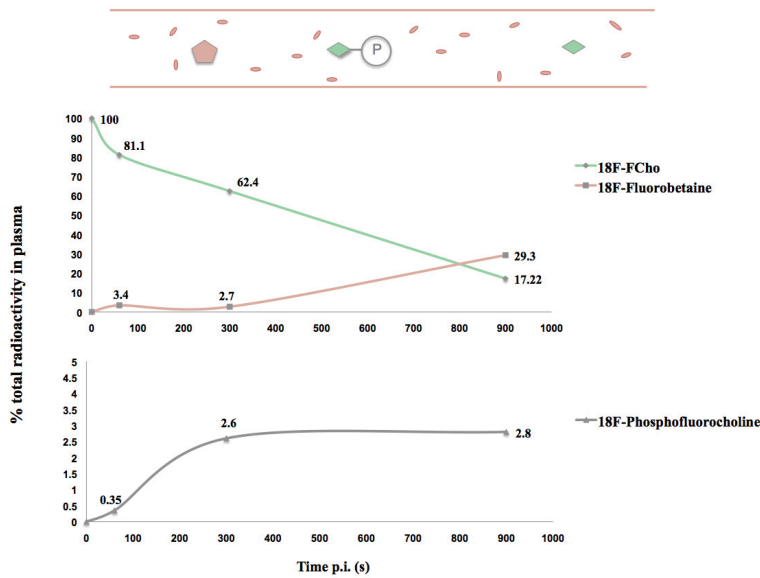
Figure 6.8. Percentage of ^{18}F-FCho metabolites present in arterial plasma.

Chapter 6. ^{18}F-FCho, ^{18}F-FET and ^{18}F-FDG PET for the discrimination between glioblastoma and radiation necrosis in rats.

Kinetic modeling.

Complete results are shown in Figure 6.9 and Table 6.3.

^{18}**F-FDG.** Figure 6.9.A. Plasma glucose level was 3.44 mmol/l. Mean k_2 was significantly higher in RN (0.28 ± 0.03 min^{-1}) compared to GB (0.19 ± 0.04 min^{-1}), while mean k_3 was significantly higher in GB (0.07 ± 0.03 min^{-1}) compared to RN (0.04 ± 0.01 min^{-1}) (p = 0.009 and p = 0.017, respectively). K_1 was not significantly different between GB and RN (p=0.662) and k_4 = 0 min^{-1} gave optimal SE values. Both K_p and K_i were significantly higher in GB compared to RN (p = 0.004 and p = 0.030, respectively).

^{18}**F-FET.** Figure 6.9.B. AIC and SC values were significantly different applying 1C1i compared to 2C1i in GB (both p = 0.05), while no significant difference was found in RN (p = 0.917 and p = 0.754, respectively). Equally, the MSC was only significantly different between 1C1i and 2C1i in GB (p = 0.05). In the RN group 1 MSC outlier value was detected. SEs were as low as possible applying 1C1i, while high values of k_3 SE (%) were found applying 2C1i (not shown). Based on these observations, 1C1i was selected (Table 6.1).
Data from 2 GB rats were excluded because of unreliable data; in one animal due to a blood clot in the venous catheter influencing the AIF and in another lesion due to a complete mismatch of the fitted TAC and the data points in PMOD.
K_1 was significantly higher in GB (0.06 ± 0.01 ml/ccm/min) compared to RN (0.02 ± 0.01 ml/ccm/min) (p = 0.036). k_2 was not significantly different in GB (0.05 ± 0.01 min^{-1}) compared to RN (0.05 ± 0.01 min^{-1}) (p = 0.250). Mean V_d was significantly higher in GB (1.09 ± 0.18 ml/ccm) than in RN (0.53 ± 0.10 ml/ccm) (p = 0.036).

^{18}**F-FCho.** Figure 6.9.C. Visual analysis of the fitted curves revealed comparable fits applying 1C1i and 2C1i, while bad fits were obtained applying 3C2i (not shown). No significant different AIC, SC and MSC values were found between 1C1i and 2C1i in GB and RN. Applying 3C2i, higher AIC and lower MSC were obtained compared to 1C1i/2C1i (Table 6.1). SEs were as low as possible applying 1C1i, while high outlier values were found for k_3 and k_4 applying 2C1i and 3C2i, both in GB and RN. As such, 1C1i was selected. K_1 (0.11 ± 0.03 min^{-1} in GB and 0.10 ± 0.02 min^{-1} in RN) and K_2 (0.05 ± 0.02 min^{-1} in GB and 0.07 ± 0.01 min^{-1} in RN) were not significantly different between GB and RN (p = 0.530 and 0.251, respectively). Consequently, V_d was not significantly different between GB (2.33 ± 1.07 ml/ccm) and RN (1.43 ± 0.37 ml/ccm) (p = 0.117).

Figure 6.9. Kinetic modeling and graphical analysis of ^{18}F-FDG (A), ^{18}F-FET (B) and ^{18}F-FCho (C) in GB and RN.

Table 6.3. Fitting parameters of ^{18}F-FDG, ^{18}F-FET and ^{18}F-FCho in GB and RN

	AICmean*			SCmean†			MSCmean‡			K1 (ml/ccm /min)	k2 (min⁻¹)	k3 (min⁻¹)	Vd§ (ml/ccm)	Vt‖ (ml/ccm)	Ki§ (ml/ccm /min)	Ki¶ (ml/ccm /min)	Kp#	SE** K1 (%)	SE** k2 (%)	SE** k3 (%)
	§§1C1i	2C1i	3C2i	1C1i	2C1i	3C2i	1C1i	2C1i	3C2i	2C1i	2C1i	2C1i	1C1i	Logan	2C1i	Patlak		2C1i	2C1i	2C1i
18F-FDG																				
GB††		28.28			33.34			3.10		0.16	0.19	0.07			0.04	0.04	0.26	4.87	12.50	10.00
RN‡‡		78.88			83.94			1.09		0.17	0.28	0.04			0.02	0.02	0.12	7.10	13.72	13.88
18F-FET	1C1i	2C1i	3C2i	1C1i	2C1i	3C2i	1C1i	2C1i	3C2i	1C1i	1C1i		1C1i	Logan	2C1i	Patlak		1C1i	1C1i	
GB††	30.77	72.01		34.10	104.07		2.64	1.59		1.09	0.05		1.09	1.09	0.01	0.02		3.09	5.32	
RN‡‡	104.07	103.70		75.88	108.65		3.02	1.05		0.53	0.05		0.53	0.52	0.00	0.01		8.39	15.8	
18F-FCho	1C1i	2C1i	3C2i	1C1i	2C1i	3C2i	1C1i	2C1i	3C2i	1C1i	1C1i		1C1i	Logan	2C1i	Patlak		1C1i	1C1i	
GB††	93.89	92.09	145.37	96.39	94.78	119.59	0.20	0.09	-1.90	0.11	0.05		2.33	1.02	0.02	0.05		10.77	145.16	
RN‡‡	91.45	88.56	149.01	93.94	91.31	122.50	0.34	0.49	-1.76	0.10	0.07		1.43	0.96	0.05	0.05		15.61	57.94	

†† Glioblastoma (GB), ‡‡ Radiation necrosis (RN), * Akaike information criterion (AIC), † Schwartz criterion (SC), ‡ Model selection criterion (MSC), § Distribution volume (Vd), ‖ Total distribution volume (Vt), §
Influx rate (Ki), ¶ Slope of the Patlak curve-metabolic flux (Ki), # Phosphorylation rate (Kp), ** Standard error (SE), §§ 1 compartmental model 1 input function (1C1i) - 2 compartmental model 1 input function
(2C1i) - 3 compartmental model 2 input functions (3C2i)

133

Graphical analysis

Complete results are shown in Figure 6.9 and Table 6.3. For a graphical illustration of the results, see Fig 6.10.

^{18}F-FDG. Figure 6.9.A. Visually, a good fit was obtained by Patlak GA. K_i was significantly higher in GB (0.04 ± 0.01 ml/ccm/min) compared to RN (0.02 ± 0.01 ml/ccm/min) (p = 0.017), visible on the parametric maps (first row, Figure 6.10). K_i was strongly correlated with the Patlak slope with a Spearman correlation coefficient of 0.98 (p = 0.01).

^{18}F-FET. Figure 6.9.B. Assuming that ^{18}F-FET is a reversible bound tracer, Logan GA was selected. An acceptable visual fit and SEs were obtained. V_t was significantly higher in GB (1.09 ± 0.20 ml/ccm) than in RN (0.52 ± 0.06 ml/ccm) (p = 0.036). Parametric images showed a heterogeneous increased V_t in GB. In RN, V_t was slightly increased but showed a more homogeneous distribution (second row, Figure 6.10). V_d and V_t were strongly correlated, with comparable values (Spearman's rho = 0.881).

^{18}F-FCho. Figure 6.9.C. Both Patlak and Logan GA were performed. Visually, a better fit was obtained using Logan GA. However, the SEs of K_i were lower than the SEs of V_t. Both K_i (0.05 ± 0.02 ml/ccm/min in GB and 0.05 ± 0.01 ml/ccm/min in RN) and V_t (1.02 ± 0.26 ml/ccm in GB and 0.96 ± 0.20 ml/ccm in RN) were not significantly different between both groups (p = 0.465 and 0.602, respectively) (Table 6.1). Parametric images of V_t showed increased values within GB and RN compared to normal brain tissue (third row, Figure 6.10). K_i (2C1i) and V_d (1C1i) were not correlated with K_i and V_t, with a Spearman's rho of 0.042 and 0.006, respectively.
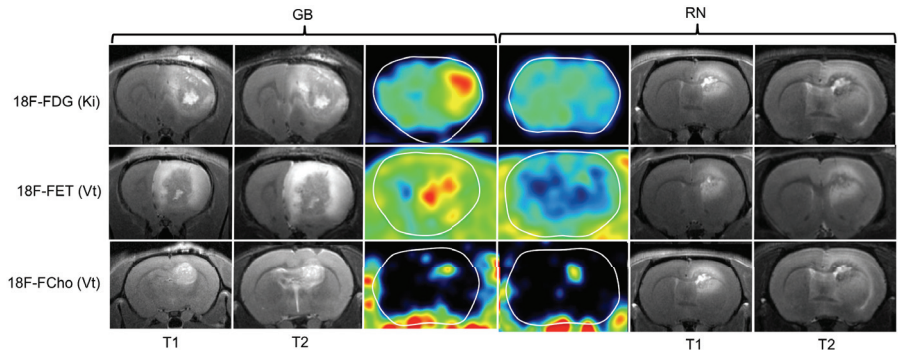

Figure 6.10. **T1- and T2-weighted MRI and parametric maps of the Patlak slope (Ki) and Logan slope (Vt) in GB and RN.** Ki of ^{18}F-FDG (row 1) and Vt of ^{18}F-FET (row 2) were higher in GB than in RN. Vt shows heterogeneously increased values both in GB and RN lesions on ^{18}F-FCho PET (row 3).

Correlation between semi-quantitative and quantitative analysis

Spearman correlations (R_s) between the kinetic/graphical measures and SUV variables were calculated for each tracer. R_s and p values can be found in Table 6.4.

^{18}F-FDG. Both on early and late ^{18}F-FDG PET k_2 was significantly negatively correlated with SUV_{max}, LNR_{mean}, and LNR_{max} (p = 0.038/0.002/0.016 and p = 0.011/0.010/0.015, respectively). K_3 was significantly positively correlated with SUV_{max}, both on the early (p = 0.037) and late (p = 0.006) scan. SUV_{max} was also correlated with K_i and K_p on the early (p = <0.001/0.004) and late (p = 0.033/0.005) ^{18}F-FDG PET scans. Scatterplots of late SUV_{max} correlations can be found in Figure 6.11.A.

^{18}F-FET. SUV_{max}, SUV_{mean}, LNR_{mean} and LNR_{max} were significantly positively correlated with K_1 (p = 0.009/0.009/0.031/0.002) and k_2 (p = 0.007/0.007/0.003/0.022). Scatterplots of SUV_{max} correlations can be found in Figure 6.11.B.

^{18}F-FCho. No significant correlations were found between ^{18}F-FCho SUV variables and kinetic/graphical parameters.

Table 6.4. Spearman correlation coefficients (Rs) between kinetic/graphical measures and SUV

|		SUV_{max}		SUV_{mean}	
		R_s	p	R_s	p
^{18}F-FDG$_{early}$	K_1	0.509	0.110	**0.818**	**0.002**
	k_2	**-0.555**	**0.011**	-0.282	0.401
	k_3	**0.765**	**0.006**	0.565	0.070
	K_p	**0.791**	**0.004**	0.564	0.071
	K_i	**0.873**	**<0.001**	**0.791**	**0.004**
	$K_{i\ Patlak}$	**0.900**	**<0.001**	**0.755**	**0.007**
^{18}F-FDG$_{late}$	K_1	0.406	0.244	0.503	0.138
	k_2	**-0.661**	**0.038**	**-0.685**	**0.029**
	k_3	**0.663**	**0.037**	0.523	0.121
	K_p	**0.806**	**0.005**	**0.697**	**0.025**
	K_i	**0.673**	**0.033**	**0.782**	**0.008**
	$K_{i\ Patlak}$	**0.733**	**0.016**	**0.782**	**0.008**
^{18}F-FET	K_1	**0.838**	**0.009**	**0.838**	**0.009**
	k_2	**0.855**	**0.007**	**0.855**	**0.007**
	V_d	0.024	0.955	0.024	0.955
	$V_{t\ Logan}$	-0.024	0.955	-0.024	0.955
^{18}F-FCho	K_1	0.207	0.567	-0.085	0.815
	k_2	0.261	0.467	0.067	0.854
	V_d	0.006	0.987	-0.085	0.815
	$V_{t\ Logan}$	0.273	0.446	0.006	0.987
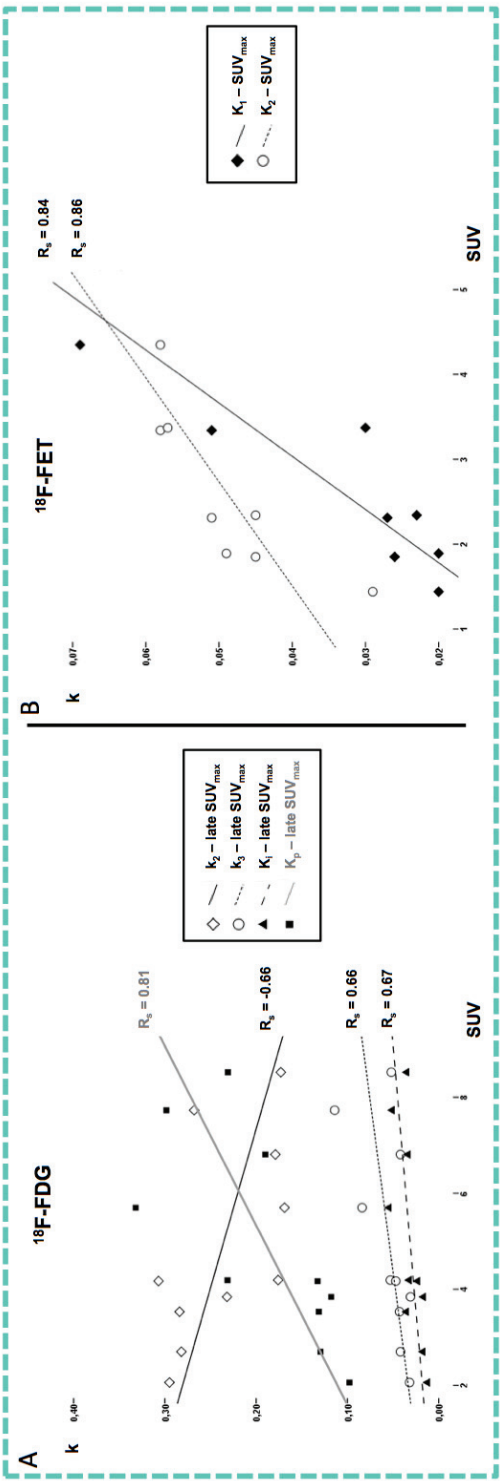
Figure 6.11. Spearman correlation (Rs) scatterplots between kinetic parameters and SUV$_{max}$ for late ^{18}F-FDG and ^{18}F-FET PET. Late ^{18}F-FDG SUV$_{max}$ is negatively correlated with k_2 and positively correlated with k_3, K_i and K_p (A). ^{18}F-FET SUV$_{max}$ is positively correlated with K_1 and k_2 (B).

Evans blue staining

Staining of EB extravasation confirmed BBB breakdown in both GB and RN, see Figure 6.12. No significant differences in TRITC signal were noted between GB (93140.75 ± 16668 gray values) and RN (106519.50 ± 38997 gray values) (p = 0.773). However, in GB, extravasation was present at the perinecrotic rim of the tumor, while in RN the center of the lesion was characterized by BBB breakdown (Figure 6.12).
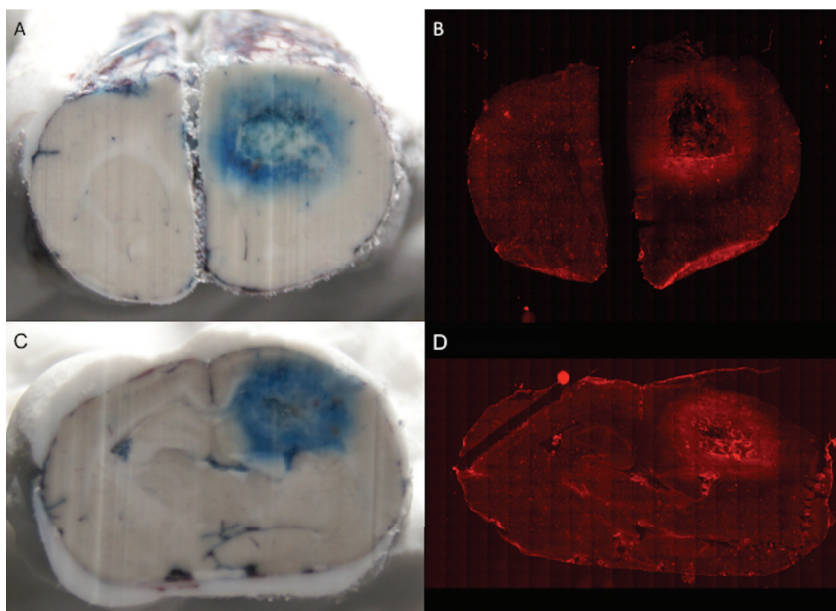

Figure 6.12. Evans blue (EB) extravasation present in glioblastoma (GB) (A and B) and radiation necrosis (RN) (C and D), confirming blood brain barrier breakdown. Cryosected rat brain 1 hour after intravenous injection of EB (A and C) and fluorescent images visualize the extravasation (B and D). Note the difference in extravasation pattern between GB and RN. EB extravasation is absent in the necrotic center of GB, while it is present at the peritumoral edge. In RN, EB extravasation is present in the entire lesion.

DISCUSSION

GB and RN are very different conditions with distinct underlying mechanisms. GB can occur as such or progress from low-grade gliomas. Deregulation of receptor tyrosine kinase signaling and the p53/retinoblastoma tumor suppressor pathway are essential steps in GB pathogenesis [32]. RN is induced by irradiation, which affects the three different types of central nervous system tissue: neurons, glial cells, and blood vessels. Acute vasodilatation, resulting in vasogenic edema, is a primary effect of RT. Subacutely, RT leads to a temporary delay in myelin synthesis, followed by occlusive vasculopathy, demyelination, and active inflammation [33]. Oligodendrocytes and the periventricular region have been shown to be very sensitive to irradiation, while gray matter is less sensitive due to the presence of non-dividing neurons [34]. In our study, RN occurred in the periventricular white matter 5-6 months post-irradiation. Wang et al. also found that RN occurred 5-6 months after irradiation, however in their study, irradiation was given to 10×10 mm^2 normal brain tissue using the SARRP with a single dose of 40 Gy [35]. Irradiation using a linear accelerator (6 MV) with a dose of 40-60 Gy has been shown to induce RN after 3 months [36] or after 2.5 months when radiosurgery (60 Gy in one fraction) was applied [37]. Acute RN has been noted 12-20 days and 2 months post-irradiation using a proton beam of 250 Gy and 150 Gy, respectively [38]. Theoretically, the dose required to cause a certain level of radiation damage is lower for low-energy kV x-rays than for MV x-rays [39]; however, the irradiated brain region and volume play a role in the temporal evolution of RN [40].

While GB and RN have clearly different histological characteristics, conventional MRI usually cannot reliably differentiate between these two entities [8]. Gadolinium, used for contrast-enhanced T1-weighted MRI, can leak out of vessels due to BBB breakdown in both GB and RN. Therefore, true progression cannot be differentiated from so-called pseudo-progression, which occurs within 2-5 months after receiving RT and chemotherapy in 15-20 % of patients. Unlike true tumor progression, pseudo-progression can resolve without additional treatment [41]. PET imaging using ^{18}F-FDG, ^{18}F-FCho, and ^{18}F-FET may help to differentiate between GB and RN, however, these tracers have generally been evaluated in clinical studies that lack pathological confirmation of either tumor recurrence or RN. Therefore, in this *in vivo* study, we investigated the differential uptake of these tracers by RN and GB.

We found significant higher values for SUV$_{max}$, SUV$_{mean}$, LNR$_{mean}$ and LNR$_{max}$ in GB compared to RN on early ^{18}F-FDG PET images (40 minutes after tracer injection) and late ^{18}F-FDG PET images (240 minutes after tracer injection). However, the difference in LNR$_{mean}$ and LNR$_{max}$ between GB and RN was higher on the delayed PET scan compared to the conventional PET scan. This finding suggests that, in the clinic, a late ^{18}F-FDG PET acquisition may be sufficient to discriminate between GB and RN. It should also be noted that, unlike the PET tracers ^{18}F-FET and ^{18}F-FCho, ^{18}F-FDG is commercially available, which is a major advantage for use in the clinic. Uptake of ^{18}F-FDG in GB was high due to a high cell proliferation rate. In RN, uptake of ^{18}F-FDG was high due to BBB breakdown and inflammation [10,38]. However, because uptake of ^{18}F-FDG is also high in normal grey matter, the uptake in RN was not distinguishable from the surrounding normal tissue.

SUV_{max}, SUV_{mean}, LNR_{mean} and LNR_{max} in ^{18}F-FET PET were also significantly higher in GB than in RN. These results are in agreement with those of Spaeth et al. [10]. The low uptake in RN is probably due to negligible uptake of ^{18}F-FET in inflammatory cells [10,38], whereas the high uptake in high-grade tumors is a result of high expression of amino acid transporters [7].

For ^{18}F-FCho PET, no significant differences were found in SUV_{max}, SUV_{mean}, LNR_{mean} and LNR_{max} between GB and RN, indicating that this tracer is not effective in discriminating between GB and RN. This may be due to the high ^{18}F-FCho uptake by macrophages in RN [38]. These results are in contrast with a previous study by Spaeth et al. who found a significant difference in uptake of ^{18}F-FCho between GB and RN using autoradiography [10,38]. A possible explanation is that the inflammatory response is more pronounced in delayed RN lesions, as in our model, than in acute RN lesions as described in the work by Spaeth et al. [10,13,33,38].

To clarify the above-mentioned results, we further explored the uptake mechanisms of the three tracers using KM and GA. KM is the most accurate method to analyze PET but required ABS and AIF corrections [15]. No metabolite correction was applied for ^{18}F-FDG and ^{18}F-FET because both are metabolically relatively stable *in vivo*. The percentage of intact ^{18}F-FET of total plasma radioactivity is 95 %, 5 min after tracer injection, and 87 %, 120 min after tracer injection, indicating that the fraction of metabolites is low [7]. For ^{18}F-FCho, metabolite correction was necessary due to the known oxidation of choline in hepatocytes and nephrocytes to betaine, which is an important donor of methyl groups for synthesis of methionine and serves as an osmolyte (Figure 6.3) [27,42,43]. This side reaction complicates data interpretation of ^{18}F-FCho PET.

A major factor influencing uptake in RN and GB is passive leakage through a damaged BBB, present in GB due to its aggressive nature and in RN due to irradiation endothelial cell damage [33]. Large molecule permeability at the BBB was confirmed by IV injection of EB, which relies on the selective binding of EB to native albumin, rapidly producing a 68 kDa compound that does not cross the BBB [44,45]. Our results confirmed the presence of BBB breakdown both in GB and RN. The amount of EB extravasation, measured by the TRITC fluorescent signal, was not different between GB and RN, however, and more importantly, a different pattern of EB extravasation was noted in these two conditions. In GB, EB extravasation was absent in the necrotic center, while it was present at the peritumoral edge where viable tumor cells are infiltrating the normal brain parenchyma. In RN, EB extravasation was present throughout the entire lesion. This BBB breakdown will influence K_1, which accounts for both the transport of the tracer from the blood to the interstitial space and the uptake from the interstitial space into the cell by certain transporters. However, K_1 is not able to differentiate between passive leakage and uptake by a transport mechanism [13].

A 2C1i was also applied to model uptake of ^{18}F-FDG in GB and RN, K_1 was not significantly different in GB and RN. Therefore, we cannot conclude that there is a higher amount of GLUT in GB compared to RN. It should be mentioned that the contribution of passive diffusion of ^{18}F-FDG due to BBB breakdown

is unknown. However, we hypothesize that K_1 in GB, influenced by the cerebral blood flow, cerebral blood volume, GLUT transport and disrupted BBB, is comparable to the K_1 in RN, predominantly influenced by severe BBB disruption. Phosphorylation of ^{18}F-FDG by hexokinase (k_3/K_p) was significantly higher in GB compared to RN while outward transportation of non-phosphorylated tracer (k_2) was higher in RN than in GB. This implies a higher influx rate in GB. Using Patlak analysis, K_i was also higher in GB. Furthermore, SUV_{max} was positively correlated with k_3, K_p, K_i and the Patlak slope. A negative correlation was found between SUV_{max} and k_2, which might indicate that the differences in SUV_{max} are related to differences in both k_2 and k_3. A higher k_2 in RN compared to GB could be due to the severe vascular damage leading to a faster wash-out. Based on these results trapping of ^{18}F-FDG predominantly occurs in GB and quantification is possible using KM or GA, however, GA is not able to discriminate K_1 from k_3 [15].

Based on the SEs, 1C1i was selected for absolute quantification of ^{18}F-FET uptake in GB and RN. This was assumed based on the Na$^+$-independent route of FET transport via LAT and the Na$^+$-dependent activity via system B$^{0,+}$ and B^0. Since large neutral amino acids enter normal brain tissue, disruption of BBB is not a prerequisite for intratumoral ^{18}F-FET accumulation [7,46]. K_1, V_d and V_t were significantly higher in GB compared to RN, probably by the presence of more LAT, B$^{0,+}$ and B^0 transporters in GB. Clinical results in different tumor types indicate that transport mechanisms of FET may be more complex and one may speculate that FET is selectively transported by LAT2 [10]. A different K_1 between GB and RN might also relate to differences in cerebral blood flow and cerebral blood volume, which is known to be higher in GB due to neoangiogenesis. An equal amount of ^{18}F-FET efflux (k_2) between GB, mediated by the LAT antiporter and partially leakage, and RN, mediated by mainly leakage, was shown. Both K_1 and k_2 were positively correlated with SUV_{max}, which could be explained by the antiporter function of the amino-acid transporter. The significant correlations found between SUV and quantitative measures could indicate that SUV captures the differences in K_1 and k_2 (Table 6.4). Although, KM allowed the absolute quantification and better characterization of ^{18}F-FDG and ^{18}F-FET uptake in GB and RN, taking into account the TACs in Figure 6.7 and based on our previous results [9], it appears that a static image 40 min after tracer injection was also able to differentiate GB and RN.

A 2C1i-model was expected to be used for the absolute quantification of ^{18}F-FCho uptake due to the presumed phosphorylation of ^{18}F-FCho with subsequent incorporation in cellular membranes [22,23]. The percentage ^{18}F-FCho in plasma decreased rapidly concomitant with the appearance of a hydrophilic metabolite, most likely ^{18}F-FBet (Figure 6.8). Phosphatidylcholine is the most important metabolite of choline. In the mitochondria of liver and kidney choline is oxidized to betaine [27]. Choline is also a precursor of the neurotransmitter acetylcholine. Acetylcholine could also be synthesized and released from non-neuronal cells, however, its role outside of neurons is not clearly defined [43]. Uptake of choline radiotracers by muscle is low, however, an increase has been shown by Bansal et al. over the first 20 min post-injection, most likely reflecting uptake of betaine metabolites [27]. However, the percentage of total plasma radioactivity attributed to ^{18}F-FBet was lower compared to the literature [23,27,42]. Verwer et al. suggested that this fast metabolization could play a role in the inability of KM to accurately

distinguish between the first compartment (K_1 and k_2), and signal originating from blood volume in the VOI, and between K_1 and k_3 [14]. It was also suggested that K_1, partly determined by angiogenesis and microvessel density, and not the phosphorylation (k_3) was the key factor for choline uptake [22]. These assumptions are in favor of a 1C1i model. Recently, 1C1i with metabolite-corrected AIF was proposed for quantifying ¹⁸F-FCho uptake in prostate cancer [22]. In this study, quantification of ¹⁸F-FCho uptake reached optimal fitting using a reversible model. However, K_1 and V_t were not significantly different between GB and RN. As such, we cannot conclude that there is an increased choline transporter-like proteins mediated transport or a higher expression of choline kinase in GB compared to RN. Unfortunately, due to the inability of differentiating K_1 and k_3, the amount of ¹⁸F-FCho uptake mediated by leakage through the damaged BBB or active trapping was not possible. Only uptake by passive diffusion was negligible due to its polar characteristics [22]. Furthermore, the immediate metabolization raises the question if leakage of ¹⁸F-FBet through the damaged BBB played a role. Probably a more metabolically stable ¹⁸F-labeled choline tracer would overcome this fast oxidation problem [47]. As such, although ¹⁸F-FCho seemed promising for differentiation of tumor recurrence and RN in the clinic [11,48], this was not confirmed in our pre-clinical study. However, we should keep in mind that the metabolism of choline tracers in humans is slower than in rodents and that the uptake was only investigated in one glioma model [14,26,42,47].

Conclusion

Using a 2C1i model, more trapping of ¹⁸F-FDG ($k3$) was found in GB compared to RN. Secondly, the influx of ¹⁸F-FET was higher in GB compared to RN using a 1C1i model. Important correlations were found between SUV and kinetic or graphical measures for ¹⁸F-FDG and ¹⁸F-FET. Based on these results we assume that SUV is able to capture kinetic differences. For ¹⁸F-FCho, a 1-compartmental model is suggested for absolute quantification, but does not allow clarifying the uptake mechanism in GB and RN.

REFERENCES

[1] Brandes AA, Tosoni A, Spagnolli F, et al. Disease progression or pseudoprogression after concomitant radiochemotherapy treatment: Pitfalls in neurooncology. Neuro-oncology 2008;10:361-367.

[2] Langleben DD, Segall GM. PET in differentiation of recurrent brain tumor from radiation injury. Journal of Nuclear Medicine 2000;41:1861-1867.

[3] Van Laere K, Ceyssens S, Van Calenbergh F, et al. Direct comparison of 18F-FDG and 11C-methionine PET in suspected recurrence of glioma: sensitivity, inter-observer variability and prognostic value. European Journal of Nuclear Medicine and Molecular Imaging 2005;32:39-51.

[4] Chao ST, Suh JH, Raja S, et al. The sensitivity and specificity of FDG PET in distinguishing recurrent brain tumor from radionecrosis in patients treated with stereotactic radiosurgery. International Journal of Cancer 2001;96:191-197.

[5] Ricci PE, Karis JP, Heiserman JE, et al. Differentiating recurrent tumor from radiation necrosis: time for re-evaluation of positron emission tomography? American Journal of Neuroradiology 1998;19:407-413.

[6] Kim YH, Oh SW, Lim YJ, et al. Differentiating radiation necrosis from tumor recurrence in high-grade gliomas: assessing the efficacy of 18F-FDG PET, 11C-methionine PET and perfusion MRI. Clinical Neurology and Neurosurgery 2010;112(9):758-765.

[7] Langen KJ, Hamacher K, Weckesser M, et al. O-(2-[18F]fluoroethyl)-l-tyrosine: uptake mechanisms and clinical applications. Nuclear Medicine and Biology 2006;33:287-294.

[8] Pöpperl G, Götz C, Rachinger W, et al. Serial 0-(2- (18F)fluoroethyl)-L-tyrosine PET for monitoring the effects of intracavitary radioimmunotherapy in patients with malignant glioma. European Journal of Nuclear Medicine and Molecular Imaging 2006;33:792-800.

[9] Bolcaen J, Descamps B, Deblaere K, et al. 18F-fluoromethylcholine (FCho), 18F-fluoroethyltyrosine (FET), and 18F-fluorodeoxyglucose (FDG) for the discrimination between high-grade glioma and radiation necrosis in rats: A PET study. Nuclear Medicine and Biology 2014;42(1):38-45.

[10] Spaeth N, Wyss MT, Pahnke W, et al. Uptake of 18F-fluorocholine, 18F-fluoro-ethyl-L-tyrosine and 18F-fluoro-2-deoxyglucose in F98 gliomas in the rat. European Journal of Nuclear Medicine and Molecular Imaging 2006;33:673-682.

[11] Tan H, Chen L, Guan Y, et al. Comparison of MRI, F-18 FDG, and 11C-Choline PET/CT for Their Potentials in Differentiating Brain Tumor Recurrence From Brain Tumor Necrosis Following Radiotherapy. Clinical Nuclear Medicine 2011;36:978-981.

[12] DeGrado TR, Coleman RE, Wang S, et al. Synthesis and evaluation of 18F-labeled choline as an oncologic tracer for positron emission tomography: initial findings in prostate cancer. Cancer Research 2001;61(1):110-117.

[13] Galldiks N, Langen KJ, Holy R, et al. Assessment of treatment response in patients with glioblastoma using O-(2-18F-fluoroethyl)-L-tyrosine PET in comparison to MRI. Journal of Nuclear Medicine 2012;53:1048-1057.

[14] Verwer EE, Oprea-Lager DE, van den Eertwegh AJM, et al. Quantification of 18F-fluorocholine kinetics in patients with prostate cancer. Journal of Nuclear Medicine 2015;56:365-371.

[15] Tomasi G, Turkheimer F, Aboagye E. Importance of quantification for the analysis of PET data in oncology: review of current methods and trends for the future. Molecular Imaging and Biology 2012;14:131-146.

[16] Dimitrakopoulou-Strauss A, Pan L, Strauss LG. Quantitative approaches of dynamic FDG-PET and PET/CT studies (dPET/CT) for the evaluation of oncological patients. Cancer Imaging 2012;12(1):283-289.

[17] Young H, Baum R, Cremerius U, et al. Measurement of clinical and subclinical tumour response using [18F]-fluorodeoxyglucose and Positron Emission Tomography: review and 1999 EORTC Recommendations. European Journal of Cancer 1999;35(13):1773-1782.

[18] Kimura N, Yamamoto Y, Kameyama R, et al. Diagnostic value of kinetic analysis using dynamic 18F-FDG-PET in patients with malignant primary brain tumor. Nuclear Medicine Communications 2009;30(8):602-609.

[19] Patlak CS, Blasberg RG. Graphical evaluation of blood-to-brain transfer constants from multiple-time uptake data. Generalizations. Journal of Cerebral Blood Flow and Metabolism 1985;5(4):584-590.

[20] Weber W, Schwaiger M, Avril N. Quantitative Assessment of Tumor Metabolism Using FDG-PET Imaging. Nuclear Medicine and Biology 2000;27:683-687.

[21] Thiele F, Ehmer J, Piroth MD, et al. The quantification of dynamic FET PET imaging and correlation with the clinical outcome in patients with glioblastoma. Physics in Medicine and Biology 2009;54:5525-5539.

[22] Takesh M. Kinetic modeling application to 18F-fluoroethylcholine positron emission tomography in patients with primary and recurrent prostate cancer using two-tissue compartmental model. World Journal of Nuclear Medicine 2013;12(3):101-110.

[23] Slaets D, De Vos F. Comparison between kinetic modelling and graphical analysis for the quantification of [18F] fluoromethylcholine uptake in mice. European Journal of Nuclear Medicine and Molecular Imaging 2013;3:66.

[24] Convert L, Morin-Brassard G, Cadorette J, et al. A new tool for molecular imaging: the microvolumetric β blood counter. Journal of Nuclear Medicine 2007;48:1197-1206.

[25] Moerman L, De Naeyer D, Boon P, et al. P-glycoprotein at the blood-brain barrier: kinetic modeling of 11C-desmethylloperamide in mice using a 18F-FDG PET scan to determine the input function. European Journal of Nuclear Medicine and Molecular Imaging 2011;1:12.

[26] Weber B, Burger C, Biro P, Buck A. A femoral arteriovenous shunt facilitates arterial whole blood sampling in animals. European Journal of Nuclear Medicine 2002;29(3):319-323.

[27] Bansal A, Shuyan W, Toshiko H, et al. Biodisposition and metabolism of [18F]fluorocholine in 9L glioma cells and 9L glioma-bearing fisher rats. European Journal of Nuclear Medicine and Molecular Imaging 2008;35:1192-1203.

[28] Muzi M, Freeman SD, Burrows RC, et al. Kinetic characterization of hexokinase isoenzymes from glioma cells: Implications for FDG imaging of human brain tumors. Nuclear Medicine and Biology 2001;28:107-116.

[29] Leten C1, Struys T, Dresselaers T, et al. In vivo and ex vivo assessment of the blood brain barrier integrity in different glioblastoma animal models. Journal of Neurooncology 2014;119(2):297-306.

[30] Schneider CA, Rasband WS, Eliceiri KW. NIH Image to ImageJ: 25 years of image analysis. Nature Methods 2012; 9:671-675.

[31] Mertens K, Ham H, Deblaere K, et al. Distribution patterns of 18F-labelled !uoromethylcholine in normal structures nand tumors of the head: a PET/MRI evaluation. Clinical Nuclear Medicine 2012;37(8):196-203.

[32] The Cancer Genome Atlas Research Network. Comprehensive genomic characterisation defines human glioblastoma genes and core pathways. Nature 2008;455(7216):1061-1068.

[33] Rahmathulla G, Marko NF, Weil RJ. Cerebral radiation necrosis: a review of the pathobiology, diagnosis and management considerations. Journal of Clinical Neuroscience 2013;20(4):485-502.

[34] Yoshii Y. Pathological review of late cerebral radionecrosis. Brain Tumor Pathology 2008;25:51-8.

[35] Wang S, Tryggestad E, Zhou T, et al. Assessment of MRI parameters as imaging biomarkers for radiation necrosis in the rat brain. International Journal of Radiation Oncology Biology Physics 2012;83(3):431-436.

[36] Hideghety K, Plangár I, Mán I, et al. Development of a small-animal focal brain irradiation model to study radiation injury and radiation-injury modifiers. International Journal of Radiation Biology 2013; 89(8):645-655.

[37] Kumar S, Arbab AS, Jain R, et al. Development of a novel animal model to differentiate radiation necrosis from tumor recurrence. Journal of Neurooncology 2012; 108(3):411-420.

[38] Spaeth N, Wyss MT, Weber B, et al. Uptake of 18F-fluorocholine, 18F-fluoroethyl-L-tyrosine, and 18F-FDG in acute cerebral radiation injury in the rat: implications for separation of radiation necrosis from tumor recurrence. Journal of Nuclear Medicine 2004;45:1931-1938.

[39] Verhaegen F, Granton P, Tryggestad E. Small animal radiotherapy research platforms. Physics in Medicine and Biology 2011; 56:R55-83.

[40] Ruben JD, Dally M, Bailey M, et al. Cerebral radiation necrosis: incidence, outcomes, and risk factors with emphasis on radiation parameters and chemotherapy. International Journal of Radiation Oncology Biology Physics 2006;65(2):499-508.

[41] Siu A, Wind JJ, Iorgulescu B, et al. Radiation necrosis following treatment of high grade glioma-a review of the literature and current understanding. Acta Neurochirurgica 2012;154:191-201.

[42] Roivainen A, Forsback S, Grönroos T, et al. Blood metabolism of [methyl-11C]choline; implications for in vivo imaging with positron emission tomography. European Journal of Nuclear Medicine 2000;27(1):25-32.

[43] Michel V, Yuan Z, Ramsubir S, et al. Choline transport for phospholipid synthesis. Experimental Biology Medicine 2006;231:490-504.

[44] Hawkins BT, Egleton RD. Fluorescence imaging of blood-brain barrier disruption. Journal of Neuroscience Methods 2006; 15:1262-1267.

[45] Rapoport SI. Osmotic Opening of the Blood–Brain Barrier: Principles, Mechanism, and Therapeutic Applications. Cellular and Molecular Neurobiology 1998;20(2):217-230.

[46] Habermeier A, Graf J, Sandhöfer BF, et al. System L amino acid transporter LAT1 accumulates O-(2-fluoroethyl)-L-tyrosine (FET). Amino Acids 2015;47(2):335-344.

[47] Challapali A, Sharma R, Hallett WA, et al. Biodistribution and radiation dosimetry of deuterium-substituted 18F-fluoromethyl-[1,2-^{2}H$_4$]choline in healthy volunteers. Journal of Nuclear Medicine 2014;55(2):256-263.

[48] Kwee SA, Ko JP, Jiang CS, et al. Solitary Brain Lesions Enhancing at MR Imaging: Evaluation with Fluorine 18–Fluorocholine PET. Radiology 2007;244(2):557-565.

Chapter 7.

In vivo DCE-MRI for the discrimination between glioblastoma and radiation necrosis in rats.

This chapter includes data from:

Julie Bolcaen M.Sc.[1], Benedicte Descamps M.Sc Ph.D.[2], Marjan Acou M.D.[3], Karel Deblaere M.D. Ph.D.[3], Caroline Van den Broecke M.D.[4], Tom Boterberg M.D. Ph.D[5], Christian Vanhove Eng. Ph.D.[2], Ingeborg Goethals M.D. Ph.D.[1]

[1]*Department of Nuclear Medicine, Ghent University Hospital*
[2]*IBiTech - MEDISIP - Department of Electronics and Information Systems, Ghent University*
[3]*Department of Radiology, Ghent University Hospital*
[4]*Department of Pathology, Ghent University Hospital*
[5]*Department of Radiation Oncology, Ghent University Hospital*

De Pintelaan 185, 9000 Gent, Belgium

Chapter 7. _In vivo_ DCE-MRI for the discrimination between glioblastoma and radiation necrosis in rats.

INTRODUCTION

Following the incorporation of irradiation and adjuvant chemotherapy in the treatment of glioblastoma (GB), the number of (late) treatment-related side effects, such as radiation necrosis (RN), has increased and ranges from 3 to 24 %, see Chapter 1 [1,2]. Differentiation between therapy-related effects and high-grade brain tumor recurrence may present a diagnostic dilemma because both entities may have similar appearance on conventional magnetic resonance imaging (MRI) [3-8]. A correct diagnosis is important for patient management because tumor recurrence requires second-line chemotherapy while for the treatment of RN steroids may suffice [9,10]. A definite diagnosis can be achieved by a brain biopsy, which is invasive and may lead to potential complications such as brain hemorrhage [11]. Hence, advanced imaging modalities are needed in addition to mere structural information.

Many studies have previously investigated the potential of positron emission tomography (PET) for the differentiation between brain tumor and RN [12-19]. Equivocal results have been published for ^{18}F-FDG with sensitivities and specificities ranging from 40 to 100 % [6,7,20-23]. High sensitivities and specificities were found for ^{18}F-fluoroethyltyrosine (^{18}F-FET) and 3,4-dihydroxy-6-[^{18}F]-fluoro-l-phenylalanine (^{18}F-FDOPA) PET [10,11]. In chapter 6 we also investigated the potential of ^{18}F-fluorodeoxyglucose (^{18}F-FDG), ^{18}F-FET and ^{18}F-fluoromethylcholine (^{18}F-FCho) in the discrimination of GB and RN, with good results for ^{18}F-FDG, preferably acquired at a delayed time point, and ^{18}F-FET.

Advanced MRI techniques (see Chapter 2) are also under investigation. Using diffusion-weighted MRI (DWI-MRI), higher apparent diffusion coefficients (ADC) were found in RN compared to tumor recurrence due to an increase in water in the interstitial spaces as a result of cell necrosis [24]. Choline/Creatine and Choline/N-acetylaspartate ratios as measured by MR spectroscopy (MRS) may also add valuable information in differentiating recurrent tumor from RN, and even a higher diagnostic accuracy was achieved when combining DWI with MRS [24,25]. Perfusion-weighted MRI (PWI-MRI), such as dynamic susceptibility contrast enhanced MRI (DSC-MRI), was found to distinguish tumor recurrence from RN by using cerebral blood volume (CBV) maps [26,27-29]. Furthermore, the use of the amide proton transfer MRI signal of endogeneous cellular proteins and peptides as an imaging biomarker has been shown to be able to differentiate viable glioma and RN in rats [6]. Although advanced MRI techniques may yield promising results, a major disadvantage is the current lack of standardization and validation which hampers the translation into the clinic. Therefore we investigated the potential of dynamic contrast enhanced MRI (DCE-MRI) in a rat model with confirmed GB or RN.

DCE-MRI is a method to estimate vascular permeability by measuring contrast medium leakage through the blood brain barrier (BBB). In Chapter 2 DCE-MRI and semi-quantitative and quantitative DCE-MRI analysis was introduced. Importantly, compared with DSC-MRI, DCE-MRI is less susceptible to artifacts associated with surgery and its high spatial resolution allows an accurate and more straightforward characterization of the vascular microenvironment of a post-treatment brain tumor [27]. Because vascular properties, such as vascular density, vascular permeability, blood flow, composition of the extracellular

and extravascular space (EES) and interstitial pressure are different between GB and RN, we hypothesized that DCE-MRI would allow to distinguish viable GB from RN [30]. So far, only a few studies have shown the potential of DCE-MRI to differentiate between treatment-related changes and tumor progression in high-grade glioma based on K_{trans}, plasma volume (V_p), initial area under the signal intensity-time curve (iAUC), CBV or model-free semi-quantitative indices [27,31-35]. In this study, we analyzed dynamic (semi-) quantitative curve parameters and contrast agent concentration changes using pharmacokinetic modeling (quantitative parameters) in a histologically confirmed GB and RN rat model.

MATERIALS AND METHODS

Rat models

Our group previously selected the orthotopic F98 GB rat model because it simulates the behavior of human GB [36]. Full details of the protocol can be found in chapter 5 [12,37]. F98 GB cells were stereotactically inoculated at a depth of 3 mm into the brain of 15 female Fischer F344 rats (Charles River®).

Induction of RN in normal brain tissue of ten female Fischer F344 rats was achieved using the small animal radiation research platform (SARRP, Xstrahl®, Surrey, UK) as previously described in chapter 6 [12]. A high-resolution treatment planning computed tomography (CT) scan was performed. The isocenter for the induction of a RN lesion was positioned in the right frontal region on coronal, axial and sagittal slices. Three arcs were used, one covering an angle of 90° (couch angle 0°) and two covering angles of 60° (couch angles 45° and 90°), to deliver 60 Gy in a single dose using a 3 × 3 mm collimator, see Figure 7.1. During irradiation, the voltage of the X-ray source was set to 220 kV with a tube current of 13 mA. A copper filter (0.15 mm) was used.

The study was approved by the Ghent University ethics committee for animal experiments (ECD 12/28).
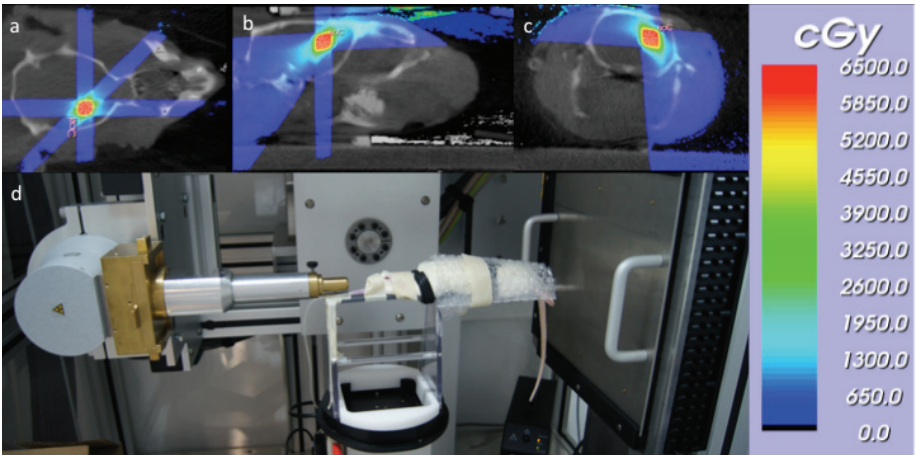

Figure 7.1. a-c: Dose plan for delivery of 60 Gy using 3 arc beams and a 3*3 mm collimator for the induction of RN. The isocenter was selected on coronal (a), sagittal (b) and axial (c) CT slices. Irradiation was performed using the SARRP system (d).

DCE-MRI

For MR imaging, a 7 tesla dedicated small animal MRI (PharmaScan 70/16, Bruker BioSpin, Ettlingen, Germany) was used. Serial MRI was done twice weekly from 8 days post-inoculation to detect tumor growth in GB rats or to detect radiation-induced brain tissue damage from 5 months post-irradiation onwards. The rats were anesthetized with 2 % isoflurane mixed with oxygen administered at a low rate of 0.3 L/min through a nose cone connected onto the animal holder. A heated blanket was placed on the animal. After fixation of the animal, a rat brain surface coil (Rapid Biomedical, Rimpar, Germany) was placed around the head. The holder was positioned in a 72 mm rat whole body transmitter coil (Rapid Biomedical, Rimpar, Germany). A localizer scan was performed followed by a T2-weighted spin-echo scan (TR/TE 3661/37.1 ms, 109 μm isotropic in plane resolution, 4 averages, TA 9'45'') to localize the tumor or the RN lesion. If GB or RN was seen on the T2-weighted images (Figure 7.2.a and 7.2.e), a DCE-MRI scan was acquired during 12 min using a fast low angle shot (FLASH) sequence in a single slice (1 mm slice thickness) with an in-plane spatial resolution of $(312\ \mu m)^2$ and a temporal resolution of 1.34 s (Figure 7.2.c and 7.2.d, GB and 7.2.g and 7.2.h, RN). Gadolinium-containing contrast agent (Dotarem, Guerbet, France; 0.4 mL/kg) was injected intravenously. For this purpose, a 30-Gauge needle connected to a 60 cm long tube was inserted intravenously into the tail vein. The DCE-MRI acquisition was started and after 30 s the gadolinium-containing contrast agent was injected. Following DCE-MRI, a contrast enhanced T1-weighted spin-echo sequence (TR/TE 1539/9.7 ms, 117 μm isotropic in plane resolution, 3 averages, TA 4'15'') was performed (Figure 7.2.b and 7.2.f).
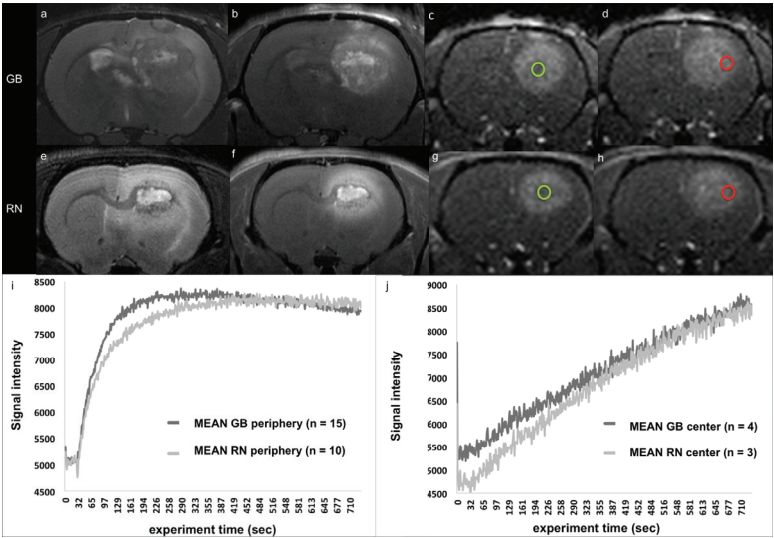

Figure 7.2. Both GB and RN are heterogeneously hyperintense on T2-weighted MR images (a, e). T1-weighted contrast enhanced MRI (b) shows a heterogeneously contrast enhancing tumor with relatively low-enhancing viable tumor cells at the outer rim of the lesion and high contrast enhancement in the center of the tumor corresponding to tumor necrosis. In late RN, a similar contrast enhancement pattern is observed (f). DCE-MRI images 6 min post-injection (c, g) show no visible contrast uptake in the center of the tumor or RN lesion. DCE-MRI images at the end of a 12-min acquisition (d, h) show equal high contrast uptake in all parts of the lesions. DCE-MR signal intensity within ROIs placed at the periphery of the lesion (red circle) and in the center of the lesion (green circle) was plotted as a function of time (raw data curves: i, j). In GB, the slope of the first exponential part is higher than in RN, reaching the maximal intensity faster than in RN.

Semi-quantitative DCE-MRI analysis

Region of interest (ROI) selection was done manually using OsiriX (Pixmeo Sarl®, v.3.9 64-bit) encompassing peripheral contrast enhancement within the lesion (GB, n = 15 and RN, n = 10) (see red ROI in Figure 7.2.d and 7.2.h). In 4 GB and 3 RN lesions, tumor necrosis or irradiation-induced necrosis was also present. In these cases, an extra ROI was manually placed in the center of the lesion (see green ROI in Figure 7.2.c and 7.2.g). The raw time series of the DCE-MRI curve within the ROIs located in the peripheral contrast enhancing part of GB and RN (initial exponential increase followed by a linear decrease in signal enhancement) were fitted to the function:

$$f(t) = C + A\left(1 - e^{-kt}\right) - Dt$$

The raw time series of the DCE-MRI curves located in the center of the lesions (exponential increase in signal enhancement only) were fitted to the function:

$$f(t) = C + A\left(1 - e^{-kt}\right)$$

Fitting was done using the solver add-in of Excel (Mac 2011, version 14.1.0). From these functions, the amplitude A, the offset from zero C, the wash-in rate of the contrast agent, represented by k, and the wash-out rate of the contrast agent, represented by D were derived. Furthermore, the maximal intensity ($Imax_F$) and the time-to-peak of the fitted curve were determined (TTP_F).

A second method for obtaining semi-quantitative DCE-MRI parameters was applied using the permeability module of the Olea Sphere® software (O). Importantly, this software is approved for clinical use. The software allows the calculation of qualitative maps extracting parameters directly from the signal curve: wash-in$_O$, wash-out$_O$, AUC_O, TTP_O and $Imax_O$.

Quantitative DCE-MRI analysis

The permeability module of the Olea Sphere® software was used for quantifying permeability maps derived from a 2-compartment tracer kinetic modeling analysis. Motion correction and spatial filtering (based on wavelet analysis) was applied. The arterial input function (AIF) was selected manually in the carotid artery (Figure 7.5). The extended Tofts model was applied to calculate the quantitative permeability maps of K_{trans} (rate constant for transfer of contrast agent from plasma to extravascular, extracellular space (EES)), K_{ep} (rate constant for transfer of contrast agent from EES to plasma), Vp (plasma volume) and Ve (fractional volume of EES) in the contrast-enhancing parts of GB and RN lesions as well as in necrosis in the center of these lesions. Semi-quantitative and quantitative DCE-MRI parameters were compared between the contrast-enhancing parts of GB and RN as well as between necrotic parts in the center of the lesions using the Mann-Whitney U test. Furthermore, ROC analysis was performed to define the optimal cut-off value for discriminating GB from RN. Correlations between all parameters were calculated using the non-parametric Spearman correlation test.

CD34 staining

For hematoxylin and eosin (H&E) staining of GB and RN, a rat brain with confirmed RN and GB on MRI was dissected and instantly frozen in isopentane (VWR®) cooled by liquid nitrogen for 2 min, followed by 30 min incubation at -20 °C. The brains were then cut into 20 μm serial sections using a cryostat (Leica®, CM30505). For CD34 staining, paraffin sections were used from a rat brain with confirmed RN on MRI. After euthanasia (lethal dose of pentobarbital sodium of 160 mg/kg), the brain was isolated, immersed for 24 h in 4 % paraformaldehyde, embedded in paraffin and the region including the necrotic lesion was cut into 5 μm slices. An indirect biotin-free system was used for immunostaining. Sections were immunolabeled for 28 min with mouse anti-CD34 antibody (QBend10, 1/10, Dako®) and 8 min with horse radish peroxidase-conjugated antibodies (ultraView universal HRP Multimer, Ventana®). Sections were immersed for 8 min in DAB (Ventana®), followed by a 8 min counterstaining with haematoxylin.

RESULTS

F98 GB and RN rat model

In GB rats, tumor growth is visible on contrast enhanced T1-weighted MRI, as described in Chapter 5 and 6. DCE-MRI was performed 8-9 days after inoculation (n = 10) or 3 weeks after inoculation (n = 5). Typical contrast enhanced T1-weighted MR images of GB and RN are shown in Figure 7.2.a and 7.2.e. Mean body weight of the rats with GB and RN at the time of DCE-MRI scan was 180 ± 24 g and 237 ± 17 g, respectively. In large GB, tumor necrosis developed in the center of GB, visible on MRI in 4 out of 5 rats imaged 3 weeks post-injection. Tumor necrosis is characterized by a hyperintense signal both on T2-weighted and contrast enhanced T1-weighted images (Figure 7.2.a and 7.2.b). Note that the T1-weighted image was acquired following DCE-MRI, hence allowing the contrast agent to leak into the core of the lesion during several minutes. H&E staining confirms presence of WHO grade 4 glioma with increased cellularity, nuclear atypia, high mitotic index, necrosis and vessel recruitment adjacent to the tumor tissue (Figure 7.3.e-f).

In RN rats, conventional MRI reveals occurrence of RN on average 29 ± 4 weeks (6-8 months) after irradiation (in 30 % of the animals no lesion is visible 34 weeks post-irradiation), see also Chapter 6. RN lesions are characterized by a heterogeneously hyperintense signal in the center of the lesion both on T2-weighted MRI and contrast enhanced T1-weighted MRI (Figure 7.2.e and 7.2.f). H&E staining confirms the presence of a large necrotic area with profound vascular changes such as fibrinoid necrosis, occlusion of blood vessels and perivascular coagulative necrosis, surrounded by a rim of macrophages (Figure 7.3.a-c). CD34 immunostaining shows vessel wall thickening (Figure 7.3.d) without microvascular proliferation.
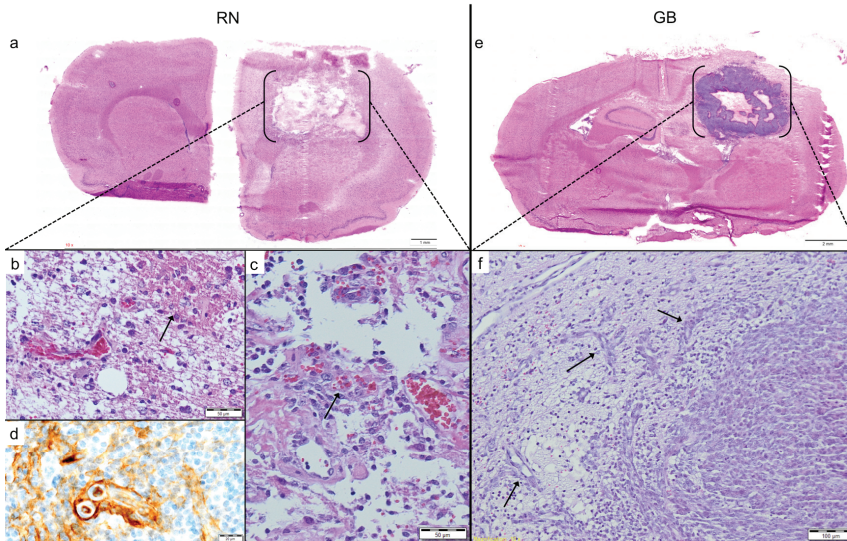
Figure 7.3. Hematoxylin and eosin staining in RN (a-c) and GB (e-f). In RN rat brain a large necrotic area is present (a) with vascular changes including hyalinization of the vessel wall, extravasation with hemolysis (see arrow in b), hemorrhage and thrombosis (see arrow in c). CD34 vascular staining in RN shows vessel wall thickening leading to the occlusion of blood vessels (d). Vessel recruitment adjacent to the tumor (see arrows in f) is seen on hematoxylin and eosin staining in F98 GB (e-f).

Semi-quantitative DCE-MRI analysis

Mean raw data of the DCE-MRI curves obtained from the contrast enhancing parts of GB (n = 15) and RN (n = 10) are depicted in Figure 7.2.i. The results of the Mann-Whitney U test are summarized in Table 7.1. and Figure 7.4. The wash-in rate, represented by k, and the wash-out rate, represented by D, are significantly higher in GB than in RN (p = 0.016 and p = 0.014, respectively) (Figure 7.4.a and 7.4.b). Furthermore, TTP_F is significantly lower in GB compared to RN (p = 0.001) (Figure 7.4.c). The offset from zero (C) and the amplitude (A) are not significantly different between GB and RN (p = 0.956 and p = 0.267, respectively).

Semi-quantitative curve parameters obtained by the Olea software confirm a significantly lower TTP_O in GB compared to RN (p = 0.005, Figure 7.4.d). Conversely, no significantly different wash-in$_O$, wash-out$_O$, AUC and Imax$_O$ were found between GB and RN (p = 0.177, p = 0.338, p = 0.765 and p = 0.723, respectively).

Mean raw data curves obtained from the central necrotic region in GB (n = 4) and RN (n = 3) are depicted in Figure 7.2.j. No significant differences were found for all semi-quantitative parameters (Table 7.1). However, a trend towards higher k values in RN compared to GB is noted (see boxplot, Figure 7.4.e).

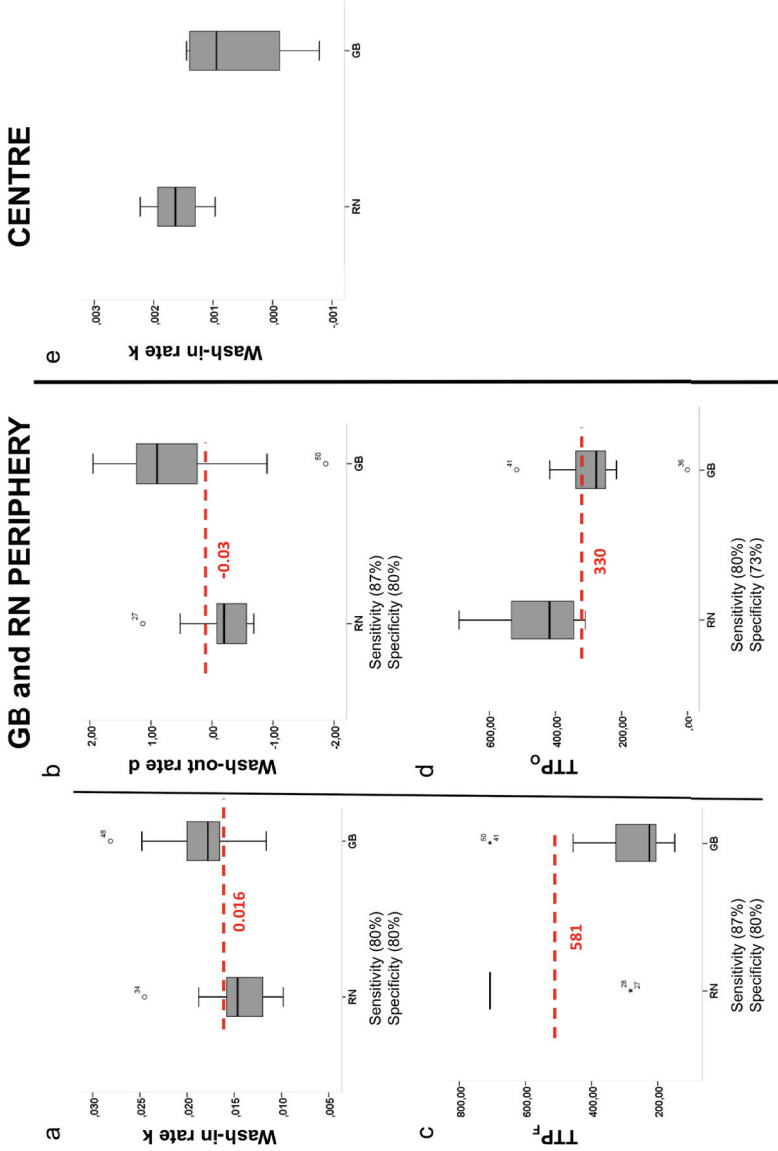**Figure 7.4. Boxplots of the parameters significantly different between the peripheral contrast enhancement in GB and RN (a-d).** Thresholds which discriminate GB from RN with the highest sensitivity and specificity are indicated (red dotted line). In the central necrotic zone of both lesions, there is no significant difference in wash-in rate, however there is a trend towards higher k values in RN compared to GB (e).

Table 7.1. Mann-Whitney U test and ROC analysis

	GB vs RN periphery					GB vs RN center
	Mann-Whitney U p-value	Area	Cut-off	Sensitivity (%)	Specificity (%)	Mann-Whitney U p-value
Manual fitting						
k	*0.016*	*0.783*	*0.016*	*80.0*	*80.0*	0.229
D	*0.014*	*0.793*	*-0.030*	*86.7*	*80.0*	n.a.
C	1.000					0.400
A	0.285					1.000
$Imax_F$	0.849					1.000
TTP_F	*0.001*	*0.880*	*581.3*	*86.7*	*80.0*	0.629
Olea sphere						
$wash-in_O$	*0.177*					0.629
$wash-out_O$	0.338					0.629
AUC_O	0.765					0.857
TTP_O	*0.005*	*0.827*	*330.1*	*80.0*	*73.3*	0.629
$Imax_O$	0.723					0.857
K_{trans}	0.311					0.400
K_{ep}	0.144					1.000
V_p	0.075					0.629
V_e	0.461					0.400

k: Rate exponential part of the curve y = C + A(1-e-kt) – Dt

D: Rate linear part of the curve y = C + A(1-e-kt) – Dt

C: Offset from zero of the curve y = C + A(1-e-kt) – Dt

A: Amplitude of the curve y = C + A(1-e-kt) – Dt

TTP_F : Time-to-peak of the curve y = C + A(1-e-kt) – Dt

$Imax_F$: Maximal intensity of the curve y = C + A(1-e-kt) – Dt

AUC_O : Area under the curve calculated using Olea Sphere

$Imax_O$: Maximum intensitiy calculated using Olea Sphere

TTP_O : Time-to-peak calculated using Olea Sphere

K_{trans} : Rate constant for transfer of contrast agent from plasma to extravascular, extracellular space

K_{ep} : Rate constant for transfer of contrast agent from EES to plasma

V_p Plasma volume

V_e : Fractional volume of the extravascular, extracellular space

Quantitative DCE-MRI analysis

Parametric maps of V_e, V_p, K_{ep} and K_{trans} are shown in Figure 7.5. Rate constants K_{trans} and K_{ep} were not significantly different between GB and RN (p = 0.311 and p = 0.114, respectively). A trend towards a higher V_p in GB was seen (p = 0.075), while no significant differences were found for V_e between GB and RN (p = 0.461). Parametric maps of K_{trans}, K_{ep}, V_e and V_p are comparable between GB (top row) and RN (bottom row) (Figure 7.5). Similarly, quantitative parameters were not significantly different in the central necrotic region between GB and RN.

ROC analysis

Receiver operating characteristic (ROC) analysis was performed for all parameters significantly different between GB and RN (Table 7.1). Threshold values and maximal sensitivities and specificities are depicted in Figure 7.4. A k-value > 0.016 has 80 % sensitivity and 80 % specificity in discriminating GB from RN. Furthermore, a D value larger than -0.03 yielded 87 % sensitivity and 80 % specificity for discriminating GB from RN. TTPF > 581s or TTPO > 330s provided a sensitivity of 87 % and 80 %, and a specificity of 80 % and 73 %, respectively, in differentiating GB from RN.
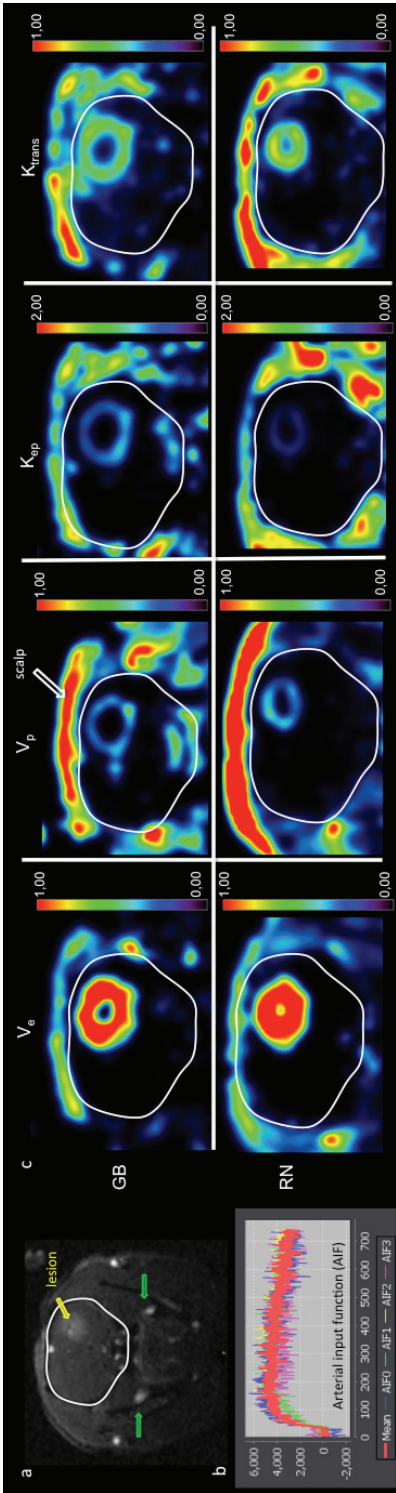
Figure 7.5. High signal-enhancement on DCE-MRI is visible within the lesion (yellow arrow) and the artery (green arrow)(a). The mean (4 pixels) arterial input function (AIF) was derived from a manually drawn ROI over the carotid artery (b). Parametric maps of V_e, V_p, K_{ep} and K_{trans} in GB (top row) and RN (bottom row) are shown (c). For clarity, the rat brain is contoured in white. Parametric maps were comparable in GB and RN.

155

DISCUSSION

GB harbor abnormal vessels marked by an atypical morphology and increased vessel permeability, characterized by large endothelial cell gaps, incomplete basement membrane, a relative lack of pericyte or smooth muscle association and vasodilatation [38-41]. In acute RN, there is endothelial cell apoptosis with capillary leakiness due to irradiation-induced endothelial damage whereas, in late RN (as in our model) an occlusive vasculopathy occurs due to vessel wall thickening [40,41]. We hypothesized that based on these differences in vascular properties we could distinguish GB from (late) RN. Assessment of (neo-)angiogenesis typically includes immunohistochemical measurements of microvessel density (MVD) in tumor tissue obtained by brain biopsy. However, a brain biopsy is invasive and samples only a small portion of the tumor tissue. Moreover, a biopsy specimen does not necessarily reflect the functional properties of the vasculature such as blood flow and vessel wall permeability [42]. Therefore, we hypothesized that DCE-MRI could be used as a surrogate to discriminate GB from RN. DCE-MRI allows studying the functional integrity of the BBB *in vivo* because the accumulation of contrast material in EES leads to an increased longitudinal relaxation rate, and therefore, increased signal intensity in T1-weighted images [30,43]. With DCE-MRI, wash-in and wash-out rates of the contrast agent can be calculated by plotting the signal intensity over time, which might be different between GB and RN. Furthermore, quantitative parameters can be derived from the concentration time curve that is mathematically fitted assuming a pharmacokinetic model [39,44].

In the literature it has been shown that DCE-MRI derived parameters may differentiate between primary brain tumor types and WHO grades [43]. In addition, in a previous study by Larsen et al., the authors found that in patients with high-grade glioma, CBV can discriminate between RN and brain tumor recurrence. An absolute CBV threshold of 2.0 ml/100 g was suggested [32]. In a more recent study in patients with high-grade glioma, a voxel-based classification for treatment-related changes versus progressive disease was investigated using DCE-MRI. The authors found that there were higher K_{trans}, K_{ep} and V_p values in progressive than in stable disease. However, pathological confirmation was lacking [34]. Hence, we used DCE-MRI in a histologically proven GB and RN rat model.

In the **peripheral contrast enhancing part** of GB and RN, the shape of the DCE-MRI curve is characterized by an initial exponential increase followed by a linear decrease (Figure 7.2.i). First, we found a higher contrast wash-in rate (k) in GB than in RN, which is probably due to a difference in vascular density because early permeability in the initial vascular phase is dependent mostly upon the blood flow and the total vascular surface area exposed to the contrast agent [33]. Importantly, neo-angiogenesis in GB leads to a high vascular density (see Figure 7.3.e-f) and high blood flow, allowing the contrast agent to reach the tumor very fast, as schematically depicted in Figure 7.6. [39-41].

Conversely, in late RN, an occlusive vasculopathy predominates due to vessel wall thickening (see Figure 7.3.d and 7.6). Also, in late RN, the interstitial transport is impaired due to radiation-induced remodeling of the interstitium resulting in the production of collagen and other stromal elements and there is little angiogenesis or microvascular proliferation [40,41]. In agreement with our findings in a preclinical model, several clinical studies also concluded that the maximal slope of the initial phase (= wash-in rate) was the best single predictor of tumor recurrence [27,33].

Secondly, we found that the wash-out rate was significantly higher in GB than in RN. This may be explained as follows: In GB, there may still be active transport mechanisms located at the endothelial wall allowing a faster wash-out than in RN. In addition, in GB, the capillary permeability and interstitial pressure due to tumor growth and angiogenesis is high, which reduces retention of contrast agent in EES and enables a flow of contrast agent back into the vascular component [33]. Conversely, in late RN, necrotic and occluded blood vessels predominate, leading to slow vascular clearance of the contrast agent. This is in agreement with a previous publication in which the authors hypothesized that fibrosis and necrosis are very slow-exchange tissues characterized by slow contrast agent elimination [39]. Using Olea Sphere, only the TTP_o was significantly different between GB and RN and a trend towards a higher V_p ($p = 0.08$) in case of GB was found, indicating increased angiogenesis. Surprisingly, the higher wash-in and wash-out rate in GB compared to RN was only found based on semi-quantitative curve fitting, but not when using parametric maps. To our opinion the rationale for this discrepancy might be two-fold. First, the analysis in Olea Sphere is based on a voxel-by-voxel basis to provide multiple parametric maps. Even though this provides a lot of information, this might be more sensitive to noise than curve fitting applied on a number of voxels averaged in the specific ROI. Secondly, Olea Sphere separately calculates the slope of the increasing and decreasing part of the DCE time-series, before and after it reaches its maximum, to obtain a measure for the wash-in and wash-out rate, respectively. In contrast, the curve-fitting method presented in this manuscript fits one mathematical function to the DCE time-series, which incorporates both the wash-in and the wash-out phase. This might be a more robust method regarding to noise present in the dynamic time-series. Finally, obtaining a smooth AIF with expected artery contrast kinetics is not easily obtained in the rat brain and should be kept in mind when performing quantitative analysis.

In a pilot study in patients treated for gliomas, which demonstrated that quantitative measurements of the wash-out of contrast agent back into the plasma were also not significantly different between recurrent high-grade glioma and RN [31]. As for the ROC analysis, we found that the AUC was not significantly different between GB and RN, which is not in agreement with other studies that found a significantly higher AUC in recurrent glioma than in RN [27,31].

In the **central necrotic part** of GB and RN, the shape of the DCE-MRI curve is characterized by a continuous increase in signal enhancement probably resulting from a continuous centripetal inflow of contrast agent from the periphery to the center (Figure 7.2.j). This can also be visually appreciated by comparing a 6-min DCE-MRI acquisition (Figure 7.2.c-g) with a 12-min DCE-MRI acquisition (Figure 7.2.d-h) [39]. Tumor necrosis occurs in the center of large tumors because hypoxia develops due to a deficient blood flow, nutrient delivery and oxygen consumption [39]. In late RN, vessel wall thickening, fibrinoid necrosis with consequent thrombosis, infarction and coagulative necrosis of the perivascular parenchyma occurs, leading to hypoxia within RN lesions [40].
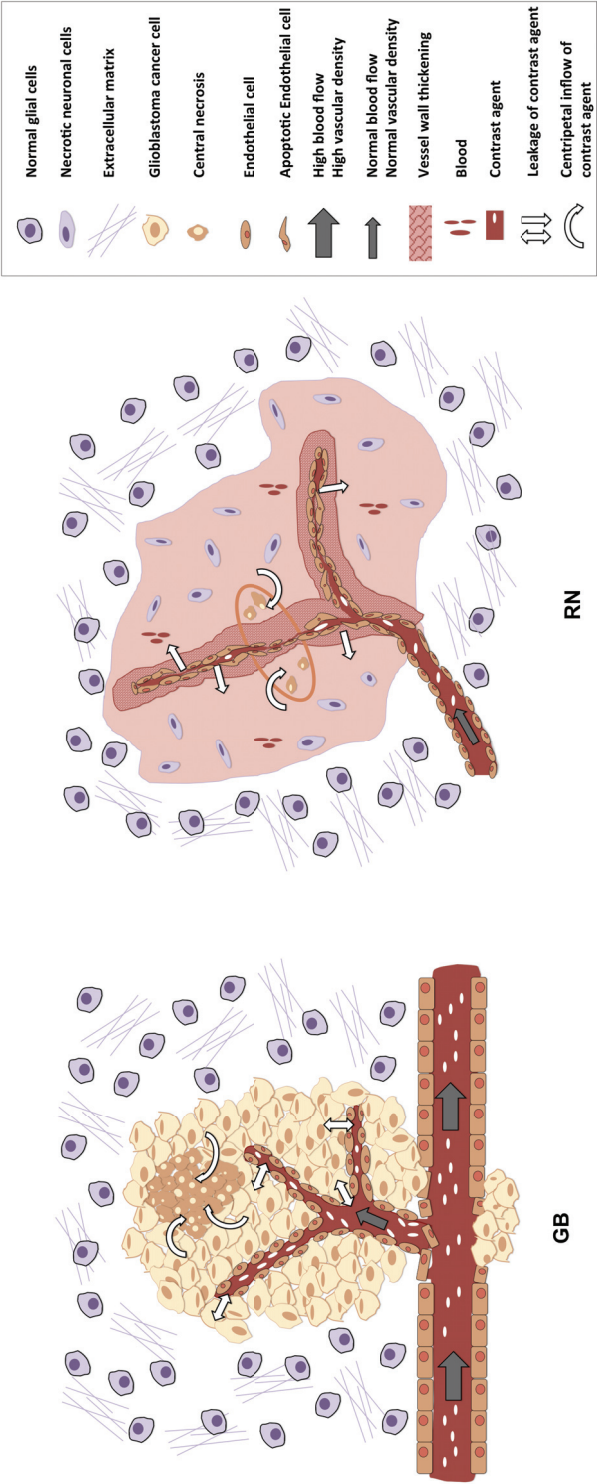
Figure 7.6. Schematic illustration of contrast leakage in GB and RN. Due to neo-angiogenesis, GB is characterized by a high vascular density and high blood flow, which allows a fast transport of contrast agent. Due to BBB disruption and the presence of large endothelial cell gaps, leakage of the contrast agent occurs. Also, high capillary permeability and active transport mechanisms at the BBB allow a fast clearance of the contrast agent from the vascular component. Conversely, in late RN, an occlusive vasculopathy occurs due to vessel wall thickening. Furthermore, there is no angiogenesis, which explains a slower wash-in rate. Due to the presence of damaged and occluded vessels, there is less vascular clearance. As a result of hypoxia, a central region of necrosis can develop in GB (tumor necrosis) and in RN (radiation necrosis). Slow centripetal inflow of contrast agent occurs in the central necrotic part.

In summary, in our rat model we found that the **wash-in rate (k), TTP_F and TTP_O of the DCE-MRI curves discriminated GB from RN**. However, we need to point out that pure tumor and pure RN is not a realistic model, as in the clinic mostly a mix of tumor recurrence and RN is present within the lesion post-treatment. As such, our results need to be confirmed in a combined model. Furthermore, it must be realized that a major disadvantage of DCE-MRI is that there is no standard method for analyzing the data [31,43]. Although quantitative parameters are more likely to reflect the underlying physiological phenomena of the contrast enhancement patterns as compared to semi-quantitative parameters, the applied pharmacokinetic model may not fully reflect the observed data, because each model makes assumptions that may not be valid for every tissue or tumor type [27,39,44]. On the other hand, semi-quantitative parameters define the signal intensity enhancement using a number of simple descriptors and are therefore straightforward to calculate and easier to use [33,39]. In the clinic, DCE-MRI is usually not incorporated in routine brain tumor MRI. Adding a DCE-MRI acquisition would lead to an increase in scan time. However, because significant differences in wash-in rate (k), TTP_F and TTP_O are evident within the first minutes of the DCE-MRI curve (Figure 7.2.i), in daily clinical routine, a DCE-MRI with an acquisition time of 5 min may suffice.

Conclusion

Based on our results in a rat model, DCE-MRI may be useful to discriminate GB from RN. Wash-in rate (k), wash-out rate (d), TTP_F and TTP_O, which can be derived from a 5-min DCE-MRI acquisition, are able to distinguish GB from RN while other quantitative and semi-quantitative parameters are not. Whether DCE-MRI will also be able to differentiate GB from RN in humans must be further explored.

REFERENCES

[1] Brandsma D, Stalpers L, Taal W, et al. Clinical features, mechanisms, and management of pseudoprogression in malignant gliomas. Lancet Oncology 2008;9:453-461.

[2] Siu A, Wind JJ, Iorgulescu JB, et al. Radiation necrosis following treatment of high grade glioma-a review of the literature and current understanding. Acta Neurochirurgica 2012;154:191-201.

[3] Bobek-Billewicz B, Stasik-Pres G, Majchrzak H, et al. Differentiation between brain tumor recurrence and radiation injury using perfusion, diffusion-weighted imaging and MR spectroscopy. Folia Neuropathology 2010;48:81-92.

[4] Alexiou GA, Tsiouris S, Kyritsis AP, et al. Glioma recurrence versus radiation necrosis: accuracy of current imaging modalities. Journal of Neurooncology 2009;95:1-11.

[5] Hustinx R, Pourdehnad M, Kaschten B, et al. PET imaging for differentiating recurrent brain tumor from radiation necrosis. Radiology Clinics of North America 2005;43:35-47.

[6] Zhou J, Tryggestad E, Wen Z, et al. Differentiation between glioma and radiation necrosis using molecular resonance imaging of endogeneous proteins and peptides. Nature Medicine 2011;17:130-134.

[7] Wang S, Chen Y, Lal B, et al. Evaluation of radiation necrosis and malignant glioma in rat models using diffusion tensor MR imaging. Journal of Neurooncology 2012;107:51-60.

[8] Mullins ME, Barest GD, Schaefer PW, et al. Radiation necrosis versus glioma recurrence: conventional MR imaging clues to diagnosis. American Journal of Neuroradiology 2005;26:1967-1972.

[9] Spaeth N, Wyss MT, Weber B, et al. Uptake of 18F-fluorocholine, 18F-fluoroethyl-L-tyrosine, and 18F-FDG in acute cerebral radiation injury in the rat: implications for separation of radiation necrosis from tumor recurrence. Journal of Nuclear Medicine 2004;45:1931-1938.

[10] Van Laere K, Ceyssens S, Van Calenbergh F, et al. Direct comparison of 18F-FDG and 11C-methionine PET in suspected recurrence of glioma: sensitivity, inter-observer variability and prognostic value. European Journal of Nuclear Medicine and Molecular Imaging 2005;32:39-51.

[11] Chao ST, Suh JH, Raja S, et al. The sensitivity and specificity of FDG PET in distinguishing recurrent brain tumor from radionecrosis in patients treated with stereotactic radiosurgery. International Journal of Cancer 2001;96:191-197.

[12] Bolcaen J, Descamps B, Deblaere K, et al. (18)F-fluoromethylcholine (FCho), (18)F-fluoroethyltyrosine (FET), and (18)F-fluorodeoxyglucose (FDG) for the discrimination between high-grade glioma and radiation necrosis in rats: a PET study. Nuclear Medicine and Biology 2015;42:38-45.

[13] Minamimoto R, Saginoya T, Kondo C, et al. Differentiation of Brain Tumor Recurrence from Post-Radiotherapy Necrosis with 11CMethionine PET: Visual Assessment versus Quantitative Assessment. Plos One 2015;13:10(7):e0132515.

[14] Galldiks N, Stoffels G, Filss CP, et al. Role of O-(2-(18)F-fluoroethyl)-L-tyrosine PET for differentiation of local recurrent brain metastasis from radiation necrosis. Journal of Nuclear Medicine 2012;53:1367-1374.

[15] Karunanithi S, Sharma P, Kumar A, et al. 18F-FDOPA PET/CT for detection of recurrence in patients with glioma: prospective comparison with 18F-FDG PET/CT. European Journal of Nuclear Medicine and Molecular Imaging 2013;40:1025-1035.

[16] Jena A, Taneja S, Gambhir A, et al. Glioma Recurrence Versus Radiation Necrosis Single-Session Multiparametric Approach Using Simultaneous O-(2-18F-Fluoroethyl)-L-Tyrosine PET/MRI. Clinical Nuclear Medicine 2016;41:e228-e236.

[17] Mehrkens JH, Pöpperl G, Rachinger W, et al. The positive predictive value of 0-(2-(18F)fluororethyl)-L-tyrosine (FET) PET in the diagnosis of a glioma recurrence after multimodal treatment. Journal of Neurooncology 2008;88:27-35.

[18] Pöpperl G, Götz C, Rachinger W, et al. Serial 0-(2-(18F)fluoroethyl)-L-tyrosine PET for monitoring the effects of intracavitary radioimmunotherapy in patients with malignant glioma. European Journal of Nuclear Medicine and Molecular Imaging 2006;33:792-800.

[19] Hustinx R, Pourdehnad M, Kaschten B, et al. PET imaging for differentiating recurrent brain tumor from radiation necrosis. Radiology Clinics North America 2005;43:35-47.

[20] Doyle WK, Budinger TF, Valk PE, et al. Differentiation of cerebral radiation necrosis from tumor recurrence by [18F]FDG and 82Rb positron emission tomography. Journal of Computer Assisted Tomography 1987;11:563-570.

[21] Kahn D, Follett KA, Bushnell DL, et al. Diagnosis of Recurrent Brain Tumor: Value of 201T1 SPECT vs 18F-fluorodeoxyglucose PET. American Journal of Roentgenology 1994;163:1459-1465.

[22] Ricci PE, Karis JP, Heiserman JE, et al. Differentiating Recurrent Tumor from Radiation Necrosis: Time for Re-evaluation of Positron Emission Tomography? American Journal of Neuroradiology 1998;19:407-413.

[23] Kim YH, Oh SW, Lim YJ, et al. Differentiating radiation necrosis from tumor recurrence in high-grade gliomas: assessing the efficacy of 18F-FDG PET, 11C-methionine PET and perfusion MRI. Clinical Neurology and Neurosurgery 2010;112(9):758-765.

[24] Shah A, Snelling B, Bregy A, et al. Discriminating radiation necrosis from tumor progression in gliomas: a systematic review what is the best imaging modality? Journal of Neurooncology 2013;112:141-152.

[25] Zeng QS, Li CF, Liu H, et al. Distinction between recurrent glioma and radiation injury using magnetic resonance spectroscopy in combination with diffusion-weighted imaging. International Journal of Radiation Oncology Biology Physics 2007;68:151-158.

[26] Ahmed R, Oborski MJ, Hwang M, et al. Malignant gliomas: current perspectives in diagnosis, treatment, and early response assessment using advanced quantitative imaging methods. Cancer Management Research 2014;6:149-170.

[27] Kim HS, Goh MJ, Kim N, et al. Which combination of MR imaging modalities is best for predicting recurrent glioblastoma? Study of diagnostic accuracy and reproducibility. Radiology 2014;273:831-843.

[28] Hu LS, Baxter LC, Smith KA, et al. Relative cerebral blood volume values to differentiate high-grade glioma recurrence from posttreatment radiation effect: direct correlation between image-guided tissue histopathology and localized dynamic susceptibility-weighted contrast-enhanced perfusion MR imaging measurements. American Journal of Neuroradiology 2009;30:552-558.

[29] Barajas RF Jr, Chang JS, Segal MR, et al. Differentiation of recurrent glioblastoma multiforme from radiation necrosis after external beam radiation therapy with dynamic susceptibility-weighted contrast-enhanced perfusion MR imaging. Radiology 2009;253:486-496.

[30] Zahra MA, Tan LT, Priest AN, et al. Semiquantitative and quantitative dynamic contrast-enhanced magnetic resonance imaging measurements predict radiation response in cervix cancer. International Journal of Radiation Oncology Biology Physics 2009;74:776-773.

[31] Bisdas S, Naegele T, Ritz R, et al. Distinguishing recurrent high-grade gliomas from radiation injury: a pilot study using dynamic contrast-enhanced MR imaging. Academic Radiology 2011;18:575-583.

[32] Larsen VA, Simonsen HJ, Law I, et al. Evaluation of dynamic contrast-enhanced T1-weighted perfusion MRI in the differentiation of tumor recurrence from radiation necrosis. Neuroradiology 2013;55:361-369.

[33] Narang J, Jain R, Arbab AS, et al. Differentiating treatment-induced necrosis from recurrent/progressive brain tumor using nonmodel-based semiquantitative indices derived from dynamic contrast-enhanced T1-weighted MR perfusion. Neuro-Oncology 2011;13:1037-1046.

[34] Artzi M, Liberman G, Nadav G, et al. Differentiation between treatment-related changes and progressive disease in patients with high grade brain tumors using support vector machine classification based on DCE MRI. Journal of Neurooncology 2016;127:515-524.

[35] Thomas AA, Arevalo-Perez J, Kaley T, et al. Dynamic contrast enhanced T1 MRI perfusion differentiates pseudoprogression from recurrent glioblastoma. Journal of Neurooncology 2015;125:183-190.

[36] Barth RF, Kaur B. Rat brain tumor models in experimental neuro-oncology: the C6, 9L, T9, RG2, F98, BT4C, RT-2 and CNS-1 gliomas. Journal of Neurooncology 2009;94:299-312.

[37] Bolcaen J, Descamps B, Deblaere K, et al. MRI-guided 3D conformal arc micro-irradiation of a F98 glioblastoma rat model using the Small Animal Radiation Research Platform (SARRP). Journal of Neurooncology 2014;120:257-266.

[38] Lemasson B, Serduc R, Maisin C, et al. Monitoring blood-brain barrier status in a rat model of glioma receiving therapy: dual injection of low-molecular-weight and macromolecular MR contrast media. Radiology 2010;257:342-352.

[39] Padhani AR, Husband JE. Dynamic contrast-enhanced MRI studies in oncology with an emphasis on quantification, validation and human studies. Clinical Radiology 2001;56:607-620.

[40] Jain R, Narang J, Sundgren PM, et al. Treatment induced necrosis versus recurrent/progressing brain tumor: going beyond the boundaries of conventional morphologic imaging. Journal of Neurooncology 2010;100:17-29.

[41] Stapleton S, Jaffray D, Milosevc M. Radiation effects on the tumor microenvironment: Implications for nanomedicine delivery. Advanced Drug Delivery Reviews 2016; doi: 10.1016/j.addr.2016.05.021.

[42] Li SP, Padhani AR. Tumor response assessments with diffusion and perfusion MRI. Journal of Magnetic Resonance Imaging 2012;35:745-763.

[43] Heye AK, Culling RD, Valdes Hernandez MC, et al. Assessment of blood-brain barrier disruption using dynamic contrast-enhanced MRI. A systematic review. NeuroImage Clinical 2014;6:262-274.

[44] Buckley DL. Uncertainty in the analysis of tracer kinetics using dynamic contrast-enhanced T1-weighted MRI. Magnetic Resonance in Medicine 2002;47:601-606.

Chapter 8.

General discussion

"Education is not the learning of facts, but the training of the mind to think"

[Albert Einstein].

Chapter 8. General discussion

High grade gliomas (HGG) are lethal brain tumors with a median survival of 12-14 months for grade 4 or glioblastoma (GB). Imaging plays an important role in the evaluation of patients with brain tumors. Computed tomography (CT) and magnetic resonance imaging (MRI) represent the two most important and commonly used imaging modalities that have a significant impact on patient care. MRI is the method of choice for evaluating patients who have symptoms and signs suggesting a brain tumor. Its superior contrast resolution and flexible protocols allow to play an important role in assessing tumor location and extent, in directing biopsies, in planning radiation therapy (RT) and evaluating the treatment results [1]. However, CT and MRI have offered limited insight on grade of malignancy, infiltration into and effects on surrounding normal tissue and on differentiation between (radio)necrosis (RN) and recurrent tumor [2]. Tumor cells have been found at quite a distance from the contrast enhancing tumor part on MRI [1]. Furthermore, 20 to 30 % of patients undergoing their first post-irradiation MRI show increased contrast enhancement that eventually subsides without any change in therapy. This phenomenon is called pseudoprogression. Pseudoresponse should also be kept in mind when glioma patients are treated with antiangiogenic agents, especially those targeting vascular endothelial growth factor (VEGF), such as bevacizumab, and the VEGF receptor, such as cediranib. The latter can produce marked decrease in contrast enhancement as early as 1 to 2 days after initiation of therapy and commonly results in high radiologic response rates of 25 to 60 %. These apparent responses to antiangiogenic therapy may be partly a result of normalization of abnormally permeable tumor vessels and not always necessarily indicative of a true antiglioma effect. Both pseudoprogression and pseudoresponse complicate response assessment in glioma using conventional MRI [3,4]. In this respect, PET could be an important asset in therapy response assessment enabling the visualization of biological changes preceding anatomical changes. With increasing availability of radioactively labeled tracers, PET allows widespread applications in diagnosis as well as assessment of prognosis and outcome after treatment of HGG [2]. Multiple tracers have been proposed, such as ^{18}F-fluorodeoxyglucose (^{18}F-FDG), ^{18}F-Fluoroethyltyrosine (^{18}F-FET), ^{18}F-fluoroazomycin arabinoside (^{18}F-FAZA) and ^{18}F-Fluoromethylcholine (^{18}F-FCho) (see Chapter 2), but currently only two are frequently used in the clinic, namely ^{18}F-FDG and ^{18}F-FET.

In this dissertation one of our goals was to investigate the potential of PET and MRI for early therapy response assessment in GB patients. An early response predictor is the premise of personalized treatment enabling change or discontinuation of therapy to prevent ineffective treatment or adverse events of treatment. For example, when resistance to chemotherapy occurs, a switch to another chemotherapeutic agent might be possible before bone marrow reserves become exhausted. Secondly, an early predictor would prevent unnecessary treatment related side effects e.g., bone marrow depression, fatigue, nausea, and vomiting, and therefore could maintain or even improve quality of life. Moreover, identification of treatment failure may help reduce costs. This is highly relevant because the expense of newer systemic treatment options (e.g., bevacizumab) is considerably higher than conventional alkylating chemotherapy (e.g., lomustine) [5].

Another important step towards personalized medicine implies that one can unequivocally discriminate between RN and tumor recurrence, allowing to select the appropriate therapy for a specific brain tumor patient. Currently, this is still a major topic of debate in neuro-oncology. To solve this problem, a clinical study investigating the potential of different biological imaging modalities in discriminating tumor

recurrence from therapy related effects is needed. When RN is suspected it is unlikely that a biopsy will be taken, hence anatomopathological diagnosis is lacking. In this thesis, we aimed to contribute to unravel the underlying mechanisms of RN and tumor recurrence by performing *in vivo* imaging. A major advantage of *in vivo* small animal PET imaging, over *ex vivo* imaging such as autoradiography, is that it allows to evaluate various PET tracers within the same animal. Moreover, this can be investigated in specific animal models of HGG or RN.

^{18}F-FDG is being used around the world in oncology since its first synthesis in the 1970s. The widespread availability of this tracer and the fact that 'new' tracers should be compared with the state-of-the-art led to the inclusion of ^{18}F-FDG PET in our preclinical studies. However, ^{18}F-FDG PET is considered not to be ideal to evaluate treatment response because of its high accumulation in nonspecific reactive changes in tissues [6,7]. Furthermore, the high uptake of ^{18}F-FDG in the normal brain decreases the contrast between the lesion and normal brain. As such, we selected two additional PET tracers which have been shown low uptake in normal brain, thus increasing the contrast between malignant and non-malignant brain tissue, namely ^{18}F-FET and ^{18}F-FCho. The feasibility and usefulness of amino-acid PET tracers, such as ^{11}C-Methionine (^{11}C-MET) and ^{18}F-FET PET for treatment assessment and follow-up after surgery, chemo- and radiotherapy have been demonstrated in several studies. The currently available data suggest that a reduction of amino acid uptake by glioma is a sign of a favorable response [8-10]. However, it is worth mentioning that studies using amino acid PET to distinguish recurrent tumor from RN are limited [11]. Thirdly, we selected ^{18}F-FCho, first introduced in PET imaging of brain tumors by Delgrado et al., because abnormal choline metabolism emerged as a metabolic hallmark that is associated with oncogenesis and tumor progression [6,12-15]. More specifically, it was hypothesized that the uptake of radiolabeled choline, which is a precursor of membrane phospholipids, would be increased in highly proliferating tumors to keep up with the increased demands for the synthesis of phospholipids [15,16]. As such, ^{18}F-FCho PET could be promising in the follow-up of high-grade glioma post-treatment. Since MRI is the standard imaging method for HGG at the moment, the three selected PET tracers were compared contrast-enhanced T1-weighted MR images. Finally, DCE-MRI was investigated to differentiate GB from RN because vascular differences between GB and RN are well known. Characterization of the vascular microenvironment of a post-treatment brain tumor typically includes immunohistochemical measurements of microvessel density in tumor tissue obtained by brain biopsy. However, a brain biopsy is invasive and samples only a small portion of the tumor tissue. Moreover, a biopsy specimen does not necessarily reflect the functional properties of the vasculature, such as blood flow and vessel wall permeability [17]. DCE-MRI allows studying the functional integrity of the blood brain barrier (BBB) *in vivo* and therefore, we hypothesized that DCE-MRI could be used as a surrogate to discriminate GB from RN.

In chapter 3, four research questions were put forward to summarize our goals.

> **Question 1: Are we able to assess therapy response in post-treatment GB patients using ^{18}F-FCho PET and MRI according to the RANO criteria?**

Currently, disease progression or treatment response is based on changes on T1-weighted, T2-weighted and fluid attenuated inversion recovery (FLAIR) MRI. Other more advanced MRI as well as PET techniques are often beyond current clinical standards [18]. However, there is now a crucial need for quantitative methods that can sensitively detect response to therapy at early follow-up times, when changes in management of non-responders has its greatest effect [19]. However, PET studies evaluating the prognostic impact of metabolic response at an early stage of treatment are rare [8]. Rapidly proliferating GB have increased membrane/fatty acid requirements, which may result in a higher ^{18}F-FCho uptake than in healthy brain tissue, and may precede post-treatment anatomical changes on conventional MRI [20]. Kwee et al. showed promising results for ^{18}F-FCho in brain tumor PET imaging with a differential uptake in HGG, brain metastases and benign lesions [16]. One of the assets of this tracer is the very low uptake in normal brain, increasing the contrast between GB and healthy brain. However, only a few studies investigated the potential of ^{18}F-FCho for therapy response assessment in gliomas. Li et al. reported that, for ^{11}C-Choline PET, a tumor to normal brain ratio (TBR) ≤ 1.4 might predict a longer overall survival in patients with suspected recurrent glioma after treatment [17]. Parashar et al. suggested that there was a good correlation between a change in SUV_{max} of the tumor during RT and response [21]. However, in the latter study, only one patient with a malignant glioma was included.

Based on our results, ^{18}F-FCho SUV values pre-RT, during RT and 1 month post-RT did not predict response. Physiological phenomena, such as therapy-induced perfusion changes due to alteration of BBB, cell repair mechanisms obscuring assessment of true cell death and aspecific uptake of PET tracers due to infiltrating macrophages, may complicate response assessment. It should also be borne in mind that GB are very heterogeneous tumors, containing clusters of tumor and normal cells, vascular structures and necrotic tissue [22], which are not fully captured when using SUV_{max} or SUV_{mean} values. Based on our results, we also noted that in 3 non-responders, absolute SUV values decreased during the course of the treatment while the metabolic tumor volume (MTV) increased, indicating that MTV is an important parameter. As such, we found that the ^{18}F-FCho PET-derived parameter, <u>MTV x SUV_{mean}, allowed prediction of therapy response as early as 1 month after the completion of RT. Interestingly, the tumor volume derived from contrast-enhanced MRI, was able to predict response earlier, at week 6 during RT.</u> Although we did not find any cases of pseudoprogression, our finding warrants caution. This is because the possibility of pseudoprogression makes the determination of response within the first 12 weeks post-RT only possible if the majority of the new enhancement is outside of the radiation field (for example, beyond the high-dose region or 80 % isodose line) or if there is pathologic confirmation of progressive disease [4]. Therefore, inclusion of PET in the RANO criteria might be helpful for early therapy response prediction in high-grade glioma, more particularly in cases with suspected pseudoprogression on post-treatment MRI.

It is important to compare our results with amino acid PET studies in the literature. Multiple clinical studies suggest that treatment response and outcome in bevacizumab therapy can be better assessed by ^{18}F-FET and 3,4-dihydroxy-6-^{18}F-fluoro-l-phenylalanine (^{18}F-FDOPA), compared to MRI [9, 23-26].

Chapter 8. General discussion

Also reliable monitoring of temozolomide (TMZ) and nitrosourea-based chemotherapy effects has been demonstrated in patients with recurrent high-grade gliomas [5,10,27-29]. In a study by Rachinger et al. ^{18}F-FET PET was able to distinguish tumor progression from stable disease with a 93 % specificity and 100 % sensitivity, while the specificity of conventional MRI alone was 50 % [30]. ^{18}F-FET PET responders, based on a decrease of more than 10 % of a lesion to normal brain ratio (LNR) after completion of therapy, also showed a significant longer overall survival than non-responders [8]. In addition, ^{18}F-FCho PET seems not to be superior to ^{18}F-FET PET because prediction of response as early as 7-10 days after the completion of treatment and earlier than MRI has been documented [8,10,31]. Also, the time-to-peak and the shape of the ^{18}F-FET time-activity curve, derived from dynamic PET acquisitions, was shown to have value in therapy response assessment, which could not be shown using ^{18}F-FCho PET. However, it is difficult to compare results of individual studies because of methodological differences and varying clinical endpoints [32]. Importantly, published cut-off values are method and often institute specific, especially, since they are also affected by acquisition protocol, reconstruction algorithm and ROI definition [33]. This means that published thresholds need to be validated in each institution separately, which is causing a delay in the incorporation of new therapy response assessment methodologies in the clinic.

Question 2: Are we able to assess the effect of therapy in a rat model of GB using PET and MRI?

Preclinical therapy response studies in glioma are needed for the analysis of new imaging modalities or treatment strategies and could be a first step before embarking on complex prospective clinical trials. However, a major requirement is the availability of preclinical glioma models that mimic the oncologic behavior and therapeutic strategies in the clinic. We succeeded in developing an orthotopic allograft GB rat model that was used to resemble human treatment. After the inoculation of F98 GB cells in the rat brain fast tumor growth was seen on MRI, which closely resembled histological characteristics of human GB on portmortem specimen. Secondly, we succeeded in applying <u>MRI-guided multiple non-coplanar arcs</u> using the small animal radiation research platform (SARRP), irradiating a 3 x 3 mm region, while minimalizing the dose to the surrounding normal brain tissue. Our overall results confirm the effectiveness of the treatment and the mean cumulative DVHs confirmed the delivery of 20 Gy to 90 % of the tumor target volume. To our knowledge, the application of multiple arcs for cranial irradiation in small animals was not described before in the literature. As such, this approach is a major step forward in bridging the gap between preclinical and clinical RT technology and this model is available for future research on new therapeutics in GB.

Secondly, we investigated if ^{18}F-FDG PET or ^{18}F-FCho PET were also able to confirm treatment response, which was shown on contrast-enhanced T1-weighted MRI (GdTV). Based on our results, and in agreement with the results of our above-mentioned clinical study, it was clear that the parameter <u>MTV x SUV$_{mean}$, including both MTV and the mean tracer uptake, was superior to MTV only in detecting the effect of therapy</u>. Due to the heterogeneous character of GB and the associated heterogeneous PET tracer uptake, MTV is highly variable during post-treatment follow-up. This probably explains why applying an automatic threshold on PET, to determine MTV, for tumor response assessment seemed not sufficient for

fully capturing treatment-induced changes. Using MTV x SUV$_{mean}$, conventional <u>[18]F-FDG PET detects</u> <u>therapy effect as soon as day 5 post-therapy, comparable to contrast-enhanced MRI</u>. Importantly, <u>delayed</u> <u>[18]F-FDG PET was able to detect the treatment effect earlier, starting at day 2 post-irradiation</u>. ^{18}F-FCho <u>PET was not able to detect the effects of treatment at any time point</u>. Several factors are known that influence the uptake of ^{18}F-FCho, such as leakage through damaged BBB, uptake by macrophages, signal arising from its ^{18}F-labeled metabolite fluorobetaine and spill-in activity by physiological uptake. Importantly, the attribution of each factor to the detected ^{18}F-FCho signal is not known. Importantly, visual comparison between clinical ^{18}F-FCho PET images and preclinical images revealed that the uptake in the small animal GB tumors was less well circumscribed compared to human GB. Several factors may contribute to this finding, such as differences in metabolism of ^{18}F-FCho between rats and humans.

Although the preclinical study showed superiority of ^{18}F-FDG compared to ^{18}F-FCho in detecting treatment response of GB to concomitant radiation and chemotherapy in rats, it should be noted that treatment response to other therapeutic modalities in GB, such as anti-angiogenic therapies, which have a different impact on the tumor and tumor micro-environment, were not investigated. Several publications showed that ^{18}F-FLT displayed earlier assessment of therapy efficacy to an antiangiogenic therapy than either tumor volume measured by MRI or ^{18}F-FDG PET [24,25,34-37]. ^{18}F-fluorothymidine (^{18}F-FLT) has also been shown to be promising in monitoring the effects of TMZ in a mouse model of GB [38]. As it was shown that ^{18}F-FLT is only retained in brain tumors where there is a breakdown of the BBB, one potential concern is that ^{18}F-FLT may be largely tracking the patency of the BBB [34]. Hypoxia PET may also have great potential in the evaluation of treatment response in HGG since the presence of hypoxia in solid tumors is a major cause of failure of both radiation therapy and chemotherapy, and is associated with a more aggressive tumor phenotype and a poor clinical outcome [6]. As such, changes in the oxygenation status in GB, evaluated using ^{18}F-fluoromisonidazole (^{18}F-FMISO) or ^{18}F-FAZA PET, may have added value for monitoring therapy. Finally, Nedergaard et al. showed promising results in evaluating response to irinotecan and anti-VEGF therapy in a murine GB model using ^{18}F-FET PET [39,40]. This group also noted that ^{18}F-FET PET appeared more sensitive than ^{18}F-FLT PET to measure early response to anti-VEGF therapy [41]. These promising results have recently been translated to the clinic with multiple clinical studies confirming the potential of ^{18}F-FET as a potential biomarker for therapy response assessment (see abovementioned discussion of question 1) [5,8-10,23-30].

Question 3: Are ^{18}F-FCho, ^{18}F-FET and ^{18}F-FDG PET able to discriminate between recurrent GB and RN in rats?

RN is difficult to differentiate from tumor recurrence on conventional MRI [43-48] and is especially challenging in early delayed and late RN injuries because tumor recurrence occurs along the same time line [4]. Both GB and RN lesions are heterogeneously hyperintense on T2-weighted MRI and contrast enhancing with surrounding edema on T1-weighted MRI. Correct diagnosis is furthermore complicated by the fact that very few studies correlate imaging results with pathological confirmation [49]. Nevertheless, a correct diagnosis is important for patient management because tumor recurrence requires second-line chemotherapy, while for the treatment of RN steroids may suffice [50,51]. Taking all this

into account, we investigated the potential of ^{18}F-FDG, ^{18}F-FCho and ^{18}F-FET PET in discriminating "pure" GB from "pure" RN in rats.

We found significant higher values for SUV_{max}, SUV_{mean}, LNR_{mean} and LNR_{max} in GB compared to RN on ^{18}F-FDG PET images at conventional time intervals (40 minutes after tracer injection). Uptake of ^{18}F-FDG in GB was higher than in the cortex, probably due to a high cell proliferation rate, whereas uptake in RN was not higher than in the cortex [50,52]. Importantly, we suggest that due to the high uptake of ^{18}F-FDG in normal grey matter, the uptake in RN due to BBB breakdown and inflammation, was not distinguishable from the surrounding normal brain tissue. In the literature, ^{18}F-FDG PET has been found to be of moderate additional value to MRI for differentiation between glioma recurrence and RN, especially due to the low specificity of the tracer [18,23,49,51,53-55]. However, available studies have several limitations: most studies were retrospective, jointly assessed gliomas of all WHO grades, used different treatments, had varying assessment strategies, and utilized varying ^{18}F-FDG thresholds of tumor to normal brain for image interpretation [23]. For ^{18}F-FDG PET, a potentially useful approach is dual-phase imaging. Previously, it was shown that delayed ^{18}F-FDG imaging 3-8 h after injection improves the distinction between tumor and normal grey matter because the outflow of glucose would be greater from normal brain tissue than from tumor tissue. These conclusions were based on kinetic modeling (KM) showing that k4 values were not significantly different between tumor and normal brain tissue at early imaging times but was lower in tumor than in normal brain tissue at delayed times [7,36,56]. This appears to be related to a slower rate of dephosphorylation of FDG-6 phosphate (via glucose 6 phosphatase) in tumor as compared to normal brain parenchyma [57]. Applying conventional and delayed ^{18}F-FDG PET, Horky et al. found that early and late SUVs of the lesion alone did not differentiate between tumor and necrosis. However, the change of LNR_{max} between early and late ^{18}F-FDG images was 95% sensitive, 100% specific and 96% accurate [57]. In our study, we found that differences in LNR_{mean} and LNR_{max} between GB and RN were higher on the delayed PET images compared to the conventional PET image. A plausible explanation is that, like normal brain tissue, necrotic tissue shows increased ^{18}F-FDG excretion at delayed times when compared with tumor [58]. Consequently, the tumor-to-normal-brain ratio increases over time for tumor, but tends to remain stable or even decreases for RN [57]. This finding suggests that, in the clinic, a late ^{18}F-FDG PET image is sufficient to discriminate between GB and RN.

Because amino acid tracers appear more sensitive than ^{18}F-FDG PET in visualizing tumor, they also have potentially better diagnostic performance than ^{18}F-FDG in evaluating RN [58]. The value of amino acid PET using ^{11}C-MET, ^{18}F-FET, and ^{18}F-FDOPA for diagnosis of tumor recurrence or progression in patients with low-grade and high-grade glioma has been investigated in many studies [5,9,30,51,59-63]. The LNR of ^{11}C-MET PET revealed a sensitivity and specificity of 70 - 80 % for the differentiation of brain metastasis recurrence from radiation-related effects [5]. A higher diagnostic accuracy was shown by Grosu et al. with ^{11}C-MET able to differentiate tumor tissue from treatment related changes with a sensitivity of 91 % and a specificity of 100 % [64]. Using ^{18}F-FET PET the detection of tumor recurrence/progression was even more accurate, with a sensitivity and specificity of 100 and 93 %, respectively, compared with 93 and 50 % for MRI alone [30,59]. Pöpperl et al. was able to distinguish recurrent tumor and RN with 100 % accuracy applying a threshold of 2.0 for LNR_{max}. Galldiks et al.

suggested that the combined evaluation of the TBR_{mean} of ^{18}F-FET uptake and the pattern of the time–activity curve can differentiate brain metastasis recurrence from RN with high accuracy [10,59]. The lower specificity of ^{11}C-MET may be explained by its higher affinity for macrophages compared with ^{18}F-FET as demonstrated in animal experiments [65,66]. Furthermore, amino-acid PET was assumed to be superior to both choline PET and ^{18}F-FDG PET for diagnostic accuracy in distinguishing glioma recurrence from RN, possibly related to a lower uptake of ^{18}F-FET in macrophages compared with ^{18}F-FDG and ^{18}F-FCho [50,52,67]. Finally, a ^{18}F-FDOPA PET study revealed a sensitivity and specificity of more than 80% to distinguish brain metastasis recurrence and radiation-related effects [11]. However, the lack of physiological ^{18}F-FET uptake in the basal ganglia when compared with ^{18}F-FDOPA PET makes ^{18}F-FET the most promising amino acid tracer for PET imaging in brain tumor patients [5]. Importantly, in many studies the post-therapeutic effects were not specified as early-delayed or late treatment effects [5]. In our study, ^{18}F-FET uptake in GB was more intense and more heterogeneous compared to RN (see Figure 6.5). This was already recognized by Pöpperl et al., who stated that focal and high ^{18}F-FET uptake was suspicious for tumor recurrence, whereas low and homogeneous uptake around the resection cavity was considered benign due to post-treatment alterations of the BBB [59]. However, it should be kept in mind that (moderately) increased ^{18}F-FET uptake can also be seen in acute inflammatory lesions such as active multiple sclerosis and brain abscesses [23]. In our study, SUV_{max}, SUV_{mean}, LNR_{mean}, LNR_{max}, and parameters derived from KM, such as K_1, V_d and V_t, were significantly higher in GB than in RN using ^{18}F-FET PET. The high uptake in high-grade tumors is a result of increased expression of amino acid transporters that is not present in post-treatment changes [28,58]. A different K1 between GB and RN may reflect differences in cerebral blood flow and cerebral blood volume, which is known to be higher in GB due to neoangiogenesis. Though KM allowed the absolute quantification of ^{18}F-FDG and ^{18}F-FET uptake in GB and RN, it appeared that a static image 40-60 min post-injection was able to differentiate GB and RN as well as the parametric images derived from the kinetic analysis. Furthermore, significant correlations found between SUV and quantitative measures indicates that SUV captures the differences in K1 and k2.

Finally, ^{18}F-FCho PET was assumed to be promising in differentiating GB from RN. ^{18}F-FCho PET was studied in patients with solitary brain lesions and correctly identified patients with RN based on LNR [16]. Tan et al. showed higher sensitivity and specificity for ^{11}C-Cho PET compared to MRI and ^{18}F-FDG and Spaeth et al. noted a higher ^{18}F-FCho uptake in HGG compared to acute radiation injury [52,68]. Although promising results for the differentiation of RN and tumor recurrence in gliomas were reported, in our *in vivo* study ^{18}F-FCho was not able to differentiate "pure" GB from "pure" RN [16,68]. Using KM and graphical analysis we tried to interpret these results. K1 and Vt were not significantly different between GB and RN. As such, we cannot conclude that there is an increased choline transporter-like proteins mediated transport or a higher expression of choline kinase in GB compared to RN. The uptake in RN is influenced by leakage through the damaged BBB, inflammation and the immediate metabolization of choline raises the question if ^{18}F-Fluorobetaine attributes to the detected choline signal. Aspecific ^{18}F-FCho uptake was already described with a weak correlation between tumor grade and choline uptake [13]. Unfortunately, due to the inability of differentiating K1 from k3, the amount of ^{18}F-FCho uptake mediated by leakage through the damaged BBB and active trapping was not

possible. Only uptake by passive diffusion was negligible due to its polar characteristics [69]. However, we should keep in mind that the metabolism of choline tracers in humans is slower than in rodents and that the uptake was only investigated in one glioma model.

Overall, based on the current literature and our results, we propose a delayed ^{18}F-FDG PET image or preferentially and if available, a ^{18}F-FET PET for a differential diagnosis of HGG recurrence and therapy-related effects.

Question 4: Is *in-vivo* DCE-MRI able to discriminate between GB and RN in rats?

Although GB and RN have remarkably different histological characteristics, conventional MRI does not seem to capture them [70]. Multiple studies hypothesized that GB could be distinguished from RN based on differences in vascular properties [70-75]. Using T2*-weighted and dynamic susceptibility weighted or contrast material-enhanced (DSC) perfusion MRI, hemodynamic measurements can be obtained within the brain, such as the cerebral blood volume (CBV) [70]. Promising results were documented applying DSC-MRI to assist in follow-up patient management strategies and discriminating glioma recurrence from RN, but evidence is limited and DSC-MRI has some significant disadvantages [70-72,74]. Importantly, when considering application to tumors, the effects of extravascular leakage of contrast material on the T2 or T2* signal are difficult to quantify and, although estimates of contrast transfer coefficient can be made these are less reliable than those obtained with comparable dynamic T1-weighted contrast-enhanced MRI (DCE-MRI). Therefore, DCE-MRI is primarily recommended for pharmacodynamical assessment of antiangiogenic and antivascular therapies [70]. The possible role for DCE-MRI in differentiating recurrent GB versus RN was suggested by multiple research groups [73-76], including Kim et al. observing a superior diagnostic performance when adding DCE-MRI to contrast-enhanced T1-weighted MRI and DWI [73].

In our study, we compared the DCE curves obtained in GB and RN rats and also peformed kinetic analysis. We found that the maximal slope of the initial phase (wash-in rate, k), wash-out rate (D), and the time to reach the maximal intensity (TTP_F and TTP_O) of the DCE-MRI curves discriminated GB from RN. The fact that the wash-in rate and the TTP is higher in GB compared to RN can be explained by the higher vascular density in GB due to neo-angiogenesis, allowing the contrast agent to reach the tumor very fast. More vessels and subsequent more active transport mechanisms at the endothelial wall, the high capillary permeability and increased interstitial pressure in GB reduce retention and explain the fast wash-out rate in GB compared to RN. In RN, immunohistochemical staining showed little micro vascular proliferation and the presence of vessel wall thickening leading to blood vessel occlusion. The difference in vascular density was also confirmed, applying KM to our data, by a trend towards a higher V_p in case of GB. Artzi et al. recently documented a statistically significantly higher K_{trans}, K_{ep} and V_e in progressive disease compared to treatment related changes [74], while Bisdas et al. only found K_{trans} to be significantly different [70]. Applying the Extended-Tofts model on our DCE-MRI data, K_{trans}, K_{ep} and V_e were not significantly higher in GB than in RN. In the central necrotic part of GB and RN a continuous centripetal flow of contrast agent occurs, leading to a continuously increasing DCE-MRI curve. No

differences in semi-quantitative and quantitative variables were found between the central necrotic part in GB and RN.

Surprisingly, the higher wash-in and wash-out rate in GB compared to RN was only found based on semi-quantitative curve fitting, but not applying quantitative analysis. This may be due to a higher noise sensitivity when creating parametric maps on a voxel-by-voxel basis compared to curve fitting applied on a number of voxels averaged in a ROI. Furthermore, wash-in and wash-out rates derived from the Olea software are calculated separately before and after the curve reaches its maximum, while applying semi-quantitative analysis we fitted the DCE time-series to one mathematical function, which might be a more robust method. Another difficulty in our KM of DCE-MRI was to obtain a smooth AIF with expected artery contrast kinetics and minimal noise.

In agreement with Narang et al. [75], we can conclude that model-free metrics, including wash-in rate (k), wash-out rate (D) and TTP are promising in the discrimination of GB and RN and could have a more practical role to play in the routine clinical setting as well as in multicenter clinical trials, as these do not depend upon technical expertise needed for the more complex model-based analysis [75]. Because these significantly different metrics are evident within the first minutes of the DCE-MRI curve, in daily clinical routine, a DCE-MRI with an acquisition time of 5 min may suffice. However, a standard method for DCE-MRI analysis is urgent [78]. Furthermore, we need to point out that, using our *in vivo* models of "pure" GB and "pure" RN, we do not mimic exactly the clinical key question, as in the clinic mostly a mix of tumor recurrence and RN is present within the lesion post-treatment. As such, our results need to be confirmed in a combined model. The only well-characterized, orthotopic rodent model of radiation-induced brain necrosis including a tumor was introduced by Kumar et al. in which stereotactic radiosurgery induced focal RN in rat brain bearing human GB [79].

Final conclusion:

Because MRI has high sensitivity but poorer specificity, it should be used first, as a screening test for imaging brain tumors. If tumor recurrence is suspected after treatment, additional ^{18}F-FET, delayed ^{18}F-FDG PET or DCE-MRI may help in discriminating between post-treatment changes and tumor recurrence. Inclusion of ^{18}F-FCho or ^{18}F-FET PET in the RANO criteria may be helpful for early therapy response prediction in high-grade glioma. We recommend further validation of imaging modalities described in this work by systematic histopathological correlation in larger prospective trials.

REFERENCES

[1] Drevelegas A, Karkavelas G. Imaging of brain tumors with histological correlations. Chapter 6: High-grade gliomas. Berlin Heidelberg: Springer-Verlag 2011;157-200.

[2] Frosina G. Positron emission tomography of high-grade gliomas. Journal of Neurooncology 2016;127:415-425.

[3] Chang JH, Kim CY, Choi BS, et al. Pseudoprogression and Pseudoresponse in the Management of High-Grade Glioma : Optimal Decision Timing According to the Response Assessment of the Neuro Oncology Working Group. Journal of the Korean Neurosurgery Society 2014;55(1):5-11.

[4] Wen PY, Macdonald DR, Reardon DA, et al. Updated response assessment criteria for high-grade gliomas: response assessment in neuro-oncology working group. Journal of Clinical Oncology 2010;28:1963-1972.

[5] Galldiks N, Langen KJ. Amino Acid PET - An Imaging Option to Identify Treatment Response, Posttherapeutic Effects, and Tumor Recurrence? Frontiers in Neurology 2016;28(7):120.

[6] Basu S1, Alavi A. Molecular imaging (PET) of brain tumors. Neuroimaging Clinics of North America 2009;19(4):625-646.

[7] Mertens K, Acou M, Van Hauwe J, et al. Validation of 18F-FDG PET at conventional and delayed intervals for the discrimination of high-grade from low-grade gliomas. Clinical Nuclear Medicine 2013;38:495-500.

[8] Piroth MD, Pinkawa M, Holy R, et al. Prognostic value of early [18F]fluoroethyltyrosine positron emission tomography after radiochemotherapy in glioblastoma multiforme. International Journal of Radiation Oncology Biology Physics 2011;80:176-184.

[9] Galldiks N, Rapp M, Stoffels G, et al. Response assessment of bevacizumab in patients with recurrent malignant glioma using [18F]Fluoroethyl-L-tyrosine PET in comparison to MRI. European Journal of Nuclear Medicine and Molecular Imaging 2013;40:22-33.

[10] Galldiks N, Langen KJ, Holy R, et al. Assessment of treatment response in patients with glioblastoma using O-(2-18F-fluoroethyl)-L-tyrosine PET in comparison to MRI. Journal of Nuclear Medicine 2012;53:1048-1057.

[11] Lizarraga KJ, Allen-Auerbach M, Czernin J, et al. 18F-FDOPA PET for Differentiating Recurrent or Progressive Brain Metastatic Tumors from Late or Delayed Radiation Injury After Radiation Treatment. Journal of Nuclear Medicine 2014;55(1):30-36.

[12] Vallabhajosula S. ^{18}F-labelled Positron Emission Tomographic Radiopharmaceuticals in Oncology: An Overview of Radiochemistry and Mechanisms of Tumor Localization. Seminars in Nuclear Medicine 2007;37:400-419.

[13] Calabria FF, Barbarisi M, Gangemi V, et al. Molecular imaging of brain tumors with radiolabeled choline PET. Neurosurgery Reviews 2016; doi 10.1007/s10143-016-0756-1.

[14] DeGrado TR, Coleman RE, Wang S, et al. Synthesis and evaluation of 18F-labeled choline as an oncologic tracer for positron emission tomography: initial findings in prostate cancer. Cancer Research 2001;61(1):110-117.

[15] Treglia G, Giovannini E, Di Franco D, et al. The role of positron emission tomography using carbon-11 and fluorine-18 choline in tumors other than prostate cancer: a systematic review. Annals of Nuclear Medicine 2012;26(6):451-461.

[16] Kwee SA, Ko JP, Jiang CS, et al. Solitary brain lesions enhancing at MR imaging: evaluation with fluorine 18-fluorocholine PET. Radiology 2007;244:557-565.

[17] Li W, Ma L, Wang X, et al. 11C-choline PET/CT tumor recurrence detection and survival prediction in post-treatment patients with high-grade gliomas. Tumor Biology 2014;35:12353-12360.

[18] Dhermain FG, Hau P, Lanfermann H, et al. Advanced MRI and PET imaging for assessment of treatment response in patients with gliomas. Lancet Neurology 2010;9:906-920.

[19] Ahmed R, Oborski MJ, Hwang M, et al. Malignant gliomas: current perspectives in diagnosis, treatment, and early response assessment using advanced quantitative imaging methods. Cancer Management Research 2014;6:149-170.

[20] Mertens K, Slaets D, Lambert B, et al. PET with (18)F-labelled choline-based tracers for tumour imaging: a review of the literature. European Journal of Nuclear Medicine and Molecular Imaging 2010;37:2188-2193.

[21] Parashar B, Wernicke AG, Rice S, et al. Early assesment of radiation response using a novel functional imaging modality-[18F] Fluorocholine PET (FCH-PET): A pilot study. Discovery Medicine 2012;14:13-20.

[22] Hoekstra CJ, Paglianiti I, Hoekstra OS, et al. Monitoring response to therapy in cancer using [18F]-2-fluoro-2-deoxy-D-glucose and positron emission tomography- an overview of different analytical methods. European Journal of Nuclear Medicine 2000;27:731-743.

[23] Albert NL, Weller M, Suchorska B, et al. Response Assessment in Neuro-Oncology working group and European Association for Neuro-Oncology recommendations for the clinical use of PET imaging in gliomas. Neuro Oncology. 2016;18(9):1199-1208.

[24] Harris RJ, Cloughesy TF, Pope WB, et al. 18F-FDOPA and 18F-FLT positron emission tomography parametric response maps predict response in recurrent malignant gliomas treated with bevacizumab. Neuro Oncology 2012;14(8):1079-1089.

[25] Schwarzenberg J, Czernin J, Cloughesy TF, et al. Treatment response evaluation usinf 18F-FDOPA PET in patients with recurrent malignant glioma on bevacizumab therapy. Clinical Cancer Research 2014;20(13):3550-3559.

[26] Hutterer M, Nowosielski M, Putzer D, et al. O-(2-18F-Fluoroethyl)-L-Tyrosine PET Predicts Failure of Antiangiogenic Treatment in Patients with Recurrent High-Grade Glioma. Journal of Nuclear Medicine 2011;52:856-864.

[27] Galldiks N, Kracht LW, Burghaus L, et al. Use of 11C-methionine PET to monitor the effects of temozolomide chemotherapy in malignant gliomas. European Journal of Nuclear Medicine and Molecular Imaging 2006;33(5):516-524.

[28] Langen KJ, Hamacher K, Weckesser M, et al. O-(2-[18F]fluoroethyl)-l-tyrosine: uptake mechanisms and clinical applications. Nuclear Medicine and Biology 2006;33:287-294.

[29] Herholz K, Coope D, Jackson A. Metabolic and molecular imaging in neuro-oncology. Lancet Neurology 2007;(8):711-724.

[30] Rachinger W, Goetz C, Pöpperl G, et al. Positron emission tomography with O-(2-[18F] fluoroethyl)-l-tyrosine versus magnetic resonance imaging in the diagnosis of recurrent gliomas. Neurosurgery 2005;57(3):505-511.

[31] Roelcke U, Bruehlmeier M, Hefti M, et al. F-18 choline PET does not detect increased metabolism in F-18 fluoroethyltyrosine-negative low-grade gliomas. Clinical Nuclear Medicine 2012;37:e1-e3.

[32] Allen-Auerbach M, Weber WA. Measuring Response with FDG-PET: Methodological Aspects. The Oncologist 2009;14:369-377.

[33] Lammerstma AA, Hoekstra CJ, Giaccone G, et al. How should we analyse FDG PET studies for monitoring tumour response? European Journal of Nuclear Medicine and Molecular Imaging 2006;33:S16-S21.

[34] Moonshi SS, Bejot R, Atcha Z, et al. A comparison of PET imaging agents for the assessment of therapy efficacy in a rodent model of glioma. American Journal of Nuclear Medicine and Molecular Imaging 2013;3(5):397-407.

[35] Bao X, Wang MW, Zhang YP, et al. Early monitoring antiangiogenesis treatment response of Sunitinib in U87MG Tumor Xenograft by (18)F-FLT MicroPET/CT imaging. Biomed Research International 2014;218578:1-9.

[36] Chen W, Delaloye S, Silvermann DHS, et al. Predicting treatment response of malignant gliomas to bevacizumab and irinotecan by imaging proliferation with (18F)Fluorothymidine positron emission tomography: A pilot study. Journal of Clinical Oncology 2007;25:4714-4721.

[37] Schiepers C, Dahlbom M, Chen W, et al. Kinetics of 3'-deoxy-3'-18F-fluorothymidine during treatment monitoring of recurrent high-grade glioma. Journal of Nuclear Medicine 2010;51(5):720-727.

[38] Viel T, Schelhaas S, Wagner S, et al. Early assessment of the efficacy of temozolomide chemotherapy in experimental glioblastoma using [18F]FLT-PET imaging. PLoS One 2013;8(7):e67911.

[39] Nedergaard MK, Kristoffersen K, Michaelsen SR, et al. The use of longitudinal 18F-FET MicroPET imaging to evaluate response to irinotecan in orthotopic human glioblastoma multiforme xenografts. PLoS One 2014;9(2):e100009.

[40] Nedergaard MK, Michaelsen SR, Urup T, et al. 18F-FET microPET and microMRI for anti-VEGF and anti-PlGF response assessment in an orthotopic murine model of human glioblastoma. PLoS One 2015;10(2):e0115315.

[41] Nedergaard MK, Michaelsen SR, Perryman L, et al. Comparison of (18)F-FET and (18)F-FLT small animal PET for the assessment of anti-VEGF treatment response in an orthotopic model of glioblastoma. Nuclear Medicine and Biology 2016;43(3):198-205.

[42] Hattingen E, Pilatus U. Brain tumor imaging. Langen KJ, Galldiks N. Chapter: PET imaging of brain tumors. Berlin, Heidelberg: Springer 2016;121-135.

[43] Bobek-Billewicz B, Stasik-Pres G, Majchrzak H, et al. Differentiation between brain tumor recurrence and radiation injury using perfusion, diffusion-weighted imaging and MR spectroscopy. Folia Neuropathology 2010;48:81-92.

[44] Zhou J, Tryggestad E, Wen Z, et al. Differentiation between glioma and radiation necrosis using molecular resonance imaging of endogeneous proteins and peptides. Nature Medicine 2011;17:130-134.

[45] Wang S, Chen Y, Lal B, et al. Evaluation of radiation necrosis and malignant glioma in rat models using diffusion tensor MR imaging. Journal of Neurooncology 2012;107:51-60.

[46] Mullins ME, Barest GD, Schaefer PW, et al. Radiation necrosis versus glioma recurrence: conventional MR imaging clues to diagnosis. American Journal of Neuroradiology 2005;26:1967-1972.

[47] Alexiou GA, Tsiouris S, Kyritsis AP, et al. Glioma recurrence versus radiation necrosis: accuracy of current imaging modalities. Journal of Neurooncology 2009;95:1-11.

[48] Hustinx R, Pourdehnad M, Kaschten B, et al. PET imaging for differentiating recurrent brain tumor from radiation necrosis. Radiology Clinics North America 2005;43:35-47.

[49] Chao ST, Suh JH, Raja S, et al. The sensitivity and specificity of FDG PET in distinguishing recurrent brain tumor from radionecrosis in patients treated with stereotactic radiosurgery. International Journal of Cancer. 2001;96:191-197.

[50] Spaeth N, Wyss MT, Weber B, et al. Uptake of 18F-fluorocholine, 18F-fluoroethyl-L-tyrosine, and 18F-FDG in acute cerebral radiation injury in the rat: implications for separation of radiation necrosis from tumor recurrence. Journal of Nuclear Medicine 2004;45:1931-1938.

[51] Van Laere K, Ceyssens S, Van Calenbergh F, et al. Direct comparison of 18F-FDG and 11C-methionine PET in suspected recurrence of glioma: sensitivity, inter-observer variability and prognostic value. European Journal of Nuclear Medicine and Molecular Imaging 2005;32:39-51.

[52] Spaeth N, Wyss MT, Pahnke W, et al. Uptake of 18F-fluorocholine, 18F-fluoro-ethyl-L-tyrosine and 18F-fluoro-2-deoxyglucose in F98 gliomas in the rat. European Journal of Nuclear Medicine and Molecular Imaging 2006;33:673-682.

[53] Ricci PE, Karis JP, Heiserman JE, et al. Differentiating Recurrent Tumor from Radiation Necrosis: Time for Re-evaluation of Positron Emission Tomography? American Journal of Neuroradiology 1998;19:407-413.

[54] Caroline I, Rosenthal MA. Imaging modalities in high-grade gliomas: pseudoprogression, recurrence, or necrosis? Journal of Clinical Neuroscience 2012;19(5):633-637.

[55] Nihashi T, Dahabreh IJ, Terasawa T. Diagnostic accuracy of PET for recurrent glioma diagnosis: a meta-analysis. American Journal of Neuroradiology 2013;34(5):944-950.

[56] Spence AM, Muzi M, Mankoff DA, et al. 18F-FDG PET of gliomas at delayed intervals: improved distinction between tumor and normal gray matter. Journal of Nuclear Medicine 2004;45(10):1653-1659.

[57] Horky LL, Hsiao EM, Weiss SE. Dual phase FDG-PET imaging of brain metastases provides superior assessment of recurrence versus post-treatment necrosis. Journal of Neurooncology 2011;103:137-146.

[58] Chen W. Clinical applications of PET in brain tumors. Journal of Nuclear Medicine 2007;48(9):1468-1481.

[59] Pöpperl G, Götz C, Rachinger W, et al. Serial 0-(2-(18F)fluoroethyl)-L-tyrosine PET for monitoring the effects of intracavitary radioimmunotherapy in patients with malignant glioma. European Journal of Nuclear Medicine and Molecular Imaging 2006;33:792-800.

[60] Mehrkens JH, Pöpperl G, Rachinger W, et al. The positive predictive value of 0-(2-(18F)fluororethyl)-L-tyrosine (FET) PET in the diagnosis of a glioma recurrence after multimodal treatment. Journal of Neurooncology 2008;88:27-35.

[61] Galldiks N, Stoffels G, Filss C, et al. The use of dynamic O-(2-18F-fluoroethyl)-l-tyrosine PET in the diagnosis of patients with progressive and recurrent glioma. Neuro Oncology 2015;17(9):1293-1300.

[62] Herrmann K, Czernin J, Cloughesy T, et al. Comparison of visual and semiquantitative analysis of 18F-FDOPA-PET/ CT for recurrence detection in glioblastoma patients. Neuro Oncology 2014;16(4):603-609.

[63] Ullrich RT, Kracht L, Brunn A, et al. Methyl-l-11C-methionine PET as a diagnostic marker for malignant progression in patients with glioma. Journal of Nuclear Medicine 2009;50:1962-1968.

[64] Grosu AL, Astner ST, Riedel E, et al. An interindividual comparison of O-(2-[18F]fluoroethyl)-L-tyrosine (FET)- and L-[methyl-11C]methionine (MET)-PET in patients with brain gliomas and metastases. International Journal of Radiation Oncology Biology Physics 2011;81(4):1049-1058.

[65] Salber D1, Stoffels G, Pauleit D, et al. Differential uptake of [18F]FET and [3H]l-methionine in focal cortical ischemia. Nuclear Medicine and Biology 2006;33(8):1029-1035.

[66] Salber D, Stoffels G, Pauleit D, et al. Differential uptake of O-(2-18F-fluoroethyl)-L-tyrosine, L-3H-methionine, and 3H-deoxyglucose in brain abscesses. Journal of Nuclear Medicine 2007;48(12):2056-2062.

[67] Takenaka S1, Asano Y, Shinoda J, et al. Comparison of (11)C-methionine, (11)C-choline, and (18)F-fluorodeoxyglucose-PET for distinguishing glioma recurrence from radiation necrosis. Neurologia medico-chirurgica 2014;54(4):280-289.

[68] Tan H, Chen L, Guan Y, et al. Comparison of MRI, F-18 FDG, and 11C-Choline PET/CT for Their Potentials in Differentiating Brain Tumor Recurrence From Brain Tumor Necrosis Following Radiotherapy. Clinical Nuclear Medicine 2011;36:978-981.

[69] Kwee SA, Wei H, Sesterhenn I, et al. Localization of Primary Prostate Cancer with Dual-Phase 18F-Fluorocholine PET. Journal of Nuclear Medicine 2006;47:262-269.

[70] Bisdas S, Naegele T, Ritz R, et al. Distinguishing recurrent high-grade gliomas from radiation injury: a pilot study using dynamic contrast-enhanced MR imaging. Academic Radiology 2011;18:575-583.

[71] Barajas RF Jr, Chang JS, Segal MR, et al. Differentiation of recurrent glioblastoma multiforme from radiation necrosis after external beam radiation therapy with dynamic susceptibility-weighted contrast-enhanced perfusion MR imaging. Radiology 2009;253:486-496.

[72] Al Sayyari A, Buckley R, McHenery C, et al. Distinguishing recurrent primary brain tumor from radiation injury: a preliminary study using a susceptibility-weighted MR imaging-guided apparent diffusion coefficient analysis strategy. American Journal of Neuroradiology 2010;31:1049-1054.

[73] Kim HS, Goh MJ, Kim N, et al. Which combination of MR imaging modalities is best for predicting recurrent glioblastoma? Study of diagnostic accuracy and reproducibility. Radiology 2014;273:831-843.

[74] Artzi M, Liberman G, Nadav G, et al. Differentiation between treatment-related changes and progressive disease in patients with high grade brain tumors using support vector machine classification based on DCE MRI. Journal of Neurooncology 2016;127:515-524.

[75] Narang J, Jain R, Arbab AS, et al. Differentiating treatment-induced necrosis from recurrent/progressive brain tumor using nonmodel-based semiquantitative indices derived from dynamic contrast-enhanced T1-weighted MR perfusion. Neuro-Oncology 2011;13:1037-1046.

[76] Hazle JD, Jackson EF, Schomer DF, et al. Dynamic imaging of intracranial lesions using fast spin-echo imaging: differentiation of brain tumors and treatment effects. Journal of Magnetic Resonance Imaging 1997;7:1084-1093.

[77] Yee S, Chinnaiyan P, Wloch J, et al. Possible Characterization of the Brain Tumor Vascular Environment by a Novel Strategy of Quantitative Analysis in Dynamic Contrast Enhanced MR Imaging: A Combination of Both Patlak and Logan Analyses. Medical Physics 2016;43(6):3343.

[78] Buckley DL. Uncertainty in the analysis of tracer kinetics using dynamic contrast-enhanced T1-weighted MRI. Magnetic Resonance in Medicine 2002;47:601-606.

[79] Kumar S, Arbab AS, Jain R, et al. Development of a novel animal model to differentiate radiation necrosis from tumor recurrence. Journal of Neurooncology 2012;108(3):411-420.

Chapter 9.

Broader international context, relevance and future perspectives

"Images are more than pictures, they are data" [Gillies RJ].

PART I: BROADER INTERNATIONAL CONTEXT AND RELEVANCE

More than 250.000 new cases of primary malignant brain tumors are diagnosed annually worldwide, 77 % of which are gliomas [1]. Glioblastoma (GB) is the most malignant and most common glioma in adults, accounting for approximately 60 % of all malignant gliomas and has a high mortality and morbidity [2]. Even with an optimal treatment protocol, the median survival is only 12-14 months. This is because brain gliomas are characterized by a high local recurrence rate after therapy [3]. Secondly, post-treatment, delayed radiation necrosis (RN) occurs in approximately 5-25 % of the patients [4-6]. The premise of personalized treatment is the assessment of treatment response as early as possible. This will allow the therapy-strategy of the patient to be changed or discontinued, which will improve the efficacy of the treatment. Accurate therapy response assessment is also important for the management of these patients, because recurrence requires second line chemotherapy, whereas RN can be treated with steroids only. Currently, the diagnosis of tumor recurrence is confirmed by biopsy with an accuracy of > 95 %. However, brain biopsy requires an invasive procedure that may have potential complications such as hemorrhage [7]. In May 2016, the world health organization (WHO) classification of tumors of the central nervous system (CNS) broke with the traditional principle of diagnosis based on histologic criteria only and incorporated molecular markers. Currently, histologic and molecular information is combined to reach an integrated diagnosis [1]. This paradigm shift will have a major impact on the management of glioma patients as well as on imaging brain tumors. Conventional structural imaging provides exquisite anatomic detail but remains limited in the evaluation of molecular characteristics of brain tumors, therefore physiologic biomarkers derived from advanced imaging techniques are needed [8]. In this dissertation different positron emission tomography (PET) tracers and dynamic contrast enhanced magnetic resonance imaging (DCE-MRI) were investigated to define their role in the follow-up of GB, predicting early response or differentiating GB from RN. The identification of new biomarkers could have a great impact on the assessment of patients with glioma, increasing the accuracy of prognosis prediction and tailoring the treatment to the characteristics of a specific patient but requires standardization and validation [9].

PART II: FUTURE PERSPECTIVES

A. Standardization and validation of imaging biomarkers

In 2010 updated response criteria in HGG were published by the Response Assessment in Neuro-Oncology (RANO) Working Group incorporating MRI characteristics to address the recognized and accepted limitations of the Macdonald Criteria. These recommendations are an attempt to develop standardized assessment criteria. Importantly, it must be emphasized that this represents a work in progress. In coming years, as new volumetric and physiologic imaging techniques (eg, perfusion, permeability, and diffusion imaging; magnetic resonance spectroscopy; metabolic imaging) and other end points such as neuropsychological testing and quality-of-life measures are developed, the RANO Working Group anticipates incorporating these parameters into the response criteria [10]. However,

before incorporating new imaging biomarkers derived from biological imaging techniques, standardization concerning image acquisition, reconstruction and post-processing and validation across multiple centers should be performed and the optimal method should always be a trade-off between accuracy and clinical applicability [9,11]. Recently, the Cancer Research UK and the European Organization for Research and Treatment of Cancer (EORTC) assembled experts to review, debate and summarize the challenges of imaging biomarker validation and qualification suggesting a tailored 'roadmap', see Figure 9.1. This consensus group produced 14 key recommendations for accelerating the clinical translation of imaging biomarkers [12].
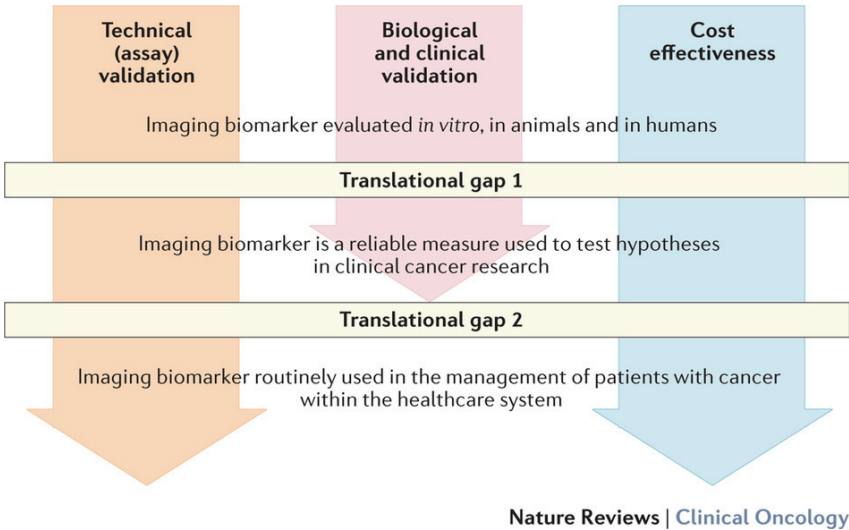

Figure 9.1. Overview of the imaging biomarker roadmap. Imaging biomarkers must cross translational gap 1 to become robust medical research tools, and translational gap 2 to be integrated into routine patient care. This goal is achieved through three parallel tracks of technical (assay) validation, biological and clinical validation, and cost effectiveness [12].

B. Radiomics

A new concept in the field of medical imaging is the high-throughput extraction of quantitative features that results in the conversion of images into mineable data and the subsequent analysis of these data for decision making; this practice is termed *radiomics*. This is in contrast with the traditional practice of treating medical images as pictures intended for visual interpretation only. Radiomic data are combined with other patient data and are mined with sophisticated bioinformatic tools to develop models that may potentially improve diagnostic, prognostic, and predictive accuracy of patients with cancer, illustrated in Figure 9.1 [13-15]. This allows further developments in the field of personalized medicine, tailoring treatment to the unique characteristics of the individual, ideally enhancing the quality of life and public health [16]. Importantly, using radiomics, more advanced MRI techniques and PET datasets can be combined to extract the maximum amount of data decoding the tumor phenotype of gliomas.
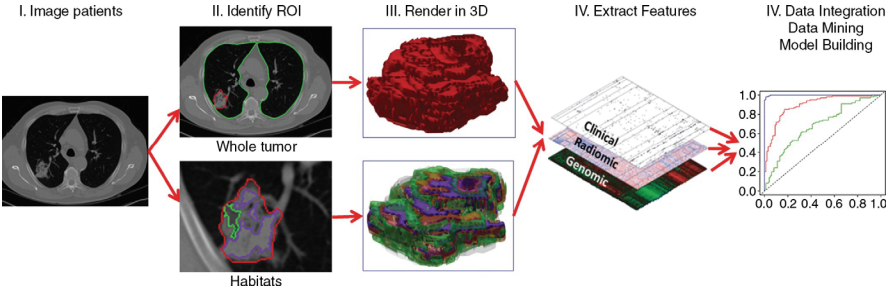
Figure 9.1. Flowchart showing the process of radiomics and the use of radiomics in decision support. Patient work-up requires information from disparate sources to be combined into a coherent model to describe where the lesion is, what it is, and what it is doing. Radiomics begins with acquisition of high-quality images. From these images, a region of interest (ROI) that contains either the whole tumor or subregions (ie, habitats) within the tumor can be identified. These are segmented with operator edits and are eventually rendered in three dimensions (3D). Quantitative features are extracted from these rendered volumes to generate a report, which is placed in a database along with other data, such as clinical and genomic data. These data are then mined to develop diagnostic, predictive, or prognostic models for outcomes of interest [13].

These multimodal imaging trials should be implemented on the basis of reader-independent image analysis and should be done as multicenter trials [17]. Enormous amounts of data are necessary with a reasonable rule of thumb that 10 samples (patients) are needed for each feature in a model based on binary classifiers. As such, the biggest challenge to establishing radiomics-based models as biomarkers to use in decision support is the sharing of image data and metadata across multiple sites [13].

Radiomics may plays a an important role in two major categories :

Personalized medicine

Combining different advanced MRI techniques and PET makes the extraction of an enormous amount of data containing a lot of valuable information possible. One important new development is _texture analysis_, which refers to a variety of mathematical methods that may be applied to describe the relationships between the grey level intensity pixels or voxels and their position within an MRI, PET or CT image [18]. This enables the determination of the heterogeneity and the spatial variation in tumors. The latter is of utmost importance in GB due to its heterogeneous phenotype with histologically variable mitotic activity, vascular proliferation, and/or necrosis, which could play a role in the poor response to therapy [19]. As an example, poor and chaotic tumor vascularization and reduced efficacy of the drug in less proliferating, hypoxic and acidic regions is known to contribute to treatment failure [20].

Different MRI techniques can be combined and extracting heterogeneity features from each of these modalities is possible delivering each valuable information, such as measuring non-enhancing tumor using diffusion weighted MRI (DWI) [21], calculating cerebral blood volume (CBV) maps using perfusion weighted MRI (PWI) and measuring metabolic ratio's using MR spectroscopy (MRS). These can be combined with PET extracted features representing measurements of local and regional uptake heterogeneity. A reasonable assumption is that their quantitation must be related to underlying

physiologic processes, such as vascularization, perfusion, tumor aggressiveness and hypoxia [22]. The wide range of radiopharmaceuticals currently available enables to visualize specific biological characteristics of glioma, including glucose consumption (^{18}F-FDG), cell membrane turnover (^{18}F-FCho), amino-acid transport (^{18}F-FET, ^{18}F-FDOPA) and hypoxia (^{18}F-FAZA). There are two main mechanisms that characterize the essential features of brain tumor tracers, namely transport across the blood-brain barrier and metabolization in tumor cells. Typically, the latter is supposed to provide differentiation and specificity, but for most tracers the former is the main factor determining tracer uptake into the tumor [23]. Currently, novel promising PET tracers are under investigation. The value of new amino acid PET tracers, such as α-^{11}C-methyl-tryptophan and ^{18}F-Fluciclovine as well as glutamine based amino acid PET tracers has been evaluated with promising results in glioma patients in terms of tumor delineation, prognostication and the differentiation of tumor recurrence from radiation injury. However, the number of examined subjects should be increased by subsequent studies [24-29]. Another interesting new PET target is the translocator protein (TSPO), a mitochondrial membrane protein highly expressed in activated microglia, macrophages and neoplastic cells. Imaging with the TSPO ligand [11]C-(R)PK11195 demonstrates increased binding in high-grade gliomas compared to low-grade gliomas and normal brain parenchyma [30,31]. More recently, the TSPO ligand ^{18}F-DPA-714 has been evaluated in glioma animal models but results in human glioma patients are pending [24,32,33]. Furthermore, a novel labeled integrin α(v)β3-targeting ^{18}F-AIF-NOTA-PRGD2 (^{18}F-RGD) tracer showed positive results in assessing sensitivity to concurrent chemoradiotherapy in GB [34]. Another approach was published by Oborski et al. suggesting the ability to image therapy-induced tumor cellular apoptosis using ^{18}F-2-(5-fluoro-pentyl)-2-methyl-malonic acid (^{18}F-ML-10) for early-therapy response assessment of a newly diagnosed GB patient [35].

Different textural parameters derived from PET have already been correlated with response in breast cancer, esophageal cancer, non-small cell lung cancer, cervical cancer and head and neck cancer [22,36-39]. ^{18}F-FET PET textural feature analysis in combination with LNRs or the combination of ^{18}F-FET uptake with Cho/Cr ratio and normalized $rCBV_{mean}$ has been suggested to be useful to distinguish brain metastasis recurrence or primary glioma recurrence from radiation injury, respectively [40,41]. However, in glioma, only limited research is conducted using texture analysis applied on PET and combined PET and MRI. Applying machine learning on these multiparametric PET and MRI extracted features could be an important step towards personalized medicine, aiming for an optimal treatment for an individual patient that is dependent on tumor characteristics in that individual [18]. As such, PET research is a hot topic at the moment with a lot of new developments in glioma imaging with a promising future in _personalized medicine_.

Genomic heterogeneity within tumors and across metastatic tumor sites in the same patient is the major cause of treatment failure and emergence of therapy resistance. The mining of radiomic data to detect correlations with genomic patterns is known as _radiogenomics_, and it has elicited especially great interest in the research community [13,16]. This potential correlation between imaging features and histologic patterns of tumors as well as tumor genetic profile can also enhance the accuracy of tumor classification

and response assessment through an integrated radio-histogenomic interpretation. One of the striking examples is the role that MR spectroscopy can play in determining the mutation status of isocitrate dehydrogenase (IDH1 and IDH2) genes, a key mutation that plays a significant role in the new WHO classification of CNS tumors. High-throughput sequencing identified recurrent mutations in the cytosolic isoform of the enzyme IDH1 in 12 % of GB. IDH1 catalyzes the oxidative decarboxylation of isocitrate to a-ketoglutarate, thereby reducing NADP+ to NADPH. NADPH is essential for the regeneration of reduced glutathione, which is important in the protection of cells against oxidative damage. Therefore, IDH1 may play an antioxidant role during oxidative stress. Some patients without IDH1 mutations harbor a mutation in the analogous amino acid residue of the IDH2 gene, encoding the mitochondrial isoform of IDH. Tumors harboring a mutation of the IDH1 gene have a better outcome than nonmutated tumors, whatever grade considered [42,43]. O^6-methylguanine-DNA methyltransferase (MGMT) is a DNA-repair enzyme that removes alkyl groups from the O^6 position of guanine, one of the most frequent sites of DNA alkylation induced by chemotherapeutic agents. Epigenetic silencing of the MGMT gene by promoter methylation is associated with loss of MGMT expression and reduced DNA-repair activity [42]. The MGMT promotor methylation status has been associated with a higher risk for pseudoprogression, increases tumor's sensitivity to the alkylating effects of temozolomide and is associated with increased risk of radiation-induced side effects [42,44]. Further studies must be done to validate radiogenomics both *in vitro* and *in vivo* using small animal models as well as image-guided spatially labeled tumor samples to achieve a comprehensive spatial profile of the tumor landscape that can be further used to accomplish the goal of precision medicine [43].

Dose painting by numbers

The invasive nature of malignant gliomas makes complete resection impossible in many cases without devastating neurologic effects. In RT, there is a well-known dose-response relationship for HGG with an increasing survival with increasing doses, but this effect seems to cap around 60 Gy, probably due to increased toxicity to the normal brain if a higher dose is delivered to the entire tumor volume. A major requirement to achieve better local tumor control, without increasing side effects to the adjacent normal brain, is an accurate definition of the most aggressive part of the tumor, which can be a target for dose escalation [17,45]. Three-dimensional (3D) conformal RT of HGG is currently based on CT and MRI. However, both contrast enhancement and hyperintense areas on MRI are not always an accurate measure of tumor extent as tumor cells have been detected far beyond the margins of contrast enhancement and the most aggressive parts within the tumor, which may be responsible for therapeutic resistance, cannot be identified. Therefore, additional information from molecular imaging techniques like PET may have an added value for RT target volume definition because these techniques enable the visualization of metabolically highly active regions and have the potential to make intra-tumoral biological heterogeneity imaging possible [3,45-47]. As HGG highly heterogeneous solid tumors, the concept of homogenously delivering the dose to the entire tumor volume seems inadequate [17]. In this perspective, in addition to the gross, the clinical and the planning target volume (GTV, CTV, and PTV, respectively), Ling et al. proposed the concept of the biological target volume (BTV) and multidimensional conformal RT [48]. This offers the opportunity to improve dose targeting applying a non-uniform dose to a target region,

delivering a higher proportion of the integral tumor dose to the more resistant regions of the tumor, called *dose-painting*. Since the introduction of the concept of dose painting of biologic image-defined regions within a target, two methods have been proposed: dose painting by contours and dose painting by numbers (DPBN). The former prescribes dose within biologic image-defined contours of the target. The latter prescribes dose to voxels throughout the target as a function of signal intensity of the corresponding voxel in a biologic image. Dose painting should lead to improved local tumor control without increasing the dose to the normal brain. Adaptive RT should also be considered as HGG have a tendency to increase their aggressiveness, even during the early chemo-radiation period [49,50]. Several PET tracers have been proposed for dose painting studies in GB in the future [51].

Multiple studies have already shown promising results with marked differences of the RT target volume between *amino acid PET* and MRI/CT [17,52]. In a prospective phase II study, Piroth et al. used a simultaneous integrated boost IMRT technique to deliver a boost dose of 72 Gy guided by ^{18}F-FET PET [53]. Rickey et al. showed that DPBN based on ^{18}F-FET PET in HGG was feasible by using a linear dose-escalation function between SUV 3 and 5 [47]. Furthermore, patients with ^{11}C-MET PET integrated into their treatment plan had a significantly longer survival time compared with patients whose treatment was planned based on MRI/CT only [17,52]. When delineating the radiation boost volumes using ^{18}F-FDOPA PET, a SUV_{max}-based threshold was recently proposed for defining high-grade portions of glioma [54]. However, prospective trials investigating the benefit of incorporating DPBN based on amino acid PET in the RT of HGG are still needed.

Hypoxia PET tracers are promising in the development of dose-painting because it is well known that tumor aggressiveness, metastatic spread, failure to achieve local tumor control, an increased rate of recurrence, and ultimate poor outcome are all associated with hypoxia. Consequently, the radiation dose necessary to achieve the same therapeutic effect is much higher for hypoxic tumors [55]. Postema et al. observed highly increased uptake of ^{18}F-FAZA in all glioma types, with a tumor-to-background (T/B) ratio ranging between 2 and 16 due to low uptake in normal brain tissue [56]. Grosu et al. demonstrated that ^{18}F-FAZA PET could be used for hypoxia directed IMRT in head and neck cancer [57]. However, ^{18}F-FAZA PET has not yet been applied in the RT treatment planning of HGG and should be selected for future trials.

Currently, we are conducting an *in vivo* proof of concept study applying ^{18}F-FET and ^{18}F-FAZA directed boost irradiation using our GB rat model. It is our interest to apply for a grant to conduct a phase I-II trial investigating the role of ^{18}F-FAZA and ^{18}F-FET in DPBN in GB patients.

Final conclusion: The identification of new MRI and PET biomarkers extracted using a radiomics or radiogenomics approach could have a great impact on the assessment of patients with glioma, increasing the accuracy of prognosis prediction and improving personalized medicine. However, standardization and validation are the key to success.

REFERENCES

[1] Louis DN, Perry A, Reifenberger G, et al. The 2016 World Health Organization Classification of Tumors of the Central Nervous System: a summary. Acta Neuropathologica 2016;131(6):803-820.

[2] Ahmed R, Oborski MJ, Hwang M, et al. Malignant gliomas: current perspectives in diagnosis, treatment, and early response assessment using advanced quantitative imaging methods. Cancer Management Research 2014;6:149-170.

[3] Grosu AL, Fieldmann HJ, Dick S, et al. Implications of IMT-SPECT for postoperative radiotherapy planning in patients with gliomas. International Journal of Radiation Oncology Biology Physics 2002;54(3):842-854.

[4] Ruben JD, Dally M, Bailey M, et al. Cerebral radiation necrosis: incidence, outcomes, and risk factors with emphasis on radiation parameters and chemotherapy. International Journal of Radiation Oncology Biology Physics 2006;65(2):499-508.

[5] Langleben DD, Segall GM. PET in differentiation of recurrent brain tumor from radiation injury. Journal of Nuclear Medicine 2000;41:1861-1867.

[6] Rahmathulla G, Marko NF, Weil RJ. Cerebral radiation necrosis: a review of the pathobiology, diagnosis and management considerations. Journal of Clinical Neuroscience 2013;20 (4):485-502.

[7] Chao ST, Suh JH, Raja S, et al. The sensitivity and specificity of FDG PET in distinguishing recurrent brain tumor from radionecrosis in patients treated with stereotactic radiosurgery. International Journal of Cancer 2001;96:191-197.

[8] Ricci PE. Imaging of adult brain tumors. Neuroimaging Clinics of North America 1999;9(4):651-669.

[9] Boellaard R. Standards for PET Image Acquisition and Quantitative Data Analysis. Journal of Nuclear Medicine 2009;50:11S-20S.

[10] Wen PY, Macdonald DR, Reardon DA, et al. Updated response assessment criteria for high-grade gliomas: response assessment in neuro-oncology working group. Journal of Clinical Oncology 2010;28:1963-1972.

[11] Lammertsma AA, Hoekstra CJ, Giaccone G, et al. How should we analyse FDG PET studies for monitoring tumour response? European Journal of Nuclear Medicine Molecular Imaging 2006;33(1):16-21.

[12] O'Connor JP, Aboagye EO, Adams JE, et al. Imaging biomarker roadmap for cancer studies. Nature Reviews Clinical Oncology 2017;14(3):169-186.

[13] Gillies RJ, Kinahan PE, Hricak H. Radiomics: Images Are More than Pictures, They Are Data. Radiology 2016;278(2):563-577.

[14] Lambin P, Rios-Velazquez E, Leijenaar R, et al. Radiomics: extracting more information from medical images using advanced feature analysis. European Journal of Cancer 2012; 48:441-446.

[15] Lu W, Chen W. Positron emission tomography/computerized tomography for tumor response assessment-a review of clinical practices and radiomics studies. Translational Cancer Research 2016;5(4):364-370.

[16] Schillaci O, Urbano N. Personalized medicine: a new option for nuclear medicine and molecular imaging in the third millennium. European Journal of Nuclear Medicine and Molecular Imaging 2017; doi: 10.1007/s00259-017-3616-5.

[18] Chicklore S, Goh V, Siddique M, et al. Quantifying tumour heterogeneity in 18F-FDG PET/CT imaging by texture analysis. European Journal of Nuclear Medicine and Molecular Imaging 2013;40(1): 133-140.

[17] Dhermain F. Radiotherapy of high-grade gliomas: current standards and new concepts, innovations in imaging and radiotherapy, and new therapeutic approaches. Chinese Journal of Cancer 2014;33(1):16-24.

[19] Omuro A, DeAngelis LM. Glioblastoma and other malignant gliomas: a clinical review. JAMA. 2013;310(17):1842-1850.

[20] Willaime JMY, Turkheimer FE, Kenny LM, et al. Quantification of intra-tumour cell proliferation heterogeneity using imaging descriptors of 18F-fluorothymidine-positron emission tomography. Physics in Medicine and Biology 2013;58:187-203.

[21] Gerstner ER1, Batchelor TT. Imaging and response criteria in gliomas. Current Opinion in Oncology 2010;22(6):598-603.

[22] Tixier F, Le Rest CC, Hatt M, et al. Intra-tumour heterogeneity characterized by textural features on baseline 18F-FDG PET images predicts response to concomitant radiochemotherapy in esophageal cancer. Journal of Nuclear Medicine 2011;52(3):369-378.

[23] Herholz K. Brain Tumors: An Update on Clinical PET Research in Gliomas. Seminars in Nuclear Medicine 2017;47(1):5-17.

[24] Galldiks N, Langen KJ. Amino Acid PET - An Imaging Option to Identify Treatment Response, Posttherapeutic Effects, and Tumor Recurrence? Frontiers in Neurology 2016;28(7):120.

[25] Kamson DO, Juhasz C, Buth A, et al. Tryptophan PET in pretreatment delineation of newly-diagnosed gliomas: MRI and histopathologic correlates. Journal of Neuro-Oncology 2013;112:121-132.

[26] Kondo A, Ishii H, Aoki S, et al. Phase IIa clinical study of [18F]fluciclovine: efficacy and safety of a new PET tracer for brain tumors. Annals of Nuclear Medicine 2016;30:608-618.

[27] Venneti S, Dunphy MP, Zhang H, et al. Glutamine-based PET imaging facilitates enhanced metabolic evaluation of gliomas in vivo. Science Translational Medicine 2015;7(274):274ra17.

[28] Alkonyi B, Barger GR, Mittal S, et al. Accurate differentiation of recurrent gliomas from radiation injury by kinetic analysis of alpha-11C-methyl-L-tryptophan PET. Journal of Nuclear Medicine 2012;53:1058-1064.

[29] Kamson DO, Mittal S, Robinette NL, et al. Increased tryptophan uptake on PET has strong independent prognostic value in patients with a previously treated high-grade glioma. Neuro-Oncology 2014;16:1373-1383.

[30] Su, Z., Herholz, K., Gerhard, A., et al. [(11)C]-(R)PK11195 tracer kinetics in the brain of glioma patients and a comparison of two referencing approaches. European Journal of Nuclear Medicine and Molecular Imaging 2013;40:1406-1419.

[31] Su Z, Roncaroli F, Durrenberger PF, et al. The 18-kDa mitochondrial translocator protein in human gliomas: a 11C-(R)PK11195 PET imaging and neuropathology study. Journal of Nuclear Medicine 2015;56,512-517.

[32] Winkeler A, Boisgard R, Awde A, et al. The translocator protein ligand [18F]DPA-714 images glioma and activated microglia in vivo. European Journal of Nuclear Medicine and Molecular Imaging 2012;39:811-823.

[33] Awde AR, Boisgard R, Theze B, et al. The translocator protein radioligand 18F-DPA-714 monitors antitumor effect of erufosine in a rat 9L intracranial glioma model. Journal of Nuclear Medicine 2013;54:2125-2131.

[34] Zhang H, Liu N, Gao S, et al. Can an ^{18}F-ALF-NOTA-PRGD2 PET/CT Scan Predict Treatment Sensitivity to Concurrent Chemoradiotherapy in Patients with Newly Diagnosed Glioblastoma? Journal of Nuclear Medicine 2016;57(4):524-529.

[35] Oborski MJ, Laymon CM, Qian Y, et al. Challenges and Approaches to Quantitative Therapy Response Assessment in Glioblastoma Multiforme Using the Novel Apoptosis Positron Emission Tomography Tracer F-18 ML-10. Translational Oncology 2014;7(1):111-119.

[36] Tan S, Kligerman S, Chen W, et al. Spatial-temporal [^{18}F]FDG-PET features for predicting pathologic response of esophageal cancer to neoadjuvant chemoradiation therapy. International Journal of Radiation Oncology Biology Physics 2013;85(5):1375-1382.

[37] Cook GJ, Yip C, Siddique M, et al. Are pre-treatment 18F-FDG PET tumour texture features in non-small cell lung cancer associated with response and survival after chemoradiotherapy? Journal of Nuclear Medicine 2013;54(1):19-26.

[38] Yu H, Caldwell C, Mah K, et al. Coregistered FDG PET/CT-based textural characterization of head and neck cancer for radiation treatment planning. IEEE Translational Medical Imaging 2009;28(3):374-383.

[39] El Naqa I, Grigsby P, Apte A, et al. Exploring feature-based approaches in PET images for predicting cancer treatment outcomes. Pattern Recognition 2009;42(6):1162-1171.

[40] Jena A1, Taneja S, Gambhir A, et al. Glioma Recurrence Versus Radiation Necrosis: Single-Session Multiparametric Approach Using Simultaneous O-(2-18F-Fluoroethyl)-L-Tyrosine PET/MRI. Clinical Nuclear Medicine 2016;41(5):e228-236.

[41] Lohmann P, Stoffels G, Ceccon G, et al. Radiation injury vs. recurrent brain metastasis: combining textural feature radiomics analysis and standard parameters may increase 18F-FET PET accuracy without dynamic scans. European Radiology 2016; doi 10.1007/s00330-016-4638-2.

[42] Ducray F, Idbaih A, Wang XW, et al. Predictive and prognostic factors for gliomas. Expert Reviews Anticancer Therapy 2011;11(5):781-789.

[43] Carrillo JA, Lai A, Nghiemphu PL, et al. Relationship between tumor enhancement, edema, IDH1 mutational status, MGMT promotor methylation, and survival in glioblastoma. American Journal of Neuroradiology 2012;33:1349-1355.

[44] Thomas AA, Arevalo-Perez J, Kaley T, et al. Dynamic contrast enhanced T1 MRI perfusion differentiates pseudoprogression from recurrent glioblastoma. Journal of Neurooncology 2015;125:183-190.

[45] Grosu AL, Weber WA, Feldmann HJ, et al. First experience with 123I-alfa-methyl-tyrosine SPECT in the 3-D radiation treatment planning of brain gliomas. International Journal of Radiation Oncology Biology Physics 2000;47(2):517-526.

[46] Niyazi M, Geisler J, Siefert A, et al. FET-PET for malignant glioma treatment planning. Radiotherapy and Oncology 2011;99:44-48.

[47] Rickhey M, Koelbl O, Eilles C, et al. A biologically adapted dose-escalation approach demonstrated for 18F-FET PET in brain tumors. Strahlentherapie und Onkologie 2008;184(10):536-542.

[48] Ling CC, Humm J, Larson S, et al. Towards multidimensional radiotherapy (MD-CRT): Biological imaging and biological conformality. International Journal of Radiation Oncology Biology Physics 2000;47:551-560.

[49] Bentzen SM, Gregoire V. Molecular imaging-based dose painting: a novel paradigm for radiation therapy description. Seminars in Radiation Oncology 2011;21:101-110.

[50] Duprez F, De Neve W, De Gersem W, et al. Adaptive dose painting by numbers for head-and-neck cancer. International Journal of Radiation Oncology Biology Physics 2011;80(4):1045-1055.

[51] Albert NL, Weller M, Suchorska B, et al. Response Assessment in Neuro-Oncology working group and European Association for Neuro-Oncology recommendations for the clinical use of PET imaging in gliomas. Neuro Oncology 2016;18(9):1199-1208.

[52] Galldiks N, Langen KJ, Pope WB. From the clinician's point of view - What is the status quo of positron emission tomography in patients with brain tumors? Neuro Oncology 2015;17(11):1434-1444.

[53] Piroth MD1, Pinkawa M, Holy R, et al. Integrated boost IMRT with FET-PET-adapted local dose escalation in glioblastomas. Results of a prospective phase II study. Strahlentherapie und Onkologie 2012;188(4):334-339.

[54] Pafundi DH, Laack NN, Youland RS, et al. Biopsy validation of 18F-DOPA PET and biodistribution in gliomas for neurosurgical planning and radiotherapy target delineation: results of a prospective pilot study. Neuro Oncology 2013;15:1058-1067.

[55] Lopci E, Grassi I, Chiti A, et al. PET radiopharmaceuticals for imaging of tumor hypoxia: a review of the evidence. Amercian Journal of Nuclear Medicine and Molecular Imaging 2014:7;4(4):365-384.

[56] Postema EJ, McEwan AJ, Riauka TA, et al. Initial results of hypoxia imaging using 1-alpha-D: -(5-deoxy-5-[18F]-fluoroarabinofuranosyl)-2-nitroimidazole (18F-FAZA). European Journal of Nuclear Medicine and Molecular Imaging 2009;36(10):1565-1573.

[57] Grosu AL, Souvatzoglou M, Röper B, et al. Hypoxia imaging with FAZA-PET and theoretical considerations with regard to dose painting for individualization of radiotherapy in patients with head and neck cancer. International Journal of Radiation Oncology Biology Physics 2007;69(2):541-551.

Chapter 10: Summary – Samenvatting – Curriculum Vitae

Chapter 10.

Summary – Samenvatting
Curriculum Vitae

"It always seems impossible until its done"
[Nelson Mandela].

Summary

Glioblastoma (GB) is the most malignant and most common glioma in adults and has a high mortality rate. Standard treatment consists of radiation therapy (RT) with concomitant chemotherapy (temozolomide). Even with an optimal treatment protocol, the median survival is only 12-14 months. This is because GB are highly proliferative and infiltrate into the normal surrounding brain tissue resulting in an inevitable local recurrence after therapy. The assessment of treatment response as early as possible is the premise of personalized medicine enabling to change or discontinue the therapy of the patient to prevent ineffective therapy or prevent unnecessary side effects of the treatment. Imaging plays an important role in the treatment follow-up of patients with brain tumors. Computed tomography (CT) and magnetic resonance imaging (MRI) represent the two most important and commonly used imaging modalities that have a significant impact on patient care. In 2010 new response criteria for Response Assessment in Neuro-Oncology (RANO) were introduced including the tumor size (in 2D) as measured on T2- and Fluid Attenuated Inversion Recovery (FLAIR)-weighted images, in addition to the contrast-enhancing tumor part on MRI. Although the RANO criteria address some of the limitations of the previous MacDonald criteria for the evaluation of therapy in high-grade glioma, they do not take into account changes in tumor biology, which may precede anatomical changes of the tumor volume. Furthermore, increased enhancement after the administration of gadolinium and FLAIR/T2 hyperintense signal abnormalities can also occur due to treatment-related inflammation, postsurgical changes, subacute irradiation effects and radiation necrosis (RN).

Therefore, in **chapter 4**, our first goal was to investigate if positron emission tomography (PET) and MRI would be able to evaluate and predict treatment response in GB at an early time point after the start of treatment. Due to well-known diagnostic limitations of ^{18}F-fluorodeoxyglucose (^{18}F-FDG) PET, related to the high uptake in normal brain tissue and nonspecific uptake, we investigated the potential of ^{18}F-fluoromethylcholine (^{18}F-FCho) PET for response prediction in GB patients treated with the Stupp regimen. Rapidly proliferating GB have increased membrane/fatty acid requirements, which may result in a higher ^{18}F-FCho uptake than in healthy brain tissue, and may precede post-treatment anatomical changes on conventional MRI. We found that the parameter (MTV x SUV_{mean}) derived from ^{18}F-FCho PET, including both the metabolic tumor volume (MTV) and the mean tracer uptake (SUV_{mean}), allowed prediction of therapy response as early as 1 month after the completion of RT. Interestingly, the tumor volume derived from contrast-enhanced MRI was able to predict response earlier, at week 6 during RT. Although we did not find any cases of pseudoprogression, our finding warrants caution. This is because the possibility of pseudoprogression makes the determination of response based on contrast-enhanced MRI difficult within the first 12 weeks post-RT. Therefore, inclusion of PET in the RANO criteria might be helpful for early therapy response prediction in high-grade glioma

In **chapter 5**, we investigated the use of PET and MRI for assessing treatment response in a rat model of GB. The first step was the development of a GB rat model that mimics human GB treatment to bridge the gap between preclinical and clinical RT technology. We described an orthotopic allograft F98 GB rat model and subsequently validated MRI-guided 3D conformal arc RT using a high-precision small animal

radiation research platform (SARRP). We concluded that using MRI guidance, dose delivery to the target volume is more homogeneous and steadily improves using a single beam, a single arc and three non-coplanar arcs, respectively. Our results also confirmed that MRI-guided non-coplanar arcs minimize the dose delivered to the normal brain tissue and the γH2AX staining of irradiated rat brain tissue confirmed a 3 x 3 mm beam with sharp beam edges. The effectiveness of the combined modality treatment (RT and TMZ) was confirmed using follow-up contrast-enhanced MRI, with a stable tumor growth until 9 days post-irradiation, while a continuous tumor growth was observed in the control group. Subsequently, we investigated if ^{18}F-FDG PET and ^{18}F-FCho PET were also able to observe the treatment effect as indicated by contrast-enhanced MRI. Based on our results, it is clear that including both the MTV and the mean tracer uptake, is superior to the MTV only in detecting the effect of therapy, both for ^{18}F-FDG at conventional and delayed time intervals. Using (SUV$_{mean}$ x MTV), conventional ^{18}F-FDG PET detects treatment effect starting as soon as day 5 post-therapy, comparable to contrast-enhanced MRI. Importantly, delayed ^{18}F-FDG PET was able to detect the treatment effect earlier, starting at day 2 post-irradiation. ^{18}F-FCho PET was not able to detect the effects of treatment at any time point.

A second issue in the treatment response assessment in GB are the unwanted but inevitably early and late therapy-related effects on healthy brain tissue. Post-treatment, RN occurs in 5-25 % of the patients. This often results in a major problem in the clinic to differentiate RN from recurrent brain tumor as both entities frequently develop at the resection site and often have a similar appearance on conventional MRI. Obviously, a correct diagnosis is important for further patient management. RN may require the administration of steroids whereas tumor recurrence necessitates second line treatment. However, a definite diagnosis requires a biopsy which is subject to sampling error, is invasive and can lead to potential complications such as brain hemorrhage.

Hence, our goal was to investigate whether non-invasive functional imaging, such as PET, was able to differentiate GB from RN. Considering the lacking pathological confirmation of RN in the clinic, we performed *in vivo* experiments, described in **chapter 6**. First, we developed a rat model for RN by irradiating the normal brain using the SARRP. RN was confirmed on MRI in the periventricular white matter 5-8 months post-irradiation. Subsequently, we compared the uptake of ^{18}F-FDG, ^{18}F-FCho, and ^{18}F-FET semi-quantitatively in GB and RN. We found significant higher values for SUV$_{max}$, SUV$_{mean}$, LNR$_{mean}$ and LNR$_{max}$ in GB compared to RN on early ^{18}F-FDG PET images (40 minutes after tracer injection), late ^{18}F-FDG PET images (240 minutes after tracer injection) and ^{18}F-FET PET. The difference in LNR$_{mean}$ and LNR$_{max}$ between GB and RN was higher on the delayed ^{18}F-FDG PET scan compared to the conventional ^{18}F-FDG PET. This finding suggests that, in the clinic, a late ^{18}F-FDG PET acquisition is preferred to discriminate between GB and RN. ^{18}F-FCho PET derived semi-quantitative variables were not able to differentiate GB from RN. To clarify the above-mentioned results, we further explored the uptake mechanisms of the three tracers using kinetic modeling (KM) and graphical analysis (GA). For ^{18}F-FDG PET, in GB, a higher phosphorylation rate by hexokinase resulting in a higher influx rate was found compared to RN. Applying a 1-compartment model for ^{18}F-FET, a higher K_1 was found in GB than in RN, probably by the presence of more LAT, B$^{0,+}$ and B^0 transporters in GB. Important correlations were found between SUV and kinetic or graphical measures for ^{18}F-FDG and ^{18}F-FET. Based on these results we assume that SUV is able to capture kinetic differences. For ^{18}F-FCho, a 1-

compartmental model is suggested for absolute quantification, but does not allow clarifying the uptake mechanism in GB and RN. As such, based on the current literature and our results, we propose a delayed ^{18}F-FDG PET image or preferentially and if available, a ^{18}F-FET PET for a differential diagnosis of HGG recurrence and therapy-related effects.

In the literature, more advanced MRI techniques also yield promising results in discriminating tumor recurrence from therapy related effects. Dynamic contrast-enhanced MRI (DCE-MRI) allows the straightforward characterization of the vascular microenvironment of a post-treatment brain tumor. As vascular properties, such as vascular density, permeability, blood flow and the composition of the extravascular space are probably different between GB and RN, DCE-MRI is a promising MRI technique for discriminating GB from RN. In **chapter 7**, we compared semi-quantitative parameters extracted from DCE-MRI signal intensity time curves and quantitative parameters derived using KM between our GB and RN rat model. Based on our results, DCE-MRI may be useful to discriminate GB from RN. The wash-in rate (k) and time to peak (TTP), which could be derived from a 5 min DCE-MRI acquisition, were able to distinguish GB from RN while other quantitative and semi-quantitative parameters were not.

A general discussion and overview of the broader international context, relevance and future perspectives were given in **chapter 8 and 9**.

Samenvatting

Glioblastoma (GB) zijn de meest kwaadaardige en meest frequente glioma's bij volwassenen en hebben een hoge mortaliteit. De standaardbehandeling bestaat uit chirurgie gevolgd door een combinatie van radiotherapie (RT) en chemotherapie (temozolomide). Ondanks een optimale behandeling is de gemiddelde overleving slechts 12-14 maanden. Dit is te wijten aan het feit dat GB sterk proliferatieve tumoren zijn die infiltreren in het normaal hersenweefsel waardoor lokaal herval na therapie nagenoeg onvermijdelijk is. Om een gepersonaliseerde therapie mogelijk te maken is het zo vroeg mogelijk vaststellen van een respons op de therapie noodzakelijk. Dit zou namelijk toe laten om de therapie te wijzigen of de therapie stop te zetten om ineffectieve behandelingen en onnodige nevenwerkingen te voorkomen. Medische beeldvorming speelt een belangrijke rol in de opvolging van patiënten met hersentumoren na therapie. Computer tomografie (CT) en magnetische resonantie beeldvorming (MRI) zijn de twee belangrijkste en meest toegepaste beeldvormingsmodaliteiten die een grote impact hebben op de patiëntenzorg. In 2010 werden nieuwe criteria, de zogenaamde 'Response Assessment in Neuro-Oncology (RANO)' criteria, geïntroduceerd voor de opvolging van therapierespons van hersentumoren. Deze criteria houden rekening met het deel van de tumor dat opkleurt op MRI beelden na het toedienen van contrast en de afmeting van de tumor (in 2D) op T2- en Fluid Attenuated Inversion Recovery (FLAIR)-gewogen MRI beelden. Ondanks dat deze nieuwe criteria een duidelijke verbetering zijn in vergelijking met de voorgaande MacDonald criteria houden de RANO criteria geen rekening met wijzigingen in de biologie van de tumor, die anatomische wijzigingen zouden kunnen voorafgaan. Bovendien kan een toename in contrastopname en hyperintens signaal op FLAIR/T2 gewogen MR beelden ook optreden als gevolg van therapie gerelateerde effecten zoals inflammatie, wijzigingen na chirurgie en subacute stralingseffecten en radionecrose (RN). Op basis van conventionele MRI is het dus niet mogelijk deze laatste te onderscheiden van heroptredende hersentumor.

Ons eerste doel in **hoofdstuk 4** was daarom om na te gaan of positron emissie tomografie (PET) en MRI therapierespons in GB patiënten kan evalueren of voorspellen op een vroeg tijdstip na het starten van de therapie. Door de beperkingen van ^{18}F-fluorodeoxyglucose (^{18}F-FDG) PET, namelijk een hoge opname in normaal hersenweefsel en aspecifieke opname (o.a. inflammatie), onderzochten we de mogelijke rol van ^{18}F-fluoromethylcholine (^{18}F-FCho) PET in het voorspellen van therapierespons in GB patiënten behandeld met RT en chemotherapie. Snel prolifererende GB cellen hebben een verhoogde nood aan fosfolipiden, zoals fosfatidylcholine, die de basis vormen voor de aanmaak van celmembranen. De kwaadaardige hersentumoren zouden dus meer ^{18}F-FCho kunnen opnemen in vergelijking met normaal hersenweefsel en dit zou anatomische wijzigingen na therapie, zichtbaar op conventionele MRI, kunnen voorafgaan. Onze resultaten tonen aan dat het product van het metabool tumor volume (MTV) en de gemiddelde ^{18}F-FCho opname in de tumor (SUV_{mean}), (MTV x SUV_{mean}), de respons op therapie kan voorspellen ten vroegste 1 maand na het beëindigen van de RT. Het was zelfs mogelijk om de therapierespons vroeger te voorspellen aan de hand van het contrast aankleurend tumorvolume op MRI, namelijk op week 6 tijdens RT. Toch is deze conclusie onder voorbehoud omdat pseudoprogressie mogelijk is waardoor het bepalen van therapierespons op basis van contrastopname op MR onzeker is

binnen 12 weken na het einde van de therapie. Daarom zou inclusie van PET in de RANO criteria wellicht kunnen helpen bij het voorspellen van therapierespons van hooggradige glioma.

In **hoofdstuk 5** hebben we onderzocht of PET en MRI kunnen gebruikt worden voor het bepalen van therapierespons in een rat model van GB. Een eerste stap was de ontwikkeling van een GB rat model dat de humane therapie van GB nabootst om zo preklinische en klinische RT technologie dichter bij elkaar te brengen. We hebben een orthotoop allograft F98 GB rat model geoptimaliseerd en vervolgens hebben we MRI geleide 3D conformele RT gevalideerd, waarbij gebruik werd gemaakt van een 'Small Animal Radiation Research Platform' (SARRP). We concludeerden dat aan de hand van MRI geleide radiotherapie het doelvolume op een meer homogene wijze bestraald werd en dat de homogeniteit respectievelijk verbetert bij gebruik van een enkele bundel, een enkele rotatie (arc) en 3 niet-coplanaire rotaties (arcs). Onze resultaten toonden ook aan dat bij het toepassen van MRI geleide niet-coplanaire rotaties de dosis ter hoogte van normaal hersenweefsel geminimaliseerd werd. Verder werd aan de hand van de γH2AX kleuring de bundelafmeting (3 x 3 mm) bevestigd. Het effect van de gecombineerde behandeling werd aangetoond aan de hand van sequentiële MR beeldvorming met contrast toediening. Hierbij werd een stabiele tumorgroei waargenomen tot 9 dagen na het einde van de RT, terwijl een continue tumorgroei zichtbaar was in een controle groep. Vervolgens werd nagegaan of ^{18}F-FDG PET en ^{18}F-FCho PET eveneens het effect van de behandeling konden aantonen zoals zichtbaar was op MRI. Onze resultaten tonen dat inclusie van zowel MTV als de SUV$_{mean}$ nodig is voor het detecteren van het effect van de therapie. Dit was geldig zowel voor de vroege als late ^{18}F-FDG PET scan. Aan de hand van (MTV x SUV$_{mean}$) kon ^{18}F-FDG PET het effect van de therapie detecteren vanaf 5 dagen na therapie, wat vergelijkbaar was met T1-gewogen MRI met contrast toediening. Een late ^{18}F-FDG PET scan kon het effect van therapie vroeger aan tonen, namelijk 2 dagen post-therapie. ^{18}F-FCho PET bleek niet in staat te zijn om het effect van de therapie waar te nemen.

Een tweede heikel punt in het bepalen van therapierespons in GB zijn de ongewenste maar onvermijdelijke late therapie-effecten op hersenweefsel. Na therapie komt RN voor bij 5-25 % van de patiënten. Dit resulteert vaak in een groot probleem in de kliniek om deze therapie geïnduceerde effecten te onderscheiden van tumorherval. Beide treden op in de rand van de resectie krater en hebben vaak een gelijkaardige presentatie op conventionele MR beeldvorming. Een correcte diagnose is nochtans van groot belang aangezien RN kan behandeld worden met steroïden terwijl voor tumorherval een tweedelijnstherapie aangewezen is. Op dit moment is een definitieve diagnose enkel mogelijk door het nemen van een biopsie waar enkele nadelen aan verbonden zijn. Een biopsie is invasief, soms niet representatief voor wat er zich in werkelijkheid afspeelt en er zijn complicaties mogelijk zoals hersenbloedingen.

Vandaar is ons doel om na te gaan of niet-invasieve functionele beeldvorming, zoals PET, in staat is om GB te onderscheiden van RN. Bij een vermoeden van RN is er vaak geen biopsie en dus geen bevestiging van de diagnose van RN. Daarom werd geopteerd om een *in vivo* studie uit te voeren, beschreven in **hoofdstuk 6**. Eerst werd een rat model voor RN ontwikkeld door het bestralen van normaal hersenweefsel met de SARRP. RN in de periventriculaire witte stof werd bevestigd aan de hand

van MRI 5-8 maanden na de bestraling. Vervolgens hebben we de opname van ^{18}F-FDG, ^{18}F-FCho, en ^{18}F-FET semi-kwantitatief vergeleken in GB en RN. Significante hogere SUV_{max}, SUV_{mean}, LNR_{mean} en LNR_{max} werden gevonden in GB in vergelijking met RN op de vroege ^{18}F-FDG PET beelden (40 minuten na tracer injectie), late ^{18}F-FDG PET beelden (240 minuten na tracer injectie) en ^{18}F-FET PET. Het verschil in LNR_{mean} en LNR_{max} tussen GB en RN was hoger op de late ^{18}F-FDG PET scan in vergelijking met de vroege ^{18}F-FDG PET scan. Deze bevinding suggereert dat in de kliniek een late ^{18}F-FDG PET scan de voorkeur heeft om GB te onderscheiden van RN. Semi-kwantitatieve variabelen afgeleid van ^{18}F-FCho PET waren niet in staat om GB te onderscheiden van RN. Om deze bovenstaande bevindingen te verklaren hebben we de opnamemechanismen van de 3 PET tracers verder bestudeerd aan de hand van kinetische modellering (KM) en grafische analyse (GA). Voor ^{18}F-FDG PET werd een verhoogde fosforylatiesnelheid waargenomen in GB in vergelijking met RN. Dit resulteert in een hogere ^{18}F-FDG influx snelheid (K_i) in GB versus RN. Door middel van een 1-compartimenteel model voor ^{18}F-FET werd een hogere K_1 waarde gevonden in GB ten opzichte van RN, waarschijnlijk doordat er meer LAT, $B^{0,+}$ en B^0 transporters aanwezig zijn in GB versus RN. Significante correlaties werden gevonden tussen SUV en variabelen uit onze kinetische of grafische analyse van ^{18}F-FDG en ^{18}F-FET. Op basis van deze resultaten mogen we dus aannemen dat de kinetische verschillen tussen GB en RN kunnen aangetoond worden op basis van SUV waarden. Voor absolute kwantificatie van ^{18}F-FCho PET is een 1-compartimenteel model aangewezen, doch laat deze niet toe om het opnamemechanisme van ^{18}F-FCho te verklaren in GB en RN. Op basis van de huidige literatuur en onze resultaten kunnen we besluiten dat een late ^{18}F-FDG PET of een ^{18}F-FET PET, indien beschikbaar, de beste keuze is voor een differentiaal diagnose tussen herval van hooggradige glioma versus RN in de kliniek.

In de literatuur werden ook veelbelovende resultaten gepubliceerd over meer geavanceerde MRI technieken om een onderscheid te maken tussen tumorherval en RN. Dynamic contrast-enhanced MRI (DCE-MRI) laat toe om de vasculaire micro-omgeving van een hersentumor na therapie te karakteriseren. Doordat vasculaire eigenschappen, zoals vasculaire densiteit, permeabiliteit, bloedstroom en de samenstelling van de extravasculaire ruimte zeer waarschijnlijk verschillend zijn tussen GB en RN, is DCE-MRI een veelbelovende MR techniek om GB te onderscheiden van RN. In **hoofdstuk 7** werden semi-kwantitatieve parameters afgeleid uit DCE-MRI signaalintensiteit curves samen met kwantitatieve parameters verkregen aan de hand van KM vergeleken tussen ons GB en RN rat model. Op basis van onze resultaten zou een 5-min gedurende DCE-MRI acquisitie kunnen gebruikt worden om GB te onderscheiden van RN aan de hand van de wash-in snelheid (k) en de tijd nodig om de maximum signaal intensiteit te bereiken (TTP). Overige kwantitatieve en semi-kwantitatieve parameters waren niet in staat GB te onderscheiden van RN.

Een algemene discussie en een overzicht van de bredere internationale context, relevantie en toekomstperspectieven werden gegeven in **hoofdstuk 8 en 9**.

Curriculum Vitae

Personal information

Julie Bolcaen
Born: December 28th 1988, Menen (Belgium)
LinkedIn: www.linkedin.com/in/julie-bolcaen-7261b57a/
Email: julie.bolcaen@gmail.com

Work Experience

2011-now   <u>PhD in medical sciences</u>
'Assessment of therapy response and differentiation between tumor recurrence and therapy related effects in high-grade glioma using PET and MRI'
Ghent University
Promotor: Ingeborg Goethals, MD, Ph.D.

Teaching experience:
Mentor of Master students Biomedical Sciences and Medical Imaging technologists
Teaching assistant Prof. Goethals
Lecture Bachelor Biomedical Sciences, Antwerp - Translational Biomedical *In vivo* Imaging, Doctoral school, UGent

Education and training

2006-2011   <u>Master of science in Biomedical sciences</u>, option radiation science
Ghent University
Magna cum laude
Thesis: 'Radiogenomics and adverse effects of radiotherapy of prostate cancer patients'.
Promotor: Prof. Hubert Thierens

2006-now   <u>Relevant training certificates</u>
ESNM/ESTRO course on molecular imaging and radiation oncology, 2016, Lisbon, Portugal
Imaging of tumor heterogeneity (ESMOFIR), 2016, Utrecht, NL
Translational Biomedical *In vivo* Imaging, 2015, UGent
PET Methodology, 2012, King's college, Londen, UK
PMOD Biomedical Image Quantification, 2012, Zürich, Switzerland
Advanced academic English writing skills, 2012, UGent
Statistical analysis using SPSS, 2012, UGent
Course in ICH-GCP, 2011, UGent
Basic course in laboratory animal sciences, FELASA B+C, 2011, UGent

Academic and scientific experience

Research methods
- Experience in planning and performing clinical and preclinical research
- Experience in the field of medical imaging
- Experience in animal handling and development of animal models
- 6 years experience with preclinical research at the Innovative Flemish IN vivo Imaging TechnologY lab of Ghent University including PET/MRI/CT imaging and small animal irradiation
- Experience in writing preclinical and clinical trial proposals including ethical committee advice forms
- Funding proposals
- MRI and PET - guided 3D conformal arc micro-irradiation

- Catheterization - surgery of small animals
- Pharmacokinetic modeling of PET tracers
- High Pressure Liquid Chromatography
- Cell cultures (tumor cell lines)
- Autoradiography
- Cryosectioning tissues - Immunostaining
- Biomedical image quantification
- Working in multidisciplinary research teams
- Data management, statistics and interpretation of scientific data
- Presentation of data at international conferences
- Reporting and publication of results and reviewer of scientific publications

Awards and grants
- 2 x FWO grant for a short research stay abroad 2017 (1 month MAASTRO clinic and 1 month Turku PET center)
- SIE scholarship 2016 (€ 8000)
- FWO travel grant 2016
- Travel grant Faculty of Medicine and Health Sciences 2015, Ghent University
- Poster prize BMIC 2015
- BBTS prize at the BANO symposium 2013 (€ 3000)

Peer reviewed publications

Julie Bolcaen, Benedicte Descamps, Karel Deblaere, Filip De Vos, Tom Boterberg, Giorgio Hallaert, Caroline Van den Broecke, Christian Vanhove, Ingeborg Goethals. Assessment of the effect of therapy in a rat model of glioblastoma using ^{18}F-FDG and ^{18}F-FCho PET compared to contrast-enhanced MRI. Submitted to Contrast Media and Molecular Imaging; March 2017. IF = 3.286 Q1

Julie Bolcaen, Benedicte Descamps, Marjan Acou, Karel Deblaere, Caroline Van den Broecke, Tom Boterberg, Christian Vanhove, Ingeborg Goethals. In-vivo DCE-MRI for the discrimination between glioblastoma and radiation necrosis in rats. Molecular Imaging Biology 2017; doi: 10.1007/s11307-017-1071-0. IF = 2.569 Q1

Julie Bolcaen, Marjan Acou, Tom Boterberg, Christian Vanhove, Filip De Vos, Caroline Van den Broecke, Roel Van Holen, Karel Deblaere, Ingeborg Goethals. 18F-fluoromethylcholine (18F-FCho) PET and MRI for the prediction of response in glioblastoma patients according to the RANO criteria. Nuclear Medicine Communications 2017;38(3):242-249. IF = 1.453 Q2

Julie Bolcaen, Kelly Lybaert, Lieselotte Moerman, Benedicte Descamps, Karel Deblaere, Tom Boterberg, Jean-Pierre Kalala, Caroline Van den Broecke, Christian Vanhove, Ingeborg Goethals. Kinetic Modeling and Graphical Analysis of 18F-Fluoromethylcholine (FCho), 18F-Fluoroethyltyrosine (FET) and 18F-fluorodeoxyglucose (FDG) PET for the Discrimination between High-grade Glioma and Radiation Necrosis in Rats. Plos One 2016;11(10):e0164208. IF = 3.057 Q1

Julie Bolcaen, Benedicte Descamps, Karel Deblaere, Tom Boterberg, Filip De Vos Pharm, Jean-Pierre Kalala, Caroline Van den Broecke, Elke Decrock, Luc Leybaert, Christian Vanhove, Ingeborg Goethals. 18F-fluoromethylcholine (FCho), 18F-fluoroethyltyrosine (FET), and 18F-fluorodeoxyglucose (FDG) for the Discrimination Between High-grade Glioma and Radiation Necrosis in Rats: a PET Study. Nuclear Medicine and Biology 2015; 42(1):38-45. IF = 2.412 Q2

Julie Bolcaen, Benedicte Descamps, Karel Deblaere, Tom Boterberg, Giorgio Hallaert, Caroline Van den Broecke, Elke Decrock, Anne Vral, Luc Leybaert, Christian Vanhove, Ingeborg Goethals. MRI-guided 3D conformal arc micro-irradiation of a F98 glioblastoma rat model using the Small Animal Radiation Research Platform (SARRP). Journal Neuro-oncology 2014; 120(2):257-266. IF = 2.787 Q2

Julie Bolcaen, Marjan Acou, Koen mertens, Giorgio Hallaert, Caroline Van den Broecke, Eric Achten, Ingeborg Goethals. Functional imaging of 2 different variants of MS: a PET/MRI study. Journal of Neuroimaging 2013; 23(3):431-436. IF = 1.818 Q2

Koen Mertens, **Julie Bolcaen**, Ham Hamphrey, Karel Deblaere, Caroline Van den Broecke, Tom Boterberg, Filip De Vos, Ingeborg Goethals. The optimal timing for imaging brain tumours and lesions with F-18 labelled fluoromethylcholine: a dynamic PET study. Nuclear Medicine Communications 2012;33(9):954-959. IF = 1.379 Q2

Oral presentations

Julie Bolcaen, Kelly Lybaert, Lieselotte Moerman, Benedicte Descamps, Karel Deblaere, Tom Boterberg, Filip De Vos, Jean-Pierre Kalala, Caroline Van den Broecke, Christian Vanhove, Ingeborg Goethals. Kinetic modelling and graphical analysis of F-18 fluoromethylcholine (Fcho), F-18 fluoroethyltyrosine (FET), and F-18 fluorodeoxyglucose (FDG) PET for the discrimination between high-grade glioma and radiation necrosis in rats.
* European Molecular Imaging Meeting (EMIM), March 2016, Utrecht, The Netherlands
* International Conference on Neuro-Oncology, June 2016, Brisbane, Australia
* Congres ANOCEF BANO, June 2016, Brussel, Belgium
* Oncopoint, March 2016, Gent, Belgium
* Science Day Ghent University, March 2016, Gent, Belgium

Julie Bolcaen, Marjan Acou, Tom Boterberg, Christian Vanhove, Filip De Vos, Caroline Van den Broecke, Roel Van Holen, Karel Deblaere, Ingeborg Goethals. 18F-fluoromethylcholine (18F-FCho) PET and MRI for the prediction of response in glioblastoma patients according to the RANO criteria.
* Science Day Ghent University, March 2015, Gent, Belgium
* Oncopoint, February 2015, Gent, Belgium

Julie Bolcaen, Benedicte Descamps, Karel Deblaere, Tom Boterberg, Jean-Pierre Kalala, Caroline Van den Broecke, Filip De Vos, Christian Van Hove, Ingeborg Goethals. F-18 fluoromethylcholine (FCho), F-18 fluoroethylthyrosine (FET), F-18 fluordeoxyglucose (FDG) PET for the discrimination between high-grade brain tumour (recurrence) and radiation necrosis: a microPET study.
* European Molecular Imaging Meeting (EMIM), June 2014, Antwerp, Belgium
* Science Day Ghent University, March 2014, Gent, Belgium
* Oncopoint, February 2014, Gent, Belgium
* Belgian Association of Neuro-Oncology (BANO), November 2013, Diegem, Belgium

Non-expert audience:

PET imaging for the discrimination between high-grade glioma and radiation necrosis in rats.
* Studenten Onderzoek Symposium (SOS), April 2016, Ghent
Nieuwe merkers om hersentumoren in beeld te brengen.
* Stichting Luka Hemelaere, 2013-2017
* Rotary club Laarne-Lochristi, April 2017
* Soroptimist Kortrijk, January 2017, Marke, Belgium
* Soroptimist international Raad van afgevaardigden, January 2017, Brussel, Belgium
* Ladies Circle, April 2012, Hof Ten Steen Orsmaal, Belgium

Poster presentations

Julie Bolcaen, Kelly Lybaert, Lieselotte Moerman, Benedicte Descamps, Karel Deblaere, Tom Boterberg, Filip De Vos, Jean-Pierre Kalala, Caroline Van den Broecke, Christian Vanhove, Ingeborg Goethals. Kinetic modelling and graphical analysis of F-18 fluoromethylcholine (Fcho), F-18 fluoroethyltyrosine (FET), and F-18 fluorodeoxyglucose (FDG) PET for the discrimination between high-grade glioma and radiation necrosis in rats.
* International symposium on Quantification and standardisation in medical and preclinical imaging: state-of-the-art and future developments, September 2016, Groningen, The Netherlands

      * World Molecular Imaging Congress (WMIC), September 2016, New York, USA
      * European Association of Neuro-Oncology (EANO), October 2016, Mannheim, Germany
      * Belgian Association of Cancer Research (BACR), January 2016, Brussel, Belgium

Julie Bolcaen, Benedicte Descamps, Karel Deblaere, Giorgio Hallaert, Jean-Pierre Kalala, Christian Vanhove, Ingeborg Goethals. *In-vivo* DCE-MRI for the discrimination between glioblastoma and radiation necrosis in rats.
      * Belgian Association of Cancer Research (BACR), January 2017, Leuven, Belgium
      * World Molecular Imaging Congress (WMIC), September 2015, Honolulu, USA
      * Belgian Molecular Imaging Congress (BMIC), April 2015, Brussel, Belgium, Awarded the poster prize

Julie Bolcaen, Benedicte Descamps, Karel Deblaere, Tom Boterberg, Jean-Pierre Kalala, Caroline Van den Broecke, Filip De Vos, Christian Van Hove, Ingeborg Goethals. F-18 fluoromethylcholine (FCho), F-18 fluoroethylthyrosine (FET), F-18 fluordeoxyglucose (FDG) PET for the discrimination between high-grade brain tumour (recurrence) and radiation necrosis: a microPET study.
      * Annual Meeting of the Society of Nuclear Medicine (SNM), June 2014, St Louis, USA

Julie Bolcaen, Marjan Acou, Tom Boterberg, Christian Vanhove, Filip De Vos, Caroline Van den Broecke, Roel Van Holen, Karel Deblaere, Ingeborg Goethals. 18F-fluoromethylcholine (18F-FCho) PET and MRI for the prediction of response in glioblastoma patients according to the RANO criteria.
      * World Molecular Imaging Congress (WMIC), September 2014, Seoul, South-Korea
      * European Association of Neuro-Oncology (EANO), October 2014, Turin, Italy
      * Belgian Association of Cancer Research (BACR), January 2015, Leuven, Belgium

Julie Bolcaen, Giorgio Hallaert, Jean-Pierre Kalala, Tom Boterberg, Benedicte Descamps, Karel Deblaere, Caroline Van den Broecke, Ingeborg Goethals, Christian Vanhove. MRI-guided 3D-conformal arc micro-irradiation of a F98 glioblastoma rat model using a small animal radiation research platform.
      * Belgian Molecular Imaging Congress (BMIC), March 2013, Leuven, Belgium
      * World Molecular Imaging Congress (WMIC), September 2013, Savannah, USA

Non-expert audience:

Neuroscience at the department of nuclear medicine.
      * PhD day Neuroscience, March 2015, Gent, Belgium